

**ANALYSIS OF FLOW IN SOLAR CHIMNEY
FOR AN OPTIMAL DESIGN PURPOSE**

Atit Koonsrisuk

A Thesis Submitted in Partial Fulfillment of the Requirements for the

Degree of Doctor of Philosophy in Mechanical Engineering

Suranaree University of Technology

Academic Year 2009

การวิเคราะห์การไหลในระบบปล่องลมแดดเพื่อหาแนวทางออกแบบ
ให้ได้ประสิทธิภาพสูงสุด

นายอาทิตย์ คุณศรีสุข

วิทยานิพนธ์นี้เป็นส่วนหนึ่งของการศึกษาตามหลักสูตรปริญญาวิศวกรรมศาสตรดุษฎีบัณฑิต
สาขาวิชาวิศวกรรมเครื่องกล
มหาวิทยาลัยเทคโนโลยีสุรนารี
ปีการศึกษา 2552

ANALYSIS OF FLOW IN SOLAR CHIMNEY

FOR AN OPTIMAL DESIGN PURPOSE

Suranaree University of Technology has approved this thesis submitted in partial fulfillment of the requirements for the Degree of Doctor of Philosophy.

Thesis Examining Committee



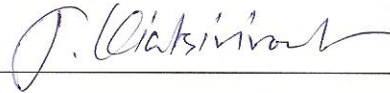
(Assoc. Prof. Dr. Kontorn Chamniprasart)

Chairperson



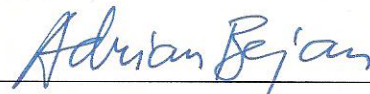
(Assoc. Prof. Dr. Tawit Chitsomboon)

Member (Thesis Advisor)



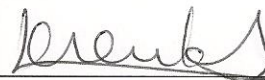
(Prof. Dr. Tanongkiat Kiatsiriroat)

Member



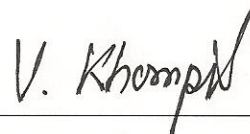
(Prof. Dr. Adrian Bejan)

Member



(Prof. Dr. Sylvie Lorente)

Member



(Assoc. Prof. Dr. Vorapot Khompis)



(Prof. Dr. Pairote Sattayatham)

Vice Rector for Academic Affairs

Dean of Institute of Engineering

อาทิตย์ คุณศรีสุข : การวิเคราะห์การไหลในระบบปล่องลมแดดเพื่อหาแนวทางออกแบบ
ให้ได้ประสิทธิภาพสูงสุด (ANALYSIS OF FLOW IN SOLAR CHIMNEY FOR AN
OPTIMAL DESIGN PURPOSE) อาจารย์ที่ปรึกษา : รองศาสตราจารย์ ดร.ทวิช
จิตรสมบูรณ์, 278 หน้า

รายงานวิทยานิพนธ์ศึกษาการไหลในระบบปล่องลมแดด ซึ่งเป็นอุปกรณ์ที่ใช้แสงแดดสร้างการไหลของลมขึ้นภายในระบบ จากนั้นใช้กังหันเทอร์ไบน์เปลี่ยนรูปพลังงานของกระแสลมไปเป็นกระแสไฟฟ้า จุดประสงค์หลักของงานวิทยานิพนธ์นี้เพื่อหาทางเพิ่มประสิทธิภาพให้ระบบ โดยศึกษาลักษณะการทำงานที่เหมาะสมสำหรับปล่องลมแดดเพื่อหาแนวทางออกแบบให้ได้ประสิทธิภาพสูงสุด

ในช่วงต้นของการศึกษานี้ ได้ใช้การวิเคราะห์มิติ (dimensional analysis) เพื่อหาตัวแปรไร้มิติ (dimensionless variables) ที่สำคัญสำหรับการไหลในระบบปล่องลมแดด เพื่อช่วยในการออกแบบการทดลอง ที่สามารถใช้ข้อมูลที่ทดสอบจากแบบจำลองระบบปล่องลมแดดขนาดเล็ก ในการทำนายผลที่จะเกิดขึ้นในโรงงานต้นแบบปล่องลมแดดได้ จากการศึกษาพบว่า เมื่อแบบจำลองขนาดเล็ก (model) มีความเสมือนทางด้านรูปทรง (geometric similarity) กับโรงงานต้นแบบ (prototype) ระบบทั้งสองจะมีความเสมือนทางด้านพลศาสตร์ (dynamic similarity) ก็ต่อเมื่อ ค่าความเข้มแสงแดด (insolation) ของระบบทั้งสองต้องไม่เท่ากัน ซึ่งเป็นสภาวะที่ทำให้ยากในทางปฏิบัติ อย่างไรก็ตาม ในการศึกษาที่บังคับให้ค่าความเข้มแสงแดดของระบบทั้งสองต้องเท่ากันพบว่า ระบบทั้งสองสามารถมีความเสมือนทางด้านพลศาสตร์ได้ หากระบบทั้งสองมีความเสมือนทางด้านรูปทรงเพียงบางส่วน (partial geometric similarity) กล่าวคือ รัศมีหลังคาร์รับแดด (solar collector) ของแบบจำลองต้องสั้นกว่าที่ควรจะเป็นสำหรับแบบจำลองที่มีความเสมือนทางด้านรูปทรงกับโรงงานต้นแบบ ในการตรวจสอบความถูกต้องของผล ที่ได้จากการวิเคราะห์มิตินี้ ผู้วิจัยได้ใช้การคำนวณเชิงตัวเลข (numerical method) เพื่อหาค่าคุณสมบัติการไหล (flow properties) ในระบบ แล้วนำผลที่ได้มาคำนวณหาค่าตัวแปรไร้มิติ ซึ่งผลการคำนวณยืนยันความน่าเชื่อถือที่พบในการศึกษานี้ และจากรูปแบบความสัมพันธ์ระหว่างตัวแปรไร้มิติที่ค้นพบในครั้งนี้ ได้นำไปสู่การยุบรวมตัวแปรที่สำคัญของระบบทั้งหมดได้เป็นตัวแปรไร้มิติเพียงหนึ่งตัวแปร ซึ่งจากการคำนวณเชิงตัวเลขและผลการทดลองจากโรงงานต้นแบบที่ได้เคยมีการสร้างไว้จริงที่ประเทศสเปนพบว่า ค่าตัวแปรไร้มิติตัวใหม่ที่มีค่าประมาณ 1 สำหรับแบบจำลองทุกขนาดที่มีการตรวจสอบ

จากนั้นได้นำผลที่ตัวแปรไร้มิติมีค่าเท่ากับ 1 นี้ ไปสร้างเป็นแบบจำลองคณิตศาสตร์ (mathematical model) เพื่อใช้ประเมินศักยภาพของระบบปล่องลมแคด และใช้เปรียบเทียบกับผลการคำนวณของแบบจำลองคณิตศาสตร์ที่นักวิจัยท่านอื่นได้พัฒนาไว้อีกจำนวน 5 แบบจำลอง โดยในการคำนวณนี้ได้ศึกษาผลกระทบเมื่อขนาดของโรงงาน ได้แก่ รัศมีกับความสูงของหลังคารับแคด และรัศมีกับความสูงของปล่องลมเปลี่ยนไป รวมทั้งผลกระทบเมื่อความเข้มแสงแคดเปลี่ยนไปด้วย เมื่อเปรียบเทียบผลการคำนวณทั้งหมดกับผลการคำนวณเชิงตัวเลขจากโปรแกรมสำเร็จรูป พบว่าแต่ละแบบจำลองมีข้อดี-ข้อเสียต่างกันไป ซึ่งในการศึกษานี้ได้ให้คำแนะนำในการเลือกใช้แบบจำลองที่เหมาะสมไว้ด้วย

เมื่อได้ศึกษาผลกระทบของการเปลี่ยนแปลงขนาดหน้าตัดการไหล โดยใช้แบบจำลองคณิตศาสตร์ร่วมกับการคำนวณเชิงตัวเลขพบว่า เมื่ออัตราส่วนระหว่างพื้นที่หน้าตัดของหลังคารับแคดที่ทางเข้าต่อด้วยที่ทางออกมีค่าน้อยกว่า 1 จะสามารถเพิ่มศักยภาพให้ระบบได้ และเมื่ออัตราส่วนระหว่างพื้นที่หน้าตัดของปล่องลมที่ทางออกต่อด้วยที่ทางเข้ามีค่ามากกว่า 1 ศักยภาพของระบบก็เพิ่มขึ้นเช่นกัน และสำหรับระบบที่ใช้หลังคารับแคดที่มีอัตราส่วนระหว่างพื้นที่หน้าตัดที่ทางเข้าต่อด้วยที่ทางออกมีค่าน้อยกว่า 1 ร่วมกับปล่องลมที่มีอัตราส่วนระหว่างพื้นที่หน้าตัดที่ทางออกต่อด้วยที่ทางเข้ามีค่ามากกว่า 16 พบว่าค่าศักยภาพของระบบเพิ่มขึ้นหลายร้อยเท่าจากระบบปกติที่ใช้กัน

ในการศึกษาที่กล่าวมาแล้วนั้น เนื่องจากการประเมินศักยภาพของระบบจึงยังไม่ได้รวมกังหันเทอร์ไบน์ไว้ในการศึกษา และเมื่อได้มีการพัฒนาแบบจำลองคณิตศาสตร์ที่รวมกังหันเทอร์ไบน์ไว้ด้วย พบว่า ค่าอัตราส่วนระหว่างความดันที่กังหันเทอร์ไบน์ดูดซับไว้ได้ต่อด้วยความดันรวมที่เกิดขึ้นในระบบมีค่าเท่ากับ $2/3$ สำหรับระบบที่กำหนดให้ความดันรวมดังกล่าวนี้มีค่าคงที่ไม่ขึ้นกับความดันที่กังหันเทอร์ไบน์ดูดซับไว้ได้ แต่สำหรับระบบที่ให้ความดันรวมแปรผันได้ตามความดันที่กังหันเทอร์ไบน์ดูดซับพบว่า ค่าอัตราส่วนของความดันดังกล่าวนี้มีค่าเปลี่ยนแปลงขึ้นกับขนาดโรงงานและความเข้มแสงแคด

เพื่อจะประเมินผลการศึกษาเชิงทฤษฎีและเชิงตัวเลข ได้มีการสร้างแบบจำลองขนาดเล็กของระบบปล่องลมแคดที่ไม่มีกังหันเทอร์ไบน์ขึ้นจำนวน 4 ชุดที่มหาวิทยาลัยเทคโนโลยีสุรนารี อ.เมือง จ.นครราชสีมา พบว่าผลการทดลองมีค่าต่างไปจากค่าที่ทำนายไว้ แต่มีแนวโน้มของข้อมูลเหมือนที่ทำนายไว้ ซึ่งคาดว่าเป็นผลเนื่องจากความเข้มแสงแคดที่ไม่คงที่ขณะทำการทดลองและเนื่องจากระบบมีหลังคาที่เล็กไปเมื่อเทียบกับขนาดของปล่องลม นอกจากนี้ ค่าตัวแปรไร้มิติที่คำนวณจากชุดทดลองที่ออกแบบให้มีความเหมือนกันทางพลศาสตร์ ก็มีความต่างกันซึ่งคาดว่าเป็นผลเนื่องจากความผันแปรของสภาพอากาศขณะวัดผล

เมื่อใช้ constructal theory ในการออกแบบระบบปล่องลมแดด สามารถหาค่าที่เหมาะสมของอัตราส่วนระหว่างความสูงของปล่องลมต่อดัวยรัศมีของหลังคารับแดด ค่าอัตราการใช้และกำลังสูงสุดที่ระบบสามารถทำได้ทั้งแบบที่มีเงื่อนไขว่าพื้นที่ผิวของระบบต้องคงที่และแบบที่ปริมาตรรวมของระบบต้องคงที่ ผลการศึกษาชี้ว่า ความดันสูญเสียที่ทางเข้าหลังคาและที่สูญเสียที่รอยต่อระหว่างหลังคา กับปล่องลมมีค่าต่ำมากสามารถตัดทิ้งจากการคำนวณได้ และในกรณีที่ค่า svelteness ของระบบมีค่ามากกว่า 6.5 ค่าความดันสูญเสียเนื่องจากแรงเสียดทานในส่วนหลังคารับแดดก็สามารถตัดทิ้งได้เช่นกัน นอกจากนี้ยังพบว่า ศักยภาพสูงสุดของโรงงานปล่องลมแดดจะเกิดขึ้นเมื่อโรงงานมีขนาดที่เหมาะสม โดยโรงงานขนาดใหญ่จะมีประสิทธิภาพสูงกว่าโรงงานขนาดเล็ก

ATIT KOONSRIK : ANALYSIS OF FLOW IN SOLAR CHIMNEY FOR AN OPTIMAL DESIGN PURPOSE. THESIS ADVISOR : ASSOC. PROF. TAWIT CHITSOMBOON, Ph.D., 278 PP.

SOLAR CHIMNEY/SOLAR TOWER/DIMENSIONAL ANALYSIS/GEOMETRIC EFFECTS/THEORETICAL MODEL/SOLAR ENERGY/CONSTRUCTAL DESIGN/NATURAL CONVECTION.

The thesis studies flow in a solar chimney, a device for generating electricity from solar energy by means of a turbine extracting the flow energy from the hot air rising through a tall chimney with the ultimate goal of a better design to obtain a higher efficiency. Operating characteristics that are significant to the flow in solar chimney are sought and studied to aid in the optimization of solar chimney design.

Dimensional analysis is applied to determine the dimensionless variables to guide the experimental study of flow in a small-scale solar chimney model. The study shows that if the model is required to be geometrically similar to the prototype, then the dynamic similarity condition requires the solar heat fluxes of the two cases to be different, an inconvenient requirement in an experimental setup. Further study shows that, to achieve the same-heat-flux condition, the roof radius between the prototype and its scaled models must be dissimilar, while all other remaining dimensions of the models remain similar to those of the prototype. The functional relationship obtained suggests that it would be possible to group all the relevant variables into a single dimensionless product. Three physical configurations of the plant were numerically tested for similarity: fully geometrically similar, partially geometrically similar, and dissimilar types. The values of the proposed single dimensionless variable for all these

cases are found to be nominally equal to unity. The value for the physical plant actually built and tested previously is also evaluated and found to be about the same as that of the numerical simulations, suggesting the validity of the proposition.

Moreover, the study compares the predictions of performances of solar chimney power plants by using five theoretical models that have been proposed in the literature. The parameters used in the study are various plant geometrical parameters and the solar heat flux. Numerical results from the carefully calibrated CFD simulations are used for comparison with the theoretical predictions. The power output and the efficiency of the solar chimney plants are used as functions of the studied parameters to compare relative merits of the five theoretical models. Models that performed better are finally recommended.

Guided by a theoretical prediction, CFD is used to investigate the changes in flow properties caused by the variation of flow area. It appears that the sloping collector affects the flow properties through the plant. The divergent-top chimney leads to significant augmentations in kinetic energy at the tower base. It is shown that the proper combination of the sloping roof and the divergent-top chimney can produce power as much as hundreds times that of the conventional solar chimney power plant.

An analytical turbine model is developed in order to evaluate the performance of the solar chimney power plant. The relationships between the ratio of the turbine pressure drop to the pressure potential (available system pressure difference), the mass flow rate, the temperature rise across the collector and the power output are presented. The model shows that, for the system with a constant pressure potential, the optimum ratio of the turbine pressure drop to the pressure potential is $2/3$. For the system with

non-constant pressure potential, it is clear that this optimum ratio is a function of the plant size and solar heat flux.

To evaluate the performance of a small-scale physical model, four experimental plants were constructed at Suranaree University of Technology, Nakhon Ratchasima Province, Thailand. The experimental results are different but show the same trends as the predicted values. This may be caused by the fluctuating solar heat flux and the effect of the large chimney diameter when compared with the roof size. Moreover, the difference in dimensionless variables between the large and the small plant is noticeable, contrary to the theoretical and numerical predictions. Reasons could be the varying atmospheric conditions when the tests were run.

Based on the method of constructal design, the optimal chimney height/roof radius, maximum mass flow rate and maximum power under the constraints of fixed surface area and volume are determined. Results indicate that the pressure drop at the collector inlet and at the transition section between the collector and chimney are negligible and the friction loss in the collector might be neglected when the svelteness is greater than 6.5. Because of the flow resistances associated with distribution of power over a territory, the size of the territory must be finite and optimally allocated to each power plant. Several patterns of the multi-scale plants on a square area are explored. The global performance of such patterns is greater when more land area is allocated for the largest plant.

School of Mechanical Engineering

Academic Year 2009

Student's Signature อรรถวิทย์ อภิธรรม

Advisor's Signature ดร.วิวัฒน์

ACKNOWLEDGEMENTS

The process of bringing this thesis to its final state has not been smooth; it has run a gauntlet of various discouraging and disappointing circumstances. However, through the support and understanding of many this thesis is now complete. It is my great pleasure to thank many people who have contributed to this thesis.

I would like to thank Dr.Tawit Chitsomboon for the role he has played as my thesis advisor. Despite a very busy schedule, he always found the time to listen and to offer constructive advice. His suggestions have always been excellent and he has been a pleasure to work with.

With gratitude, I acknowledge the advice and expertise of the brilliant teachers who helped me learn thermal physics, Dr.Vorapot Khompis. I also would like to thank Dr.Kontorn Chamniprasart for the support and encouragement he has given me. In addition, I am also thankful for the support and useful advice from Dr.Eckart Schulz.

It has been a pleasure to know Dr.Arjuna Peter Chaiyasena and his wife, Mantana, whose confidence in my ability has always exceeded my own. To them, I express my warm appreciation and sincere thanks.

I am greatly indebted to Prof. Adrian Bejan, Duke University, and Prof. Sylvie Lorente, Université de Toulouse, for their generous support in so many ways. I would like to thank them for their kind encouragements. I would also like to thank Duke University for their support of my research activities as a Visiting Research Scholar in the Constructal Design Group at Duke University.

I thank the faculty and staff of Suranaree University of Technology, for providing support in a multitude of forms, and especially for creating an environment

in which research work was valued and encouraged. I take this opportunity to extend my very sincere thanks to Mr.Prasittichai Dumnoentitikij, Mr.Satip Churirutporn and Mr.Satta Posawang, the staff of the Center for Scientific and Technological Equipment of Suranaree University of Technology, for their ungrudging moral and technical support in this work.

I owe special thanks to my friends and their families for their invaluable help and encouragement. Their influence and stimulation are impossible to quantify or detail in full. Six people, however, may be fondly acknowledged: Mr.Chatchai Chanprasert, Mr.Chawean Chaiyapoom, Mr.Choowong Chareonsawat, Mr.Khajornwit Uttawat, Mr.Methee Sophon, and Mr.Somporn Srichoo. It was and is a pleasure to know all of them.

This research has been supported financially by the Royal Golden Jubilee (RGJ) Ph.D. Program of the Thailand Research Fund (TRF). The support is gratefully acknowledged.

Finally, I shall be failing in my obligation if I do not express a special acknowledgement to my mother, Mrs.Neeracha Koonsrisuk. She endured missing me for a long time while the thesis was being studied, but provided me steadfast support and understanding. Her encouragement and patience have been unlimited.

Let me end the list here and note that, despite all the help and advice I received, I remain responsible for errors and infelicities of this thesis.

Atit Koonsrisuk

TABLE OF CONTENTS

	Page
ABSTRACT (THAI)	I
ABSTRACT (ENGLISH)	IV
ACKNOWLEDGEMENT	VII
TABLE OF CONTENTS	IX
LIST OF TABLES	XV
LIST OF FIGURES	XVII
LIST OF SYMBOLS AND ABBREVIATIONS	XXVI
CHAPTER	
I INTRODUCTION	1
1.1 Rationale of the Study	1
1.2 Research Objectives	7
1.3 Thesis Contents	7
1.4 Expectation	10
1.5 Reference	10
II LITERATURE REVIEW	11
Reference	14

TABLE OF CONTENTS (continued)

	Page
III DYNAMIC SIMILARITY IN SOLAR	
CHIMNEY MODELING	17
3.1 Abstract	17
3.2 Introduction	17
3.3 Dimensional Analysis.....	21
3.4 CFD Modeling.....	29
3.5 Results and Discussion.....	33
3.6 Conclusion.....	41
3.7 Reference.....	43
IV PARTIAL GEOMETRIC SIMILARITY FOR SOLAR	
CHIMNEY POWER PLANT MODELING	45
4.1 Abstract	45
4.2 Introduction	46
4.3 Dimensional Analysis.....	50
4.4 Computational Work	55
4.5 Results and Discussion.....	58
4.6 Engineering Interpretation of the Dimensionless variables	63
4.7 Conclusion.....	64
4.8 Reference.....	65

TABLE OF CONTENTS (continued)

		Page
V	A SINGLE DIMENSIONLESS VARIABLE FOR SOLAR CHIMNEY POWER PLANT MODELING	68
	5.1 Abstract	68
	5.2 Introduction	69
	5.3 Dimensional Analysis.....	72
	5.4 Computational Work	74
	5.5 Results and Discussion.....	78
	5.6 Conclusion.....	88
	5.7 Reference.....	89
VI	ACCURACY OF THEORETICAL MODELS IN THE PREDICTION OF SOLAR CHIMNEY POWER PLANT PERFORMANCE	91
	6.1 Abstract	91
	6.2 Introduction	91
	6.3 Theoretical Models.....	93
	6.4 Computational Work	98
	6.5 Results and Discussion.....	100
	6.6 Conclusion.....	111
	6.7 Reference.....	112

TABLE OF CONTENTS (continued)

	Page
VII EFFECT OF FLOW AREA CHANGE ON THE POTENTIAL OF SOLAR CHIMNEY POWER PLANT	114
7.1 Abstract	114
7.2 Introduction	114
7.3 Derivation of the Theoretical Models.....	117
7.4 Computational Work	121
7.5 Results and Discussion.....	126
7.6 Conclusion.....	130
7.7 Reference.....	138
VIII THEORETICAL TURBINE POWER YIELD IN SOLAR CHIMNEY POWER PLANT.....	140
8.1 Abstract	140
8.2 Introduction	141
8.3 Optimal Pressure Ratio.....	143
8.4 Analytical Model.....	146
8.5 Analytical Solution Procedure.....	149
8.6 Results and Discussion.....	150
8.7 Conclusion.....	163
8.8 Reference.....	170

TABLE OF CONTENTS (continued)

	Page
IX EXPERIMENTAL PERFORMANCE OF A DEMONSTRATION SOLAR CHIMNEY MODEL	173
9.1 Abstract	173
9.2 Introduction	174
9.3 The physical Models	175
9.4 Experimental Methodology	175
9.5 Computational Works.....	176
9.6 Results and Discussion.....	177
9.7 Conclusion.....	224
9.8 Problems and Challenges in the Research.....	225
9.9 Reference.....	226
X CONSTRUCTAL SOLAR CHIMNEY CONFIGURATION AND MULTI-SIZE DISTRIBUTION ON LAND	227
10.1 Abstract	227
10.2 Introduction	228
10.3 Geometry	231
10.4 Pumping Effect.....	231
10.5 More Air Flow Rate	234
10.6 More Power	236
10.7 Volume Constraint	238

TABLE OF CONTENTS (continued)

	Page
10.8 Model Validation.....	239
10.9 Additional Losses	244
10.10 Few large, or many small?	246
10.11 Conclusion.....	261
10.12 Reference.....	262
XI CONCLUSION AND RECOMMENDATION.....	264
 APPENDICES	
APPENDIX A A SET UP OF THE ANSYS-CFX 10.0 SOLVER.....	268
APPENDIX B LIST OF PUBLICATIONS	275
BIOGRAPHY.....	278

LIST OF TABLES

Table	Page
1.1 Advantages and disadvantages of the solar chimney technology	8
1.2 Categories of the approaches used in each chapter.....	9
3.1 Powers of primitive variables in terms of fundamental dimensions.....	25
3.2 Solar heat absorption per unit volume (S.H.A.V.) requirements for dynamic similarity.....	42
4.1 Specification of prototype and models	56
5.1 Specification of prototype and models	76
5.2 Dimensionless variable for prototype and models.....	81
6.1 List of unknowns in theoretical models.....	101
6.2 Boundary conditions (based on the settings for ANSYS CFX).....	101
7.1 List of models illustrated in Fig. 7.2.....	124
7.2 Power at the chimney base scaled by the power of the reference case, the square of AR_{43} and the efficiency at chimney entrance, $\eta = 100 \times 0.5 \dot{m} V_3^2 / q'' A_r$	137
8.1 Geometrical dimensions of the pilot plant in Manzanares, Spain	154
8.2 Comparison between measured data from Manzanares pilot plant and theoretical results; data on 2 nd September 1982.....	154
8.3 Data of Manzanares pilot plant for 1 st September 1989.	155

LIST OF TABLES (Continued)

Table	Page
8.4 Comparison between measured data from Manzanares pilot plant and theoretical results. (data on 1 st September 1989)	155
9.1 Specification of the Experimental Sets	179
9.2 Details of measuring locations	188
9.3 Descriptions of the test cases	195
9.4 Power of the test cases scaled by the power of its reference case	211
9.5 Comparative data for dimensional analysis	222
10.1 The global power output of the multi-size arrangements (a) – (e) shown in Fig. 10.6.....	258

LIST OF FIGURES

Figure	Page
1.1 .Schematic layout of solar chimney power plant.....	3
3.1 .Schematic layout of solar chimney power plant.....	20
3.2 Unstructured mesh used for the 5 degree axis-symmetric computational domain.....	31
3.3 Π_1 vs. number of grid elements.....	32
3.4 Typical velocity field around the junction of the roof and the chimney	36
3.5 Numerical prediction of velocity profiles for insolation = 800 W/m ²	37
3.6 Numerical prediction of temperature profiles for insolation = 800 W/m ²	38
3.7 Numerical prediction of pressure profiles for insolation = 800 W/m ²	39
3.8 $\Pi_1 - \Pi_2$ characteristics.....	40
4.1 Schematic layout of solar chimney power plant.....	47
4.2 Computational domain: (a) 5 degree axis-symmetric section; (b) numerical grid.	57
4.3 Numerical prediction of updraft velocity at tower top as a function of insolation.....	60

LIST OF FIGURES (Continued)

Figure	Page
4.4	Numerical prediction of flow power as a function of insolation. 61
4.5	$\Pi_1 - \Pi_2$ characteristics..... 62
5.1	Schematic layout of solar chimney power plant. 70
5.2	Computational domain: (a) 5 degree axis-symmetric section; (b) computational grid..... 77
5.3	Numerical prediction of updraft velocity at tower top as a function of insolation 79
5.4	Numerical prediction of temperature at roof exit as a function of insolation 80
5.5	Numerical prediction of temperature profiles for insolation $= 1,000 \text{ W/m}^2$ 85
6.1	Schematic layout of solar tower plant..... 94
6.2	Computational domain: (a) 5 degree axis-symmetric section; (b) numerical grid 102
6.3	Effect of roof radius on plant performance for insolation $= 800 \text{ W/m}^2$ 106

LIST OF FIGURES (Continued)

Figure	Page
6.4	Effect of roof height on plant performance for insolation = 800 W/m ² 107
6.5	Effect of tower radius on plant performance for insolation = 800 W/m ² 108
6.6	Effect of tower height on plant performance for insolation = 800 W/m ² 109
6.7	Effect of insolation on plant performance 110
7.1	The main features of a solar chimney 116
7.2	Schematic layout of (a) reference plant; (b) a sloping collector with a constant-area chimney; (c) a constant-height collector with a convergent-top chimney; (d) a constant-height collector with a divergent-top chimney; (e) a sloping collector with a convergent-top chimney; (f) a sloping collector with a divergent-top chimney 123
7.3	Computational domain: (a) 5 degree axis-symmetric section; (b) Side view of the domain 125
7.4	Effect of area variation on the pressure profiles 131
7.5	Effect of area variation on the mass flow rate (scaled by the mass flow rate of the reference case) 132

LIST OF FIGURES (Continued)

Figure	Page
7.6	Effect of area variation on the collector temperature rise (scaled by the temperature rise of the reference case) 133
7.7	Effect of AR_{12} on the flow power (scaled by the flow power of prototype at position 3) 134
7.8	Effect of AR_{43} on the flow power (scaled by the flow power of prototype at position 3) 135
7.9	Combined effect of AR_{12} and AR_{43} on the flow power (scaled by the flow power of prototype at position 3) 136
8.1	Schematic layout of solar chimney power plant 142
8.2	Momentary measurements on 2 nd September 1982 from Manzanares prototype plant: a) global radiation I and T_1 152 b) thermal efficiency of the collector 152 c) ΔT_{12} and V_c 153 d) pressure differences 153
8.3	Influence of the mass flow rate on the power output for solar irradiation = 600 W/m ² . ($h_r = 2$ m and $r_c = 4$ m for all plants) 157
8.4	Influence of the pressure ratio [cf. Eq. (8.2)] on the power output for solar irradiation = 600 W/m ² . ($h_r = 2$ m and $r_c = 4$ m for all plants) 158

LIST OF FIGURES (Continued)

Figure	Page
8.5 Influence of the mass flow rate on the collector temperature rise for solar irradiation = 600 W/m^2 . ($h_r = 2 \text{ m}$ and $r_c = 4 \text{ m}$ for all plants)	159
8.6 Influence of the mass flow rate on the power output along lines of constant solar irradiation. ($h_r = 2 \text{ m}$, $r_r = 200 \text{ m}$, $h_c = 400 \text{ m}$ and $r_c = 4 \text{ m}$ for all cases)	160
8.7 Influence of the pressure ratio on the power output along lines of constant solar irradiation. ($h_r = 2 \text{ m}$, $r_r = 200 \text{ m}$, $h_c = 400 \text{ m}$ and $r_c = 4 \text{ m}$ for all cases)	161
8.8 Influence of the mass flow rate on the total pressure potential along lines of constant solar irradiation. ($h_r = 2 \text{ m}$ and $r_c = 4 \text{ m}$ for all plants)	164
8.9 Influence of the mass flow rate on the turbine pressure drop along lines of constant solar irradiation. ($h_r = 2 \text{ m}$ and $r_c = 4 \text{ m}$ for all plants)	165
8.10 Influence of the mass flow rate on the useful heat gain extracted from the collector along lines of constant solar irradiation ($h_r = 2 \text{ m}$ and $r_c = 4 \text{ m}$ for all plants)	166

LIST OF FIGURES (Continued)

Figure	Page
8.11 Influence of the mass flow rate on the collector efficiency [cf. Eq. (8.26)] along lines of constant solar irradiation. ($h_r = 2$ m and $r_c = 4$ m for all plants)	167
8.12 Influence of the mass flow rate on the dimensionless Δp_{13} [cf. Eq. (8.29)] along lines of constant solar irradiation. ($h_r = 2$ m and $r_c = 4$ m for all plants)	168
8.13 Influence of the mass flow rate on the plant total pressure loss along lines of constant solar irradiation. ($h_r = 2$ m and $r_c = 4$ m for all plants)	169
9.1 Schematic layout of solar chimney power plant	178
9.2 Layout of Experimental Set 1	180
9.3 Layout of Experimental Set 2	182
9.4 Layout of Experimental Set 3	184
9.5 Layout of Experimental Set 4	186
9.6 Layout of measuring locations.....	189
9.7 Descriptions of flow parameters for the calculations of average properties.....	190

LIST OF FIGURES (Continued)

Figure	Page	
9.8	Computational domain of Experimental Sets 1, 2 and 4: (a) 5 degree axis-symmetric section; (b) computational grid of Experimental Set 1; (c) computational grid of Experimental Set 2; (d) computational grid of Experimental Set 4.....	191
9.9	Computational domain of Experimental Set 3: (a) layout; (b) computational grid	192
9.10	Boundary settings of computation domain	193
9.11	Airflow properties of experimental Case 1: (a) velocity distribution; (b) temperature distribution	196
9.12	Illustration of the shadow of the chimney casting on the roof.....	200
9.13	Airflow properties of experimental Case 2: (a) velocity distribution; (b) temperature distribution	201
9.14	Airflow properties of experimental Case 3: (a) velocity distribution; (b) temperature distribution.	204
9.15	Airflow properties of experimental Case 4: (a) velocity distribution; (b) temperature distribution	205
9.16	Airflow properties of experimental Case 5: (a) velocity distribution; (b) temperature distribution	206
9.17	Airflow properties of experimental Case 6: (a) velocity distribution; (b) temperature distribution	207

LIST OF FIGURES (Continued)

Figure	Page
9.18	Illustration of the flow direction under the sloping roof..... 210
9.19	Airflow properties of experimental Case 7: (a) velocity distribution; (b) temperature distribution. 214
9.20	Illustration of the roof access system of Experiment Set 3..... 215
9.21	(a) velocity vectors of flow under the roof of Experiment Set 3; (b) magnification of the recirculation zone..... 217
9.22	Airflow properties of experimental Case 8: (a) velocity distribution; (b) temperature distribution. 219
9.23	Airflow properties of experimental Case 9: (a) velocity distribution; (b) temperature distribution. 220
9.24	Airflow properties of experimental Case 10: (a) velocity distribution; (b) temperature distribution. 221
10.1	The main features of a solar chimney..... 229
10.2	Comparison between theoretical model and numerical model..... 242
10.3	The power predictions from theoretical model..... 243
10.4	Pressure losses scaled by the pressure acceleration in a collector as a function of svelteness..... 248
10.5	Designs of the projection pattern for multi-scale solar chimneys on the square land. 254

LIST OF FIGURES (Continued)

Figure	Page
10.6 Redesign of the patterns in Fig. 10.5, in which all designs share the same territory (X) and the same largest element (D_0). (Note: Fig. 10.6a is exactly the same as Fig. 10.5a)	256
10.7 Compactness [cf. Eq. (10.56)] and dimensionless power [cf. Eq. (10.45)] of the power plants in Fig. 10.6.	259

LIST OF SYMBOLS AND ABBREVIATIONS

a	constant
A	flow area, m ²
A	horizontal area, m ²
A_c	cross-sectional area, m ²
A_r	roof area, m ²
AR_{12}	ratio of the collector inlet area to the collector outlet area
AR_{43}	ratio of the chimney outlet area to the chimney inlet area
b	constant
b	number of basic dimensions involved
C	compactness
$C_{1,2,3,4}$	constants
c_p	specific heat at constant pressure, J/(kg.K)
D_i	disc diameters, m
f	friction factor
g	gravitational acceleration, m/s ²
Gr	Grashof number
h	height, m
h_c	chimney height, m
h_r	roof height above the ground, m

LIST OF SYMBOLS AND ABBREVIATIONS (Continued)

h_{total}	total enthalpy, m^2/s^2
I	solar irradiation, W/m^2
K_{inlet}	collector inlet loss coefficient
l	constant
M	Mach number
\dot{m}	mass flow rate, kg/s
n	constant
n	total number of quantities involved
p	pressure, Pa
q	heat transfer rate per unit mass, W/kg
q''	insolation, W/m^2
q'''	solar heat source per unit volume, W/m^3
R	ideal gas constant, $J\ kg^{-1}K^{-1}$
r	radius, m
R_i	disc radii, m
Re	Reynolds number
Ri	Richardson number
r_c	chimney radius, m
r_r	roof radius, m
S	source term in ANSYS CFX
S	territory, m^2

LIST OF SYMBOLS AND ABBREVIATIONS (Continued)

s	number of dimensionless variables
S_E	source term in energy equation, W/m^3
S_M	source term in momentum equations, N/m^3
S_ϕ	source term
Sv	svelteness
T	absolute temperature, K
T_0	atmospheric temperature, K
t	time, s
U	collector loss coefficient, $\text{W/m}^2\cdot\text{K}$
u	velocity vector
V	flow velocity, m/s
Vol	volume, m^3
\dot{W}	flow power, W
X	side of square territory, m^2
x	general coordinate
x	pressure ratio, Eq. (8.2)
z	cartesian coordinate in vertical direction
∇	chimney volume, m^3

LIST OF SYMBOLS AND ABBREVIATIONS (Continued)

Greek symbols

α	collector absorption coefficient
β	volumetric coefficient of thermal expansion, 1/K
Δp	pressure drop, Pa
Δp_{acc}	acceleration pressure drop, Pa
Δp_{inlet}	collector inlet pressure drop, Pa
$\Delta p_{junction}$	pressure drop at the collector-to-chimney transition section, Pa
ΔT	temperature difference in roof portion, K
$\Delta \rho$	density difference
$\varepsilon_{junction}$	loss coefficient at the collector-to-chimney transition section
Φ	auxiliary function, Eq. (10.17)
ϕ	flow variable
Γ_{ϕ}	diffusion coefficient, Ns/m^2
γ	specific heat ratio
γ_{∞}	lapse rate of temperature (K/m)
η	efficiency
η_{col}	collector efficiency
λ	Lagrange multiplier
λ	thermal conductivity, W/mK
ν	specific volume

LIST OF SYMBOLS AND ABBREVIATIONS (Continued)

Π	dimensionless parameter
ρ	density, kg/m ³
ρ_0	air density at T_0 , kg/m ³
Σ	quantity proportional to the total power generation rate
τ	fluid shear stress
Ψ	auxiliary function, Eq. (10.22)
<i>Subscripts</i>	
1	position at roof inlet
2	position at roof outlet
3	position at chimney inlet
4	position at chimney outlet
<i>c</i>	chimney
<i>const</i>	constant
<i>dyn</i>	dynamic pressure component
<i>ext</i>	extraction by the turbine
<i>i</i>	component i
<i>j</i>	component j
<i>loss</i>	difference between the total pressure potential and the turbine pressure drop
<i>m</i>	model

LIST OF SYMBOLS AND ABBREVIATIONS (Continued)

<i>max</i>	maximum
<i>no turb</i>	without turbine
<i>o</i>	overall
<i>opt</i>	optimum
<i>p</i>	constant pressure process or potential or prototype
<i>r</i>	roof
<i>ref</i>	reference state
<i>t</i>	turbine
<i>tot</i>	total pressure component
<i>turb</i>	turbine
<i>w</i>	wall
<i>with turb</i>	with turbine
<i>x</i>	horizontal passage
<i>y</i>	vertical passage
∞	free stream

CHAPTER I

INTRODUCTION

1.1 RATIONALE OF THE STUDY

Current electricity production from fossil fuels like natural gas, oil or coal is damaging to the environment and stresses the limitation that it relies upon non-renewable energy sources. Many developing countries cannot afford these conventional energy sources, and in some of these locations nuclear power is considered an unacceptable risk. It has been shown that a lack of energy may be connected to poverty and power to population explosions. The need for an environmentally friendly and cost effective electricity generating scheme is thus clearly indicated and will become more pronounced in the future.

A possible solution to this ever-increasing problem is solar energy. It is an abundant, renewable source of energy that only needs to be harnessed to be of use. Solar power plants in use in the world are equipped to transform solar radiation into electrical energy via any one of a number of cycles or natural phenomena. Few, however, have the ability to store sufficient energy during the day so that a supply can be maintained during the night as well; when the solar radiation is negligible. The necessary capacity of this storage is usually too high to be viable.

The solar chimney power plant concept proposed by Schlaich (1995) in the late 1970's is possibly a good solution to the problems involved with conventional power generators. The operation of a solar chimney power plant is based on a simple principle: when air is heated by the greenhouse effect under the large glass solar

collector, this less dense hot air rises up a chimney at the centre of the collector. At the base of the chimney is the turbine driving a generator (Figure 1.1). The only operational solar chimney power plant built was an experimental plant in Manzanares, Spain (Haaf *et al.*, 1983); however, it proved that the concept works.

There are a number of different methods of generating power from solar radiation. It is useful to investigate these briefly and compare them to the solar chimney. The comparison given here is largely based on the work by Trieb *et al.* (1997) supplemented with additional knowledge gained by studying the solar chimney plant. The main solar technologies that are being investigated on a large scale are listed along with their primary characteristics below.

Parabolic Trough Solar Electric Generating System (SEGS): The solar receiver consists of rows of reflective parabolic troughs. Along the focal line of these troughs are black absorber tubes that contain either a synthetic oil or water. In the case of oil it is used to heat water in a separate heat exchanger. In the case of water, steam is created directly and used to drive a turbine to create electrical power. The system can be built in a modular fashion with a power range of 30-150 MW.

Central Receiver Power Plants: In this type of plant, a large field of two axis tracked mirrors (heliostats) concentrates direct beam radiation onto a central receiver, mounted on the top of a tower. A number of absorber concepts have been tested: direct steam generating tubular receivers, open volumetric air receiver, molten salt tubular or film receiver and others. Usually a normal steam cycle is connected to the system for the electricity generation. Heat storage can be included in the system to reduce the effect of solar fluctuations. The molten salt concept is especially well suited to this.

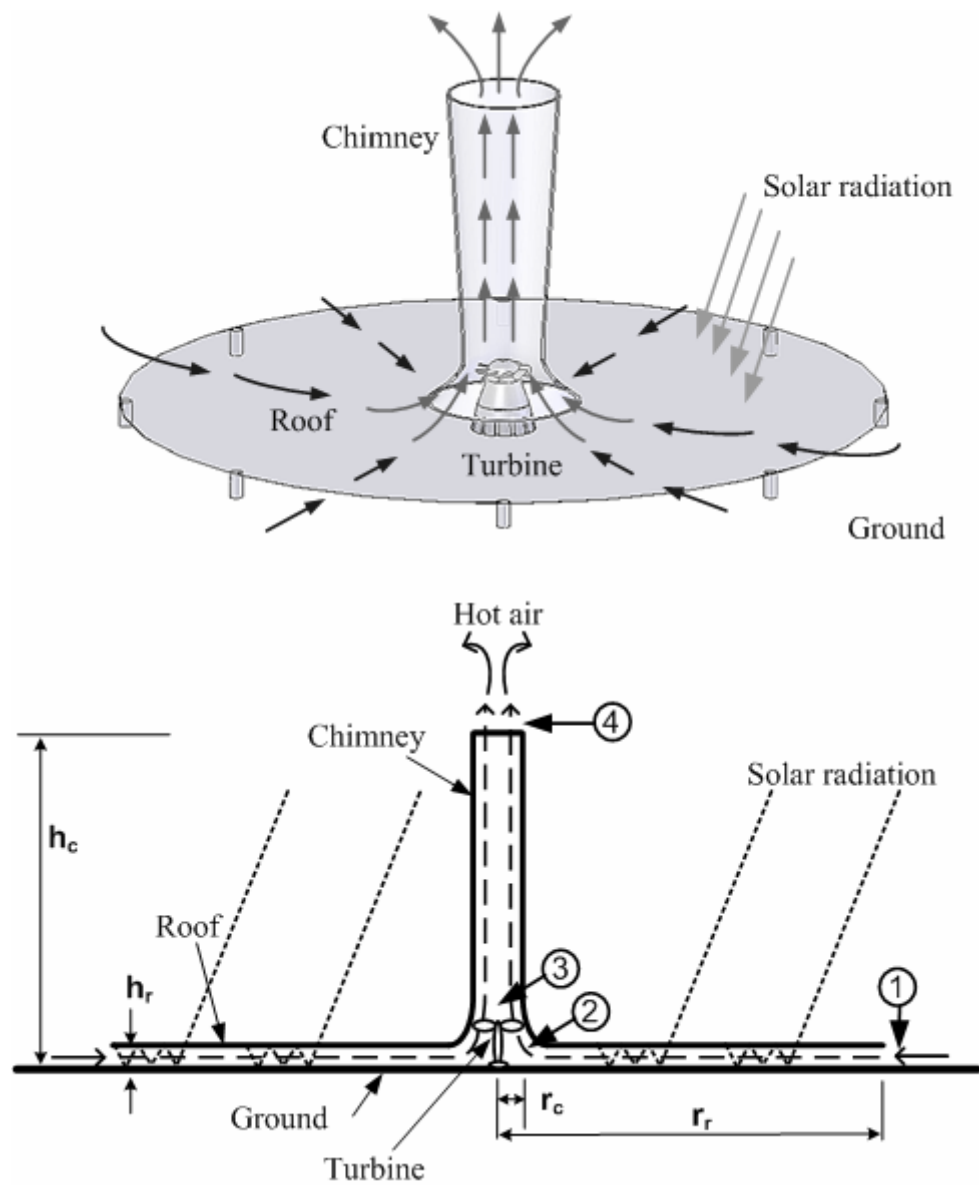


Figure 1.1 Schematic layout of solar chimney power plant.

Solar Chimney Power Plant: This concept uses both the diffuse and direct incoming solar radiation. Heat storage in the ground is inherent to the solar collector and it could be vastly improved through the use of water bags. The small temperature gradients found in the solar chimney make heat storage effective as heat losses to the environment are low.

Dish-Stirling Systems: This type of plant makes use of direct beam radiation that is focused using a paraboloidal dish reflector that is tracked in two axes. The heat absorber is usually a tube- or heat-pipe-absorber that is placed at the focal point of the dish reflector. The Stirling engine is an externally heated reciprocating piston engine with working fluids of either hydrogen or helium.

Solar Pond Power Plants: The naturally occurring phenomenon of a salt gradient in ponds allows hot water to rest on the bottom. High temperature water is able to dissolve more salt. The density of the liquid increases with the salt concentration, resulting in a higher density and temperature stable layer at the bottom of the ponds. A black absorbing surface is placed on the pond bottom and temperatures here can reach 90°C without convection losses. A fluid with a boiling point of less than 100°C is used to generate power in a separate cycle. Significant energy storage is possible in salt gradient ponds.

Photovoltaic Power Plant: This is probably one of the most commonly known methods of solar electricity generation. These semiconductor devices have the ability to convert sunlight into direct current electricity. They can be coupled in series and parallel to generate high voltages and powers. Energy storage is only possible using batteries.

Summary: The following table is taken from Trieb *et al.* (1997) with some changes. It summarizes the advantages and disadvantages of the solar chimney power plant generation scheme. For more details, please consult Trieb *et al.* (1997), where will be found the advantages and disadvantages of the various solar power generation schemes allowing for easier comparison. The following table summarizes their views on the solar chimney.

Since the Manzanares plant, there has been no construction of any other operational plants. A full-scale solar chimney is a capital-intensive undertaking, hence before building one, a good understanding of plant operation is required. The analyses that have been performed have tended to simulate the plant operation at a particular operating point. The turbine of the solar chimney is an important component of the plant as it extracts the energy from the air and transmits it to the generator. It has significant influence on the plant as the turbine pressure drop and plant mass flow rate are coupled. The turbine must operate efficiently and be correctly matched to the system to ensure proper plant operation. To design the turbine effectively its operating region must be defined. Designing a turbine for an incorrect operating point may result in unpredictable plant operation. Phenomena such as stalling may occur resulting in a sudden decrease in the turbine pressure-drop. The raw data showing pressure drop, volume flow rate and power output allowed rudimentary turbine efficiencies to be calculated for the Manzanares plant (Haaf, 1984). The turbine efficiency based on these readings was found to be lower than predicted. This is thought to be due to the turbine operating away from its design region. The need exists to demonstrate that a suitable turbine can be built that can operate at a high efficiency in the required design range for a full-scale plant.

Several commercial plants have been proposed in research literatures. All of them consist of the thousands-meters-in-diameter collector and thousands-meters-high chimney. In the 1990s, a project in which a solar chimney power plant with the capacity of 100 MW was proposed for construction in Rajasthan, India, and was about to be implemented. Its collector had a radius of 1,800 m and a chimney height and diameter of 950 m and 115 m, respectively (Rohmann, 2000). However, the project was cancelled owing to the potential danger of nuclear competition between India and Pakistan. The Australian government planned to build a 200 MW commercial plant with a chimney 1,000 m high. Recently, the plant was downsized to 50 MW and a 480 m-high chimney, in order to make it economically viable and eligible for government funding (EnviroMission, 2006). The construction and safety of a massive structure poses significant engineering challenges. Consequently, the work described in this thesis is stimulated by the quest for better designs of a plant with the roof radius and chimney height of order of 100 m.

Large-scale production of electricity from solar power is the goal of a solar chimney power plant. Experimental study of a full scale solar chimney prototype is very expensive and time consuming since a “small” power plant is of the order of 100 m in height. Small-scale model testing is obviously desirable but a similarity scaling law must first be established. The dimensional analysis methodology focuses on combining the effects of various primitive variables into fewer dimensionless variables, thereby scaling the primitive variables to exhibit similar effects on the different physical models. Aside from the scaling law, dimensional analysis also helps reduce the number of independent variables resulting in lesser experimental trials.

1.2 RESEARCH OBJECTIVES

The overall objective of the proposed thesis is to study the flow within the solar chimney and its operating characteristics that are significant in optimizing the solar chimney design.

1.3 THESIS CONTENTS

This thesis diversified approaches to find ways to improve the efficiency of a solar chimney. The approaches can be divided into categories of theoretical, experimental and numerical methodologies. The categories of approaches used in each chapter are listed in Table 1.2. Chapter I describes the objectives, the problems and rational, and the methodology of the research. Chapter II presents the results of literature review. Dimensional analysis was used in Chapters III – V to determine the scaling law for the flow in solar chimney systems and the results obtained were verified by using the Computational Fluid Dynamics technique (CFD). The finding of Chapter V leads to the development of the mathematical in Chapter VI. Inspection of the mathematical model suggests the flow area ratio that can increase the plant performance. To support the idea, the mathematical analysis was carried out in Chapter VII and then proved by CFD. The mathematical model of the system with a turbine was developed in Chapter VIII to evaluate the plant performance. Chapter IX shows the experimental performance of four small-scale physical models. It aimed to prove the findings of Chapters II and VII. Finally, the method of constructal design was used to search for a better design of the flow system in Chapter X. Chapter XI concludes the research results and provides recommendations for the future research

Table 1.1 Advantages and disadvantages of the solar chimney technology.

Advantages	Disadvantages
<ul style="list-style-type: none"> • The glass collector uses diffuse and beam radiation. • The soil under the collector acts as heat storage, avoiding sharp fluctuations and allowing power supply after sunset. • Easily available and low cost materials for construction. • Simple fully automatic operation. • No water requirements. • Potential for large amount of energy storage in collector to extend operating hours. 	<ul style="list-style-type: none"> • Low thermodynamic efficiency. • Hybridization not possible. • Large, completely flat areas required for the collector. • Large material requirements for the chimney and for the collector. • Very high chimney is necessary for high power output (e.g. 750m for a 30MW plant). • High cosine losses for low solar angles.

Table 1.2 Categories of the approaches used in each chapter.

Chapter	Approach used	Category
III	Dimensional analysis CFD	Theoretical Numerical
IV	Dimensional analysis CFD	Theoretical Numerical
V	Dimensional analysis CFD	Theoretical Numerical
VI	Mathematical model	Theoretical
VII	Mathematical analysis CFD	Theoretical Numerical
VIII	Mathematical model	Theoretical
IX	Experimental setup	Experimental
X	Constructal design Mathematical model	Theoretical Theoretical

studies. The thesis was written as the series of research articles. Consequently, some parts of the content might seem repetitive between chapters.

1.4 EXPECTATIONS:

- To obtain the important dimensionless parameters for the flow in solar chimneys
- To obtain the efficient mathematical model of flow in solar chimney.
- To obtain the flow area configuration that can augment the plant performance.

1.5 REFERENCE

EnviroMission's Solar. **Tower Of Power**, <<http://seekingalpha.com/article/14935-enviromission-s-solar-tower-of-power>>, 2006.

Haaf, W., Friedrich, K., Mayr, G., Schlaich, J., 1983. Solar chimneys: part I: principle and construction of the pilot plant in Manzanares. **International Journal of Solar Energy**, Vol. 2, pp 3-20.

Haaf, W., 1984. Solar chimneys: part II: preliminary test results from the Manzanares plant. **International Journal of Solar Energy**, Vol. 2, pp 141-161.

Rohmann, M., 2000. **Solar Chimney Power Plant**, Bochum University of Applied Sciences.

Schlaich, J., 1995. **The Solar Chimney**. Edition Axel Menges: Stuttgart, Germany.

Trieb, F., Langniss, O., Klaiss, H., 1997. Solar electricity generation: -a comparative view of technologies, costs and environmental impact. **Solar Energy**, Vol. 59, pp. 89-99.

CHAPTER II

REVIEW OF THE LITERATURE

A solar chimney power plant is a rather new technology proposed to be a device that generates electricity in large scale by transforming solar energy into mechanical energy. The idea of the solar chimney was proposed initially by two German engineers, Jörg Schlaich and Rudolf Bergemann in 1976 (Hoffmann and Harkin, 2001). In 1979 they developed the first prototype with a designed peak output of 50 kW in Manzanares, about 100 miles south of Madrid, Spain. It consisted of a chimney with a radius of 5 m and a height of 195 m and collector with a radius of 120 m and a variable height of between 2 m at the inlet to 6 m at the junction with the tower. This pilot plant ran from the year 1982 to 1989. Tests conducted have shown that the concept is technically viable and operated reliably (Haaf *et al.*, 1983; Haaf, 1984). The energy balance, design criteria and cost analysis were discussed in Haaf *et al.* (1983). It indicates that the power production cost for the plant is 0.25 DM/kWh (0.098 USD/kWh based on the exchange rate in 1983). A second paper (Haaf, 1984) dealt with the preliminary test results from the plant. Inspection of the available experimental data shows that the plant efficiency is only about 0.1%. Since then, power plant using solar chimney technology has not been built yet, but the operating and design characteristics of such plant have been extensively reported by several researchers.

Mullett (1987) presents an analysis for evaluating the overall plant efficiency. It was inferred that solar chimney power plants have low efficiency, making large

scale plants the only economically feasible option. This deduction is confirmed by Schlaich (1995). Studied by Yan *et al.* (1991) and Padki and Sherif (1989a, 1989b, 1999) conducted some of the earliest work on the thermo-fluid analysis of a solar tower plant. The articles just mentioned assumed the flow through the system as incompressible. On the other hand, Von Backström and Gannon (2000) presented a one-dimensional compressible flow approach for the calculation of the flow variables as dependence on chimney height, wall friction, additional losses, internal drag and area change. Afterward they also carried out an investigation of the performance of a solar chimney turbine (Gannon and Von Backström, 2003). Lodhi (1999) and Bernardes *et al.* (2003) developed a comprehensive mathematical model independently. They both neglected the theoretical analysis of pressure in the system but gave a comparatively simple driving force expression. Chitsomboon (2001) proposed an analytical model with a built-in mechanism through which flows in various parts of a solar chimney can naturally interact. Moreover, thermo-mechanical coupling was naturally represented without having to assume an arbitrary temperature rise in the system. Schlaich and Weinrebe (2005) developed theory, practical experience, and economy of solar tower plant to give a guide for the design of 200 MW commercial plant systems. Bilgen and Rheault (2005) designed a solar chimney system at high latitudes and its performance has been evaluated. Suitable mountain hills act as the sloped collector and chimney which seems a good way to weaken the difficulty to build a high chimney. Onyango and Ochieng (2006) considered the applicability of a solar tower plant to rural villages and have indicated that the minimum dimension of a practical solar tower plant would serve approximately fifty households in a typical rural setting. Pretorius and Kröger (2006) evaluated a

convective heat transfer equation, more accurate turbine inlet loss coefficient and various types of soil on the performance of a large scale solar tower plant. The resultant optimal plant collector height is not as predicted by Kröger and Buys (2001) or Pretorius *et al.* (2004). Tingzhen *et al.* (2006) proposed a mathematical model in which the effects of various parameters, such as the tower height and radius, collector radius and solar radiation, on the relative static pressure, driving force, power output and efficiency can be investigated.

The research mentioned above consisted of analytical and numerical approaches. Some have compared their results with the experimental data obtained from the prototype in Manzanares. Furthermore, there are many other studies carried out with small-sized physical models constructed onsite. Krisst (1983) built a solar tower setup of 10 W in Connecticut, U.S.A., with its collector of 6 m diameter and 10 m height. Kulunk (1985) demonstrated a plant with 9 m² collector and 2 m high tower of 3.5 cm radius with power output of 0.14 W in Izmit, Turkey. Pasumarthi and Sherif (1998a) developed an approximate mathematical model for a solar tower plant and followed with a subsequent article (Pasumarthi and Sherif, 1998b) validating the model against experimental results from small-scale plant models in the University of Florida. In particular, the influence of various geometrical configurations on the performance and efficiency is investigated. Zhou *et al.* (2007a) built a pilot experimental setup in China with 10 m roof diameter and 8 m tower height and 0.3 m diameter, with a rated power of 50 W. Later Zhou *et al.* (2007b) changed the structural and operation parameters of tower during simulation and obtained a primary optimization. Ferreira *et al.* (2007) assessed the feasibility of a solar chimney for food drying. A pilot model with a roof diameter of 25 m and a tower of 12.3 m high and

1 m diameter was built in Brazil. The yearly average mass flow was found to be 1.40 ± 0.08 kg/s and a yearly average rise in temperature of 13 ± 1 °C compared to the ambient temperature.

REFERENCES

- Bernardes, M. A., Dos, S., Voß, A., Weinrebe, G., 2003. Thermal and technical analyses of solar chimneys. **Solar Energy**, Vol. 75 (6), pp. 511–524.
- Bilgen, E., Rheault, J., 2005. Solar chimney power plants for high latitudes. **Solar Energy**, Vol. 79, pp. 449-458.
- Chitsomboon, T., 2001. A validated analytical model for flow in solar chimney. **International Journal of Renewable Energy Engineering**, Vol. 3(2), pp. 339-346.
- Ferreira, A. G., Maia, C. B., Cortez, M. F. B., Valle, R. M., 2007. Technical feasibility assessment of a solar chimney for food drying. **Solar Energy**, doi: 10.1016/j.solener.2007.08.002
- Gannon, A. J., Von Backström, T. W., 2003. Solar chimney turbine performance. **ASME Journal of Solar Energy Engineering**, Vol. 125(1). pp. 101-106.
- Haaf, W., Friedrich, K., Mayr, G., Schlaich, J., 1983. Solar chimneys: part I: principle and construction of the pilot plant in Manzanares. **International Journal of Solar Energy**, Vol. 2, pp 3-20.
- Haaf, W., 1984. Solar chimneys: part II: preliminary test results from the Manzanares plant. **International Journal of Solar Energy**, Vol. 2, pp 141-161.
- Hoffmann, P., Harkin, T., 2001. **Tomorrow's energy: hydrogen, fuel cells, and the prospects for a cleaner planet**. MIT Press, Massachusetts.

- Krisst, R. J. K., 1983. Energy transfer system. **Alternative Sources of Energy**, Vol. 63, pp. 8–11.
- Kröger, D. G., Buys, J. D., 2001. Performance evaluation of a solar chimney power plant. **ISES 2001 Solar World Congress**, Adelaide, Australia.
- Kulunk, H., 1985. A prototype solar convection chimney operated under Izmit conditions. In: **Proceedings of the 7th Miami International Conference on Alternative Energy Sources**, Veiroglu TN (ed.), Vol. 162.
- Lodhi, M. A. K., 1999. Application of helio-aero-gravity concept in producing energy and suppressing pollution. **Energy Conversion and Management**, Vol. 40, pp. 407-421.
- Mullett, L. B., 1987. The solar chimney - overall efficiency, design and performance. **International Journal of Ambient Energy**, Vol. 8(1), pp. 35-40.
- Onyango, F. N., Ochieng, R. M., 2006. The potential of solar chimney for application in rural areas of developing countries. **Fuel**, Vol. 85, pp. 2561-2566
- Padki, M. M., Sherif, S. A., 1989a. Solar chimney for medium-to-large scale power generation. In: **Proceedings of the Manila International Symposium on the Development and Management of Energy Resources**, Manila, Philippines, Vol. 1, pp. 423-437.
- Padki, M. M., Sherif, S. A., 1989b. Solar chimney for power generation in rural areas. **Seminar on Energy Conservation and Generation Through Renewable Resources**, Ranchi, India, pp. 91-96.
- Padki, M. M., Sherif, S. A., 1999. On a simple analytical model for solar chimneys. **International Journal of Energy Research**, Vol. 23, no. 4, pp 345-349.

- Pasumarthi N., Sherif S. A., 1998a. Experimental and theoretical performance of a demonstration solar chimney model Part I: mathematical model development. **International Journal of Energy Research**, Vol. 22, pp.277–288.
- Pasumarthi N., Sherif S. A., 1998b. Experimental and theoretical performance of a demonstration solar chimney model Part II: experimental and theoretical results and economic analysis. **International Journal of Energy Research**, Vol. 22, pp. 443–461.
- Pretorius, J. P., Kröger, D. G. 2006. Critical evaluation of solar chimney power plant performance. **Solar Energy**, Vol. 80, pp. 535-544.
- Pretorius, J. P., Kröger, D. G., Buys, J. D., Von Backström, T. W., 2004. Solar tower power plant performance characteristics. In: **Proceedings of the ISES EuroSun2004 International Sonnenforum 1**, Freiburg, Germany, pp. 870–879.
- Schlaich J. 1995. **The Solar Chimney**. Edition Axel Menges: Stuttgart, Germany.
- Schlaich J., Weinrebe, G., 2005. Design of commercial solar updraft tower systems utilization of solar induced convective flows for power generation. **Journal of Solar Energy Engineering**, Vol. 127, pp.117–124.

CHAPTER III

DYNAMIC SIMILARITY IN SOLAR

CHIMNEY MODELING

3.1 ABSTRACT

Dimensionless variables are proposed to guide the experimental study of flow in a small-scale solar chimney: a solar power plant for generating electricity. Water and air are the two working fluids chosen for the modeling study. Computational fluid dynamics (CFD) methodology is employed to obtain results that are used to prove the similarity of the proposed dimensionless variables. The study shows that air is more suitable than water to be the working fluid in a small-scale solar chimney model. Analyses of the results from CFD show that the models are dynamically similar to the prototype as suggested by the proposed dimensionless variables.

3.2 INTRODUCTION

Solar chimney is a rather new solar technology proposed to be a device that generates electricity in large scale by transforming solar energy into mechanical energy. In other words, it can be classified as an artificial wind generator. The schematic of a typical solar chimney power plant is sketched in Fig. 3.1. Solar radiation strikes the transparent roof surface, heating the air underneath as a result of the greenhouse effect. Due to buoyancy effect, the heated air flows up the chimney and induces a continuous flow from the perimeter towards the middle of the roof where the

chimney is located. Shaft energy can be extracted from thermal and kinetic energy of the flowing air to turn an electrical generator (Schlaich, 1995).

Numerous analytical investigations to predict the flow in solar chimney had been proposed (Gannon and Von Backström, 2000; Haaf *et al.*, 1983; Padki and Sherif, 1988; Padki and Sherif, 1989a; Padki and Sherif, 1989b; Padki and Sherif, 1992; Schlaich, 1995; Von Backström and Gannon, 2000; Yan, et al., 1991). There are common features of all these investigations in that they developed mathematical models from the fundamental equations in fluid mechanics. In doing this the temperature rise due to solar heat gain had been assumed to be a reasonable value using engineering intuition. Flows in the roof and the chimney were studied individually without a mechanism to let them interact. Chitsomboon (2001a) proposed an analytical model with a built-in mechanism through which flows in various parts of a solar chimney can naturally interact. Moreover, thermo- mechanical coupling was naturally represented without having to assume an arbitrary temperature rise in the system. The results predicted were compared quite accurately with numerical solutions from CFD.

Experimental study of a full scale solar chimney prototype is very expensive and time consuming since a “small” power plant is of the order of 100 m in height. Small-scale model testing is obviously desirable but a similarity scaling law must first be established. The dimensional analysis methodology focuses on combining the effects of various primitive variables into fewer dimensionless variables, thereby scaling the primitive variables to exhibit similar effects on the different physical models. Aside from the scaling law, dimensional analysis also helps reduce the number of independent variables resulting in lesser experimental trials.

To the present time, there has been only one experimental solar chimney plant constructed for testing. This was done in Spain as a result of a joint venture between the German government and a Spanish utility. This pilot plant, with the chimney height and the roof diameter nominally at 200 m, had been running from 1982 to 1989. Theoretical and numerical results must ultimately be validated by experimental findings of model testing. However, the high cost and long time involved in constructing and testing of large scale model stipulates the use of a small-scale experimental plant. This paper proposes to use dimensional analysis methodology to establish scaling law to extrapolate results from small-scale model to the full scale prototype. The characteristic scaling method of Chitsomboon (2001b) is used to find the dimensionless variables. Finally, the similarities between the model and the prototype attained by the dimensionless variables are verified by scaling the numerical results obtained from a computational fluid dynamics (CFD) code.

While air is the natural working fluid in the prototype, water is also tested for its suitability as a test fluid in small scale models. Due to its much higher density water might offer an advantage in small scale testing as is well known in aerodynamic testing. Some researchers also used water as the working fluid in their small-scale solar chimney models (Chenvidyakarn and Woods, 2005; Khalifa and Sahib, 2002; Spencer, S., 2001), albeit without mentioning its theoretical advantages, if any.

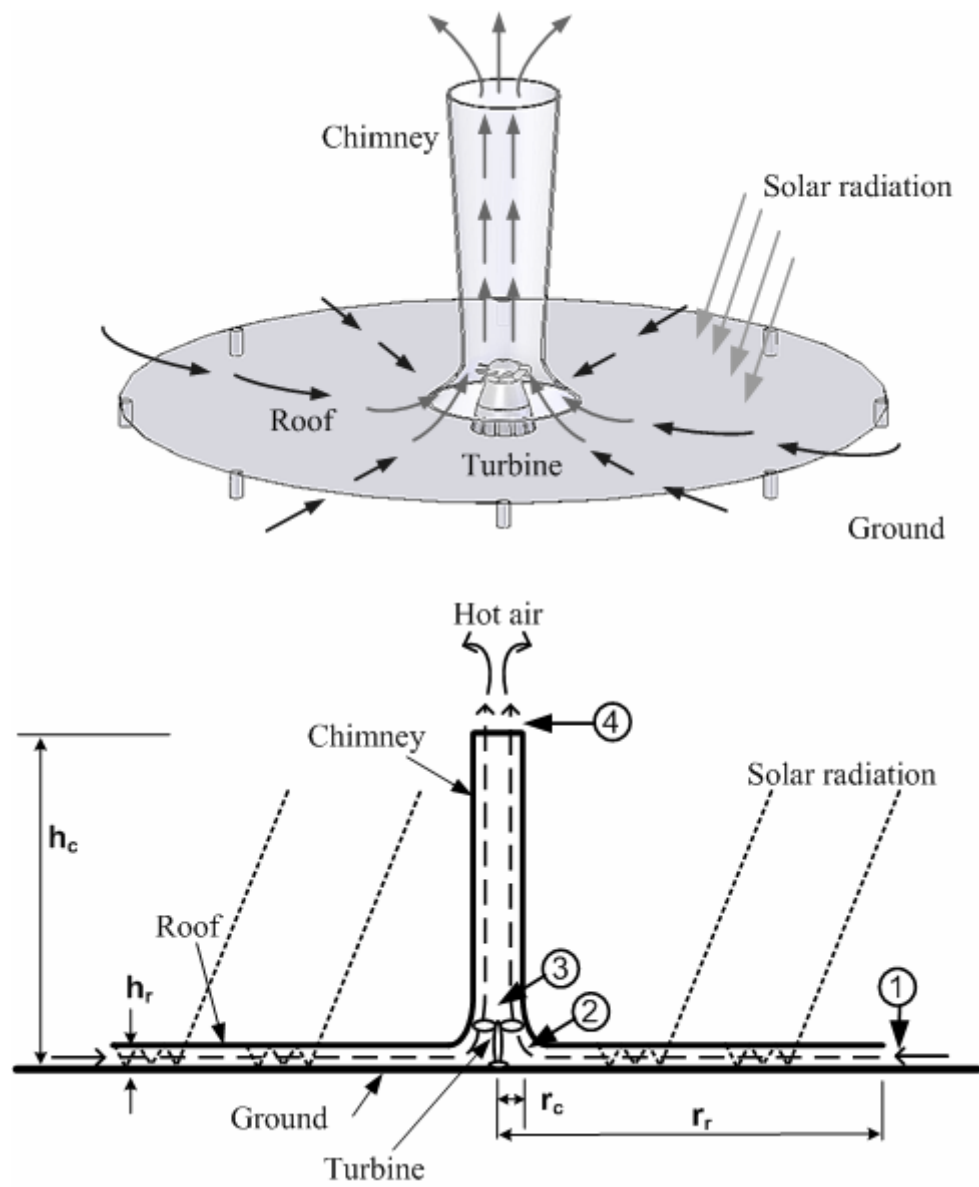


Figure 3.1 Schematic layout of solar chimney power plant.

3.3 DIMENSIONAL ANALYSIS

In Chitsomboon (2001a), by synthesizing the conservation equations of mass and energy together with ideal gas relations, the mathematical model for the frictionless, one-dimensional flow in a solar chimney was proposed as,

$$\frac{1}{2} \dot{m} V_1^2 \left[\rho_1 - 2\rho_1 A_1^2 \int_1^2 \frac{dA}{A^3} + \frac{2A_1 q''}{V_1 c_p T_1} \int_1^2 \frac{dA_r}{A^2} + \frac{2\rho_1 A_1^2 g h}{\gamma R T_1} \int_1^2 \frac{dA}{A^3} \right] = \frac{\rho_1 g h q''}{c_p T_3} \int_1^2 dA_r \quad (3.1)$$

The results obtained from the above model were compared with numerical results from the self-developed CFD computer code (Chitsomboon, 2001a). This CFD code solved the full two-dimensional, compressible Navier-Stokes equations using an implicit finite volume methodology. The test cases investigated represent the solar chimney system with a roof radius of 100 m, roof height of 2 m and chimney radius of 4 m. Two parameters were used in the test: 1) the chimney height, and 2) the insolation. Good agreements between analytical and numerical results in terms of kinetic power predictions, both quantitatively and qualitatively, were observed. Therefore various parameters appeared in Eq. (3.1) perhaps could be used to guide the development of the present dimensional analysis. In particular by realizing that the heat flux term always appears together with c_p , the term $\frac{q''}{c_p}$ is therefore proposed as a single fundamental variable in the analysis (physically this term should represent the temperature rise). The variable, however, is modified to be $\frac{q'''}{c_p}$ (volumetric heat source) so that it is compatible with the way the CFD code handles the heat flux. q''' can be obtained from q'' simply by dividing by the roof height. Obviously this is

correct only in the ideal situation wherein the incident energy is totally and uniformly absorbed by the air under the roof that is the assumption presumed in this study. The uniformity assumption should be quite realistic because the dominant mode of heat transfer is that of radiation through a thin gas while the totality assumption tends to overestimate the heat absorption; this is not a serious issue since at this level we are just trying to establish mathematical similarity among various parameters involved in the problem. In practice, an empirical factor (less than 1) should be found to help adjust the heat absorption to be close to the true value and this should depend on the type of roof material and the ground conditions as well.

The primitive variables involved are proposed to be $\rho, A, V, q''', c_p, \beta, h_c, g$. It should be noted that a solar chimney system without a turbine is considered here. In addition, viscous effect is ignored at this level. Past numerical testing (Koonsrisuk and Chitsomboon, 2004) have confirmed that viscous effect is negligible in solar chimney flow. By the guidance of Eq. (3.1), the principal dependent variable is proposed to be $\dot{m}V^2/2$ or $(\rho AV)V^2/2$ instead of just V since it gives a good engineering meaning of the total kinetic energy in the chimney. The procedural steps to find the dimensionless variables are now listed as follows:

Step 1 Propose the variables affecting the power as:

$$\rho AV \frac{V^2}{2} = f^n \left(\rho, g, \frac{q'''}{c_p}, \beta, h_c \right) \quad (3.2)$$

All other variables on the right hand side, except for β , are those that would be intuitively expected (given that q'''/c_p stands for temperature rise). β comes in to represent the effect of buoyancy which is the main driving force for this problem.

Step 2 Use mass (M), length (L), time (t), and temperature (Θ) as the fundamental dimensions.

Step 3 The fundamental dimensions of the listed variables can be expressed in multiple powers of M, L, t, Θ as shown in Table 3.1.

Step 4 Choose $g, q'''/c_p, \beta$, and h_c as the scaling (repeating) variables. While the choice of scaling variables is quite arbitrary, in so far as they are not mutually dependent and can form a complete dimensional bases for all other dimensions, but a judicious selection can help in engineering interpretation (which will be elucidated later). The methodology proposed in Chitsomboon (2001b) is used to form dimensionless groups. In this method ‘pure’ dimensions are extracted from ‘compound’ dimensions embedded in the fundamental variables by combining them together which could be analogized to chemical reaction processes in extracting pure substance.

$$L = h_c \quad (3.3)$$

$$\Theta = \frac{1}{\beta} \quad (3.4)$$

$$t = \sqrt{\frac{h_c}{g}} \quad (3.5)$$

$$M = \frac{q''' \beta (h_c)^{\frac{7}{2}}}{c_p \sqrt{g}} \quad (3.6)$$

Most of the time (including this one) the pure dimension can be extracted simply by observation, without having to solve algebraic equations. In rare cases, solving algebraic equations might be necessary but then they need to be solved only once and for all.

Step 5 The dimension of $\rho AV \frac{V^2}{2}$ is $M^1 L^2 t^{-3}$. The relations for M, L, t from Eqs. (3.6), (3.3) and (1.5), respectively, can now be easily inserted without having to solve a system of algebraic equations as conventionally practiced in the Buckingham's

pi theorem. The scaling variable so obtained is $\left(\frac{q''' \beta (h_c)^{\frac{7}{2}}}{c_p \sqrt{g}} \right)^1 (h_c)^2 \left(\sqrt{\frac{h_c}{g}} \right)^{-3}$.

After some rearranging, the final dimensionless group is,

$$\Pi_1 = \frac{\rho AV \frac{V^2}{2}}{\frac{q''' \beta g}{c_p} h_c^4} \quad (3.7)$$

Repeating the same procedure for ρ ,

Table 3.1 Powers of primitive variables in terms of fundamental dimensions.

	M	L	T	Θ
$\rho AV \frac{V^2}{2}$	1	2	-3	0
ρ	1	-3	0	0
g	0	1	-2	0
$\frac{q'''}{c_p}$	1	-3	-1	1
β	0	0	0	-1
h_c	0	1	0	0

$$\Pi_2 = \frac{\rho}{[M][L]^{-3}} = \frac{\rho}{\left[\frac{q''' \beta (h_c)^2}{c_p \sqrt{g}} \right]^1 [h_c]^{-3}} = \frac{\rho}{c_p \sqrt{g} \frac{q''' \beta}{\sqrt{h_c}}} \quad (3.8)$$

Step 6 Finally, the functional relationship is, $\Pi_1 = f^n(\Pi_2)$, or

$$\frac{\rho A V \frac{V^2}{2}}{\frac{q''' \beta g}{c_p} h_c^4} = f^n \left(\frac{\rho}{c_p \sqrt{g} \frac{q''' \beta}{\sqrt{h_c}}} \right) \quad (3.9)$$

Hence the original eight primitive variables ($\rho, A, V, q''', c_p, \beta, h_c, g$) in Eq. (3.2), have been combined and the number is reduced to only two dimensionless variables. Note that the Buckingham's pi theorem dictates that the number of dimensionless variables is four. The reduction of another two dimensionless variables is made possible by combining primitive variables together by using engineering intuition and the guidance from the above mathematical model (Eq. (3.1)). This should help make the ensuing experiments much simpler. The use of traditional Buckingham's pi theorem procedure also leads to the same dimensionless variables; the advantage of using the present methodology is that the algebraic work is reduced. The validity and completeness of the derived dimensionless variables, however, remain to be proven. To this end, a commercial CFD code "CFX" is employed to obtain numerical solutions of three different-size solar chimneys. The primitive-valued results are used to calculate the values of Π_1 and Π_2 in order to verify the validity of the proposed dimensionless variables.

Engineering Interpretation

As alluded to earlier, physical meaning of a dimensionless group helps in engineering interpretation, which deepens the understanding of the problem. The scaling variable of Π_1 , $\left(\frac{q'''\beta g}{c_p}\right)h_c^4$, could be interpreted as the energy that the buoyant force produces in floating from the base to the top of the chimney. To clarify this, first note that $\frac{q'''}{c_p}$ is proportional to $\tilde{m}\Delta T$, where \tilde{m} is mass flow rate through the 1 m^3 volume being received the solar heat absorption per unit volume, q''' . When this term is multiplied to β ($= \frac{1}{\rho}\left(\frac{\partial\rho}{\partial T}\right)$), the term is proportional to $\frac{\Delta\rho}{\Delta t}$, where Δt is time scale of the problem (time for flowing past 1 m^3 volume). Further multiplication by $gh_c^4 = gh_c^3h_c = g\forall h_c$, resulting into, $(\Delta\rho g\forall)h_c/\Delta t$. The term in the parenthesis is the buoyant force in the chimney; this force acts through the distance h_c in time Δt , which is the energy the air expends in floating from the base to the top as mention earlier. So, Π_1 could be interpreted as total kinetic energy of the system measured in the scaling unit that is proportional to the buoyant energy of the heated air.

As for the scaling variable for Π_2 $\left(\frac{q'''\beta}{c_p}\right)\sqrt{\frac{h_c}{g}}$ this could be interpreted as the buoyant force. Note from above discussion that $\frac{q'''\beta}{c_p}$ could be interpreted as $\frac{\Delta\rho}{\Delta t}$, and that $\sqrt{\frac{h_c}{g}}$ is time scale which should be of the same order as Δt . Therefore the entire term is proportional to $\Delta\rho$. Π_2 now becomes $\frac{\rho}{\Delta\rho}$, the invert of

which could be interpreted as the buoyant force scaled by the weight of the fluid of the same volume.

The entire relation of $\Pi_1 = f^n(\Pi_2)$ can be summarized as trying to find the relation of kinetic energy (the intuitive output) as a function of the principal driving force of the system (the intuitive input).

Similarity Requirements

For two flows to be completely similar it is necessary that their geometries and dynamics be similar. Geometric similarity is quite trivial in most cases and is already a basic requirement in this study, hence only dynamic similarity is a concern left to be studied. It is necessary to duplicate all but one of the significant dimensionless groups to achieve complete dynamic similarity between geometrically similar flows (Fox and McDonald, 1994). Thus, if the proposed dimensionless variables are valid, duplicating Π_2 between models and prototype ensured dynamically similar flows. The stipulation required by Π_2 in Eq. (3.8) is

$$\left[\frac{\rho}{\frac{q''' \beta}{c_p} \sqrt{h_c}} \right]_m = \left[\frac{\rho}{\frac{q''' \beta}{c_p} \sqrt{h_c}} \right]_p \quad (3.10)$$

where subscript m stands for model and p stands for prototype. After some manipulations, there is obtained,

$$q_m''' = q_p''' \frac{\rho_m}{\rho_p} \frac{c_{p,m}}{c_{p,p}} \frac{\beta_p}{\beta_m} \sqrt{\frac{h_{c,p}}{h_{c,m}}} \quad (3.11)$$

It had been hoped that water would offer a good alternative as a test working fluid, as in aerodynamic testing. By using Eq. (3.11), the solar heat absorption per unit volume required for three geometrically similar models are presented in Table 3.2, for air and water as the test working fluids. It is seen from the table that the solar heat absorption per unit volume required for water are very high, making it unpractical, if not impossible, in experimental set up. In numerical modeling, of course, high solar heat absorption per unit volume can be easily implemented; but the difficulty may arise in terms of thermodynamic states and properties of water at very high temperatures. As a result of the anticipated difficulties and inconveniences, water was dropped from consideration as a test working fluid.

3.4 CFD Modeling

As real experiments in this type of flow are very expensive and time consuming, at this early stage it should be sufficient to perform ‘numerical experiments’ to verify the validity of the proposed similarity because CFD has over time proven to be quite a reliable tool in fluid dynamic research and application especially when only global phenomena is being sought after. CFX was chosen since it has been widely accepted in the research and application communities and partly because of its versatility with grid generation and boundary conditions. For this purpose, CFX solves the conservation equations for mass, momenta, and energy using a finite volume method. Adaptive unstructured tetrahedral meshes are used in the present study. The plants studied are modeled as axis-symmetry where the centerline of the chimney is the axis of symmetry. To simulate axis-symmetry, a 5 degree section of the plant is cut out from the entire periphery as shown in Fig. 3.2. To make certain

that similarity (or the lack thereof) was not affected by grid-topology irregularity, grid similarity for all the test cases was enforced. Grid similarity means that when the small-scale model is scaled up to be the same size as the prototype, its grid is exactly the same as that of the prototype. Moreover, grid convergence was also ensured by varying the numbers of grid until no change in output parameter was noticed. Fig. 3.3, as an example of grid convergence examination, illustrates the plot of Π_1 vs. number of grid elements.

The solar heat absorption per unit volume of the air is modeled as a uniform heat source within the air that is flowing underneath the roof. This should not incur significant errors since the dominant mode of heat transfer is that of solar radiation through a thin gas. For buoyancy calculations, a source term is added to the momentum equations as follows:

$$S_{buoyancy} = (\rho - \rho_{ref})g \quad (3.12)$$

where the density difference $\rho - \rho_{ref}$ is evaluated directly from equation of state, not approximately by the Boussinesq's model.

High flow gradients occur in the vicinity of the roof-chimney juncture. In order to accurately capture flow features, several grid points have to be located at this region. A typical mesh system for the computational domain is shown in Fig. 3.2.

Proper boundary conditions are needed for a successful computational work. At the roof inlet, the total pressure and temperature are specified; whereas at the chimney

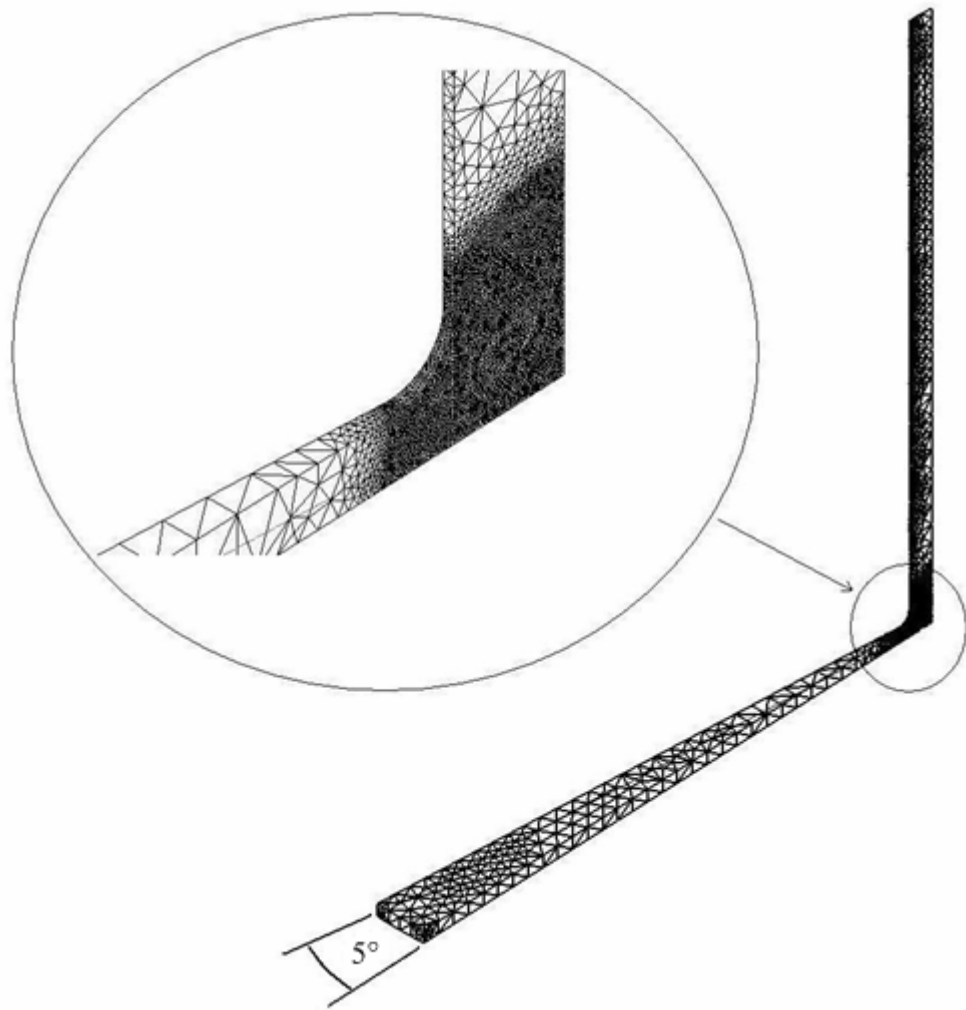


Figure 3.2 Unstructured mesh used for the 5 degree axis-symmetric computational domain.

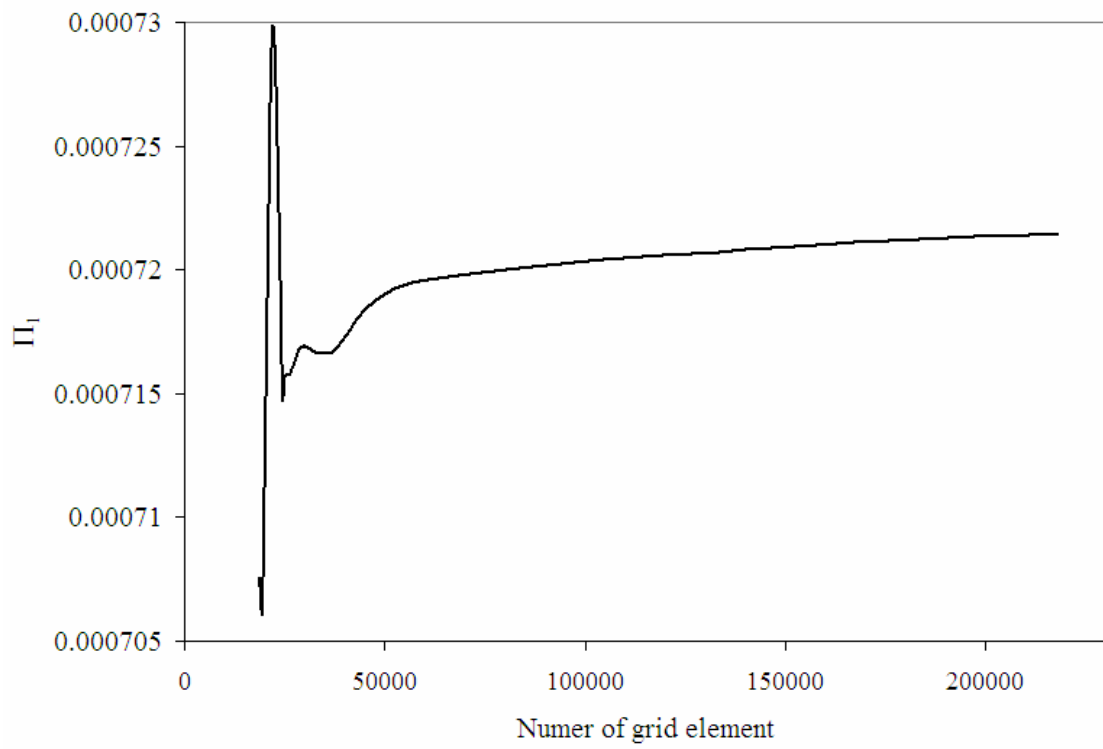


Figure 3.3 Π_1 vs. number of grid elements

exit the ‘outlet’ condition with zero static pressure is prescribed. Additionally, the ‘symmetry’ boundary conditions are applied at the two sides of the sector. The adiabatic free-slip conditions are prescribed to the remaining boundaries. As specified above that frictionless flow be modeled, then the free-slip conditions are applied to all walls. All test cases were computed until residuals of all equations had reached their respective minimum. Moreover, global conservation of mass had been rechecked to further ascertain the convergence of the test cases.

3.5 RESULTS AND DISCUSSION

A typical velocity field in the vicinity of the roof-chimney juncture is shown in Fig. 3.4 wherein a flaring of the turn angle is used to mitigate separation caused by the 90 degree flow deflection. All plots to be subsequently presented are displayed along the scaled flow path, which is the non-dimensioned streamwise location of the flow, equaling zero at inlet and one at outlet (chimney top). Incidentally, 0.5 is the location at which the roof-chimney juncture is located. The results using air as the working fluid are illustrated in Figs. 3.5 - 3.7. The numerical solutions by MOYA, a self-developed CFD code (Chitsomboon, 2001a), are also presented in the figures for comparison purpose. Quasi one dimensional model is used in MOYA, whereas axis-symmetry model is used in this study. The different coordinate systems used in MOYA and CFX is believed to be the reason behind the discrepancies in the computational results of the two CFD codes shown in Figs. 3.5 - 3.7.

Figure 3.5 shows the average velocity along the flow path; it can be seen that the velocities of the flow under the roof increase along the flow path, resulting from

the flow area reduction but constant mass flow rate, and remains unchanging along the chimney.

In Fig. 3.6, the temperature rises toward the chimney because the air accumulates thermal energy along the flow path in the roof section. The air temperature drops slightly while rising in the chimney. This drop is in accord with the pressure drop through isentropic relation. A numeral check shows that this temperature reduction did indeed undergo an isentropic change.

In Fig. 3.7, the pressure distributions are seen to be nominally constant under the roof before falling linearly in the chimney portion, to meet the hydrostatic pressure distribution at the chimney top. Note that the ordinate is the gauge pressure scaled such that pressures at the top of chimney are always zero.

Figures 3.5 - 3.7 showed the differences of the primitive flow variables between the prototype with $q'' = 800 \text{ W/m}^2$ and the different-size models, which are geometrically similar and Π_2 -similar to the prototype. Π_2 for all cases are already set to be equaled before hand because it was used to compute the similar solar heat absorptions per unit volume required for the test cases. If similarity existed as proposed, scaled data of the various cases in Figs. 3.5 - 3.7 must collapse. To this end,

Figures 3.8 presents the distributions of the dimensionless variable, Π_1 , computed from the involved primitive variables. The figure displays the values of Π_1 when Π_2 are at 164.1, 246.1, 492.2, and 984.4, which correspond to the condition when the insolation of prototype are at 1200, 800, 400, and 200 W/m^2 , respectively. It is clearly seen that the once scattered data now collapse, suggesting similarity. Despite

there are slight variation from prototype's values of model's values, the Π_1 characteristics follow the same pattern over a wide range of Π_2 .

The deviation of Π_1 (about 15%) at high value of Π_2 might be the result of viscous effects. Note that though the inviscid equations are being solved, but there exists the so-called 'numerical viscosity' in the numerical scheme. As is well known in CFD, numerical viscosity is an inescapable quantity associated with numerical discretization of the differential convective terms. Note also that Π_2 could be interpreted as $\rho/\Delta\rho$, then for the same physical model, high value of Π_2 means low

value of numerical Grashof number ($= \frac{g \Delta\rho / \rho x^3}{\nu_n^2}$), where ν_n is the numerical

viscosity whose size being proportional to Δx which in turns is proportional to x . Since the grids are also similar so for the different physical models being studied the ratio of the Grashof numbers should be scaled by x . At the same Π_2 , the ratios of the Grashof number values for model II, model I and the prototype are then 1, 5 and 125. It is possible that the low values of the numerical Grashof numbers, in conjunction with their vast different in magnitudes, are contributable to the 15% departures of the similarity curves of the cases being studied.

Table 3.2 suggests that when the plant size reduces, the plant needs higher solar heat per unit volume. Actually, as the plant size decreases, the roof height also decreases; this makes the volume under the roof decrease accordingly. When the solar radiation per unit volume for each plant is converted to solar radiation per unit roof

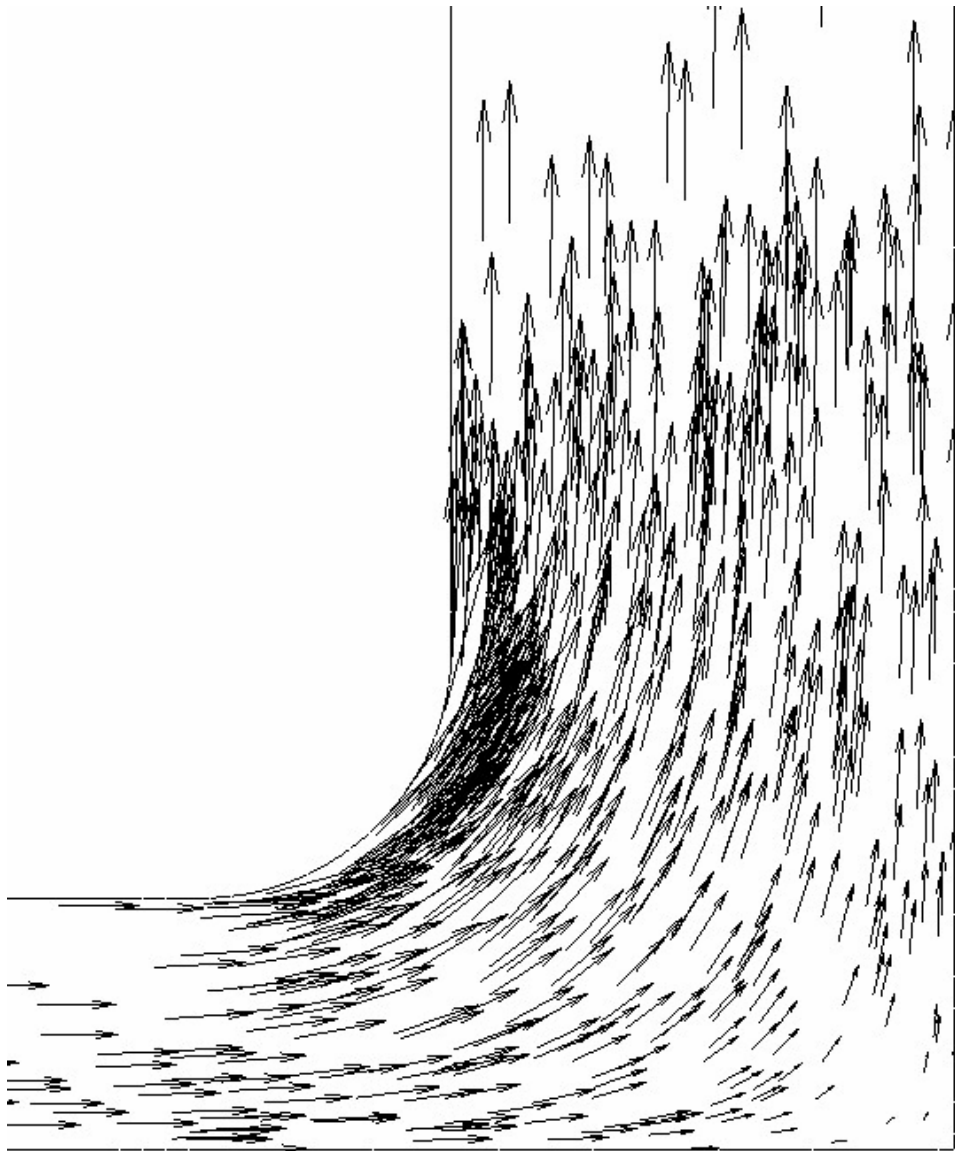


Figure 3.4 Typical velocity field around the junction of the roof and the chimney.

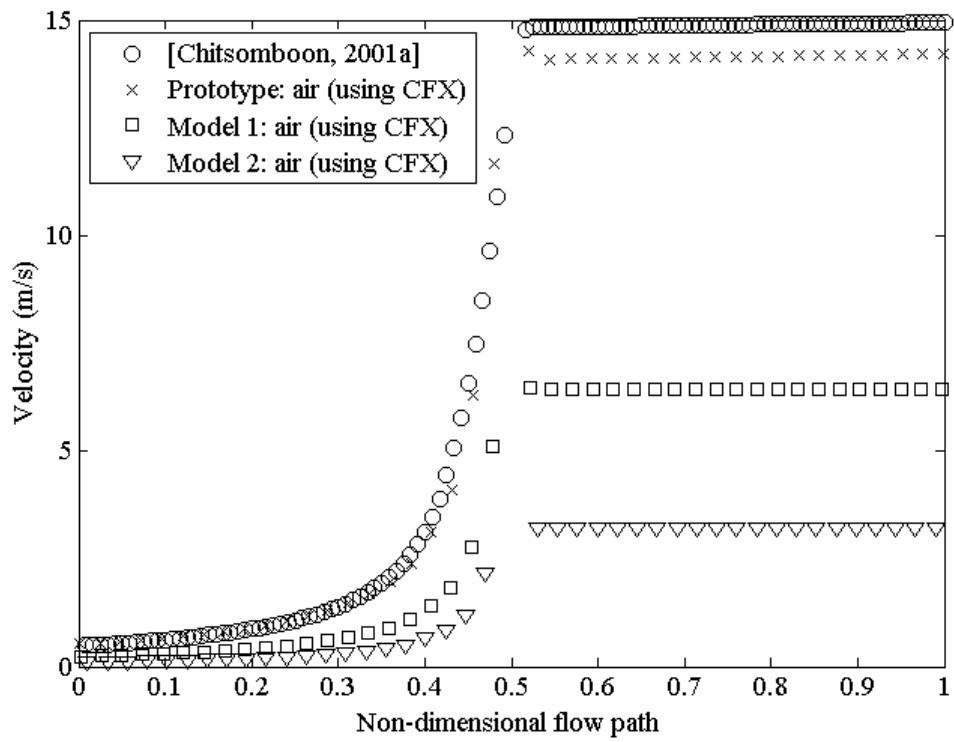


Figure 3.5 Numerical prediction of velocity profiles for insolation = 800 W/m^2 .

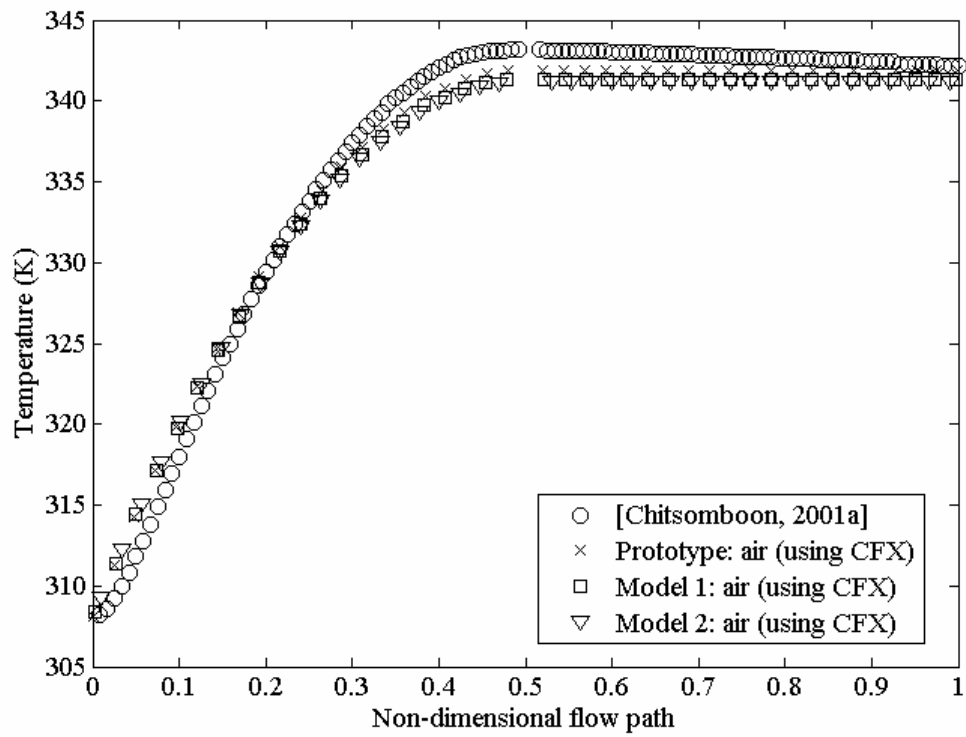


Figure 3.6 Numerical prediction of temperature profiles for insolation = 800 W/m^2 .

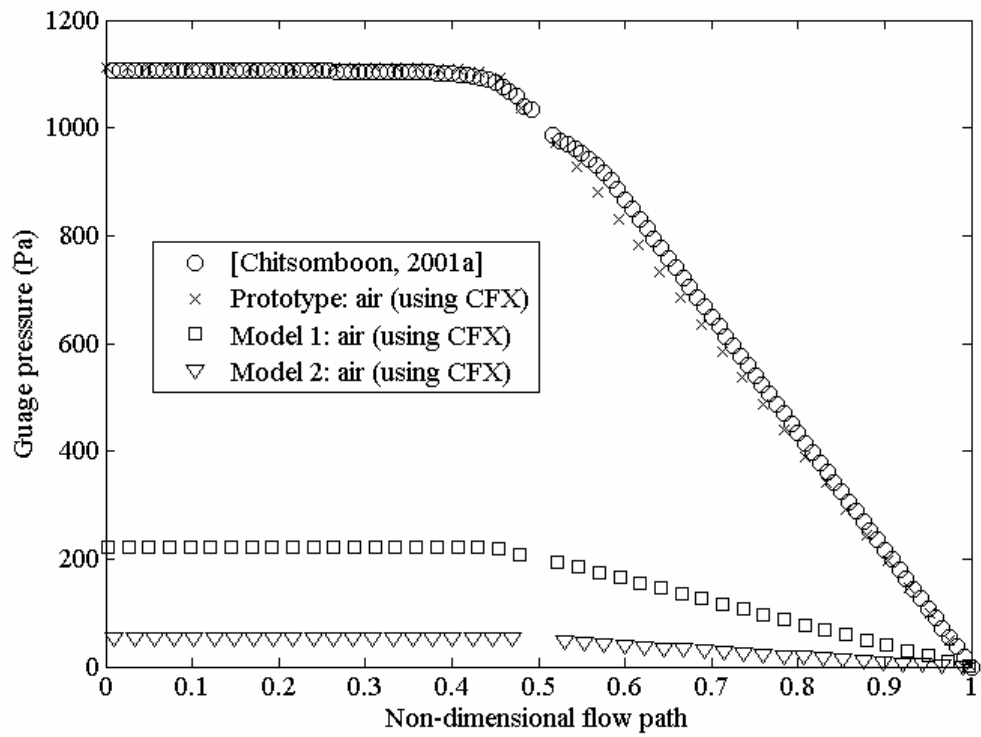


Figure 3.7 Numerical prediction of pressure profiles for insolation = 800 W/m^2 .

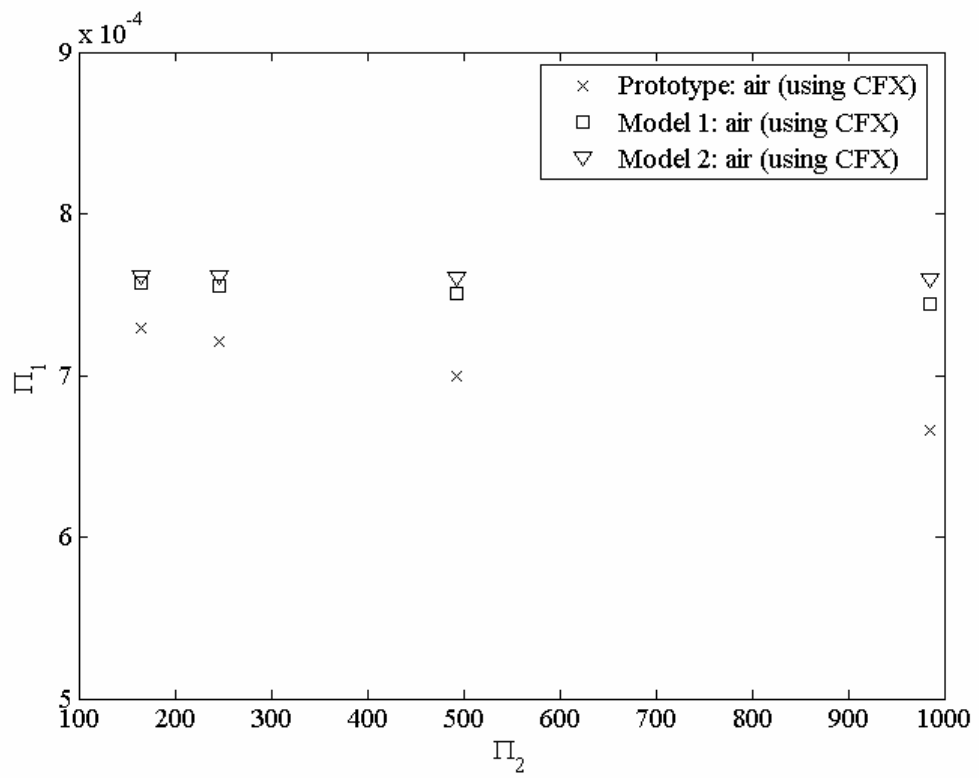


Figure 3.8 Π_1 - Π_2 characteristics.

area, it shows that, for similar condition, as the plant size decreases, the plant needs lower solar radiation per unit area. This should pose a serious obstacle for conducting a “similar” experiment using a small model because means for reducing insolation is needed, such as by using glass of various shades of colors. Better similarity variables that do not require different insolutions are obviously desirable.

3.6 CONCLUSION

CFD study in three geometrically similar cases indicated that the proposed dimensionless variables are appropriate for obtaining similarity for flows in prototype and small-scale models of a solar chimney. By using engineering intuition and guidance from a mathematical model, the number of dimensionless variables developed is less than that dictated by the Buckingham’s pi theorem; this helps reduce the complexity of experimental work. The study shows that water is not suitable as a test working fluid because the solar heat absorption per unit volume required for similarity is too high. Using air for a small-scale model, though quite natural, requires lower insolutions than that of the prototype for dynamic similarity; this requires roof material treatments such as tinting or using artificial insolation.

Table 3.2 Solar heat absorption per unit volume (S.H.A.V.) requirements
for dynamic similarity

Case	Working fluid	Chimney height (m)	Roof height (m)	Chimney radius (m)	Roof radius (m)	S.H.A.V. (W/m ³)
Prototype	Air	100	2	4	100	400
Model 1	Air	20	0.4	0.8	20	894.43
Model 2	Air	5	0.1	0.2	5	1,788.85
Model 3	Water	20	0.4	0.8	20	30,053,033
Model 4	Water	5	0.1	0.2	5	60,106,066

Note: The specification of prototypical plant is the same as the plant studied in Chitsomboon (2001a).

3.7 REFERENCES

- Chenvidyakarn, T., Woods, A., 2005. Multiple steady states in stack ventilation. **Building and Environment**, 40(2005), pp. 399-410.
- Chitsomboon, T., 2001a. A validated analytical model for flow in solar chimney. **International Journal of Renewable Energy Engineering**, 3(2), pp. 339-346.
- Chitsomboon, T., 2001b. Construction and interpretation of dimensionless variables in a new way. In: **Proceedings of the 15th National Mechanical Engineering Conference**, Vol. 1, pp. TF39-TF45.
- Fox, R. W., McDonald, A. T., 1994. **Introduction to fluid mechanics**, 4th edition, John Wiley & Sons, United States of America.
- Gannon, A.J., Von Backström, T.W., 2000. Solar chimney cycle analysis with system loss and solar collector performance. **ASME Journal of Solar Energy Engineering**, Vol. 122, no. 3, pp. 133-137.
- Haaf, W., Friedrich, K., Mayr, G., Schlaich, J., 1983. Solar chimneys: part I: principle and construction of the pilot plant in Manzanares. **International Journal of Solar Energy**, Vol. 2, no. 1, pp. 3-20.
- Khalifa, A.J.N., Sahib, W.K., 2002. Turbulent buoyancy driven convection in partially divided enclosures. **Energy Conversion and Management**, 43(2002), pp. 2115-2121.
- Koonsrisuk, A., Chitsomboon, T., 2004. Frictional effect on the flow in a solar chimney. In: **Proceedings of the 4th National Symposium on Graduate Research**, Chiang Mai, Thailand.

- Padki, M.M., Sherif, S.A., 1988. Fluid dynamics of solar chimney. In: **Proceedings of the ASME Winter Annual Meeting**, Chicago, Illinois, FED-Vol.70, pp. 43-46.
- Padki, M.M., Sherif, S.A., 1989a. Solar chimney for medium-to-large scale power generation. In: **Proceedings of the Manila International Symposium on the Development and Management of Energy Resources**, Manila, Philippines, 1, pp. 423-437.
- Padki, M.M., Sherif, S.A., 1989b. Solar chimney for power generation in rural areas. **Seminar on Energy Conservation and Generation Through Renewable Resources**, Ranchi, India, pp. 91-96.
- Padki, M.M., Sherif, S.A., 1992. A mathematical model for solar chimneys. In: **Proceedings of the 1992 International Renewable Energy Conference**, Amman, Vol. 1, pp. 289-294.
- Schlaich, J., 1995 . **The Solar Chimney: Electricity from the Sun**, Axel Menges, Stuttgart.
- Spencer, S., 2001. **An experimental investigation of a solar chimney natural ventilation system**, Master Thesis, Concordia University, Montreal, Quebec, Canada.
- Von Backström, T.W., Gannon, A.J., 2000. Compressible flow through solar power plant chimneys. **ASME Journal of Solar Energy Engineering**, Vol. 122, no. 3, pp. 138-145.
- Yan, M.Q., Sherif, S.A., Kridli, G.T., Lee, S.S., Padki, M.M., 1991. Thermo-fluid analysis of solar chimneys. **Ind. Applic. Fluid Mech.** ASME FED-2, pp. 125-130.

CHAPTER IV

PARTIAL GEOMETRIC SIMILARITY FOR SOLAR CHIMNEY POWER PLANT MODELING

4.1 ABSTRACT

A solar chimney power plant derives its mechanical power from the kinetic power of the hot air which rises through a tall chimney, the air being heated by solar energy through a transparent roof surrounding the chimney. In our previous studies, the achievement of complete dynamic similarity between a prototype and its models imposed the use of different solar heat fluxes between them. It is difficult to conduct an experiment by using dissimilar heat fluxes with different physical models. Therefore, this study aimed to maintain dynamic similarity for a prototype and its models while using the same solar heat flux. The study showed that, to achieve the same-heat-flux condition, the roof radius between the prototype and its scaled models must be dissimilar, while all other remaining dimensions of the models are still similar to those of the prototype. In other words, the models are ‘partially’ geometrically similar to the prototype. The functional relationship that provides the condition for this partial similarity is proposed and its validity is proved by scaling the primitive numerical solutions of the flow. Engineering interpretations of the similarity variables are also presented.

4.2 INTRODUCTION

Solar chimney (sometimes called solar tower) was proposed as an alternate means to harness energy from the sun (Schlaich, 1995). The schematic of a typical solar chimney power plant is sketched in Fig. 4.1. A hot air is obtained under the transparent roof surface as a result of the greenhouse effect. Due to buoyancy, the heated air flows up the hollow tower (chimney) inducing a continuous flow from the perimeter towards the middle of the roof where the tower is located. Shaft energy can be extracted from the thermal and kinetic energy of the flowing air to turn an electrical generator.

An experimental solar chimney power plant, with tower height and roof diameter nominally at 200 m, design peak electrical output at 50 kW, was constructed in Manzanares desert (Spain) as a joint effort between the German government and a Spanish utility company. The experiment indicated that the solar chimney concept was technically viable and the plant had been operating productively from 1982 to 1989 before its collapse due to a storm. The design criteria and cost analysis of this plant were discussed in Haaf *et al.* (1983) and the preliminary test results from the plant were reported in Haaf (1984). An inspection of the available experimental data showed, however, that the overall plant efficiency was only about 0.1%. Since then, no solar chimney power plant has been built again, though a number of theoretical and numerical studies have been carried out by some researchers. It is apparent that much more research is needed before solar chimney power plant can become a serious competitor to other forms of renewable energy technology.

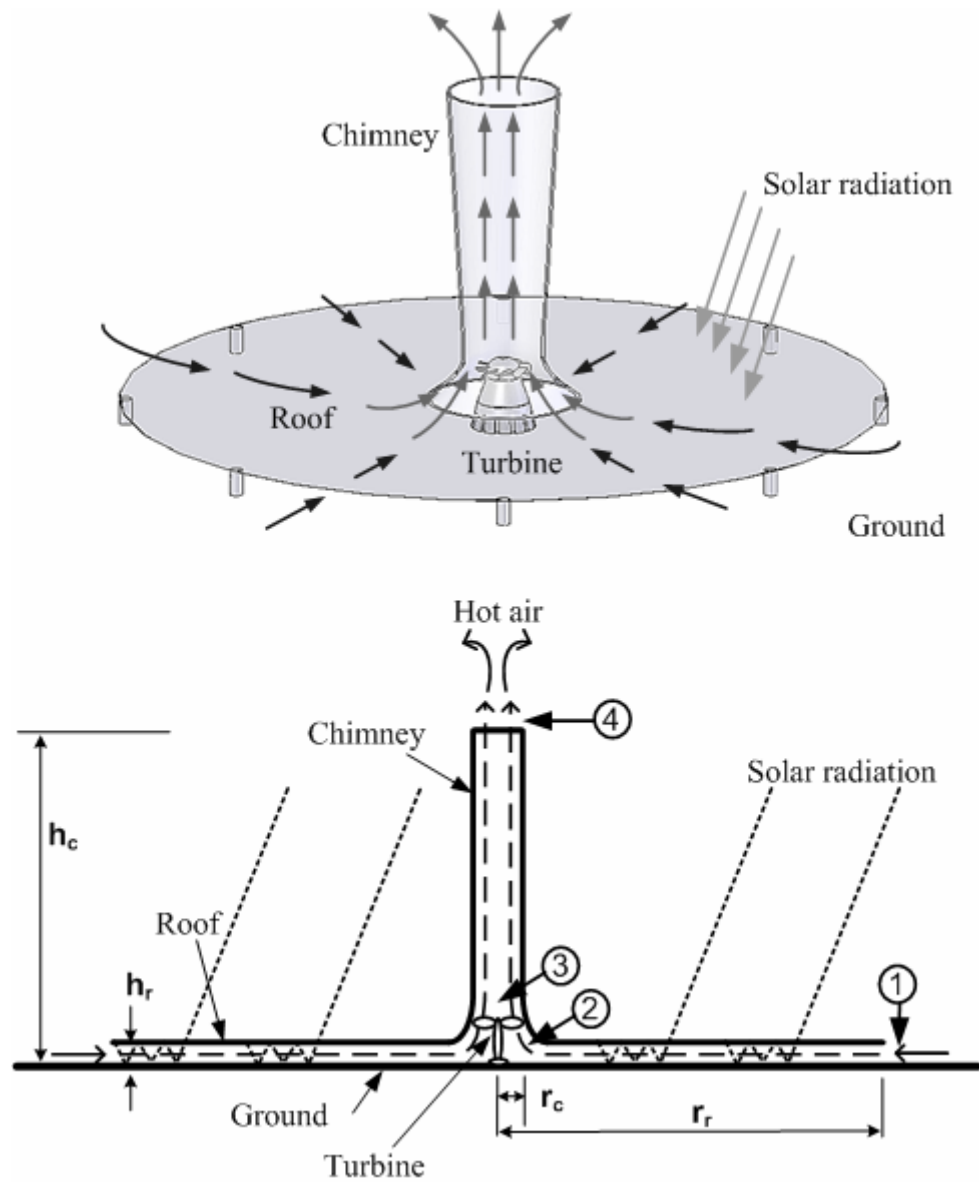


Figure 4.1 Schematic layout of solar chimney power plant.

Padki and Sherif (1989a, 1989b, 1999) and Yan *et al.* (1991) conducted some of the earliest works on thermo-fluid aspects of solar chimney power plants by using various quasi-one-dimensional approaches. Pasumarthi and Sherif (1998a) presented a more detailed mathematical model which was validated with the experimental results of their own (Pasumarthi and Sherif, 1998b) and of the Manzanares plant. Von Backström and Gannon (2000) used a one-dimensional compressible flow approach to conduct their study which included important effects such as wall friction, internal drag and area change. Subsequently, they also investigated the performance of a solar chimney turbine (Gannon and Von Backström, 2003). Chitsomboon (2001) proposed an analytical model with thermo-mechanical mechanisms that allow flows in various parts of a solar chimney to interact. Bernardes *et al.* (2003) developed analytical and numerical models and compared the predicted results with the experimental results from the pilot plant at Manzanares. Guidelines for the design of a 200 MW commercial plant, based on engineering theories, economics and experience, were developed by Schlaich and Weinrebe (2005). Onyango and Ochieng (2006) considered the suitability of solar chimney power plants for small rural villages. Pretorius and Kröger (2006) solved a convective heat transfer equation, evaluated a more accurate turbine inlet loss coefficient and the effects of various types of soil on the performance of a large scale solar chimney power plant. Their resultant optimal plant collector height was not the same as that predicted by Kröger and Buys (2001) or Pretorius *et al.* (2004). In the work of Tingzhen *et al.* (2006), a mathematical model was proposed that could predict the effects of various parameters, such as the tower height and its radius, the collector radius and the solar radiation, on the relative static pressure, the driving force, the power output and the efficiency of a solar chimney.

An experimental study of a full scale prototypical solar chimney power plant would be costly and time consuming since even a “small” plant is of the order of 100 m in height. The experimental study of a solar chimney power plant therefore should be performed on a small-scale model. A similarity condition(s), however, is needed in order to scale the model’s experimental results up to those of the prototype. A dimensional analysis study (Koonsrisuk and Chitsomboon, 2007) found that a complete similarity between a small-scale model and a full-scale prototype could be achieved only when the solar heat fluxes (insolation) between them were different. This is very inconvenient in an experimental setup since it suggests the use of a material of an exact transmittance for the roof of the model. Therefore, the main objective of the present study is to find an alternate similarity condition that permits a small-scale model experiment to use the same insolation as that of the large-scale prototype. The study found that the same-insolation condition could indeed be achieved, but the concept of geometrical similarity must be modified; in other words, only a partial geometrical similarity is allowed.

Since there were limitations due to cost, actual experiments in physical models were not conducted to confirm the validity of the proposed partial similarity condition. Instead, “numerical experiments” were carried out by using computational fluid dynamics (CFD) (ANSYS, 2005). Data similarities between the models and the prototype were compared by scaling the numerical results.

4.3 DIMENSIONAL ANALYSIS

According to the work of Chitsomboon (2001), the mathematical model of the flow in a solar chimney power plant was proposed as

$$\frac{1}{2} \dot{m} V_1^2 \left[\rho_1 - 2\rho_1 A_1^2 \int_1^3 \frac{dA}{A^3} + \frac{2A_1 q''}{V_1 c_p T_1} \int_1^3 \frac{dA_r}{A^2} + \frac{2\rho_1 A_1^2 g h_c}{\gamma R T_1} \int_1^3 \frac{dA}{A^3} \right] = \frac{\rho_1 g h_c q''}{c_p T_3} \int_1^3 dA_r \quad (4.1)$$

This mathematical model was obtained by a synthesis of the conservation equations of mass, momentum and energy, together with the ideal gas relation. The forms of the terms appearing in this equation could be used as a guide for selecting primitive variables in the dimensional analysis. Accordingly, the dependence of the kinetic power, $(\rho AV)V^2/2$, on the independent variables is proposed as

$$\rho AV \frac{V^2}{2} = f^n \left(\rho, g, \frac{q'' A_r}{c_p}, \beta, h_c \right). \quad (4.2)$$

Note that the viscosity is not included as a variable in Eq. (4.2) since we wish to focus on the inviscid effect first. Including viscosity would further cloud the similarity issue, especially when the numerical approach is used to verify the similarity condition since CFD has its own problems of turbulence modeling. Besides our previous work (Koonsrisuk and Chitsomboon, 2004) found that friction loss in a typical solar chimney was negligible. Temperature rise (intuitively a very important variable) does not appear explicitly but is hidden in $q'' A_r / c_p$ via the energy conservation principle ($q'' A_r = \dot{m} c_p \Delta T$). The thermal expansion coefficient, β

$(= -1/\rho \left(\frac{\partial \rho}{\partial T} \right)_p)$, is a most important variable because it represents the buoyant driving force for the system as a result of the temperature rise.

Koonsrisuk and Chitsomboon (2007) used q'''/c_p instead of $q''A_r/c_p$ as a variable ($q''' = q''/h_r$); they proposed the dimensionless relation as,

$$\frac{\rho A V \frac{V^2}{2}}{\frac{q''' \beta g}{c_p} h_c^4} = f^n \left(\frac{\rho}{\frac{q''' \beta}{c_p} \sqrt{\frac{h_c}{g}}} \right). \quad (4.3)$$

The validity of Eq. (4.3) was proved by scaling and comparing the numerical results of various models. To ensure the dynamic similarity required by Eq. (4.3), the roof height ratio was related to the insolation ratio by

$$\frac{q''_m}{q''_p} = \left(\frac{h_{r,m}}{h_{r,p}} \right)^{1/2} \quad (4.4)$$

with subscripts p and m denoting “prototype” and “model”, respectively. The condition in Eq. (4.4) imposes a lesser insolation level for a small-scale model than that of a prototype.

Later on, it was determined by the author that the undesirable condition of our previous study might be due to the use of $q''' (= q''/h_r)$ instead of q'' . Therefore, this study proposes the use of q'' . Eq. (4.1) shows, however, that this term always appears in combination as $q''A_r/c_p$. Hence this quantity, rather than just q'' , is proposed in this study.

The procedural steps in finding the similarity variables are listed as follows:

Step 1 Propose the primitive-variable functional relationship:

$$\rho AV \frac{V^2}{2} = f^n(\rho, g, \frac{q'' A_r}{c_p}, \beta, h_c, r_c, h_r). \quad (4.5)$$

Note the additional geometric variables from that of Eq. (4.2), an attempt to be more inclusive than our previous study. The size of the plant is characterized by the tower height (h_c), tower radius (r_c), roof height (h_r) and roof radius (r_r) (hidden in A_r)

Step 2 Use mass (M), length (L), time (t), and temperature (Θ) as the fundamental dimensions. The dimensional matrix of the various variables becomes

	$\rho AV \frac{V^2}{2}$	ρ	g	$\frac{q'' A_r}{c_p}$	β	h_c	r_c	h_r
M	1	1	0	1	0	0	0	0
L	2	-3	1	0	0	1	1	1
t	-3	0	-2	-1	0	0	0	0
Θ	0	0	0	1	-1	0	0	0

Step 3 Choose ρ, g, β , and h_c as the scaling variables (or repeating variables).

The fundamental dimensions can now be extracted from the scaling variables as:

$$L = h_c \quad (4.6)$$

$$M = \rho h_c^3 \quad (4.7)$$

$$t = \sqrt{\frac{h_c}{g}} \quad (4.8)$$

$$\Theta = \frac{1}{\beta}. \quad (4.9)$$

(Note: The methodology used here is presented in Chitsomboon (2003). It yields the same result as the familiar Buckingham's pi theorem but with much less algebraic complexity).

Step 4 Scale the remaining variables according to the powers of their fundamental dimensions (see the matrix above):

$$\Pi_1 = \frac{\rho AV \frac{V^2}{2}}{(\rho h_c^3)^1 (h_c)^2 (\sqrt{h_c/g})^{-3} (1/\beta)^0} = \frac{\frac{1}{2} \dot{m} V^2}{\rho h_c^{7/2} g^{3/2}} \quad (4.10)$$

$$\Pi_2 = \frac{q'' A_r / c_p}{(\rho h_c^3)^1 (h_c)^0 (\sqrt{h_c/g})^{-1} (1/\beta)^1} = \frac{q'' A_r \beta / c_p}{\rho h_c^{5/2} g^{1/2}} \quad (4.11)$$

$$\Pi_3 = \frac{r_c}{h_c} \quad (4.12)$$

$$\Pi_4 = \frac{h_r}{h_c} \quad (4.13)$$

Finally, the functional relationship is found to be $\Pi_1 = f^n(\Pi_2, \Pi_3, \Pi_4)$, or

$$\frac{1}{2} \frac{mV^2}{\rho h_c^{7/2} g^{3/2}} = f^n \left(\frac{q'' A_r \beta}{\rho c_p h_c^{5/2} g^{1/2}}, \frac{r_c}{h_c}, \frac{h_r}{h_c} \right). \quad (4.14)$$

Similarity Requirements

Consider Eq. (4.14), for a geometrically similar model r_c/h_c and h_r/h_c are taken care of by the requirements that they are of the same value for both the models and the prototype. The remaining similarity requirement is,

$$\left[\frac{q'' A_r \beta}{\rho c_p h_c^{5/2} g^{1/2}} \right]_m = \left[\frac{q'' A_r \beta}{\rho c_p h_c^{5/2} g^{1/2}} \right]_p. \quad (4.15)$$

If the same working fluid and the ‘fully’ geometrical similar condition were assumed, Eq. (4.15) would, again, reduce to Eq. (4.4); this repeats the ‘dissimilar’ solar-heat-flux condition as established in the previous study. Alternatively, we now force the insulations of the two cases to be the same. Thus from Eq. (4.15) the required condition for dynamic similarity now is

$$\frac{r_{r,m}}{r_{r,p}} = \left(\frac{h_{c,m}}{h_{c,p}} \right)^{5/4} \quad (4.16)$$

Equation (4.16) implies that the ratio $r_{r,p}/h_{c,p}$ is not equal to $r_{r,m}/h_{c,m}$ as required by the usual geometric similarity condition. It is apparent that two types of dimension distortion are possible in order to achieve the partial similarity condition, namely, distortion of r_r and distortion of h_c . The distortion of h_c , however, is not acceptable since it is a fundamental scaling variable. Its distortion would nullify the

constancy assumptions made earlier of the scaled geometrical values: r_c/h_c and h_r/h_c . Therefore, only the distortion of r_r is acceptable. Recall that, in order to achieve a dynamic similarity, the scaled driving forces between the two flows must be identical. Because the principal driving force for this system is the solar heat gain ($= q'' \pi r_r^2$), therefore adjustment of the heat gain could be controlled by altering the magnitude of r_r .

As a result, Eq. (4.16) indicates that the roof radius scales with the tower height to the power of $5/4$ while all the remaining length dimensions scale with the power of 1. As such, the model's roof radius is distorted from a truly physically similar model. In other words, the scaled model must be partially geometrically similar to the prototype.

The dimensions of the prototype, four fully geometrically similar models and four partially geometrically similar models (using Eq. (4.16)) that were used to simulate the numerical test cases are presented in Table 4.1. The three test cases that were set up and the insulations for each plant are also listed in Table 4.1.

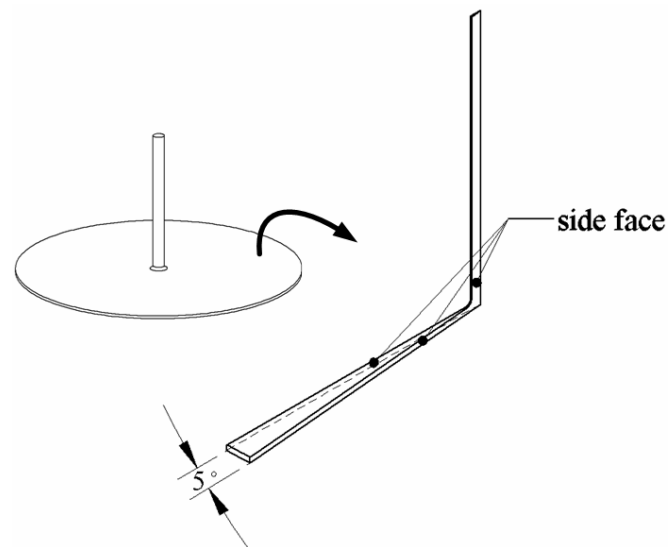
4.4 COMPUTATIONAL WORK

For the numerical simulations, the CFD code (ANSYS, 2005) solves the conservation equations for mass, momentum, and energy using the finite volume method. To simulate the axis-symmetry condition in the 3-dimensional setting, a pie shape domain was created by cutting a 5 degree wedge out of the whole power plant geometry. The side faces of the domain were taken as symmetric boundary conditions as shown in Fig. 4.2a. Adaptive unstructured tetrahedral meshes were used to

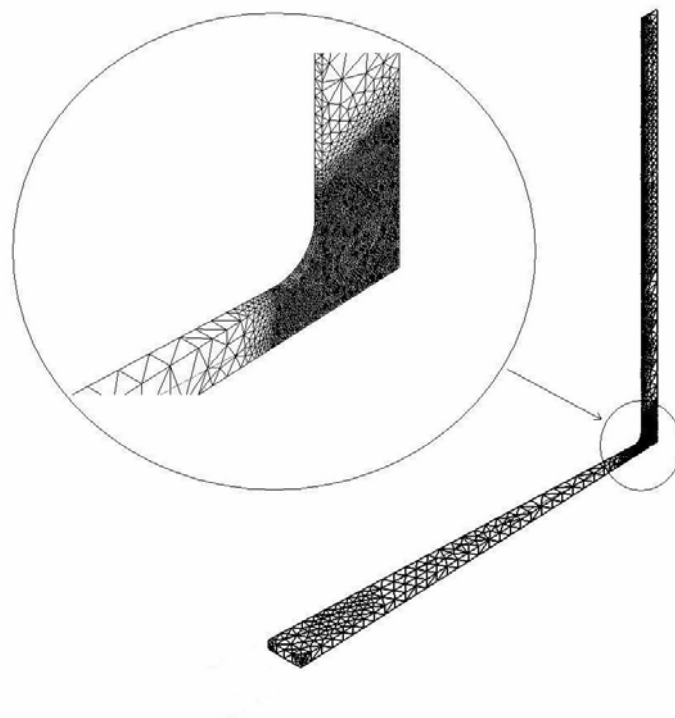
Table 4.1 Specification of prototype and models

<i>Plant</i>	<i>Chimney height, h_c (m)</i>	<i>Roof height, h_r (m)</i>	<i>Chimney radius, r_c (m)</i>	<i>Roof radius, r_r (m)</i>	<i>Insolation (W/m^2)</i>		
					<i>Case 1</i>	<i>Case 2</i>	<i>Case 3</i>
Prototype (reference)	100	2	4	100	200	600	1,000
Model 1-f (fully similar)	5	0.1	0.2	5	44.72	134.16	223.61
Model 2-f (fully similar)	20	0.4	0.8	20	89.44	268.33	447.21
Model 3-f (fully similar)	40	0.8	1.6	40	126.49	379.47	632.46
Model 4-f (fully similar)	80	1.6	3.2	80	178.89	536.66	894.43
Model 1-p (partially similar)	5	0.1	0.2	2.36	200	600	1,000
Model 2-p (partially similar)	20	0.4	0.8	13.37	200	600	1,000
Model 3-p (partially similar)	40	0.8	1.6	31.81	200	600	1,000
Model 4-p (partially similar)	80	1.6	3.2	75.66	200	600	1,000

Note: The specification of prototype, model 1-f, and model 2-f are the same as the plants studied in Koonsrisuk and Chitsomboon (2007).



(a)



(b)

Figure 4.2 Computational domain: (a) 5 degree axis-symmetric section;
(b) numerical grid.

discretize the domain and the grid convergence issue was already investigated previously (Koonsrisuk and Chitsomboon, 2007). Thus those grid configurations are adopted in this work. A typical grid for the computational domain is shown in Fig. 4.2b.

Proper boundary conditions are needed for a successful computational work. At the roof perimeter (inlet), the flow direction was set as normal to the periphery and the total pressure and the static temperature were specified. Zero static pressure (gauge) was prescribed at the chimney exit. Symmetry conditions were applied at the two side walls of the pie-shape domain while adiabatic free-slip conditions were prescribed to the remaining boundaries (since the flow is assumed to be inviscid). All the test cases were computed until the residuals of all the governing equations reached their required convergence precisions. It should be mentioned that the numerical procedure used in this study had already been carefully calibrated and validated in our previous studies to achieve a satisfactory level of confidence.

4.5 RESULTS AND DISCUSSION

Computations were conducted for the test cases listed in Table 4.1. Their results are illustrated in Figs. 4.3 - 4.5. In these figures, the solid symbols were used to identify the data points for the fully geometrically similar models (model 1f – 4f) whereas the hollow symbols were used for the partially geometrically similar models (model 1p– 4p).

Figure 4.3 shows the computed updraft velocities at the tower top of all the test cases, as a function of insolation. All distributions display the expected increasing trends as the insolation increases. The rates of increase of the velocities appear to be

slightly lower as the insolation increases. It should be noted again that the insulations for the fully similar models were less than that of the prototype (according to Eq. (4.4)) while the partially similar models used the same insolation as the prototype. The kinetic powers (output) at the chimney tops are presented in Fig. 4.4 as functions of insulations (input).

Huge discrepancies in the distributions for all the different-size models and the prototype are observed. These discrepancies are intuitively expected for physical models of widely different sizes since the data are presented in primitive (dimensional) forms.

When the data in Fig. 4.4 were scaled according to the proposed scaling law in this study, the results are as shown in Fig. 4.5. It can be clearly seen that the once widely scattered lines of dimensional data all collapse (almost) into a single line in this non-dimensional plot. This confirms the validity of the partial similarity law being proposed in this study. It also confirms the different-insulations similarity law that was proposed in our previous study. The slight non-overlapping of the data lines might be attributable to various numerical errors (such as discretization error and numerical diffusion), as well as the neglected viscous effect. These should be resolved in further studies.

Further inspection of Fig. 4.5 reveals that all curves have a slope of unity and pass through the origin. This suggests a linear fit as

$$\frac{\frac{1}{2} \dot{m} V^2}{\rho h_c^{7/2} g^{3/2}} = \frac{q'' A_r \beta}{\rho c_p h_c^{5/2} g^{1/2}}$$

or, after simplifying

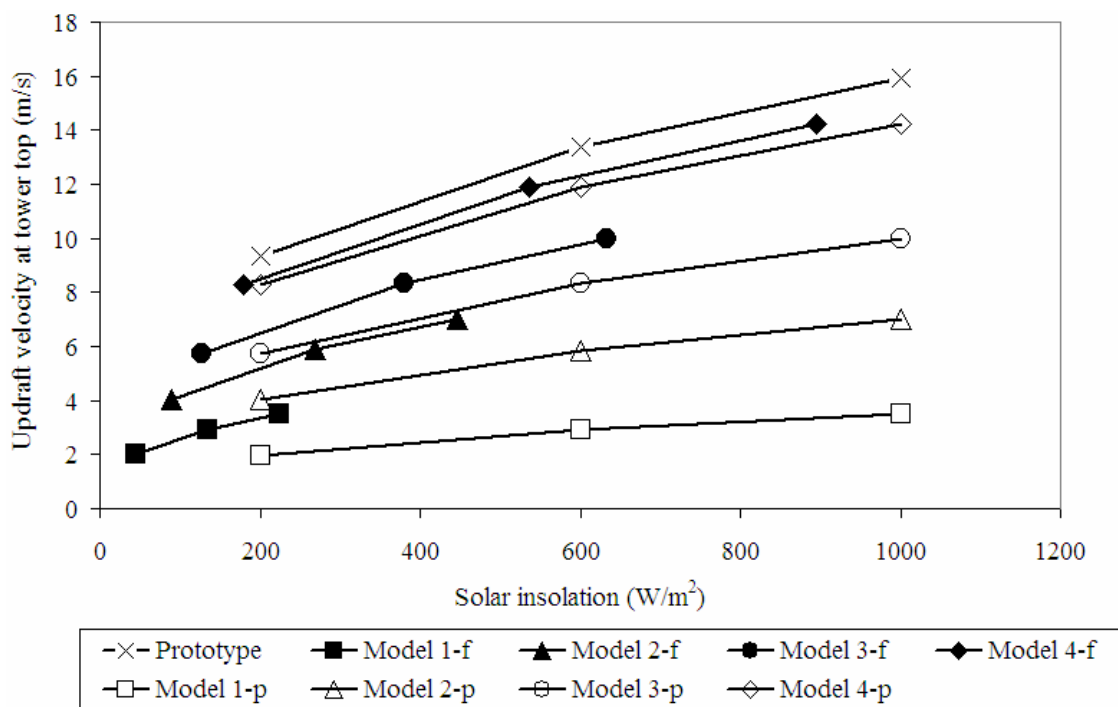


Figure 4.3 Numerical prediction of updraft velocity at tower top as a function of insolation.

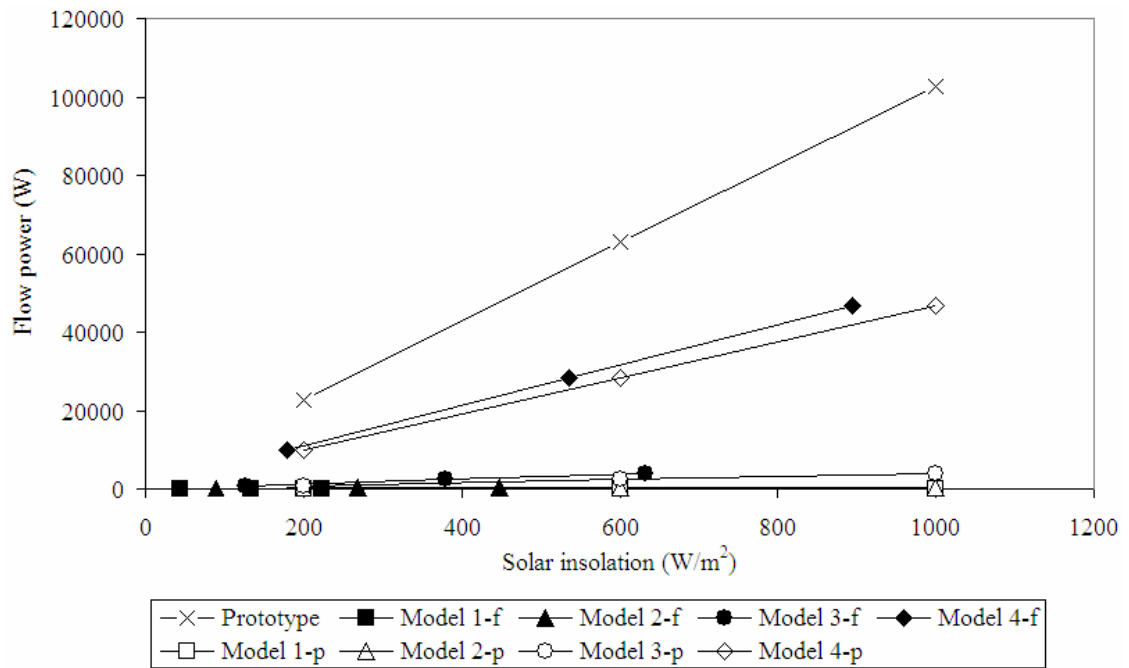


Figure 4.4 Numerical prediction of flow power as a function of insolation.

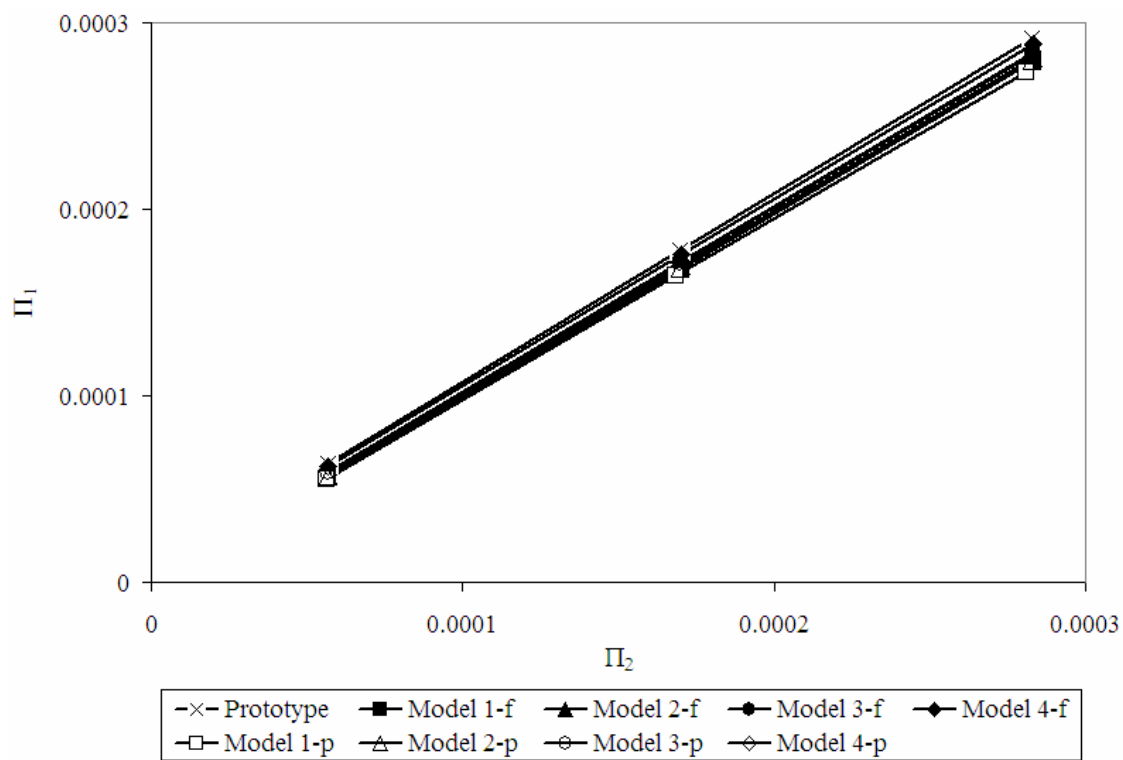


Figure 4.5 $\Pi_1 - \Pi_2$ characteristics.

$$\frac{1}{2} \dot{m} V^2 = \frac{q'' A_r \beta}{c_p} g h_c . \quad (4.17)$$

Recall that, Eq. (4.1) can be rearranged as

$$\frac{1}{2} \dot{m} V_3^2 = \frac{1}{\left\{ 1 + \frac{gh}{\gamma R T_1} \left[\left(\frac{A_3}{A_1} \right)^2 - 1 \right] + \frac{q''}{\rho_1 V_3 c_p T_1} \frac{D_c}{h_r} \ln \frac{D_c}{D_r} \right\}} \frac{q'' A_r \beta}{c_p} g h_c . \quad (4.18)$$

When the term multiplying $q'' A_r \beta g h_c / c_p$ on the right-hand side of the equation is computed from the primitive variables involved, it was found that the average values of each case are about unity. Consequently, the equation practically reduces to

$$\frac{1}{2} \dot{m} V_3^2 = \frac{q'' A_r \beta}{c_p} g h_c . \quad (4.19)$$

This is the same as Eq. (4.17), reassuring that the results obtained here are in accord with the theoretical predictions (and vice versa).

4.6 ENGINEERING INTERPRETATION OF THE DIMENSIONLESS VARIABLES

Engineering interpretation often results in a deeper understanding of the physical phenomenon represented by the mathematics. The scaling variables for Π_1 , $\rho h_c^{7/2} g^{3/2}$, could be interpreted as the *flow work*. To clarify this, first note that $\sqrt{g h_c}$ could be interpreted as the velocity scale of the problem. Accordingly,

$$\rho h_c^{7/2} g^{3/2} = (\rho g h_c) (h_c^2) (\sqrt{g h_c}) \sim \Delta p \cdot A \cdot V \sim F \cdot V = \text{Flow work in chimney.}$$

So, Π_1 could be interpreted as the kinetic power of the system measured in the scaling unit that is proportional to the quantity of the flow work.

The first law of thermodynamics stipulates that $q''A_r\beta/c_p \approx \dot{m}\beta\Delta T$.

Accordingly, the scaling variable for Π_2 (Eq. 4.11) could be interpreted as

$$\rho h_c^{5/2} g^{1/2} = \rho h_c^2 \sqrt{gh_c} \sim \rho AV = \dot{m}.$$

Π_2 now becomes $\beta\Delta T$ which is proportional to $\Delta\rho/\rho$ and thus could be interpreted as the buoyant force ($\Delta\rho$) scaled by the weight of the fluid of the same volume.

Therefore, the entire relation of $\Pi_1 = f^n(\Pi_2)$ could be interpreted simply and rationally as the effect of the principal characteristic driving force (input) on the characteristic kinetic energy (output).

4.7 CONCLUSION

The study showed that a complete dynamic similarity for scaled models and a full scale solar chimney prototype, while maintaining the same insolation, is achievable provided that the model's roof radius is distorted from its fully similar configuration according to a prescribed rule that was proposed in the study. This 'partially similar' proposition was proven to be valid which was evident by the collapse of the scaled numerical results of the widely disparate test cases. The seemingly complicated similarity variables were interpreted simply as the characteristic output power (scaled kinetic energy) and the characteristic input power (scaled buoyant force).

4.8 REFERENCES

- ANSYS, Inc. **ANSYS CFX**, Release 10.0: reference guide. ANSYS, 2005.
- Bernardes, M. A., Dos, S., Voß, A., Weinrebe, G., 2003. Thermal and technical analyses of solar chimneys. **Solar Energy**, Vol. 75(6), pp. 511-524.
- Chitsomboon, T., 2001. A validated analytical model for flow in solar chimney. **International Journal of Renewable Energy Engineering**, Vol. 3(2), pp. 339-346.
- Chitsomboon, T., 2003. **Fluid Mechanics**. McGraw-Hill/Top, Thailand.
- Gannon, A. J., Von Backström, T. W., 2003. Solar chimney turbine performance. **Journal of Solar Energy Engineering**, Vol. 125(1). pp. 101-106.
- Haaf, W., Friedrich, K., Mayr, G., Schlaich, J., 1983. Solar chimneys: part I: principle and construction of the pilot plant in Manzanares. **International Journal of Solar Energy**, Vol. 2, pp 3-20.
- Haaf, W., 1984. Solar chimneys: part II: preliminary test results from the Manzanares plant. **International Journal of Solar Energy**, Vol. 2, pp 141-161.
- Koonsrisuk, A., Chitsomboon, T., 2004. Frictional effect on the flow in a solar chimney. In: **Proceedings of the 4th National Symposium on Graduate Research**, Chiang Mai, Thailand.
- Koonsrisuk, A., Chitsomboon, T., 2007. Dynamic similarity in solar chimney modeling. **Solar Energy**, Vol. 81, pp. 1439-1446.
- Kröger, D. G., Buys, J. D., 2001. Performance evaluation of a solar chimney power plant. **ISES 2001 Solar World Congress**, Adelaide, Australia.
- Onyango, F. N., Ochieng, R. M., 2006. The potential of solar chimney for application in rural areas of developing countries. **Fuel**, Vol. 85, pp. 2561-2566.

- Padki, M. M., Sherif, S. A., 1989a. Solar chimney for medium-to-large scale power generation. In: **Proceedings of the Manila International Symposium on the Development and Management of Energy Resources**, Manila, Philippines, Vol. 1, pp. 423-437.
- Padki, M. M., Sherif, S. A., 1989b. Solar chimney for power generation in rural areas. **Seminar on Energy Conservation and Generation Through Renewable Resources**, Ranchi, India, pp. 91-96.
- Padki, M. M., Sherif, S. A., 1999. On a simple analytical model for solar chimneys. **International Journal of Energy Research**, Vol. 23, no. 4, pp 345-349.
- Pasumarthi, N., Sherif, S. A., 1998a. Experimental and theoretical performance of a demonstration solar chimney model – part I: mathematical model development, **International Journal of Energy Research**, Vol. 22, no. 3, pp 277-288.
- Pasumarthi, N., Sherif, S. A., 1998b. Experimental and theoretical performance of a demonstration solar chimney model – part II: experimental and theoretical results and economic analysis, **International Journal of Energy Research**, Vol. 22, no. 5, pp 443-461.
- Pretorius, J. P., Kröger, D. G., 2006. Critical evaluation of solar chimney power plant performance. **Solar Energy**, Vol. 80, pp. 535-544.
- Pretorius, J. P., Kröger, D. G., Buys, J. D., Von Backström, T. W., 2004. Solar tower power plant performance characteristics. In: **Proceedings of the ISES EuroSun2004 International Sonnenforum 1**, Freiburg, Germany, pp. 870–879.
- Schlaich, J., 1995. **The Solar Chimney**. Edition Axel Menges: Stuttgart, Germany.

- Schlaich, J., Weinrebe, G., 2005. Design of commercial solar updraft tower systems utilization of solar induced convective flows for power generation. **Journal of Solar Energy Engineering**, Vol. 127, pp.117–124.
- Tingzhen, M., Wei, L., Guoliang, X., 2006. Analytical and numerical investigation of the solar chimney power plant systems. **International Journal of Energy Research**, Vol. 30, pp. 861-873.
- Von Backström, T. W., Gannon, A. J., 2000. Compressible flow through solar power plant chimneys. **ASME Journal of Solar Energy Engineering**, Vol. 122(3), pp. 138-145.
- Yan, M. Q., Sherif, S. A., Kridli, G. T., Lee, S. S., Padki, M. M., 1991. Thermo-fluid analysis of solar chimneys. **Ind. Applic. Fluid Mech.** ASME FED-2, pp. 125-130.

CHAPTER V

A SINGLE DIMENSIONLESS VARIABLE FOR SOLAR CHIMNEY POWER PLANT MODELING

5.1 ABSTRACT

The solar chimney power plant is a relatively new technology for generating electricity from solar energy. In this paper dimensional analysis is used together with engineering intuition to combine eight primitive variables into only one dimensionless variable that establishes a dynamic similarity between a prototype and its scaled models. Three physical configurations of the plant were numerically tested for similarity: fully geometrically similar, partially geometrically similar, and dissimilar types. The values of the proposed dimensionless variable for all these cases were found to be nominally equal to unity. The value for the physical plant actually built and tested previously was also evaluated and found to be about the same as that of the numerical simulations, suggesting the validity of the proposition. The physical meaning of this dimensionless (similarity) variable is also interpreted; and the connection between the Richardson number and this new variable was found. It was found also that, for a fixed solar heat flux, different-sized models that are fully or partially geometrically similar share an equal excess temperature across the roof outlet.

5.2 INTRODUCTION

Large-scale production of electricity from solar power is the goal of a solar chimney power plant. The basic idea of the solar chimney power plant, as shown in Fig. 5.1, is to combine the greenhouse effect, in which air and soil are heated underneath the transparent roof (collector) by solar radiation, with the chimney effect. The combined effects create a strong upward air draft due to a density differential which drives a turbine, to which an electrical generator is connected.

The idea of the solar chimney power plant was proposed initially by two German engineers, Jörg Schlaich and Rudolf Bergermann in 1976 (Hoffmann and Harkin, 2001). In 1979 they developed the first prototype with a designed peak output of 50 kW in Manzanares, about 100 miles south of Madrid, Spain. It consisted of a chimney with a radius of 5 m and a height of 195 m and collector with a radius of 120 m and a variable height of between 2 m at the inlet to 6 m at the junction with the tower. This pilot plant ran from the year 1982 to 1989. Tests conducted have shown that the prototype plant operated reliably and the concept is technically viable (Haaf *et al.*, 1983; Haaf, 1984). The energy balance, design criteria and cost analysis were discussed in Haaf *et al.* (1983). An analysis showed that the power production cost for the plant was 25 DM/kWh (0.098 USD/kWh based on the exchange rate in 1983.) Since then, no solar chimney power plant has been built but numerous theoretical and numerical studies have been carried out by many researchers.

Several commercial plants have been proposed in research literatures. Solar chimneys with thousands-meters-in-diameter collector and thousands-meters-high chimney were presented in Schlaich (1995) as power plants with an electrical power

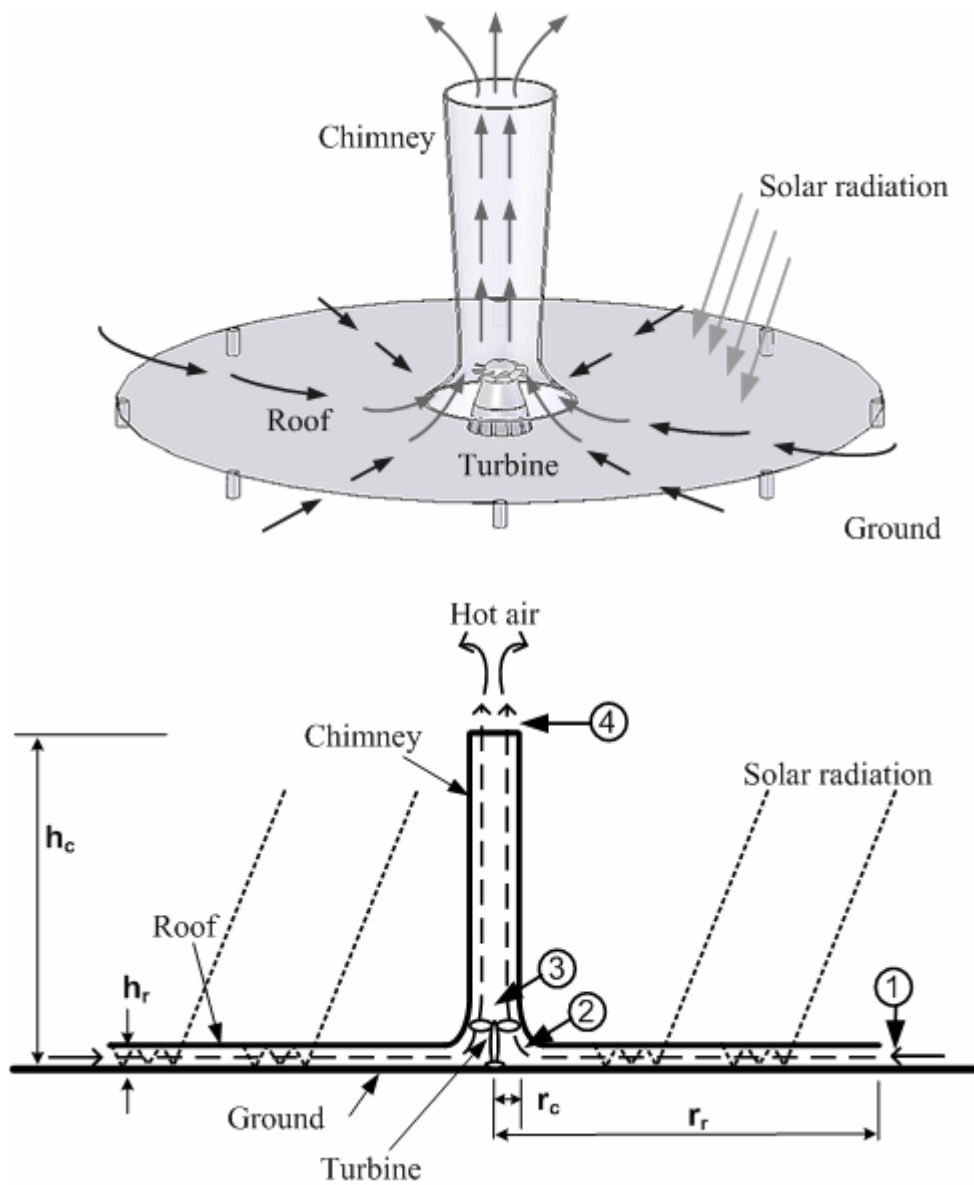


Figure 5.1 Schematic layout of solar chimney power plant.

capacity of hundreds MW. A case study in the Northwestern regions of China (Dai *et al.*, 2003) concluded that the solar chimney power plant in which the height and diameter of the chimney are 200 m and 10 m, respectively, and the collector's radius is 500 m is able to produce 110-190 kW electric power. Another group of researchers (Bilgen and Rheault, 2005) proposed to construct a solar chimney on a sloped surface or on suitable hills in a high latitude area. It was found analytically that a nominal power of 5 MW would be produced by a system with a collector area of 950,000 m² and an equivalent chimney height (= hill + chimney) of 547 m. A system with a 1500m high chimney was simulated by several authors (Gannon and Von Backström, 2000; Von Backström, 2003; Pretorius and Kröger, 2006a). Some researchers (Pretorius and Kröger, 2006b; Bernardes *et al.*, 2008) carried out their analysis with a plant that has a chimney of 1,000 m high, 210 m in diameter and a collector of radius 5,000 m. It is obvious that these plants required a large amount of investment in construction and operation. Consequently, a small-scale physical model should be built, tested and altered experimentally until the unit function properly and economically. The satisfactory use of the model requires a clear understanding of the principles involved in the relationship between model and prototype.

Koonsrisuk and Chitsomboon (2009) developed a scaling law that enabled a reliable prediction to be made from observations on a small-scale model. This law describes the qualitative relationship between two dimensionless variables of the system [cf. Eq. (5.2)]. When graphed, it appeared that these variables have a linear relationship with a slope of unity. In other words, they have the same magnitude for fixed solar radiation. This insight suggested that the ratio between them is a constant, and that it would be possible to reduce two governing dimensionless variables into a

single dimensionless product. The present study utilizes dimensional analysis to establish that single dimensionless variable. Additionally, the validation is performed using data from numerical simulations and measurements from the Manzanares prototype.

5.3 DIMENSIONAL ANALYSIS

It was earlier suggested that the significant variables governing the flow in a solar chimney were $\rho, A, V, q''', c_p, \beta, h_c, g$ (Koonsrisuk and Chitsomboon, 2007). In a subsequent work (Koonsrisuk and Chitsomboon, 2009), certain primitive variables were grouped together and presented as

$$\rho A V \frac{V^2}{2} = f^n \left(\rho, g, \frac{q'' A_r}{c_p}, \beta, h_c \right) \quad (5.1)$$

and the dimensionless relationship was found to be $\Pi_1 = f^n(\Pi_2)$, or

$$\frac{\frac{1}{2} \dot{m} V^2}{\rho h_c^{\frac{7}{2}} g^{\frac{3}{2}}} = f^n \left(\frac{q'' A_r \beta}{\rho c_p h_c^{\frac{5}{2}} g^{\frac{1}{2}}} \right) \quad (5.2)$$

According to the Buckingham Pi theorem,

$$s = n - b \quad (5.3)$$

In this case, one dimensionless variable is desired and four basic dimensions [mass (M), length (L), time (t), and temperature (Θ)] are involved, or $s = 1$ and $b = 4$.

Hence only five quantities are required.

Equation (5.1) has six quantities involved, which are $\rho AV^3/2$, ρ , g , $q''A_r/c_p$, β and h_c . So we start with this set of quantities, and then select two from among six of them to merge into one new term.

The chimney effect, which depends on g and h_c , is one of the driving mechanisms in the solar chimney system. Therefore, $g \cdot h_c$ is chosen to be a new variable in this work. As a result, the pertinent variables are reduced to

$$\rho AV \frac{V^2}{2} = f^n \left(\rho, \frac{q''A_r}{c_p}, \beta, gh_c \right) \quad (5.4)$$

The matrix of dimensions for this case is

	$\rho AV \frac{V^2}{2}$	ρ	$\frac{q''A_r}{c_p}$	β	gh_c
M	1	1	1	0	0
L	2	-3	0	0	2
t	-3	0	-1	0	-2
Θ	0	0	1	-1	0

Using Pi theorem, the result becomes

$$\Pi_{const} = \frac{\rho AV \frac{V^2}{2}}{\frac{q''A_r \beta}{c_p} gh_c} \quad (5.5)$$

When only one non-dimensional group exists, it cannot be a function of any other variable. Therefore it must equal a constant. Thus,

$$\Pi_{const} = \frac{\rho A V \frac{V^2}{2}}{\frac{q'' A_r \beta}{c_p} g h_c} = \text{constant} . \quad (5.6)$$

Now the original eight primitive variables ($\rho, A, V, q'', c_p, \beta, h_c, g$) have been combined and the number of variables is reduced to only one. This should help make the ensuing experiments much simpler and more economical. The validity of the derived dimensionless variable, however, remains to be proven. To this end, Computational Fluid Dynamics (CFD) was employed to obtain numerical solutions of several solar chimneys of different sizes. The numerical results of those plants were scaled to obtain Π_{const} , and compared to verify the validity of the proposed dimensionless variable.

5.4 COMPUTATIONAL WORK

To validate the reliability of the proposed dimensionless variable, three classes of scaled models are set up as listed in Table 5.1. Geometrically similar models, being scale reproductions of the prototype, form the first category to which belong models 1 and 2 in this paper. The second category, distorted or partially similar models, to which belong models 3 and 4, is adopted from Koonsrisuk and Chitsomboon (2009), where the solar chimney model's roof radius does not 'fully' satisfy the geometric similarity condition, but is calculated from the relation $r_{r,m} = (h_{c,m}/h_{c,p})^{5/4} r_{r,p}$. The advantage of this 'partial similarity' is that it produces dynamic similarity without having to resort to different insulations for a prototype and scale models. The last

category, that of dissimilar models which do not bear any similarity (fully or partial) to the prototype, consists of models 5 and 6 in this paper.

The governing equations for mass, momentum, and energy for each plant are solved using the commercial CFD code (ANSYS, 2005). The iteration continues until the RMS error of all equations converges to a specified value. A typical run takes four to six hours on a desktop computer. The computation is performed using the assumption of steady laminar inviscid flow with a uniform heat source added to the collector portion. To correctly handle the body force due to buoyancy effect, source terms for momentum and energy equations are added and defined in the following manner:

$$S_M = (\rho - \rho_{ref})g \quad (5.7)$$

$$S_E = q''/h_r . \quad (5.8)$$

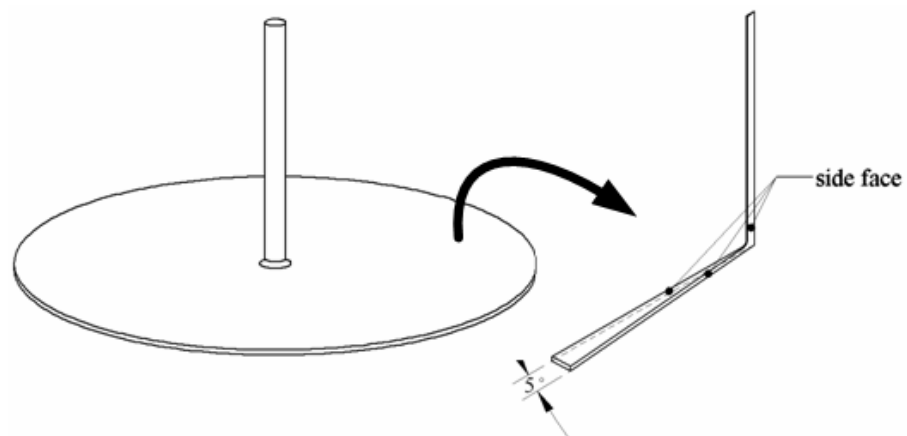
The code is implemented in 3D through the axis-symmetry approximation. As illustrated in Fig. 5.2a, only a 5-degree pie-shape of the whole domain is modeled with the side faces treated as symmetric boundaries.

In our previous work (Koonsrisuk and Chitsomboon, 2007) suitable grid and time step size were carefully chosen after performing grid and time step independence tests of the numerical results, thus those configurations are adopted in this work. An example of grid-independence mesh system is presented in Fig. 5.2b.

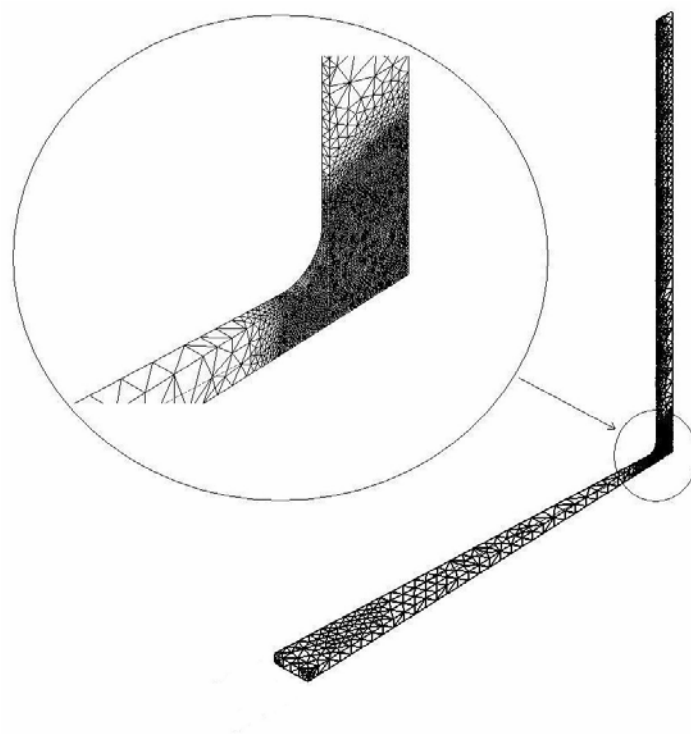
Table 5.1 Specification of prototype and models

<i>Case</i>	<i>Tower height (m)</i>	<i>Roof height (m)</i>	<i>Tower radius (m)</i>	<i>Roof radius (m)</i>	<i>Geometric similarity characteristics</i>
Prototype	100	2	4	100	reference
Model 1	20	0.4	0.8	20	similar
Model 2	5	0.1	0.2	5	similar
Model 3	20	0.4	0.8	13.37	partially similar
Model 4	5	0.1	0.2	2.36	partially similar
Model 5	50	1	2	25	dissimilar
Model 6	200	1	2	50	dissimilar
Model 7	194.6	1.85	5.08	122	dissimilar

Note: The specification of prototype, model 1, and model 2 are the same as the plants studied in Koonsrisuk and Chitsomboon (2007); models 3 and 4 are the distorted models of models 1 and 2, respectively; models 5 and 6 are the non-geometrically similar models of prototype; model 7 is the Manzanares plant.



(a)



(b)

Figure 5.2 Computational domain: (a) 5 degree axis-symmetric section;
(b) computational grid.

The same boundary condition settings in the previous work are also employed here. The total pressure and temperature were imposed at the collector entrance and the flow direction was set as normal to the roof perimeter. At the chimney top, the ‘outlet’ boundary condition with zero static gauge-pressure was prescribed. Symmetry boundary conditions were applied at the side faces of the sector (Fig. 5.2a) and adiabatic free-slip conditions were imposed at the remaining exposed surfaces.

5.5 RESULTS AND DISCUSSION

The numerical flow properties of the prototype and model 1-6 are computed for representative values of insolation. Fig. 5.3 depicts the comparisons of velocity at the chimney top of each plant. The distributions of the graphs appear to be in accord with their physical sizes and the requirements of the governing conservation principles.

The temperature distributions at the collector exit are displayed in Fig. 5.4 wherein it can be seen that the exit temperature of the prototype and all fully and partially similar models, despite their wide differences in geometry, are closely identical. This rather intriguing phenomenon will be elaborated further, after the main results are presented.

Table 5.2 presents the values of II_{const} that were computed from the involved variables of each plant. It is evident that the numerical values of the proposed II_{const} for all the cases are about the same, of the order of 1.0, even though the operating conditions were widely different. It is interesting to note that the dissimilarity of

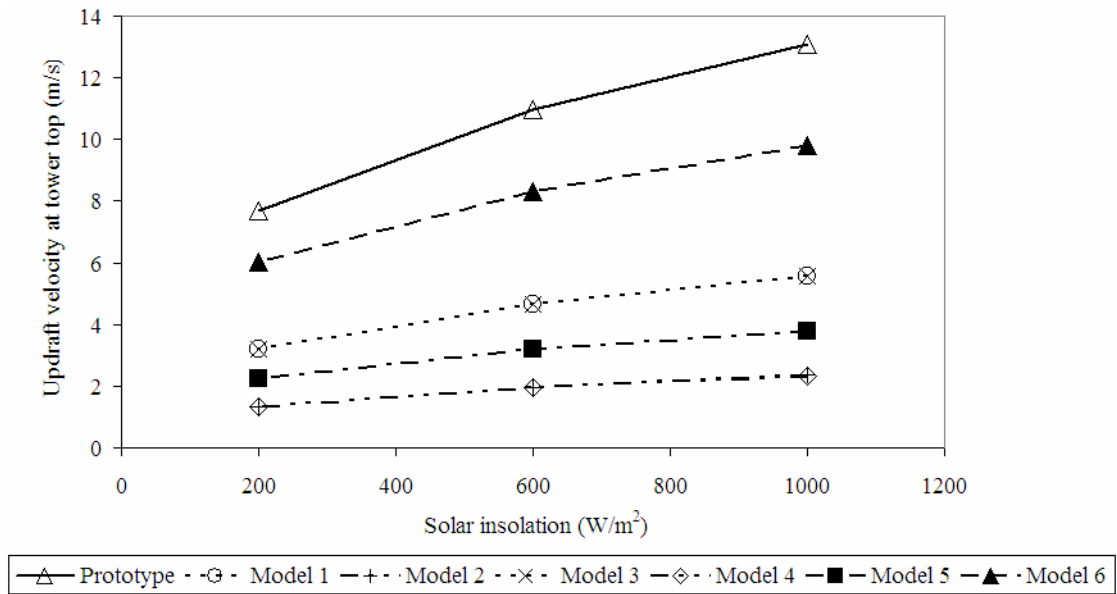


Figure 5.3 Numerical prediction of updraft velocity at tower top as a function of insolation.

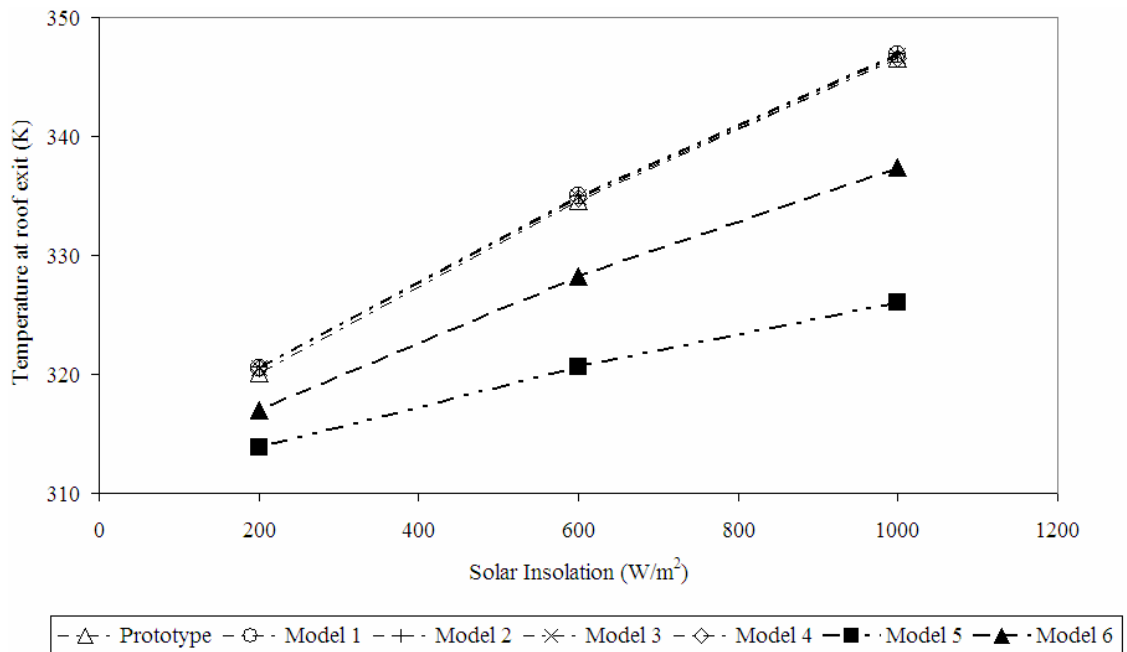


Figure 5.4 Numerical prediction of temperature at roof exit as a function of insolation.

Table 5.2 Dimensionless variable for prototype and models.

Case	q'' (W/m ²)	Π_{const}	Percent Difference
Prototype	1,000	1.03	-
	600	1.05	1.97
	200	1.13	9.55
Model 1	1,000	1.00	3.71
	600	1.00	3.28
	200	1.01	1.71
Model 2	1,000	0.99	4.37
	600	0.99	4.23
	200	0.99	3.87
Model 3	1,000	0.99	4.07
	600	0.99	3.61
	200	1.01	2.00
Model 4	1,000	0.98	5.42
	600	0.98	5.19
	200	0.98	4.68
Model 5	1,000	1.02	0.71
	600	1.04	1.34
	200	1.13	9.15
Model 6	1,000	1.11	7.80
	600	1.16	12.97
	200	1.38	25.17
Model 7	1,017	0.95	8.33

Note: The percentage difference for each cases are based on the case of prototype with $q'' = 1,000$ W/m².

model 5 does not strongly affect the condition of Π_{const} but model 6 departs quite significantly from the condition. This could be due to the fact that model 5 is only slightly dissimilar from the partially similar condition while model 6 departs significantly from both the similar and partially similar conditions.

To test the similarity issue further, Π_{const} for the prototype that was actually built and tested in the Manzanares desert in southern Spain is also computed. Experimental data taken from Weinrebe and Schiel (2001), compensated with the 0.32 collector efficiency, the $2/3$ ratio of p_t/p_p (Haaf *et al.*, 1983) and the 0.15 pressure loss co-efficient (Weinrebe and Schiel, 2001), were used in the computation. This is shown in Table 5.2 as the data in model 7, in which it is shown that the value of Π_{const} is only about 8% off the bench mark value of 1.0. Here we noticed that the similarity between plants is acceptable.

The unified values of this variable under wide (even partially dissimilar) conditions have prompted us to investigate further. It is noted that without an extracting turbine the whole buoyant energy resulting from the insolation is converted into kinetic energy. The overall efficiency of the system can be defined in conjunction with Eq. (5.6) as

$$\eta_o = \frac{\rho AV \frac{V^2}{2}}{q'' A_r} = \Pi_{const} \times \frac{\beta}{c_p} gh_c. \quad (5.9)$$

It has been well established that $\beta = 1/T$ for an ideal gas, then Π_{const} could be arranged as

$$\Pi_{const} = \eta_o \div \left(\frac{gh_c}{c_p T_1} \right). \quad (5.10)$$

Considering that the overall efficiency was proposed by Gannon and Von Backström (2000) and Schlaich and Weinrebe (2005) as $gh_c/c_p T_1$, then it was not a surprise that the value of Π_{const} should be nominally equal to 1.0 since it is obviously an efficiency divided by “itself”. In other words, the similarity variable (Pi group) proposed in this study could be interpreted from another perspective which is related to the overall efficiency formulated by other researchers.

Physical meaning of a Pi group aids in engineering interpretation to deepen the understanding of a problem. The scaling variable of Π_{const} , $(q''A_r\beta/c_p)gh_c$, could be interpreted as the rate of energy that the air expends in floating from the base to the top of tower. To clarify this, first note that according to the first law of thermodynamics $q''A_r/c_p$ is equal to $\dot{m}\Delta T$ (when kinetic energy is neglected), where $\dot{m} = \rho AV$. When this term is multiplied by β ($= 1/\rho \left(\partial\rho/\partial T \right) \approx 1/\rho \left(\Delta\rho/\Delta T \right)$), it is then approximately proportional to $\Delta\rho AV$. Further multiplication by gh_c results in $(g\forall\Delta\rho)V$. The term in the parenthesis is the buoyant force in chimney; thus, the whole term is the flow power due to buoyancy of the hot air in tower. So, Π_{const} could be interpreted, from yet another perspective, as total kinetic energy of the system measured in the scaling unit that is proportional to the buoyant energy of the heated air.

The peculiar nature of the proposed similarity variable will now be further elaborated. Note that the Richardson number, which is sometimes interpreted as a

measure of the relative importance of free and forced convections (Cebeci and Bradshaw, 1988), is defined as

$$Ri = \frac{Gr}{Re^2} = \frac{\beta g \Delta T h_c^3 / \nu^2}{(Vh/\nu)^2} = \frac{\Delta \rho}{\rho} \frac{g h_c}{V^2} \quad (5.11)$$

With similar order of magnitude representations as used in the previous paragraph, it can be shown that $\Pi_{const} = \frac{1}{2 \cdot Ri}$.

It is ironic that this study, which began as an inviscid study, should end up with a Pi group that could be interpreted in a viscous context that is related to the Richardson number. To elaborate this irregularity, we can rewrite the Richardson number as

$$Ri = \Delta \rho \forall g V / \rho A V^3 \quad (5.12)$$

The above relation can be interpreted, in the same fashion as the proposed similarly variable, as the ratio of buoyant energy to the kinetic energy, precluding the viscous effect altogether. From this view point, the Richardson number seems to exhibit a dual character.

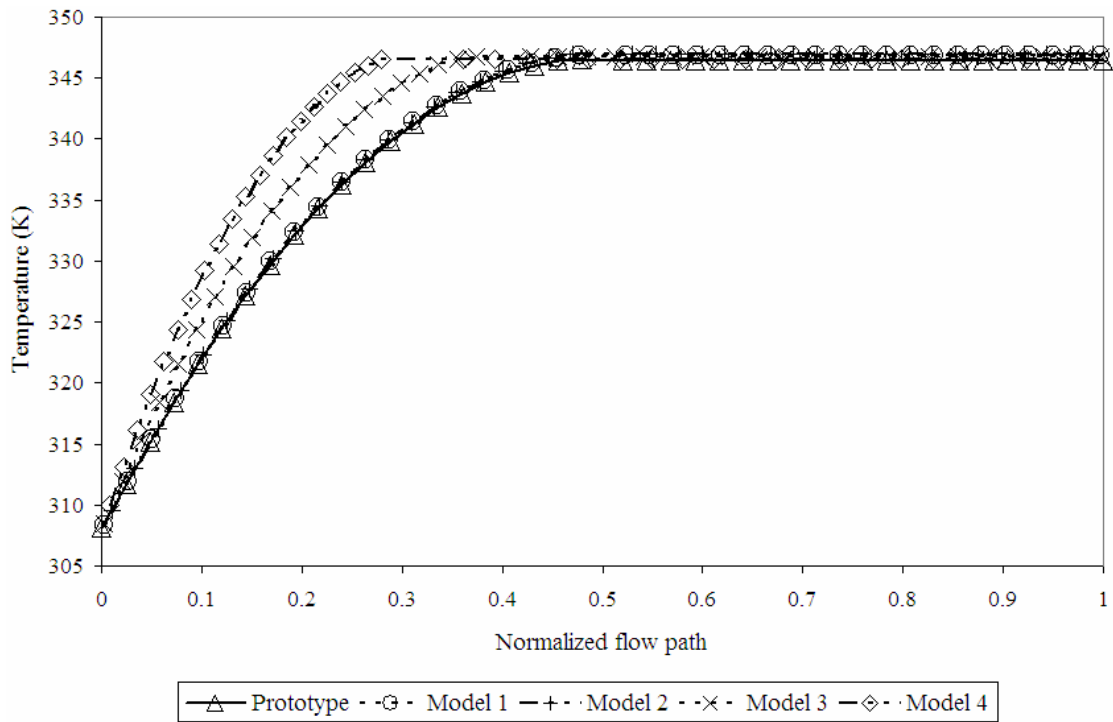


Figure 5.5 Numerical prediction of temperature profiles for insolation = 1,000 W/m².

Let us return to the side issue of temperature similarity between the prototype and its fully and partially similar models mentioned earlier. To further investigate this similarity, the temperature distribution along the normalized flow path for the prototype and models 1-4, using an insolation of 1000 W/m^2 , are shown in Fig. 5.5. It is seen that the temperatures along the towers are the same but are slightly different along the roofs. The reason for this similarity might be explained by considering the governing equation in non-dimensional form.

The theoretical model of Chitsomboon (2001) will be used as the basis for the investigation because it was fairly simple but contained important interactions of the flows between roof and chimney portions. The model proposed the governing equation for a solar chimney system as

$$\frac{1}{2} \dot{m} V_1^2 \left[1 - 2A_1^2 \int_1^3 \frac{dA}{A^3} + \frac{2q''}{\rho_1 V_1 c_p T_1} A_1 \int_1^3 \frac{dA_r}{A^2} + \frac{2gh_c}{\gamma R T_1} A_1^2 \int_1^3 \frac{dA}{A^3} \right] = \frac{gh_c q''}{c_p T_3} \int_1^3 dA_r . \quad (5.13)$$

The variables will now be scaled in the following manner:

$$\dot{m}^* = \frac{\dot{m}}{\rho_{ref} h_{ref}^2 V_{ref}} ; \quad V_1^* = \frac{V_1}{V_{ref}} ; \quad \rho_1^* = \frac{\rho_1}{\rho_{ref}} ; \quad A^* = \frac{A}{h_{ref}^2} ;$$

$$A_1^* = \frac{A_1}{h_{ref}^2} ; \quad A_r^* = \frac{A_r}{h_{ref}^2} ; \quad h_c^* = \frac{h_c}{h_{ref}} ; \quad T_1^* = \frac{T_1}{\Delta T} ; \quad T_3^* = \frac{T_3}{\Delta T}$$

Rewriting Eq. (5.13) in terms of these dimensionless variables yields

$$\frac{1}{2} \dot{m}^* V_1^{*2} \left[\begin{array}{l} 1 - 2A_1^{*2} \int_1^3 \frac{dA^*}{A^{*3}} \\ + \left(\frac{q''}{\rho_{ref} V_{ref} c_p \Delta T} \right) \frac{2A_1^*}{\rho^* V_1^{*2} T_1^*} \int_1^3 \frac{dA_r^*}{A^{*2}} \\ + \left(\frac{gh_{ref}}{\gamma R \Delta T} \right) \frac{2h_c^* A_1^{*2}}{T_1^*} \int_1^3 \frac{dA^*}{A^{*3}} \end{array} \right] = \left(\frac{gh_{ref} q''}{\rho_{ref} V_{ref}^3 c_p \Delta T} \right) \frac{h_c^*}{T_3^*} \int_1^3 dA_r^* \quad (5.14)$$

The three terms in parentheses, namely, $\Pi'_1 = q'' / \rho_{ref} V_{ref} c_p \Delta T$, $\Pi'_2 = gh_{ref} / \gamma R \Delta T$ and $\Pi'_3 = gh_{ref} q'' / \rho_{ref} V_{ref}^3 c_p \Delta T$, are dimensionless. Consequently, the solutions for these plants will be identical when expressed in dimensionless forms if the three variables Π'_1 , Π'_2 and Π'_3 for all the plants take on the same values. Moreover, since any combination of these variables is also a system variable, a new variable Π_1'' can be formed by letting

$$\Pi_1'' = \Pi_1'^3 \times \Pi_2' \div \Pi_3' = \left(\frac{q''}{\rho_{ref} V_{ref} c_p \Delta T} \right)^3 \cdot \left(\frac{gh_{ref}}{\gamma R \Delta T} \right) \cdot \left(\frac{\rho_{ref} V_{ref}^3 c_p \Delta T}{gh_{ref} q''} \right) = \frac{q''^2}{\gamma R \rho_{ref}^2 c_p^2 \Delta T^3}. \quad (5.15)$$

For complete similarity of a multivariate problem, Π_1'' must be identical between a prototype and its model, thus

$$\left[\frac{q''^2}{\gamma R \rho_{ref}^2 c_p^2 \Delta T^3} \right]_p = \left[\frac{q''^2}{\gamma R \rho_{ref}^2 c_p^2 \Delta T^3} \right]_m. \quad (5.16)$$

For the same working fluid with the same insolation, this yields,

$$\Delta T_p = \Delta T_m. \quad (5.17)$$

Surprisingly, this is also applicable for the partially geometrically similar plants too; but evidently this does not apply to the dissimilar cases as indicated in Figs 5.4 and 5.5.

Finally, it could be expected that this temperature similarity would occur only in the ideal situations as assumed in this study were met where the heat gain is totally and uniformly absorbed by the air under the roof, and the system is perfectly adiabatic and frictionless. In practice, the scale effect might contribute to a dissimilarity of solar heat absorption between plants, and friction losses will further complicate the similarity issue.

5.6 CONCLUSION

This study proposed a single dimensionless similarity variable for the solar chimney power plant that has proved to be valid for both the fully similar case and the partially similar case. This should enable the experimental study of a solar chimney power plant to be simpler and more economical. This variable was interpreted as the total kinetic energy scaled by the buoyant energy of the rising hot air. The proposed variable was examined from various perspectives and was found to be related to the overall efficiency proposed by other researchers and also to the Richardson number. The equality of temperature rises across roof portions for the prototype and its fully and partially similar models (a dimension quantity) was observed and explained in the context of similarity.

5.7 REFERENCES

- ANSYS, Inc. **ANSYS CFX**, Release 10.0: reference guide. ANSYS, 2005.
- Bilgen, E., Rheault, J., 2005. Solar chimney power plants for high latitudes. **Solar Energy**, Vol.79, pp. 449-458.
- Bernardes, M. A. S., Von Backström, T. W., Kröger, D. G., 2008. Analysis of some available heat transfer coefficients applicable to solar chimney power plant collectors. **Solar Energy**, doi: 10.1016/j.solener.2008.07.019.
- Cebeci, T., Bradshaw, P., 1988. **Physical and computational aspects of convective heat transfer**. Springer-Verlag, New York.
- Chitsomboon, T., 2001. A validated analytical model for flow in solar chimney. **International Journal of Renewable Energy Engineering**, Vol. 3(2), pp. 339-346.
- Dai, Y. J., Huang, H. B., Wang, R. Z., 2003. Case study of solar chimney power plants in northwestern regions of China. **Renewable Energy**, Vol. 28, pp. 1295-1304.
- Gannon, A. J., Von Backström, T. W., 2000. Solar chimney cycle analysis with system loss and solar collector performance. **Journal of Solar Energy Engineering**, Vol. 122. pp. 133-137.
- Haaf, W., Friedrich, K., Mayr, G., Schlaich, J., 1983. Solar chimneys: part I: principle and construction of the pilot plant in Manzanares. **International Journal of Solar Energy**, Vol. 2, pp 3-20.
- Haaf, W., 1984. Solar chimneys: part II: preliminary test results from the Manzanares plant. **International Journal of Solar Energy**, Vol. 2, pp 141-161.
- Hoffmann, P., Harkin, T., 2001. **Tomorrow's energy: hydrogen, fuel cells, and the prospects for a cleaner planet**. MIT Press, Massachusetts.

- Koonsrisuk, A., Chitsomboon, T., 2007. Dynamic similarity in solar chimney modeling. **Solar Energy**, Vol. 81, pp. 1439-1446.
- Koonsrisuk, A., Chitsomboon, T., 2009. Partial geometric similarity for solar chimney power plant modeling. **Solar Energy**, Vol. 83, pp. 1611-1618.
- Pretorius, J. P., Kröger, D. G., 2006a. Critical evaluation of solar chimney power plant performance. **Solar Energy**, Vol. 80, pp. 535-544.
- Pretorius, J. P., Kröger, D. G., 2006b. Solar chimney power plant performance. **Journal of Solar Energy Engineering**, Vol. 128, pp. 302-311.
- Schlaich, J., 1995. **The Solar Chimney**. Edition Axel Menges: Stuttgart, Germany.
- Schlaich, J., Weinrebe, G., 2005. Design of commercial solar updraft tower systems utilization of solar induced convective flows for power generation. **Journal of Solar Energy Engineering**, Vol. 127, pp. 117–124.
- Von Backström, T. W., 2003. Calculation of pressure and density in solar power plant chimneys. **Journal of Solar Energy Engineering**, Vol. 125, pp. 127-129.
- Weinrebe, G., Schiel, W., 2001. Up-draught solar tower and down-draught energy tower – A comparison. In: **Proceedings of the ISES solar world congress 2001**, Adelaide, Australia.

CHAPTER VI

ACCURACY OF THEORETICAL MODELS IN THE PREDICTION OF SOLAR CHIMNEY PERFORMANCE

6.1 ABSTRACT

A solar chimney is a solar power plant which generates mechanical energy (usually in terms of turbine shaft work) from a rising hot air that is heated by solar energy. The present paper compares the predictions of performances of solar chimney plants by using five simple theoretical models that have been proposed in the literature. The parameters used in the study were various plant geometrical parameters and the insolation. Computational Fluid Dynamics (CFD) simulation was also conducted and its results compared with the theoretical predictions. The power output and the efficiency of the solar chimney plants as functions of the studied parameters were used to compare relative merits of the five theoretical models. Models that performed better than the rest are finally recommended.

6.2 INTRODUCTION

A typical solar chimney power plant consists of a solar collector, a chimney and a turbine. The solar collector is a round, transparent roof, elevated above the ground and open at its periphery. The chimney is located at the center of the collector and the turbine is installed at its base (see Fig. 6.1). The air under the roof is heated up by solar radiation with the help of the greenhouse effect causing it to flow up the

chimney due to the difference of air density within the chimney and its surroundings. The flowing air is used to drive the turbine to generate electricity. Schlaich (1995) was credited as being the first to propose solar chimney as a means to harness energy from the sun.

Even though the technology involved in constructing a solar chimney plant is quite simple, considerable insights concerning many aspects are required before the plant can be designed for an optimal performance. Two of these aspects are the effects of geometry and insolation level on the plant performance. These issues have been examined by several researchers. The study of Haaf *et al.* (1983) showed that an increase of the collector radius increased output power but reduced plant efficiency. On the other hand, efficiency increased with the tower height, and mass flow rate increased with the tower radius while the flow velocity remained constant. Pasumarthi and Sherif (1998a, 1998b) reported that increase of tower height resulted in higher velocity and mass flow rate; and when the insolation was fixed, an increase in the mass flow rate was accompanied by a lower air temperature at the collector outlet. Chitsomboon (2000) found that efficiency of the plant was invariant with respect to the insolation level, the size of the roof and the tower diameter. He also found that the functional relationships between the power and the efficiency with the tower height were linear. Dai *et al.* (2003) demonstrated that the power output increased nonlinearly with the size of the plant, rapidly when the size was small and at a slower rate when the size was larger. Gannon and Backström (2000) and Schlaich *et al.* (2005) proposed that the overall efficiency was influenced only by the tower height. More recently, Tingzhen *et al.* (2006) reported that efficiency should also be affected by solar radiation and collector radius.

The common unfortunate features of all the findings are that the plant efficiency is very low. However, the efficiency increases with the plant size. Consequently, only large-scale plants, which require large amount of investment, were proposed in literatures. To design an economically practical system, geometric optimization is needed. It is advantageous to have a simple, but accurate, theoretical model as a tool to optimize the system mathematically. The objective of this study was to evaluate five simple theoretical models that had been proposed in the literature for their relative merits in comparison with the results of an accurate CFD procedure.

6.3 THEORETICAL MODELS

Only the ‘simple’ theoretical models found in the literature by the authors were selected to be evaluated for their relative merits. The theoretical models evaluated in this study (in chronological order) are: Chitsomboon (2001), Schlaich *et al.* (2005), Tingzhen *et al.* (2006), Zhou *et al.* (2009) and Koonsrisuk and Chitsomboon (2009). The CFD code (see reference 1) was also used to obtain numerical solutions. The numerical procedure used in this work had been carefully validated in a previous study (Koonsrisuk and Chitsomboon, 2007). The five theoretical models investigated in this study will be briefly presented in chronological order.

Model 1 Chitsomboon (2001) proposed his model as:

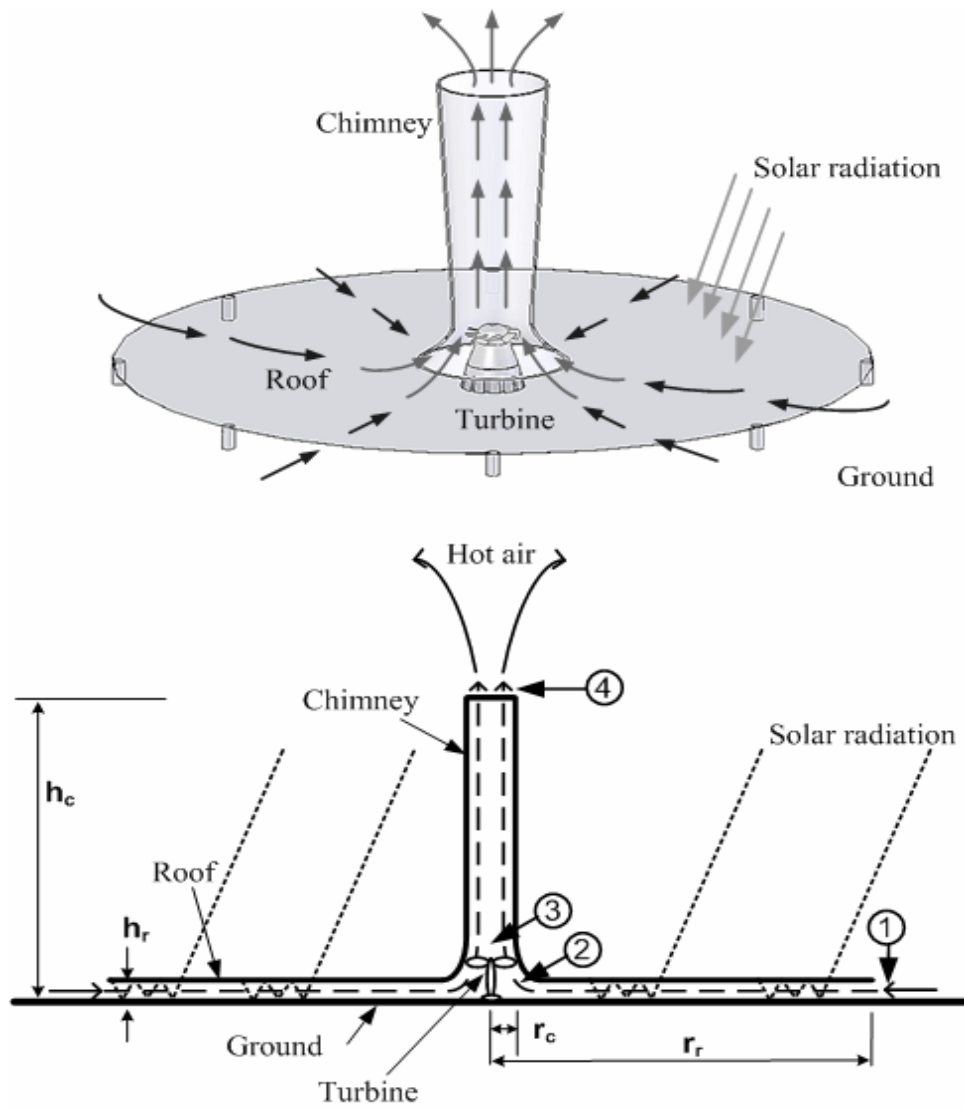


Figure 6.1 Schematic layout of solar tower plant.

$$\frac{1}{2} \dot{m} V_1^2 \left[\rho_1 - 2\rho_1 A_1^2 \int_1^3 \frac{dA}{A^3} + \frac{2A_1 q''}{V_1 c_p T_1} \int_1^3 \frac{dA_r}{A^2} + \frac{2\rho_1 A_1^2 g h_c}{\gamma R T_1} \int_1^3 \frac{dA}{A^3} \right] = \frac{\rho_1 g h_c q''}{c_p T_3} \int_1^3 dA_r. \quad (6.1)$$

The model was the result of a synthesis of the conservation equations of mass, momentum and energy, together with the ideal gas relation. After some manipulations, the flow power of the plant becomes

$$\frac{1}{2} \dot{m} V_3^2 = \frac{g h_c q'' A_r / c_p T_3}{\left\{ 1 + \frac{g h_c}{\gamma R T_1} \left[\left(\frac{r_c^2}{2r_r h_r} \right)^2 - 1 \right] + \frac{q''}{\rho_1 V_3 c_p T_1} \frac{r_c^2}{h_r^2} \ln \frac{r_c}{r_r} \right\}}. \quad (6.2)$$

Therefore, the efficiency is represented as

$$\eta = \frac{\frac{1}{2} \dot{m} V_3^2}{q'' A_r} = \frac{g h_c / c_p T_3}{\left\{ 1 + \frac{g h_c}{\gamma R T_1} \left[\left(\frac{r_c^2}{2r_r h_r} \right)^2 - 1 \right] + \frac{q''}{\rho_1 V_3 c_p T_1} \frac{r_c^2}{h_r^2} \ln \frac{r_c}{r_r} \right\}}. \quad (6.3)$$

Model 2 Schlaich *et al.* (2005), by balancing the kinetic and potential energies of the flow, proposed that the speed reached by the free convection current can be expressed as

$$V_3 = \left(2 g h_c \frac{\Delta T}{T_1} \right)^{1/2}. \quad (6.4)$$

Accordingly, the available flow power can be written as

$$\frac{1}{2}\dot{m}V_3^2 = \frac{1}{2}\rho_3 A_c \left(2gh_c \frac{\Delta T}{T_1} \right)^{\frac{3}{2}} \quad (6.5)$$

The heat gain through the collector is $\dot{Q} = q''A_r$, thus the efficiency can be written as

$$\eta = \frac{gh_c}{c_p T_1} \quad (6.6)$$

Note that this efficiency is a function of h_c only.

Model 3 Tingzhen *et al.* (2006) modeled the static pressure difference between the outside and the inside of a chimney and coupled it to the continuity and the energy equations for the solar collector. The corresponding power output and efficiency of this model are

$$\dot{W} = \frac{\rho_1}{\rho_3} \frac{\pi g}{c_p T_1} h_c r_r^2 q'' \quad (6.7)$$

$$\eta = \frac{\rho_1}{\rho_3} \frac{gh_c}{c_p T_1} \quad (6.8)$$

Model 4 Zhou *et al.* (2009) determined the pressure difference between the chimney base and the ambient by an empirical relation. When combined with the energy equation for the flows in the collector and chimney, the model becomes

$$\dot{W} = 0.00353 \cdot V_3 A_c g h_c \left(\frac{\pi r_r^2 q''}{c_p \dot{m}} - \frac{g}{2c_p} h_c + \frac{1}{2} \gamma_\infty h_c \right) \quad (6.9)$$

$$\eta = \frac{0.00353 \cdot V_3 A_c g h_c}{\pi r^2 q''} \left(\frac{\pi r^2 q''}{c_p \dot{m}} - \frac{g}{2c_p} h_c + \frac{1}{2} \gamma_\infty h_c \right). \quad (6.10)$$

When the dry adiabatic lapse rate ($\gamma_\infty = g/c_p$) is employed in the analysis, it yields

$$\dot{W} = 0.00353 \frac{g h_c \pi r^2 q''}{c_p \rho_3} \quad (6.11)$$

$$\eta = 0.00353 \frac{g h_c}{c_p \rho_3}. \quad (6.12)$$

Model 5 Koonsrisuk and Chitsomboon (2009) proposed a dimensionless variable for a solar chimney power plant as

$$\frac{\rho A V \frac{V^2}{2}}{\frac{q'' A_r \beta}{c_p} g h_c} = 1. \quad (6.13)$$

As a result, the flow power can be written as

$$\frac{1}{2} \dot{m} V_3^2 = \frac{q'' A_r \beta}{c_p} g h_c. \quad (6.14)$$

and the system efficiency is defined by

$$\eta = \frac{\beta g h_c}{c_p}. \quad (6.15)$$

Recall that $\beta = 1/T$ for a perfect gas. Using this relation, Eqs. (6.6) and (6.15) are identical. However, in this study β was taken from a table for the properties of air; therefore the predictions of Eqs. (6.6) and (6.15) might be slightly different.

It can be seen that, although the five theoretical models presented above have some common features, there are also disagreements among them. All models (except the last one) were developed from the fundamental equations in fluid mechanics and the distinct assumptions made in each of them are the reason for their disagreements

Normally, simple theoretical models like these five models cannot represent faithfully the results of all the related and interacting parameters over a wide range. On the other hand, Computational Fluid Dynamics (CFD) procedures solve all the interacting governing equations in a coupled manner, albeit in a finite frame work. With a careful use of CFD, its results could be used to validate those of the theoretical models, at least qualitatively. Therefore this study will employ CFD to obtain numerical solutions to the problem and compare its results with those of the theoretical models.

To compute the power production and efficiency of a solar chimney, each model needs unknowns and these unknowns are listed in Table 6.1. The values of these unknowns could be judiciously assumed. In this study, however, they were obtained directly from the CFD results. Note that model 5 needs no unknown and this is its advantage over the other models; though its accuracy has yet to be proven.

6.4 COMPUTATIONAL WORKS

A commercial CFD code (ANSYS, 2005) was used in this study. Steady inviscid, laminar assumptions were employed in order to be consistent with the

conditions used in the theoretical models. The set of conservation equations used by CFD are:

$$\text{Mass conservation: } \frac{\partial}{\partial x_i} (\rho u_i) = 0. \quad (6.16)$$

$$\text{Momentum conservation: } \frac{\partial}{\partial x_j} (\rho u_i u_j) = -\frac{\partial p}{\partial x_j} + S_M. \quad (6.17)$$

$$\text{Energy conservation: } \frac{\partial}{\partial x_i} (\rho u_i h_{total}) = \frac{\partial}{\partial x_i} \left(\lambda \frac{\partial T}{\partial x_i} \right) + u_i S_M + S_E. \quad (6.18)$$

Source terms are added to the momentum and energy equation as follows,

$$S_M = (\rho - \rho_{ref})g \quad (6.19)$$

$$S_E = q''/h_r. \quad (6.20)$$

where $(\rho - \rho_{ref})$ is evaluated directly from the equation of state for a perfect gas, and not from the Boussinesq approximation.

This approach involves discretizing the spatial domain into finite control volumes using a mesh system. The code uses a non-staggered grid layout such that the control volumes are identical for all transport equations. Finite element shape functions are used to evaluate spatial derivatives for all the diffusion terms and the pressure gradient term within mesh elements. The convection terms in conservation equations are represented by the high resolution upwind differencing scheme (ANSYS,

2005). With this scheme, the derivatives are approximated locally between the first-order and second-order upwind schemes, depending upon local discontinuities.

The geometry of the solar chimney is selected to be a circular collector (roof) with a vertical cylindrical chimney at its center. A turbine is not included in the solar chimney model in order to be compatible with the theoretical model configurations. Due to symmetry only a 5-degree wedge of the whole geometry was simulated, with the two side faces defined as symmetry planes as shown in Fig. 6.2a.

Adaptive unstructured tetrahedral mesh system was used in the present study. The grid convergence issue was already investigated in the previous study (Koonsrisuk and Chitsomboon, 2007), hence those grid configurations were adopted in this work. A typical mesh system for the computational domain is illustrated in Fig. 6.2b.

The boundary conditions used in the numerical scheme are summarized in Table 6.2. Note that the condition at the inlet was of ‘opening’ type rather than the usual ‘inlet’ type. This was determined from our past experience that the inlet type often caused a non-convergent solution due to flow reversal at the inlet. Finally, convergences of the numerical results were assured by requiring that the RMS residuals of all the conservation equations reached their respective minima.

6.5 RESULTS AND DISCUSSION

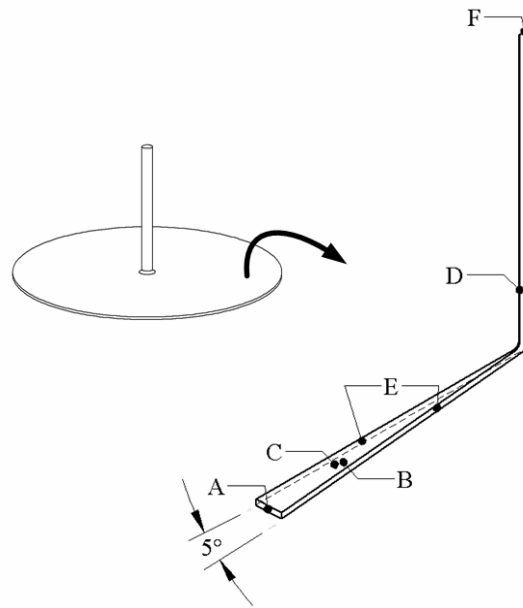
The parameters investigated in this study were: roof height, roof radius, tower height, tower radius and insolation. The prototypical plant has the following

Table 6.1 List of unknowns in theoretical models.

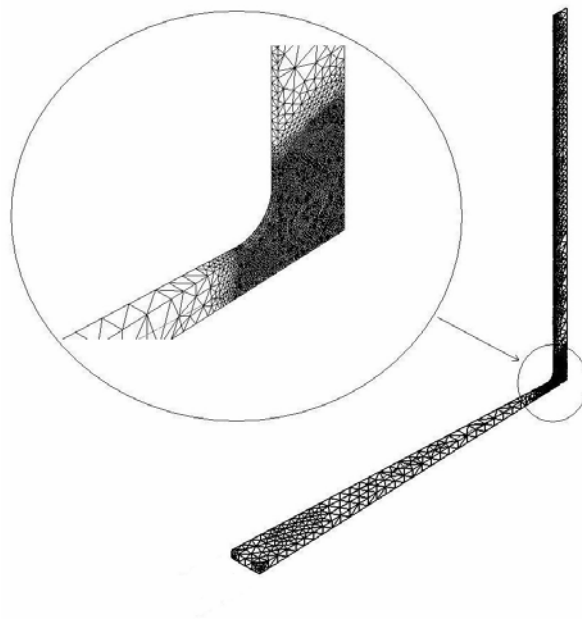
Reference article	Equations	Unknowns
Chitsomboon (2001)	(6.2) and (6.3)	V_3 and T_3
Schlaich <i>et al.</i> (2005)	(6.5) and (6.6)	ρ_3 and ΔT
Tingzhen <i>et al.</i> (2006)	(6.7) and (6.8)	ρ_3
Zhou <i>et al.</i> (2009)	(6.11) and (6.12)	ρ_3
Koonsrisuk and Chitsomboon (2009)	(6.14) and (6.15)	none

Table 6.2 Boundary conditions (based on the settings for ANSYS CFX, release 10.0)

Place	Position in Figure 2a	Type	Boundary details
Collector entrance	A	Opening	Total pressure = 0, T = 308K
Ground surface	B	Wall	adiabatic free-slip
Roof surface	C	Wall	adiabatic free-slip
Chimney surface	D	Wall	adiabatic free-slip
Sector sides	E	Symmetry	-
Chimney outlet	F	Outlet	Static pressure = 0



(a)



(b)

Figure 6.2 Computational domain: (a) 5 degree axis-symmetric section;
(b) numerical grid.

dimensions: roof radius, 100 m; roof height above ground, 2 m; tower radius, 4 m; and tower height, 100 m. Figs. 6.3 - 6.6 show the effects of the plant geometric parameters on the output power and efficiency while holding insolation constant at 800 W/m^2 .

In Figure 6.3, the values of r_r were varied from 25 to 200 m. It is apparent that the flow power increases with r_r while the opposite is generally true for the efficiency. The CFD results agree generally well with all the theoretical predictions.

For the sake of brevity, acronyms will be used to refer to the five theoretical models as follows: Ch = Chitsomboon (2001), Se = Schlaich *et al.* (2005), Te = Tingzhen *et al.* (2006), Ze = Zhou *et al.* (2009), KC = Koonsrisuk and Chitsomboon (2009). When compared to CFD, Te and Ze models show reverse trends in the efficiency prediction. Ch model appreciably underestimates power and efficiency but it is the only model that shows qualitative consistency with the CFD prediction in that it predicted the reduction of efficiency as the radius increased. The underestimations of the power and efficiency are consistent with its intended built-in feature (so called conservative modeling.) The powers and efficiencies predicted by Se and KC models are very close together and seem to be invariant with respect to r_r . These two models show good quantitative comparisons with CFD especially at roof radius larger than about 150 m. Considering that practical collector of a solar chimney would be much larger than 150 m., this suggests the validity of these two models for a practical case.

Figure 6.4 shows the effects of roof height (h_r) which was varied from 1 to 4 m. All models, as well as of CFD, predict flat results for both power and efficiency. This suggests that h_r might be assumed fixed in an optimization study. Se and KC are the two models which compare most favorably with CFD.

The effects of chimney radius (r_c) variation are displayed in Fig. 6.5, where r_c was varied from 2 to 8 m. It is clearly seen that the power and efficiency predicted by CFD increase with r_c . Ch model again quantitatively underestimates the CFD values but again it is the only model that shows qualitative agreement with the CFD trend. Te and Ze models again show trend reversal when compared to CFD. Se and KC models predict flat responses for both power and efficiency. The results of these two models compare well with those of CFD at low radius value but are worsen as the radius increases further. Note that only Ch model took the momentum equation inside the chimney into consideration. It is thus not a surprise that this is the only model that gives a plausible response to the chimney area variation.

The finding of CFD that the power increases with r_c is interesting and deserves a further investigation. If the trend predicted here were true it would be another means to increase solar chimney efficiency. In our on-going study using a more versatile theoretical model we also predicted a power increase when the chimney was gradually expanded. This power increase is believed to be the same effect as was found in this study whereby the chimney area is abruptly increased at its base.

The effects of the chimney height, h_c , will now be considered. The values of h_c were varied from 25 to 400 m. Not surprisingly, an increase of h_c results in increases of power and efficiency as shown in Fig. 6.6. It is evident that CFD predicts the flow power and efficiency as weak nonlinear functions of h_c but all the theoretical models predict linear responses and underestimate the CFD results. The differences between the theoretical and CFD predictions may be caused by the fact that the simple

1-dimensional models used here cannot represent accurately the highly accelerating radial flow occurring inside the collector, especially when $h_c > 100$ m .

Figure 6.7 shows the effect of the insolation, q'' . It is evident that the powers increase with q'' while the efficiencies are relatively constant. All of the output powers compare reasonably with one another and seem to be linearly dependent on q'' . The efficiencies predicted by Se and KC models are constant whereas those of Te and Ze models exhibit increasing trends. Ch model is the only one that predicts a decreasing trend which is in qualitative agreement with the CFD prediction but it underestimates the flow power and efficiency by about 15%.

The discrepancies between the predictions of CFD and theoretical models in Figs. 6.3 - 6.7 might be related to the fact that all theoretical models are based on the 1-dimensional flow assumption; on the contrary, CFD simulations solved the system of 3-dimensional equations. Referring to Eqs. (6.3), (6.8) and (6.12), $\eta_{Ch} \sim f(1/T_3)$, while $\eta_{Te} \& \eta_{Ze} \sim f(1/\rho_3) \sim f(T_3)$ and this might be the reason why Te and Ze models always predict results in opposite trends to those of Ch model (which is always in the same trends as those of CFD).

The results shown in Figs. 6.3 - 6.7 indicate a general trend that the power productions are strong functions of r_c , h_c and q'' but the efficiencies depend significantly on h_c only. Se and KC models predict almost identical results in all cases except for the effect of r_c case, which deserves a further investigation.

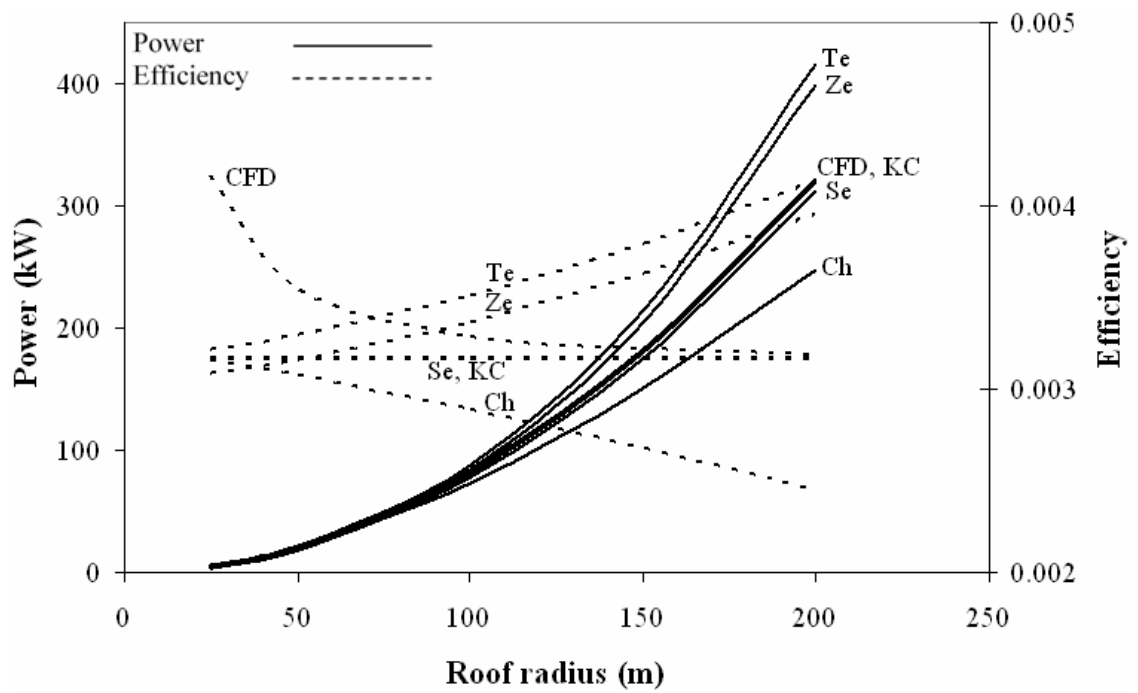


Figure 6.3 Effect of roof radius on plant performance for insolation = 800 W/m^2 .

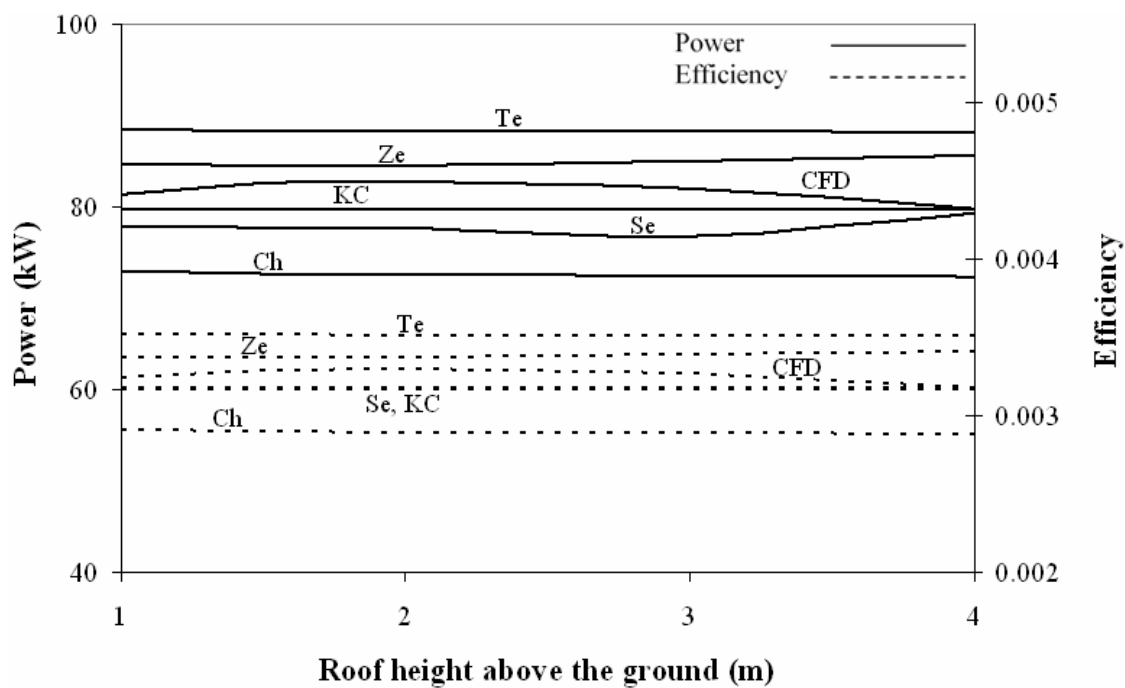


Figure 6.4 Effect of roof height on plant performance for insolation = 800 W/m^2 .

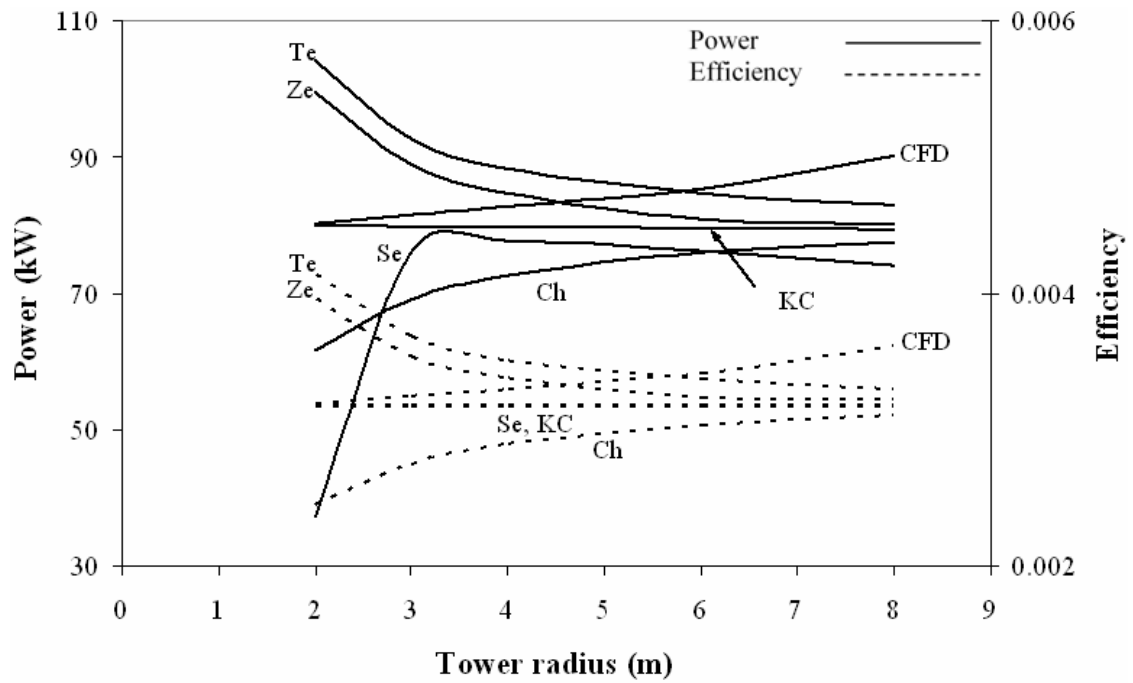


Figure 6.5 Effect of tower radius on plant performance for insolation = 800 W/m^2 .

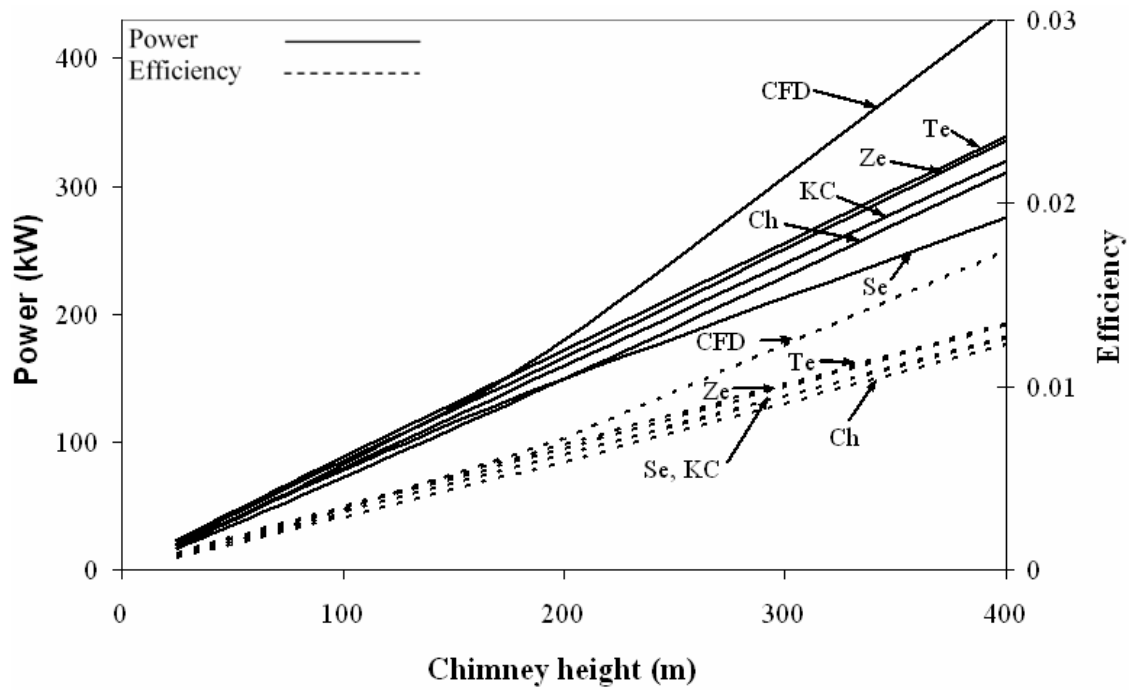


Figure 6.6 Effect of tower height on plant performance for insolation = 800 W/m^2 .

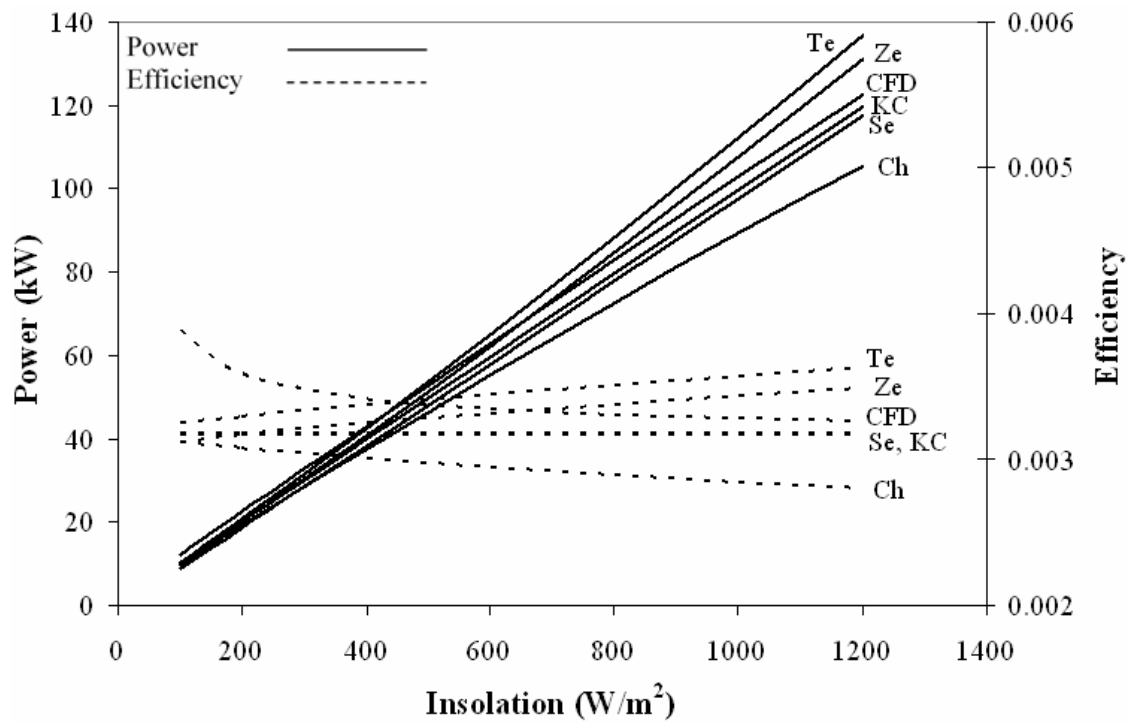


Figure 6.7 Effect of insolation on plant performance.

6.6 CONCLUSION

The influences of roof height, roof radius, tower height, tower radius, and insolation on solar chimney power plant performances have been studied by using five simple theoretical models from the literature and a carefully calibrated CFD procedure.

Important observations are concluded as follows:

- 1) Model of Chitsomboon (2001) underestimates plant performances by about 15% in all cases that were investigated due probably to its built-in conservative error estimation procedure; but it is the only model that predicts qualitatively trends when compared to CFD results.
- 2) Model of Schlaich *et al.* (2005) is easy to use and gives reasonable results. However, its use requires a judicious guess of a temperature difference in the plant.
- 3) Model of Tingzhen *et al.* (2006) is easy to use but requires a judicious guess of the density in the tower. The model tends to over-predict plant performances.
- 4) Model of Zhou *et al.* (2009) has features that are quite similar to the model of Tingzhen *et al.* The model tends to over-predict plant performances but to a lesser degree than Tingzhen *et al.* model.
- 5) Model of Koonsrisuk and Chitsomboon (2009) is easy to use and gives reasonable solutions comparable to the model of Schlaich *et al.*; it has an advantage over the latter in that it does not require any guessed parameter as an input.

According to this study, the models of Schlaich et al. and Koonsrisuk and Chitsomboon are recommended because they compared more favorably with the CFD results than the other models for all the test cases that were investigated.

6.7 REFERENCES

ANSYS, Inc. **ANSYS CFX**, Release 10.0: reference guide. ANSYS, 2005.

Chitsomboon, T., 2000. Potential and efficiency of solar chimney in the production of electrical energy. **Research and Development Journal of the Engineering**, Institute of Thailand, Vol.11(3), pp. 38-44.

Chitsomboon, T., 2001. A validated analytical model for flow in solar chimney. **International Journal of Renewable Energy Engineering**, Vol. 3(2), pp. 339-346.

Dai, Y. J., Huang, H. B., Wang, R. Z., 2003. Case study of solar chimney power plants in northwestern regions of China. **Renewable Energy**, Vol.28, pp. 1295-1304.

Gannon, A. J., Von Backström, T. W., 2000. Solar chimney cycle analysis with system loss and solar collector performance. **Journal of Solar Energy Engineering**, Vol. 122. pp. 133-137.

Haaf, W., Friedrich, K., Mayr, G., Schlaich, J., 1983. Solar chimneys: part I: principle and construction of the pilot plant in Manzanares. **International Journal of Solar Energy**, Vol. 2, pp. 3-20.

Koonsrisuk, A., Chitsomboon, T., 2007. Dynamic similarity in solar chimney modeling. **Solar Energy**. Vol. 81(2007), pp. 1439-1446.

Koonsrisuk, A., Chitsomboon, T., 2009. A single dimensionless variable for solar tower plant modeling. **Solar Energy**. doi:10.1016/j.solener.2009.07.015.

- Pasumarthi, N., Sherif, S. A., 1998a. Experimental and theoretical performance of a demonstration solar chimney model – part I: mathematical model development, **International Journal of Energy Research**, Vol. 22, no. 3, pp. 277-288.
- Pasumarthi, N., Sherif, S. A., 1998b. Experimental and theoretical performance of a demonstration solar chimney model – part II: experimental and theoretical results and economic analysis, **International Journal of Energy Research**, Vol. 22, no. 5, pp. 443-461.
- Schlaich, J., 1995. **The Solar Chimney**. Edition Axel Menges: Stuttgart, Germany.
- Schlaich, J., Bergemann, R., Schiel, W., Weinrebe, G., 2005. Design of commercial solar updraft tower systems utilization of solar induced convective flows for power generation. **Journal of Solar Energy Engineering**, Vol. 127, pp. 117–124.
- Tingzhen, M., Wei, L., Guoliang, X., 2006. Analytical and numerical investigation of the solar chimney power plant systems. **International Journal of Energy Research**, Vol. 30, pp. 861-873.
- Zhou, X., Yang, J., Xiao, B., Hou, G., Xing, F., 2009. Analysis of chimney height for solar chimney power plant. **Applied Thermal Engineering**, Vol. 29, pp. 178-185.

CHAPTER VII

EFFECT OF FLOW AREA CHANGE ON THE POTENTIAL OF SOLAR CHIMNEY POWER PLANT

7.1 ABSTRACT

The solar chimney power plant is a solar power plant for electricity generation by means of air flow induced through a tall chimney. Guided by a theoretical prediction, this paper uses CFD technology to investigate the changes in flow properties caused by the variation of flow area. It was found that the sloping collector affects the flow properties through the plant. The divergent-top chimney leads to augmentations in kinetic energy at the tower base significantly. The proper combination between the sloping roof and the divergent-top chimney can produce the power as much as hundreds times that of the conventional solar chimney power plant.

7.2 INTRODUCTION

The solar chimney power plant is a power plant proposed to generate electricity in large scale by transforming solar energy into mechanical energy. The schematic of a typical solar chimney power plant is sketched in Fig. 7.1. It consists of a transparent circular roof or solar collector with a chimney at its center and a turbine, which is generally installed at the chimney's base. Solar radiation penetrates the roof and heats the air underneath as a result of the greenhouse effect. Due to buoyancy effect, the heated air flows up the tower and induces a continuous flow from the perimeter

towards the tower. Mechanical energy can be extracted from the energy of the flowing air to turn an electrical generator.

Research works on solar tower started around 1970s, after the construction of a 50 kW prototype in Manzanares, Spain. This pilot plant operated from the year 1982 to 1989 and was connected to the local electric network between 1986 and 1989 (Haaf *et al.*, 1983; Haaf, 1984). Tests conducted have shown that the prototype plant operated reliably and the concept is technically viable.

The effects of various geometrical parameters on the plant performance were examined by several researchers. Padki and Sherif (1999) reported that the power and efficiency could be increased by tapering the top end of the tower. Chitsomboon (1999) developed a mathematical model and it showed that, as the tower top is made convergent, the power and efficiency does not increase but stays relatively constant. Von Backström and Gannon (2000) employed a one-dimensional compressible flow model for the calculation of the thermodynamic variables as functions of several parameters, including the chimney area change. The study showed that, for a given chimney height, an increase in area ratio leads to augmentations in static pressure in the chimney. Based on a mathematical model, Schlaich (1995) reported that optimal dimensions for a solar chimney do not exist. However, if construction costs are taken into account, thermoeconomically optimal plant configurations may be established for individual sites. It was shown numerically in Pretorius and Kröger (2007) that plant power production is a function of the collector roof shape and inlet height. Maia *et al.* (2008) carried out a simulation study and found that the height and diameter of the chimney are the most important geometric dimensions for solar chimney design. Zhou

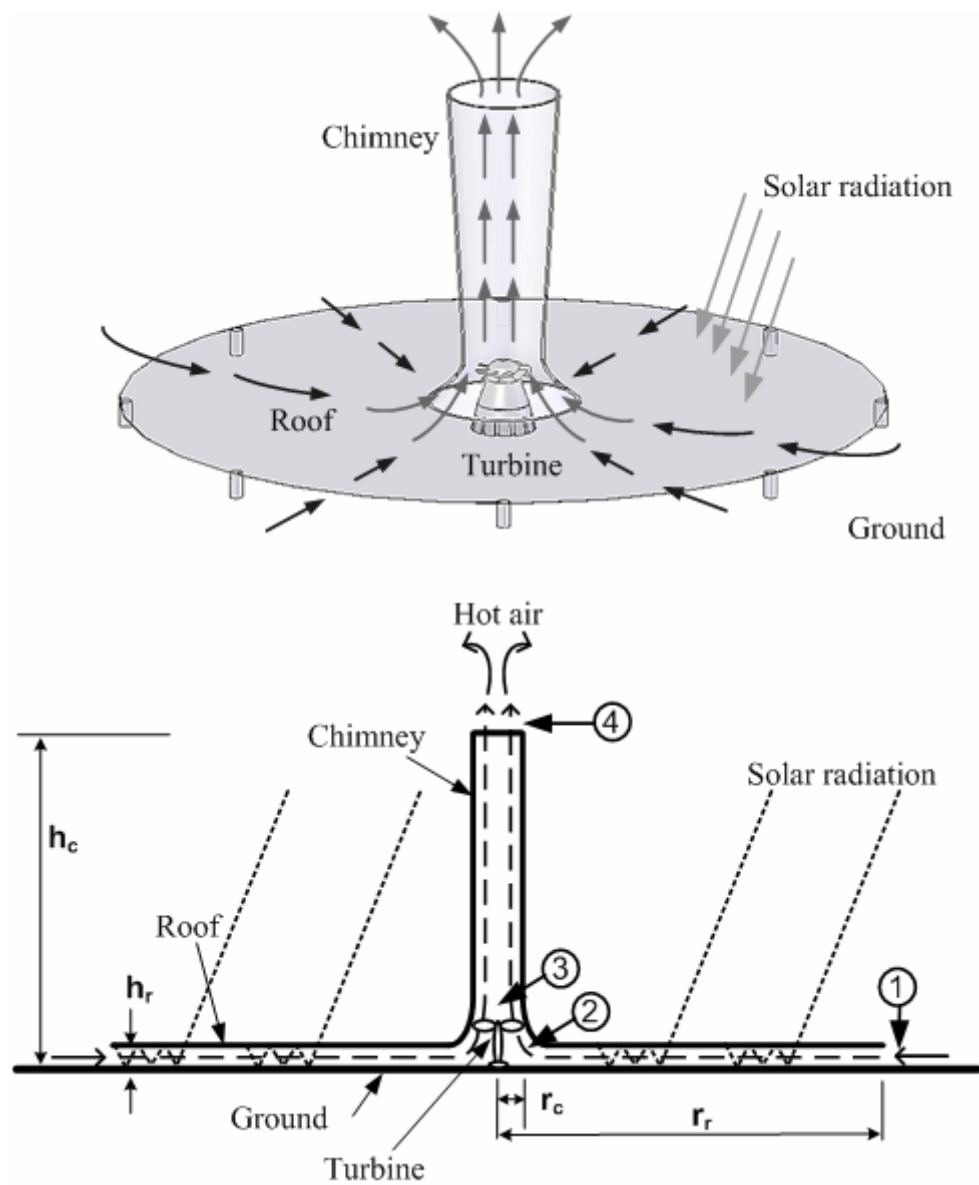


Figure 7.1 The main features of a solar chimney.

et al. (2009) reported the maximum chimney height in order to avoid negative buoyancy, and the optimal chimney height for maximum power output. They found that the maximum height and the optimal height increase with collector radius. A common feature in these findings is that the plant efficiency is very low, and that it increases with the plant size.

The work described in this paper is stimulated by the quest for a better design, and focused on increasing the plant performance by controlling the flow area of the system. It is guided by the theoretical investigation along with the CFD-based design analysis. Based on the results of the computational simulation, the influence of the flow area parameters of the solar chimney on the behavior of the airflow was assessed. The area parameters analyzed were the areas at the collector entrance and chimney exit, while the areas at the collector exit and the chimney entrance were kept constant.

7.3 DERIVATION OF THEORETICAL MODEL

In this simple analysis the power generated by a solar chimney power plant as shown in Fig. 7.1 can be expressed as

$$\dot{W} = \frac{\dot{m}}{\rho_{turb}} \Delta p_{turb} \approx - \frac{\dot{m}}{(\rho_2 + \rho_3)/2} (p_3 - p_2). \quad (7.1)$$

Equation (7.1) shows that \dot{W} becomes larger when p_3 is amplified and p_2 is attenuated. To determine the geometry layout that can fulfill this, the governing equations for the movement of air within the collector and chimney are considered separately.

Collector. The one-dimensional steady compressible flow in a variable-area passage is considered here. It is assumed that the solar heat gain is totally absorbed by the air under the roof. In the absence of friction and heat loss, the conservation equations in differential form are as follows

$$\text{Continuity:} \quad \frac{d\rho}{\rho} + \frac{dV}{V} + \frac{dA}{A} = 0 \quad (7.2)$$

$$\text{Momentum:} \quad \frac{dp}{\rho} = -VdV \quad (7.3)$$

$$\text{Energy:} \quad c_p dT + VdV = dq \quad (7.4)$$

$$\text{State equation:} \quad \frac{dp}{p} - \frac{d\rho}{\rho} - \frac{dT}{T} = 0. \quad (7.5)$$

Let $dq = q'' dA_r / \dot{m}$ and the height of the roof is given by $h_r = a \cdot r$ where a is the constant and r is the roof radius. Combining all equations, we have

$$dp = \frac{\dot{m}^2}{\rho} \left(\frac{dA}{A^3} - \frac{q'' dr}{2\pi \dot{m} c_p T r^3 a^2} \right). \quad (7.6)$$

Next we assume that q'' , c_p , ρ and T are approximately constant. Integrate from the entrance to the outlet of the collector, Eq. (7.6) becomes,

$$p_2 = p_1 - \frac{\dot{m}^2}{2\rho_1} \left(\frac{1}{A_2^2} - \frac{1}{A_1^2} \right) + \frac{q'' \dot{m}}{4\pi a^2 \rho_1 c_p T_1} \left(\frac{1}{r_2^2} - \frac{1}{r_1^2} \right). \quad (7.7)$$

Chimney. The air movement inside a chimney is assumed a frictionless adiabatic process. The system of equations for a one-dimensional steady compressible flow in a variable-area chimney is as follows

$$\text{Continuity:} \quad \frac{d\rho}{\rho} + \frac{dV}{V} + \frac{dA}{A} = 0 \quad (7.8)$$

$$\text{Momentum:} \quad \frac{dp}{\rho} + gdz = -VdV \quad (7.9)$$

$$\text{Energy:} \quad c_p dT + VdV + gdz = 0 \quad (7.10)$$

$$\text{State equation:} \quad \frac{dp}{p} - \frac{d\rho}{\rho} - \frac{dT}{T} = 0. \quad (7.11)$$

Combining Eqs. (7.8) – (7.11) gives

$$dp = -\rho g dz + \dot{m}^2 \frac{dA}{\rho A^3}. \quad (7.12)$$

Integrating between chimney's inlet and outlet yields

$$p_3 = p_4 + \rho_3 g h_c + \frac{\dot{m}^2}{2\rho_3} \left(\frac{1}{A_4^2} - \frac{1}{A_3^2} \right). \quad (7.13)$$

For a variable area collector and chimney,

$$A_1 = \sqrt{n} A_2 \quad (7.14)$$

$$A_4 = \sqrt{l}A_3. \quad (7.15)$$

where n and l are any constants.

Substituting Eqs. (7.7), (7.13), (7.14) and (7.15) into Eq. (7.1):

$$\dot{W} = -\frac{\dot{m}}{(\rho_2 + \rho_3)/2} \left[\frac{\dot{m}^2}{2\rho_3} \left(\frac{1-l}{lA_3^2} + \frac{n-1}{nA_2^2} \right) - \frac{q''\dot{m}}{4\pi a^2 \rho_1 c_p T_1} \left(\frac{1}{r_2^2} - \frac{1}{r_1^2} \right) \right] \quad (7.16)$$

It should be noted that when the heat loss and friction are not included in the analysis, the power is not a function of the shape of collector or chimney. An order of magnitude analysis reveals that, on the right-hand side of Eq. (7.16), the first term is much greater than the second term. Thus Eq. (7.16) becomes

$$\dot{W} \cong -\frac{\dot{m}^3}{\rho_2^2} \left(\frac{1-l}{lA_3^2} + \frac{n-1}{nA_2^2} \right) \quad (7.17)$$

When l and n are changed, \dot{m} and ρ_2 will be changed correspondingly. However, Eq. (7.17) suggests that \dot{W} may be increased when $l > 1$ and $n < 1$. In other words,

$$A_1 < A_2. \quad (7.18)$$

$$A_3 < A_4. \quad (7.19)$$

This finding makes recommendations regarding the arrangement of plant's area ratio. To evaluate it, numerical calculations of several solar chimneys with different

collector and chimney's shapes were carried out to illustrate the varying behavior of the plant performances.

7.4 Computational work

The plant layouts studied in this work are schematically depicted in Fig. 7.2. They are: (a) a constant-height collector with a constant-area chimney, (b) a sloping collector with a constant-area chimney, (c) a constant-height collector with a convergent-top chimney, (d) a constant-height collector with a divergent-top chimney, (e) a sloping collector with a convergent-top chimney, and (f) a sloping collector with a divergent-top chimney. Their details are listed in Table 7.1. To investigate the effect of flow area variation, we define the dimensionless measures

$$AR12 = A_1/A_2 \quad (7.20)$$

$$AR43 = A_4/A_3 . \quad (7.21)$$

To date, the performance of solar chimney has been widely investigated for the limiting case of configuration (a). The collector is customarily of a circular shape, while its height is relatively constant with some inclination angle, and the chimney is modeled as a constant-diameter tube. Thus a reference plant's geometry is simplified to that of a horizontal disc above the ground with a constant-diameter chimney in the center of the disc. Configuration (a) is the reference plant in this study. Its collector has a diameter of 200 m and a height of 2 m, and it has a 100 m high chimney with a diameter of 8 m. So $AR12_a = 25$ and $AR43_a = 1$.

The commercial CFD code “CFX” (ANSYS, 2005) has been proven to be a reliable tool to simulate the flow in solar chimney (Koonsrisuk and Chitsomboon, 2007). Consequently, the numerical model had been built using CFX in this work. In CFX, equations for the conservation of mass, momentum and energy equations are solved using a control volume technique. The steady transport equations can be written in general form as follows:

$$\nabla \cdot (\rho u \phi - \Gamma_{\phi} \nabla \phi) = S_{\phi} \quad (7.22)$$

The buoyancy term in the momentum equation and the solar heat gain in the energy equation are given as

$$S_M = (\rho - \rho_{ref})g \quad (7.23)$$

$$S_E = q''/h_r \quad (7.24)$$

where ρ_{ref} is the reference operating density specified at the inlet fluid condition of 308 K and 1 atm absolute pressure. The equations were discretized by a non-staggered grid scheme. A high resolution upwind differencing scheme (ANSYS, 2005) was applied for the convective terms of equations. The convergence criterion was that the normalized residuals for mass, momentum and energy were required to be below than 10^{-7} .

A solar chimney is a cylindrical structure, so an axis-symmetric representation is assumed. As a result, a 5-degree pie shape of the plant was simulated as shown in Fig. 7.2a. An unstructured, non-uniform mesh was constructed. In order to ensure the

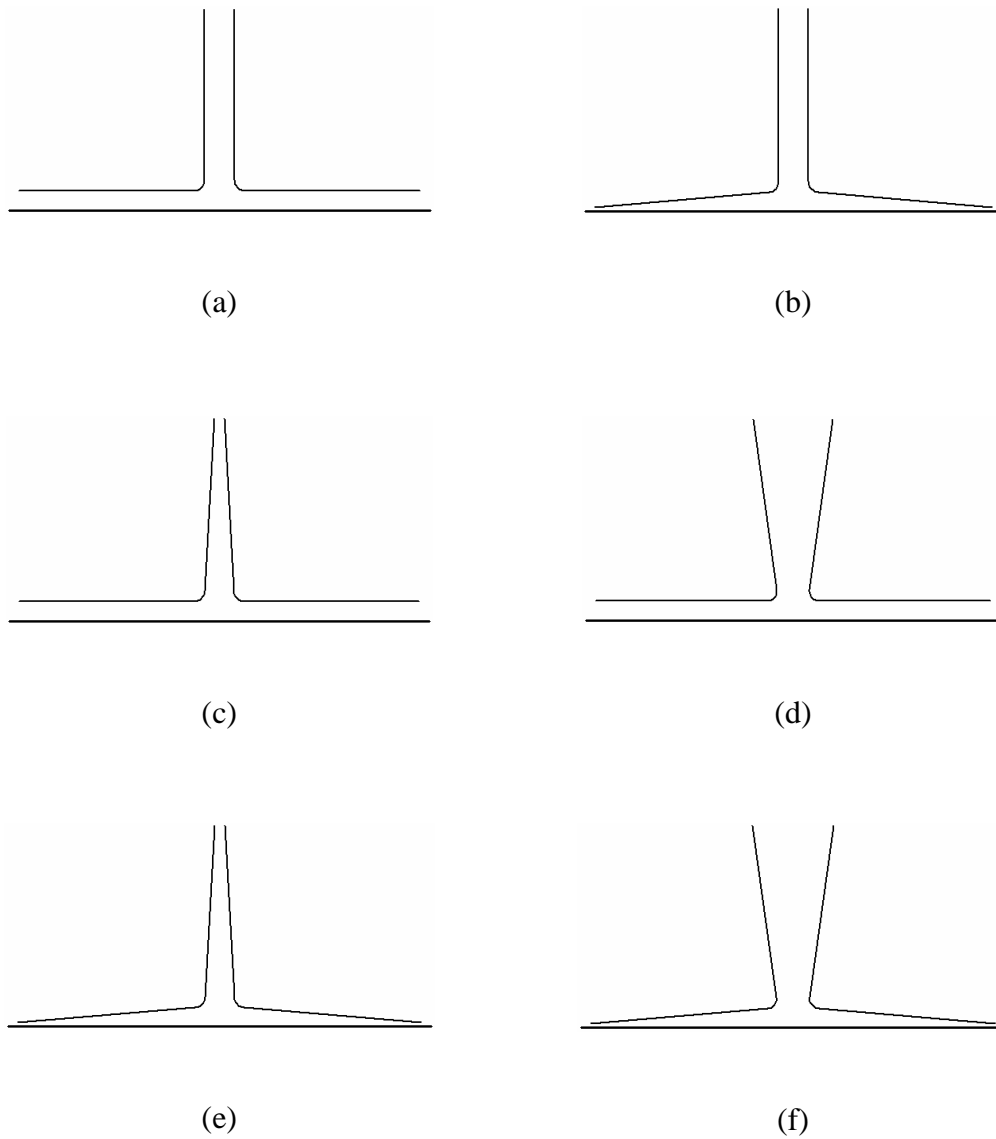
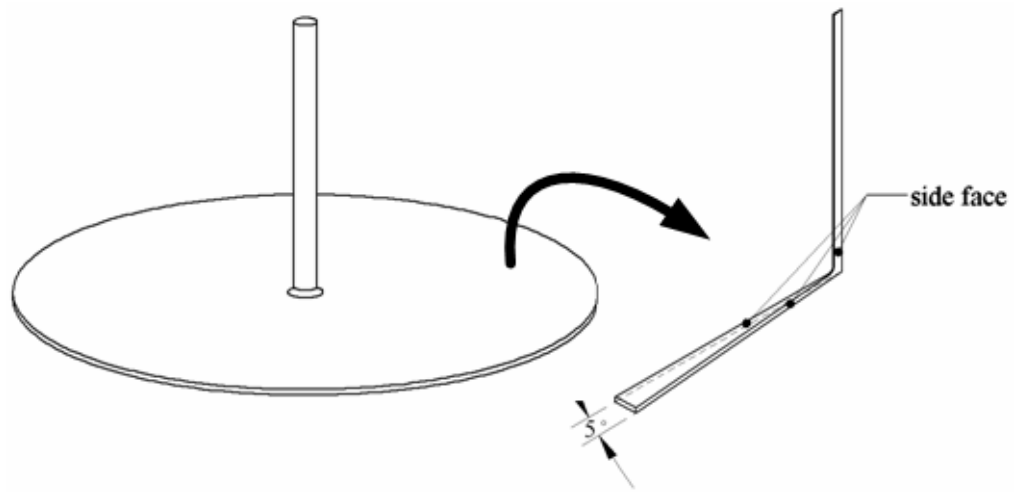


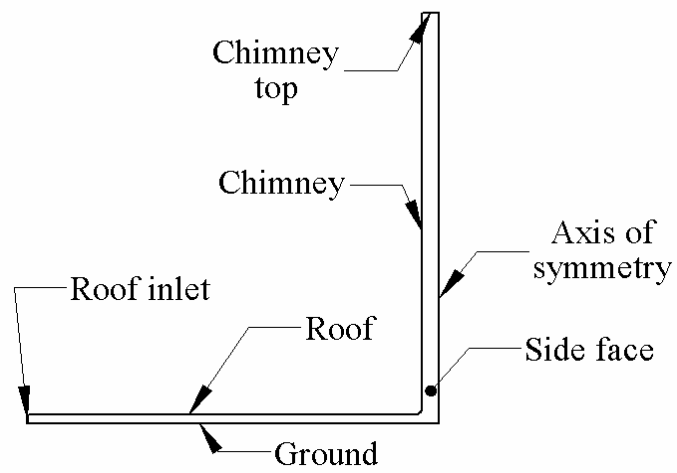
Figure 7.2 Schematic layout of (a) reference plant; (b) a sloping collector with a constant-area chimney; (c) a constant-height collector with a convergent top chimney; (d) a constant-height collector with a divergent-top chimney; (e) a sloping collector with a convergent-top chimney; (f) a sloping collector with a divergent-top chimney.

Table 7.1 List of models illustrated in Fig. 7.2.

Configuration	Objective	Remark
(a) A constant-height collector with a constant-area chimney	Reference plant	A simple geometry version of the conventional solar chimney power plant
(b) A sloping collector with a constant-area chimney	Investigate the system when $A_1 < A_2$ and $A_4 = A_3$.	cf. expression (18).
(c) A constant-height collector with a convergent-top chimney	Investigate the effect of $A_3 > A_4$ on the system with a constant-height collector.	Adopt the idea from Padki and Sherif (1999).
(d) A constant-height collector with a divergent-top chimney	Investigate the effect of $A_3 < A_4$ on the system with a constant-height collector.	cf. expression (19).
(e) A sloping collector with a convergent-top chimney	Investigate the combined effect of $A_1 < A_2$ and $A_3 > A_4$.	-
(f) A sloping collector with a divergent-top chimney	Investigate the combined effect of $A_1 < A_2$ and $A_3 < A_4$.	-



(a)



(b)

Figure 7.3 Computational domain: (a) 5 degree axis-symmetric section;
(b) Side view of the domain.

accuracy of the numerical results, a grid dependence study was realized. Furthermore, the adaptive grid refinement algorithm locally refined the mesh only where needed based on regionally velocity variation. It should be mentioned that the numerical procedure used in this study had already been carefully calibrated and validated in Koonsrisuk and Chitsomboon (2007) to achieve a satisfactory level of confidence.

The boundary conditions used are shown in Fig. 7.3b. At the center of the plant, axis-symmetric conditions were utilized. At the walls, free-slip and adiabatic boundary conditions were used. These conditions were applied at the roof, transition section, chimney wall and ground surface. The total pressure and temperature are prescribed at the roof inlet and the flow direction was set as normal to the roof perimeter. At the chimney top, the ‘outlet’ boundary condition with zero static gauge-pressure is imposed.

7.5 RESULTS AND DISCUSSION

Figure 7.4 shows the gauge pressure distributions inside the plants. It should be noted that the gauge pressures were scaled so that they are equal zero at the chimney top. It can be observed that $(p_2 - p_3)$ of configuration (b) increases a little when compare with configuration (a). One can notice that $(p_1 - p_2)_b < (p_1 - p_2)_a$ while $(p_3 - p_4)_b \cong (p_3 - p_4)_a$. For configuration (c), $p_{3,c} > p_{3,a}$ and $p_{2,c} > p_{2,a}$ in such a way that $(p_2 - p_3)_c \cong (p_2 - p_3)_a$. On the other hand, $p_{3,d} < p_{3,a}$ and $p_{2,d} < p_{2,a}$ and we found that $(p_2 - p_3)_d > (p_2 - p_3)_a$. It was found that the numerical computation of configuration (e) had convergence difficulties, causing a failed simulation. To mitigate the problem, instead of testing the case of $A_1 < A_2$ together with $A_3 > A_4$, we traded

off configuration (e) to the case of $A_1 = A_2$ together with $A_3 > A_4$. In that case we found that $p_{3,e} > p_{3,a}$ and $p_{2,e} > p_{2,a}$ in the manner that $(p_2 - p_3)_e \cong (p_2 - p_3)_a$. For configuration (f) it appears that $(p_2 - p_3)_f > (p_2 - p_3)_a$. It is important to notice that the pressure change inside the system does not show a strong sensitivity to the change of AR_{12} (configuration (b)), as it does to the change of AR_{43} (configuration (d)). When we combine the effect of changing AR_{12} and AR_{43} together (configuration (f)), however, the reduction of AR_{12} can yield a vacuum pressure inside the system as shown in Fig. 7.4.

The favorable flow behavior when $A_1 < A_2$ can be explained by the fact that the flow velocity and pressure do not change measurably under the roof for this area ratio layout. The flow area is increasing along the divergent-top chimney, this affects the flow velocity and can reduce the flow acceleration, resulting in the decrease of the pressure gradient across the chimney. The order of magnitude reveals that the pressure drop due to the flow acceleration along the chimney is large when compared with other pressure drops. Therefore using the appropriate AR_{43} can increase $(p_2 - p_3)$ significantly.

The effect of the flow area variation on the mass flow rate is presented in Fig. 7.5. The mass flow ratio depicted in Fig. 7.5 is defined as the mass flow rate of the test cases divided by the mass flow rate of the reference case, in which $AR_{12} = 25$ and $AR_{43} = 1$. The results show that the varying AR_{12} does not affect the mass flow rate for the system with a constant-area chimney. On the other hand, an increase in AR_{43} produces an increase in the mass flow rate. The augmentation of mass flow rate is

observed in cases of varying AR_{43} and $AR_{12} > 0.75$, except the case of $AR_{12} = 0.25$ and $AR_{43} = 8$ in which the flow recirculation occurred around the chimney exit.

Figure 7.6 shows the temperature rise across the roof. It is presented in dimensionless form and defined as the ratio of the temperature rise of the test cases to the temperature of the reference case. The values of temperature rise are consistent with the differences in mass flow rates presented in Fig. 7.5, since, in accordance with the conservation of energy principle, a higher mass flow rate should give a lower temperature rise for an equal amount of energy input.

Figures 7.7 and 8 present the sensitivity of the flow power ($= \dot{m}V^2/2$) with respect to the changes of AR_{12} and AR_{43} , respectively. The ordinates of the figures are the normalized power, which is the power of the test cases scaled by the power at position 3 of the reference case, while the abscissas are the positions depicted in Fig. 7.1. The chimney diameter of the cases tested in Fig. 7.7 is constant. It is obvious that the power at position 1 is a function of AR_{12} and a sloping roof leads to the power reduction inside the chimney. Although decreasing AR_{12} can increase the power at position 1 notably, but this power rise is still lower than the power inside the chimney. Further inspection reveals that the collector efficiency ($= \dot{m}c_p \Delta T / q'' A_r$) of the system with a sloping collector and a constant-area chimney is a weak function of AR_{12} , and its overall efficiency ($= 0.5 \dot{m} V_3^2 / q'' A_r$) is relatively constant.

It is apparent in Fig. 7.8, in which the roof height is constant, that the power at position 3 is a strong function of AR_{43} . It should be noted that the case of $AR_{43} = 16$ offers higher power than that of $AR_{43} = 32$ due to the flow recirculation occurring near the chimney exit when $AR_{43} = 32$.

Table 7.2 presents the normalized power at the chimney base (position 3); the square of AR_{43} of each case is also shown. It is observed that the power increases in proportion to $(AR_{43})^2$ when AR ranges between 0.25 to 8 and at a lower rate thereafter. This quadratic trend is suggested by Eq. (7.17). It would seem that there is an upper bound on AR_{43} that can boost up the power. Too high AR_{43} would eventually lead to boundary layer separation. Friction that comes with high velocity would also reduce the benefit. Further inspection of Table 7.2 shows that the efficiency also increases as AR_{43} increases. Efficiency in this case is defined as power at tower base divided by the total solar heat gain. This definition is unfair to the convergent-top case because its potential is at the top, not at the base. However, numerical results reveal that the power at the top of the convergent tower remains the same as the constant area case. So, its potential remains unchanged in relation to the constant area case.

The combined effect of AR_{12} and AR_{43} was shown in Fig 7.9. Because the flow velocity of the cases of $AR_{12} = 0.25$ is very high, so the flow recirculation is presented when $AR_{43} > 1$. This is the reason that the power of the cases of $AR_{12} = 0.25$ is less than those of $AR_{12} = 0.5$. As observed in the plots of pressure and mass flow rate that the ‘proper’ combination between AR_{12} and AR_{43} offers the largest power. It was found that the ‘proper’ combination depends on the whole size of the plant.

In any case, it is evident that high AR_{43} leads to augmentation in power at the tower base. This suggests the potential of harnessing more turbine power from the high AR_{43} system.

7.6 CONCLUSION

A solar chimney system with varying flow area was studied and its performance was evaluated. Theoretical analysis suggests that the solar chimney with sloping collector and divergent-top chimney would perform better than that of a conventional system. CFD calculations show that a divergent tower helps increase the static pressure, mass flow rate and power over that of the constant area tower. For the convergent tower, the power remains the same as the constant area case. The sloping collector helps increase the static pressure across the roof and the power at the roof entrance. The system with the sloping collector and divergent-top chimney of tower area ratio of 16 can produce power as much as 400 times that of the reference case.

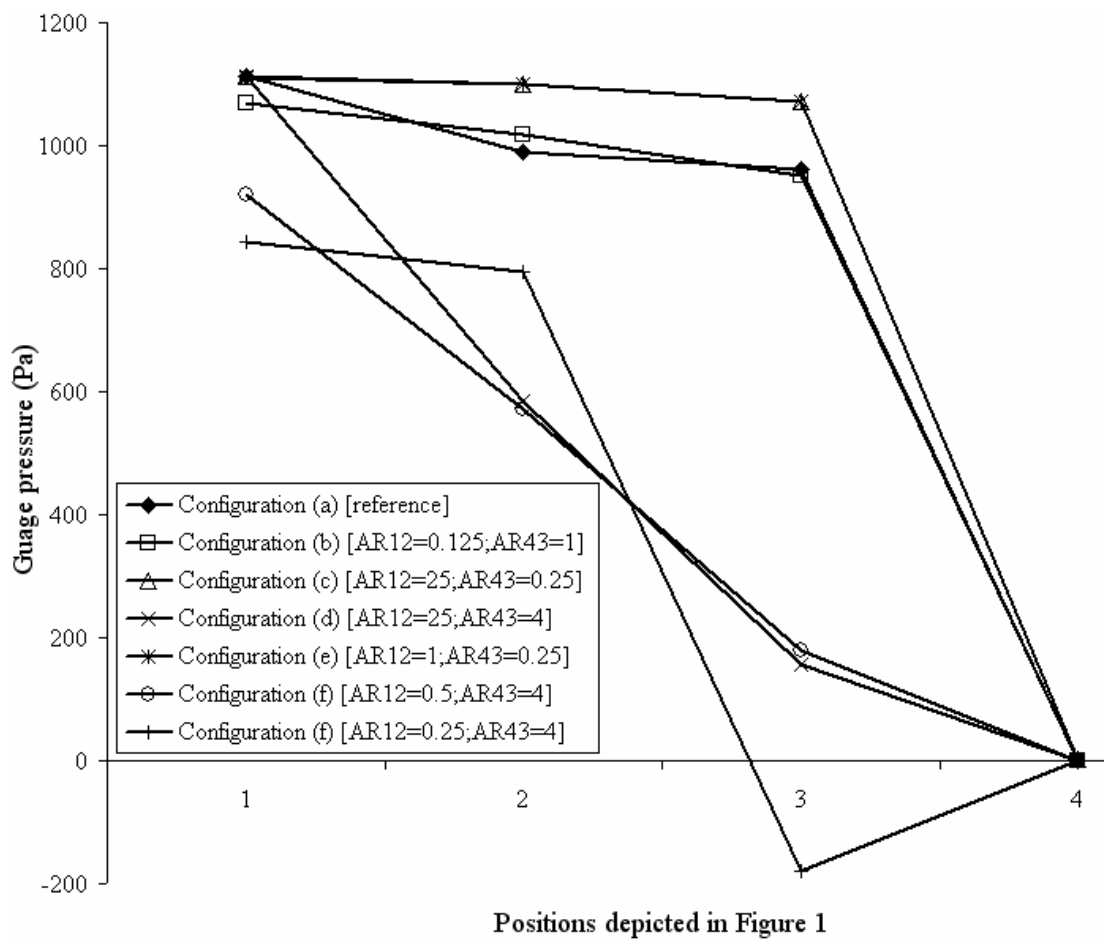


Figure 7.4 Effect of area variation on the pressure profiles.

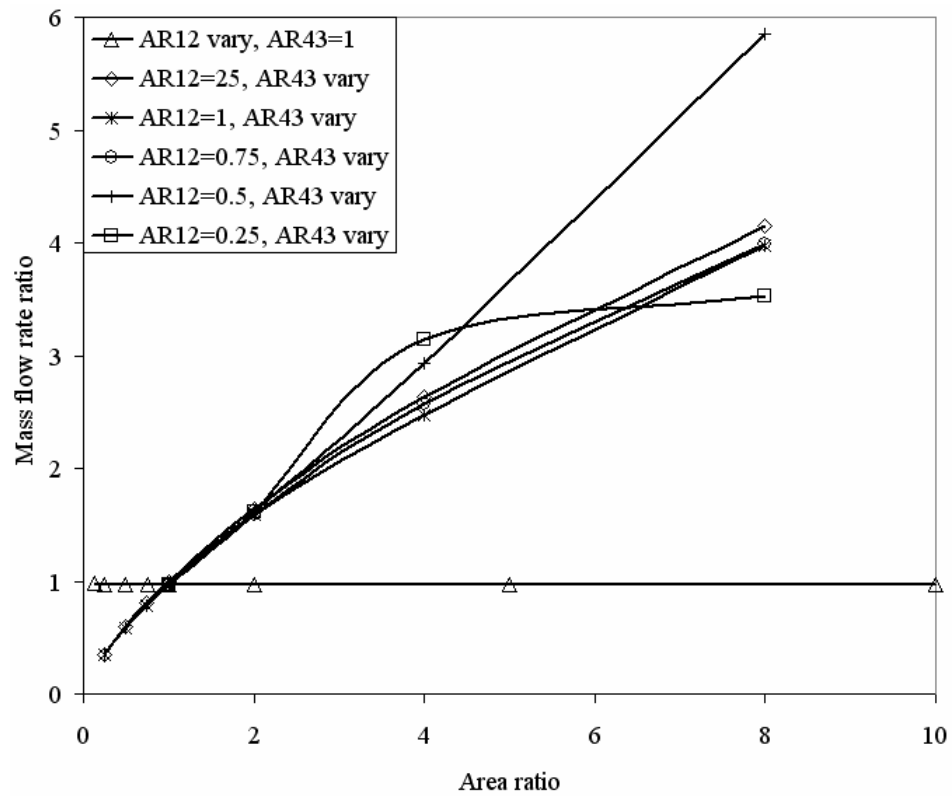


Figure 7.5 Effect of area variation on the mass flow rate (scaled by the mass flow rate of the reference case).

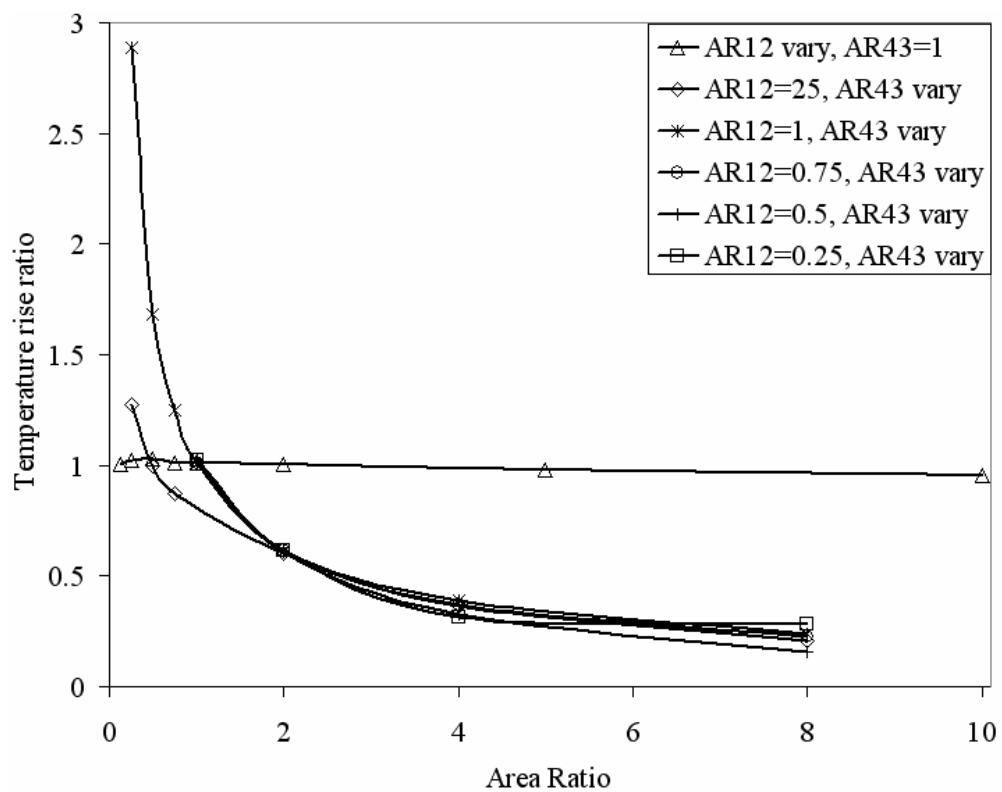


Figure 7.6 Effect of area variation on the collector temperature rise (scaled by the temperature rise of the reference case).

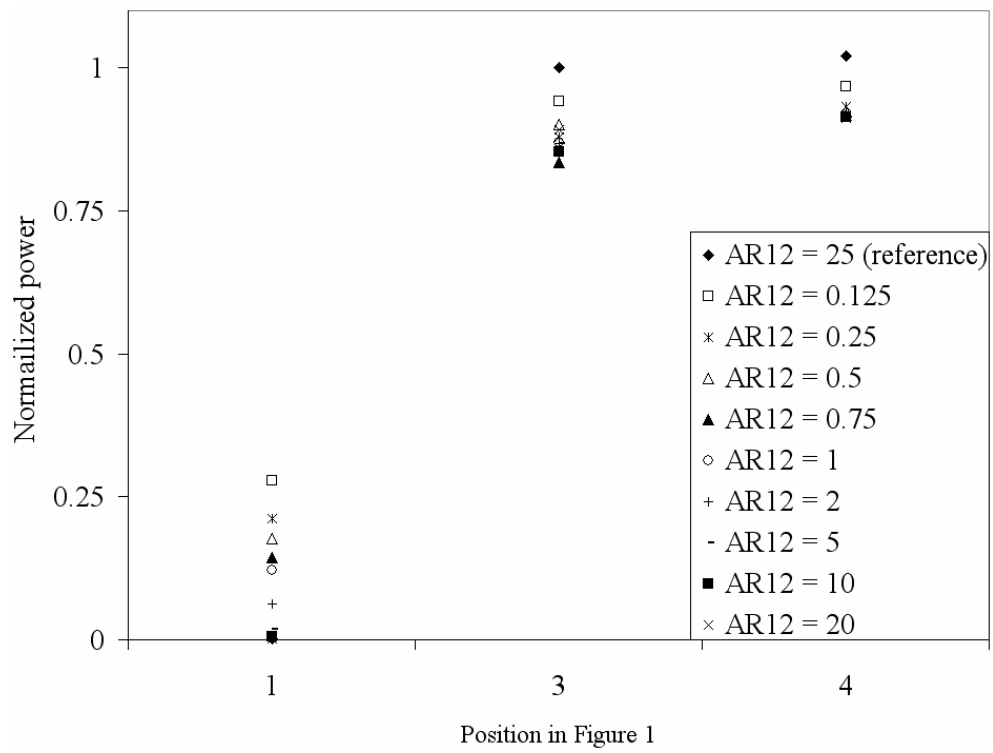


Figure 7.7 Effect of $AR12$ on the flow power (scaled by the flow power of prototype at position 3).

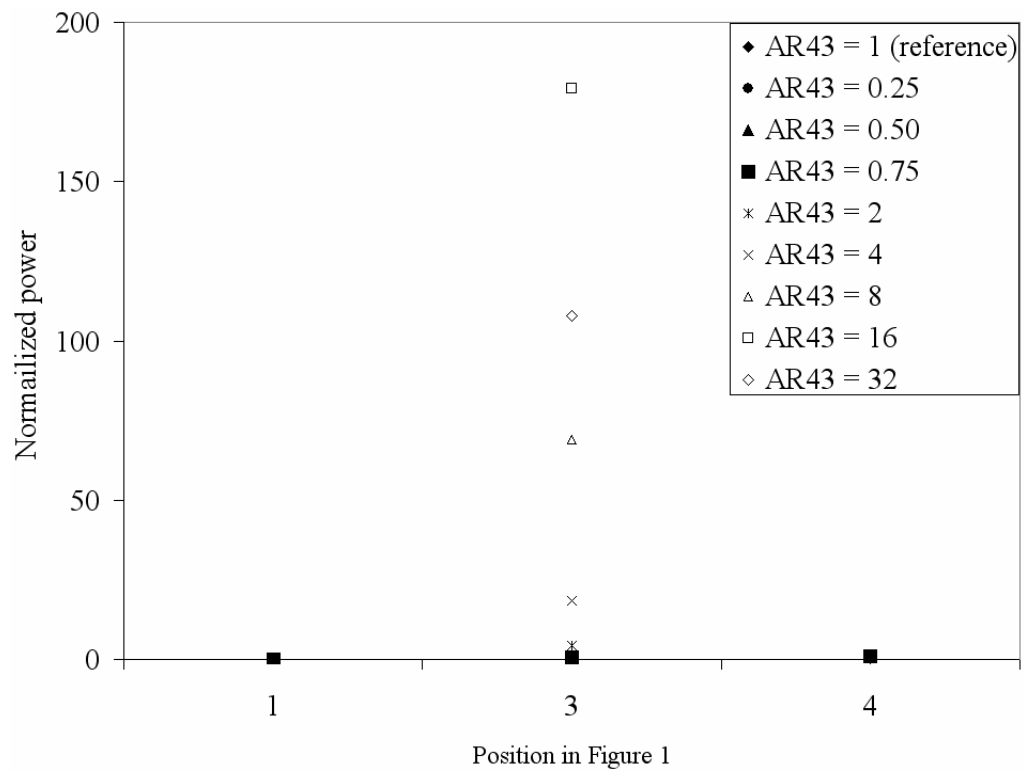


Figure 7.8 Effect of $AR43$ on the flow power (scaled by the flow power of prototype at position 3).

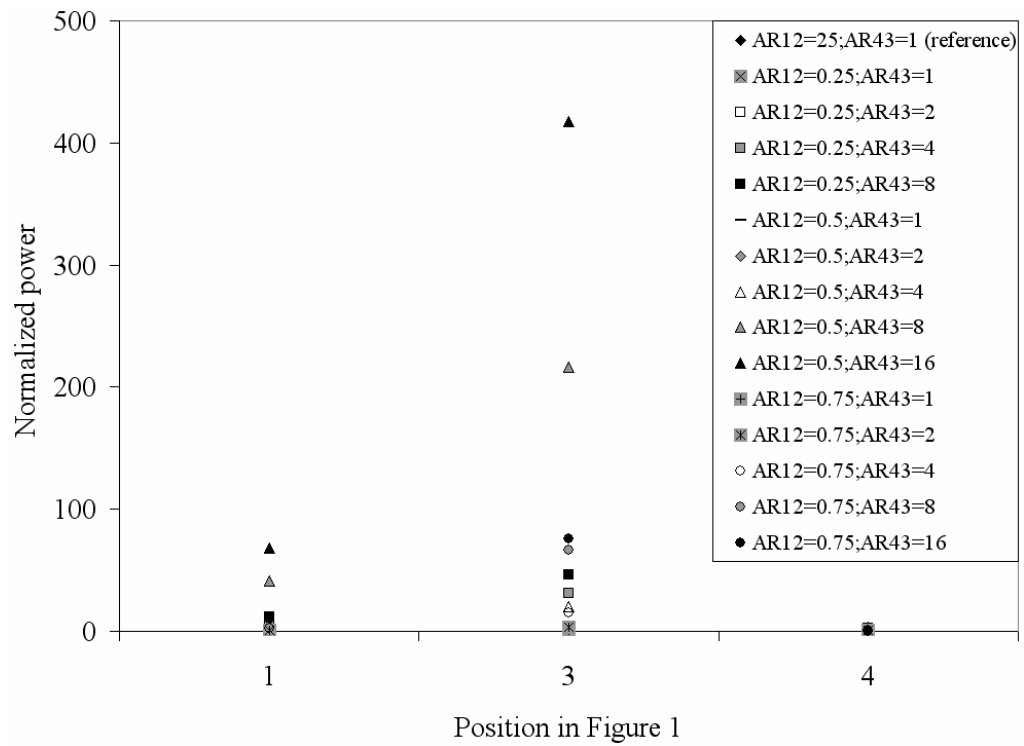


Figure 7.9 Combined effect of AR_{12} and AR_{43} on the flow power (scaled by the flow power of prototype at position 3).

Table 7.2 Power at the chimney base scaled by the power of the reference case, the square of $AR43$ and the efficiency at chimney entrance,

$$\eta = 100 \times 0.5 \dot{m} V_3^2 / q'' A_r .$$

$AR43$	$(AR43)^2$	Power	η (%)	Note
1	1	1	0.36	Reference case
0.25	0.06	0.06	0.02	
0.5	0.25	0.25	0.09	
0.75	0.56	0.54	0.19	
2	4	4.27	1.54	
4	16	18.49	6.66	
8	64	69.07	24.89	
16	256	179.16	64.55	

Note: All test cases use the constant-diameter chimney.

7.7 REFERENCES

- ANSYS, Inc. **ANSYS CFX**, Release 10.0: reference guide. ANSYS, 2005.
- Chitsomboon, T., 1999. The effect of chimney-top convergence on efficiency of a solar chimney. In: **Proceeding of the 13th National Mechanical Engineering Conference**, Thailand.
- Von Backström, T. W. and Gannon, A. J., 2000. Compressible flow through solar power plant chimneys. **ASME Journal of Solar Energy Engineering**, Vol. 122(3), pp. 138-145.
- Haaf, W., Friedrich, K., Mayr, G., Schlaich, J., 1983. Solar chimneys: part I: principle and construction of the pilot plant in Manzanares. **International Journal of Solar Energy**, Vol. 2, pp. 3-20.
- Haaf, W., 1984. Solar chimneys: part II: preliminary test results from the Manzanares plant. **International Journal of Solar Energy**, Vol. 2, pp. 141-161.
- Koonsrisuk, A., Chitsomboon, T., 2007. Dynamic similarity in solar chimney modeling. **Solar Energy**, Vol. 81(12), pp. 1439-1446.
- Maia, C. B., Ferreira, A. G., Valle, R. M., Cortez, M. F. B., 2008. Theoretical evaluation of the influence of geometric parameters and materials on the behavior of the airflow in a solar chimney. **Computers & Fluids**, doi: 10.1016/j.compfluid.2008.06.005
- Padki, M. M., Sherif, S. A., 1999. On a simple analytical model for solar chimneys, **International Journal of Energy Research**, Vol. 23, pp. 289-294.
- Pretorius, J. P., Kröger, D. G., 2007. Sensitivity analysis of the operating and technical specifications of a solar chimney power plant. **ASME Journal of Solar Energy Engineering**, Vol. 129, pp. 171-178.

Schlaich, J., 1995. **The Solar Chimney**. Edition Axel Menges: Stuttgart, Germany.

Zhou, X., Yang, J., Xiao, B., Hou, G., Xing, F., 2009. Analysis of chimney height for solar chimney power plant. **Applied Thermal Engineering**, Vol. 29, pp. 178-185.

CHAPTER VIII

THEORETICAL TURBINE POWER YIELD IN SOLAR CHIMNEY POWER PLANTS

8.1 ABSTRACT

The solar chimney power plant is a promising system to generate electrical power from free solar energy. The analysis was carried out to improve the description of the operation mode and efficiency. The solar collector, chimney and turbine are modeled together theoretically, and iteration techniques were then carried out to solve the mathematical model developed. This model was developed to estimate power output of solar chimneys as well as to examine the effect of solar heat flux and structural dimensions on the power output. Results from the mathematical model were validated by measurements from the physical plant actually built and the model was further used to predict the performance characteristics of large-scale commercial solar chimneys. The results show that the plant size, the factor of pressure drop at the turbine and the solar heat flux are the important parameters for the performance enhancement.

8.2 INTRODUCTION

The solar chimney power plant is a solar electricity production facility employing solar radiation to increase the internal energy of air flowing through the system. The schematic of a typical solar chimney is sketched in Fig. 8.1. In this plant, air is heated as a result of the greenhouse effect under a translucent roof (collector). As

the roof is open at its periphery, buoyancy drives a continuous flow from the roof perimeter into the chimney which is located at the middle of the roof. An electricity-generating turbine is set in the path of the air current to convert the kinetic energy of the flowing air into electricity.

Solar chimney power plants can convert only a small portion of the solar energy collected into electricity, but their cheap, robust construction and low maintenance costs make up for this disadvantage (Schlaich, 1995). To make this technology economically viable, the optimum configurations of each component are needed. Efficient conversion of fluid power to shaft power depends primarily on the operation of turbine. During the day, mass flow through the system is varying due mainly to variation of solar radiation. Accordingly, the turbine blade pitch should be adjusted during operation to regulate power output. Seemingly, there should be a relevant optimum turbine setting for maximum power output.

To evaluate the available plant power output, researchers defined the ratio of the pressure drop across the turbine to the total available system pressure difference. This ratio is symbolized as p_{turb}/p_{tot} herein. Most investigators have assumed that the optimum p_{turb}/p_{tot} is 2/3 (Haaf *et al.*, 1983; Mullett, 1987; Schlaich, 1995; Lodhi, 1999; Von Backström and Gannon, 2000; Dai *et al.*, 2003; Zhou *et al.*, 2007).

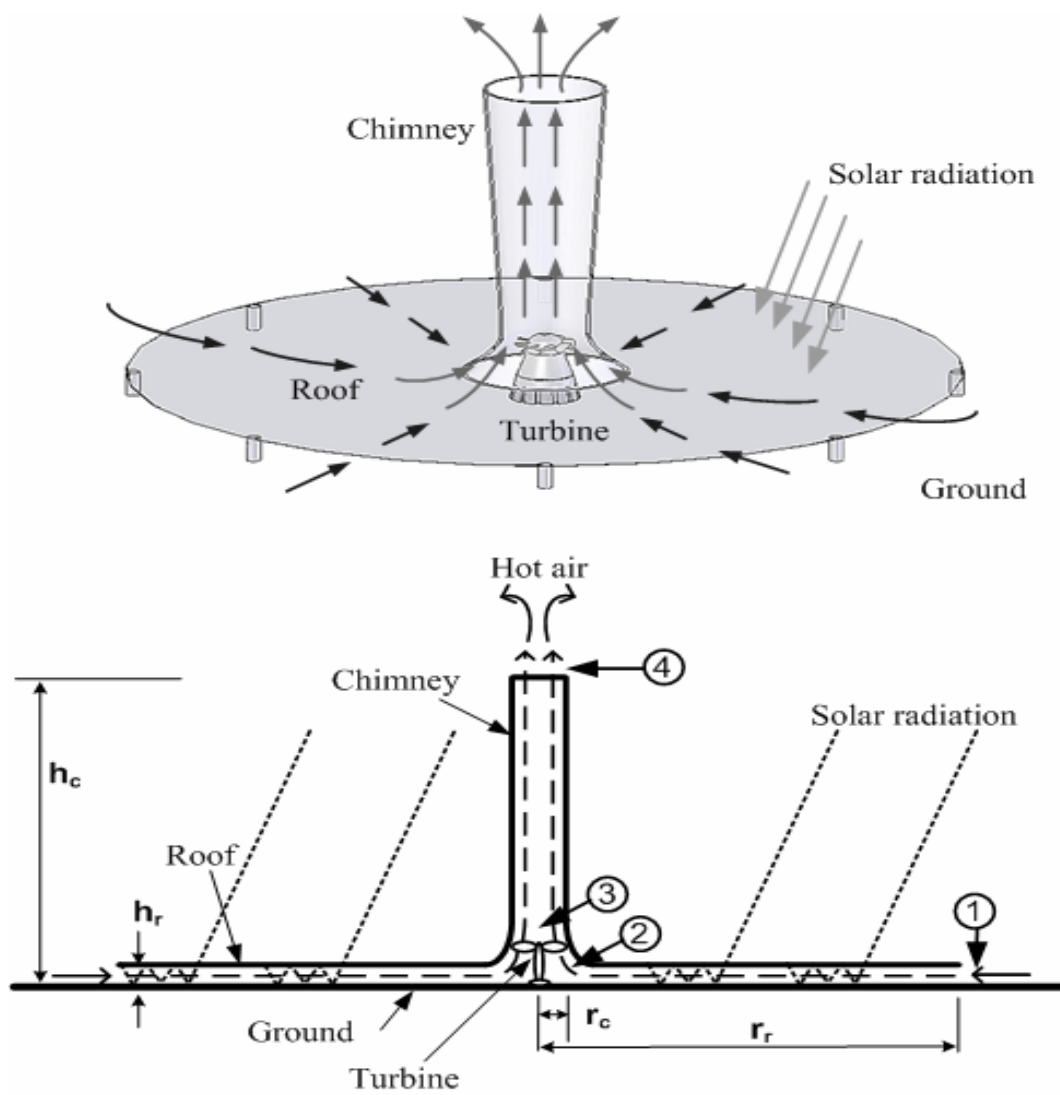


Figure 8.1 Schematic layout of solar chimney power plant

Though computations of the values taken from a table of data given by Schlaich (1995) showed that p_{turb}/p_{tot} used is 0.82. Hedderwick (2001) illustrated that the ratio is between 0.66-0.7 during the day. Furthermore, Schlaich *et al.* (2005) presented, without reference, that the optimum ratio is 0.8. Meanwhile, Bernardes *et al.* (2003) reported an optimum value of 0.97. Although the turbine under consideration is encased by the tower, some authors use the ratio as 16/27 (Pasumarthi and Sherif, 1998; Pastohr *et al.*, 2004; Onyango and Ochieng, 2006), which is the Betz limit obtained for an actuator disc in a free stream situation.

Here a detailed theoretical model is developed to evaluate the performance of solar chimney power system. The present paper also presents the operating range of the turbine. It tries to determine how to maximize the fluid power by adjusting the pressure drop across the turbine and the flow through it.

8.3 OPTIMAL PRESSURE RATIO

According to the operation principle mentioned above, the air inside the system is less dense than the atmospheric air outside. A driving pressure generated Δp_{tot} can be subdivided into a static pressure difference, drops at the turbine, and the dynamic component, describes the kinetic energy of the airflow, neglecting friction losses:

$$\Delta p_{tot} = \Delta p_{turb} + \Delta p_{dyn} \quad (8.1)$$

Let's define the ratio p_{turb}/p_{tot} as x , it yields

$$\Delta p_{turb} = x\Delta p_{tot} \quad (8.2)$$

Using the standard definition for dynamic pressure:

$$\Delta p_{dyn} = \frac{1}{2} \rho_c V_{with\ turb}^2 \cdot \quad (8.3)$$

Without turbine, a maximum flow speed is achieved and the whole driving potential is used to accelerate the flow thus,

$$\Delta p_{tot} = \frac{1}{2} \rho_c V_{no\ turb}^2 \cdot \quad (8.4)$$

Substituting Eqs. (8.2), (8.3) and (8.4) into Eq. (8.1), this yields

$$V_{with\ turb} = V_{no\ turb} \sqrt{(1-x)} \cdot \quad (8.5)$$

The theoretical power extracted by the turbine can be determined from the energy equation and the Gibb's relation from classical thermodynamic which can be written as

$$\dot{W}_{ext} = \dot{m} \int v dp \approx \frac{\dot{m}}{\rho_{turb}} \Delta p_{turb} \cdot \quad (8.6)$$

Substituting Eqs. (8.2) and (8.5) into Eq. (8.6) yields

$$\dot{W}_{ext} = A_c \cdot \sqrt{1-x} \cdot V_{no\ turb} \cdot x \cdot \Delta p_{tot} \cdot \quad (8.7)$$

The optimal x for maximum power extraction can be obtained by assuming that $V_{no\ turb}$ and Δp_{tot} are not the function of x and solving $\partial \dot{W}_{ext} / \partial x = 0$. The result for the optimal pressure ratio is

$$x_{opt} = \frac{2}{3}. \quad (8.8)$$

Consequently, the maximum power is obtained when the turbine pressure drop is 2/3 of the no-flow pressure drop. It corresponds to the value that most researchers have utilized. From the assumptions made, the result is true for all systems with a constant pressure potential.

Equation (8.7) shows that the plant power output can be increased by adjusting the turbine pressure drop. Later in the analysis, it will be shown that the mass flow rate and turbine pressure drop are coupled.

In addition, with the stations numbering as given in Fig. 8.1, the temperature rise can be estimated from the energy equation across the roof portion,

$$\dot{m}c_p(T_2 - T_1) + \frac{1}{2}\dot{m}(V_2^2 - V_1^2) = q''A_r \quad (8.9)$$

where, for simplicity, frictional effect is ignored because the velocity in this region is quite low. Because the flow is in the very low Mach number regime, the kinetic energy contribution can be safely neglected, therefore,

$$\dot{m}c_p\Delta T = q''A_r. \quad (8.10)$$

When the inlet solar radiation is assumed constant, Eq. (8.10) shows that the mass flow rate is inversely proportional to the temperature rise. Accordingly, the pressure potential is dependent on the flow. As a result, the assumption that $V_{no\ turb}$ and Δp_{tot} are not the function of x would make the predicted power inexact.

8.4 ANALYTICAL MODEL

In this analysis, the turbine is treated as the Rankine-Froude actuator disc (Eggleston and Stoddard, 1987). The assumptions on which this actuator disc is based are as follows:

1. Steady, homogeneous wind.
2. Uniform flow velocity at disc.
3. Static pressure decreases discontinuously across the disc.
4. No rotation of flow produced by disc.

Accordingly, Eq. (8.6) becomes,

$$\dot{W}_{ext} = \frac{\dot{m}}{(\rho_2 + \rho_3)/2} (p_2 - p_3). \quad (8.11)$$

By synthesizing equations for continuity, momentum and energy of the flow under the roof, Chitsomboon (2001) proposed that

$$p_2 - p_1 = \int_1^2 \frac{\rho V^2}{(1 - M^2)} \left(\frac{dA}{A} - \frac{q'' dA_r}{\dot{m} c_p T} \right). \quad (8.12)$$

Assuming that q'' , c_p and \dot{m} are constant while ρ and T can be approximated to be ρ_1 and T_1 without significantly affecting the numerical values of

the terms. The Mach number is presumed to be very low and thus is neglected; the equation is then simplified to be,

$$p_2 = p_1 + \frac{\dot{m}q''}{2\pi h_r^2 \rho_1 c_p T_1} \ln \frac{r_r}{r_c} - \frac{\dot{m}^2}{2\rho_1} \left(\frac{1}{A_2^2} - \frac{1}{A_1^2} \right) \quad (8.13)$$

where p_1 , ρ_1 and T_1 are approximated as p_∞ , ρ_∞ and T_∞ , respectively. Eq. (8.13)

shows that p_2 is the combination of the inlet pressure, p_1 , with the pressure increase

due to heat addition, $\frac{\dot{m}q''}{2\pi h_r^2 \rho_1 c_p T_1} \ln \frac{r_r}{r_c}$, and the pressure decrease due to flow area

reduction, $\frac{\dot{m}^2}{2\rho_1} \left(\frac{1}{A_2^2} - \frac{1}{A_1^2} \right)$ towards the roof center. Order of magnitude analysis

reveals that $\frac{\dot{m}^2}{2\rho_1} \left(\frac{1}{A_2^2} - \frac{1}{A_1^2} \right)$ is significantly greater than $\frac{\dot{m}q''}{2\pi h_r^2 \rho_1 c_p T_1} \ln \frac{r_r}{r_c}$.

Refer to Eq. (8.10), rearranging yields

$$T_2 = T_1 + \frac{q'' A_r}{\dot{m} c_p} \quad (8.14)$$

where

$$q'' = \alpha \cdot I - U \cdot \Delta T \quad (8.15)$$

(Duffie and Beckman, 1991).

Accordingly,

$$\Delta T = \frac{\alpha \cdot I}{\dot{m} \cdot c_p / A_r + U}. \quad (8.16)$$

If the turbine work extraction process is assumed to be an isentropic process, then

$$T_3 = T_2 \left(\frac{p_3}{p_2} \right)^{\frac{\gamma-1}{\gamma}} . \quad (8.17)$$

Furthermore, the momentum equation for flow through a constant area vertical tower of height, h_c is

$$p_3 = p_4 + \frac{1}{2}(\rho_3 + \rho_4) \cdot g \cdot h_c + \left(\frac{\dot{m}}{A_c} \right)^2 \left(\frac{1}{\rho_4} - \frac{1}{\rho_3} \right) . \quad (8.18)$$

The hydrostatic equilibrium requires that

$$\frac{dp}{dz} = -\rho g . \quad (8.19)$$

According to Calvert (1990), when the atmospheric air parcel is regarded as unsaturated medium and expand slowly to a lower atmospheric pressure without exchange of heat, the dry adiabatic temperature lapse rate equation can be written as

$$T = T_\infty - \frac{g}{c_p} z . \quad (8.20)$$

Let us assume that the air behaves as a perfect gas. Eq. (8.20) can be substituted into Eq. (8.19) to give p_4 as

$$p_4 = p_\infty \left(1 - \frac{g}{c_p T_\infty} h_c \right)^{\frac{c_p}{R}}. \quad (8.21)$$

Consider that a dry adiabatic lapse rate can be applicable to the flow in a tower.

In accordance with Eq. (8.19),

$$T_4 = T_3 - \frac{g}{c_p} h_c. \quad (8.22)$$

For a thermally perfect air,

$$\rho_2 = \frac{p_2}{RT_2}, \rho_3 = \frac{p_3}{RT_3}, \rho_4 = \frac{p_4}{RT_4}. \quad (8.23)$$

Consider the pressure potential as the available pressure difference between the tower base and the surroundings. Consequently, in this analysis,

$$\Delta p_{tot} = p_1 - p_3. \quad (8.24)$$

8.5 ANALYTICAL SOLUTION PROCEDURE

According to the formulation above, if mass flow rate is known or assumed then the power output can be attained. The steps of calculating the plant power output are:

1. Choose the mass flow rate,
2. Calculate T_2 using Eq. (8.16),
3. Calculate q'' using Eq. (8.15),

4. Calculate p_2 using Eq. (8.13),
5. Calculate ρ_2 using Eq. (8.23),
6. Calculate p_4 using Eq. (8.21),
7. Estimate p_3 , then calculate T_3 , ρ_3 , T_4 , ρ_4 using Eq. (8.17), Eq. (8.23), Eq. (8.22) and Eq. (8.23), respectively. Calculate p_3 using Eq.(8.18), then compare the new p_3 to the former p_3 . Perform the iteration process until the difference between corresponding new and old p_3 is less than the acceptable value.
8. Calculate \dot{W}_{ext} using Eq. (8.11),
9. Calculate Δp_{tot} using Eq. (8.24).

8.6 RESULTS AND DISCUSSION

Validity of the method for the Manzanares prototype

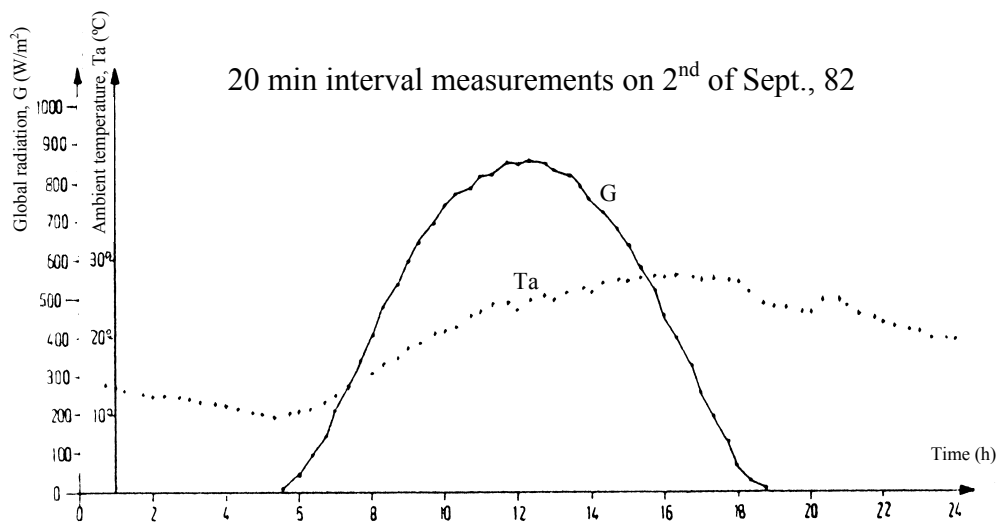
To validate the analytical models, the theoretical data were compared with the experimental results of the prototype from Manzanares, Spain. The plant dimensions are given in Table 8.1.

Firstly, according to Haaf (1984) the measured data for September 2nd, 1982 are displayed in Fig. 8.2. The comparisons between theoretical and experimental are presented in Table 8.2. Based on the data provided by the reference article, q'' for these data set, instead of using Eq. (8.15), are computed from

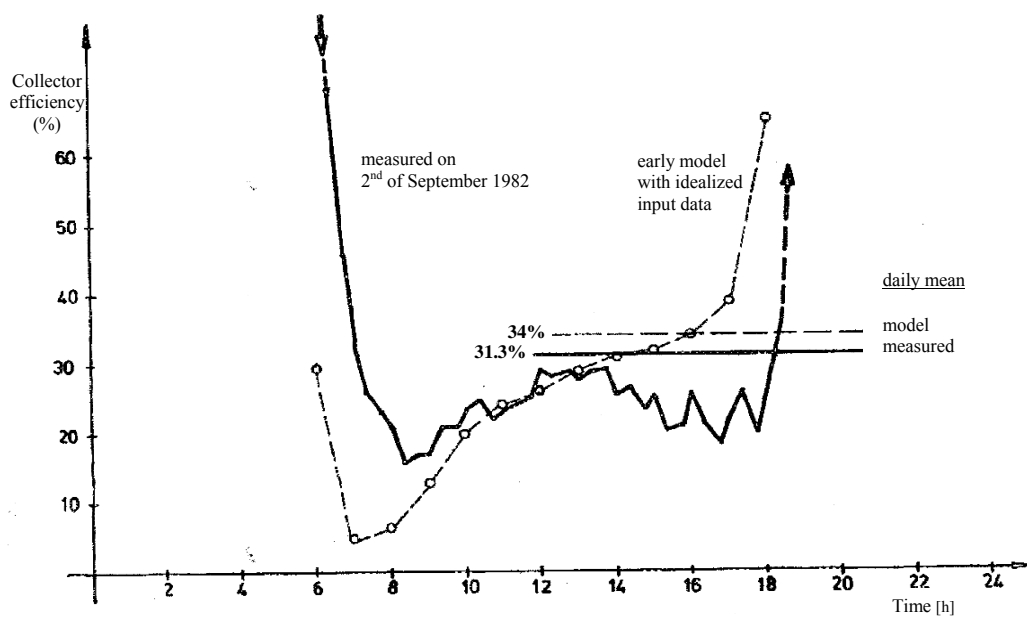
$$q'' = \eta_{coll} \cdot I . \quad (8.25)$$

where η_{coll} is the collector efficiency computed from the experiment data. It is obvious that all prediction values are underestimated. This is consistent with the intended built-in feature of p_2 as stated in Chitsomboon (2001) (so called conservative modeling). It should also note that the differences between the experimental data and prediction of Δp_{tot} are very large. Though Haaf (1984) claimed that the total pressure differences, presented in Fig. 8.2(d), were from the roof entrance to the tower top, these differences are close to the theoretical Δp_{13} which are the total pressure differences proposed in this present work.

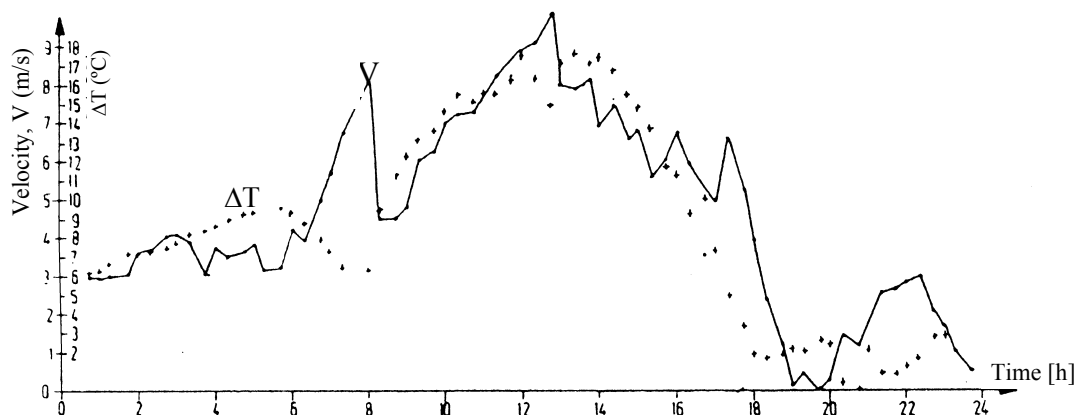
Furthermore, the measured data from Manzanares prototype plant for September 1st, 1989 are taken from Weinrebe (2001). The data adopted is presented in Table 8.3. The comparisons are shown in Table 8.4. The results show good agreement between analytical models and experimental results. These should warrant the reliability of the proposed models.



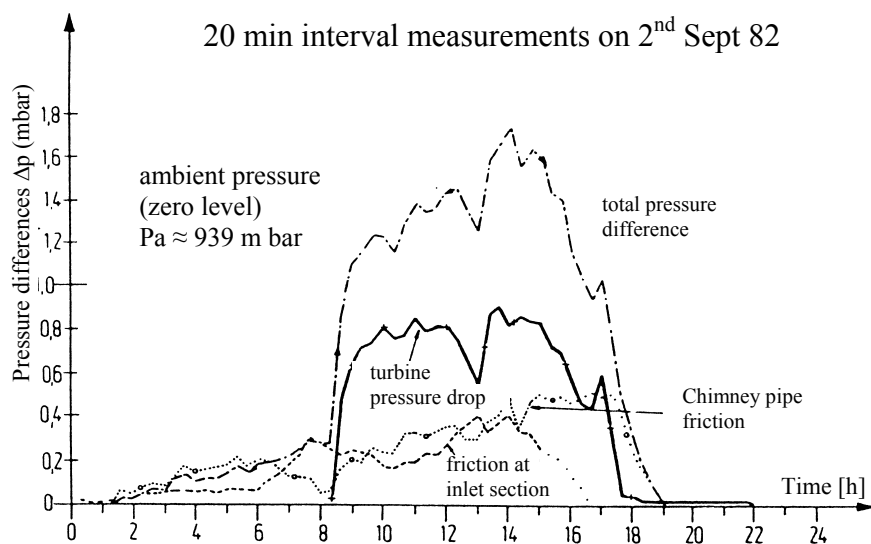
(a)



(b)



(c)



(d)

Figure 8.2 Momentary measurements on 2nd September 1982 from Manzanares

prototype plant: a) global radiation I and T_1 ; b) thermal efficiency of the collector; c) ΔT_{12} and V_c ; d) pressure differences

(adapted from Haaf (1984)).

Table 8.1 Geometrical dimensions of the pilot plant in Manzanares, Spain.

Mean roof radius, r_r	122 m
Average roof height, h_r	1.85 m
Tower height, h_c	194.6 m
Tower radius, r_c	5.08 m

Table 8.2 Comparison between measured data from Manzanares pilot plant and theoretical results; data on 2nd September 1982 taken from Haaf (1984).

Time	I (W/m ²)	η_{coll} (%)	T_1 (°C)	ΔT_{12} (°C)	V_4 (m/s)		Δp_{turb} (mbar)		Δp_{14} (mbar)		Δp_{13} (mbar)
					measured	theory	measured	theory	measured	theory	theory
10.00	744.4	24.3	21.1	14.8	7	6.72	0.8	0.62	1.24	21.1	1.0
12.00	850	27.1	23.4	17.8	9	7.25	0.8	0.74	1.44	20.9	1.18
14.00	755.6	25.7	26.1	17.4	7	6.29	0.84	0.81	1.7	20.7	1.14
16.00	455.6	23.6	27.9	11.3	7.7	5.28	0.6	0.51	1.2	20.6	0.74

Table 8.3 Data of Manzanares pilot plant for 1st September 1989 taken from Weinrebe (2001).

Global solar radiation (W/m^2), I	1,017
Ambient temperature ($^{\circ}\text{C}$), T_1	18.5
Ambient pressure (Pa), p_1	92,930
Collector absorption coefficient , α	0.65
Collector loss coefficient ($\text{W}/\text{m}^2\cdot\text{K}$), U	15
Turbine efficiency	0.85
Generator and gearbox efficiency	0.9
Upwind velocity (m/s), V_4	8.1

Table 8.4 Comparison between measured data from Manzanares pilot plant and theoretical results. (data on 1st September 1989)

Parameter	Measured	Theory
T_2 ($^{\circ}\text{C}$)	38	41.5
\dot{W}_{ext} (kW)	48.4	48.3

Characteristic of turbine power output

Figures 8.3 and 8.4 show the calculated power output as a function of the mass flow rate and $\Delta p_{turb}/\Delta p_{tot}$. The parameters $\alpha = 0.75$ and $U = 5 \text{ W/m}^2\text{K}$ for Eq. (8.15) are taken from Schlaich (1995). All plants studied have $h_r = 2 \text{ m}$ and $r_c = 4 \text{ m}$. The temperature rise across the collector is presented in Fig. 8.5. According to the total maximum demand of electricity and the number of electrified villages in Thailand reported by the Provincial Electricity Authority of Thailand (2007), the power demand of each village is approximately 200 kW. If the maximum allowable temperature rise is less than 50 K, the favorable plant, which can serve the electricity demand for each village in Thailand and the investment cost would be affordable by the local government, is the one with a collector radius 200 m and a chimney height of 400 m. The designed solar heat flux in Figs. 8.3 – 8.5 is 600 W/m^2 .

To study the characteristic of the favorable plant, the variations of the power as a function of the solar heat flux are shown in Figs. 8.6 and 8.7. In addition to the system with the useful solar heat gain computed from Eq. (8.15), which is called as “ q ” (with loss)” in the figure, the characteristics of the system that absorbed the solar radiation completely, which is called as “ q ” (no loss)”, are also illustrated. It can be seen that the maximum powers of the system with heat loss occur somewhere between the maximum and minimum mass flow rate while the maximum powers for the system without heat loss occur at the point that offers the minimum mass flow rate. Apparently the post calculated x-factor depends on the magnitude of the solar heat flux. It is not equal $2/3$, but is approximately 0.84.

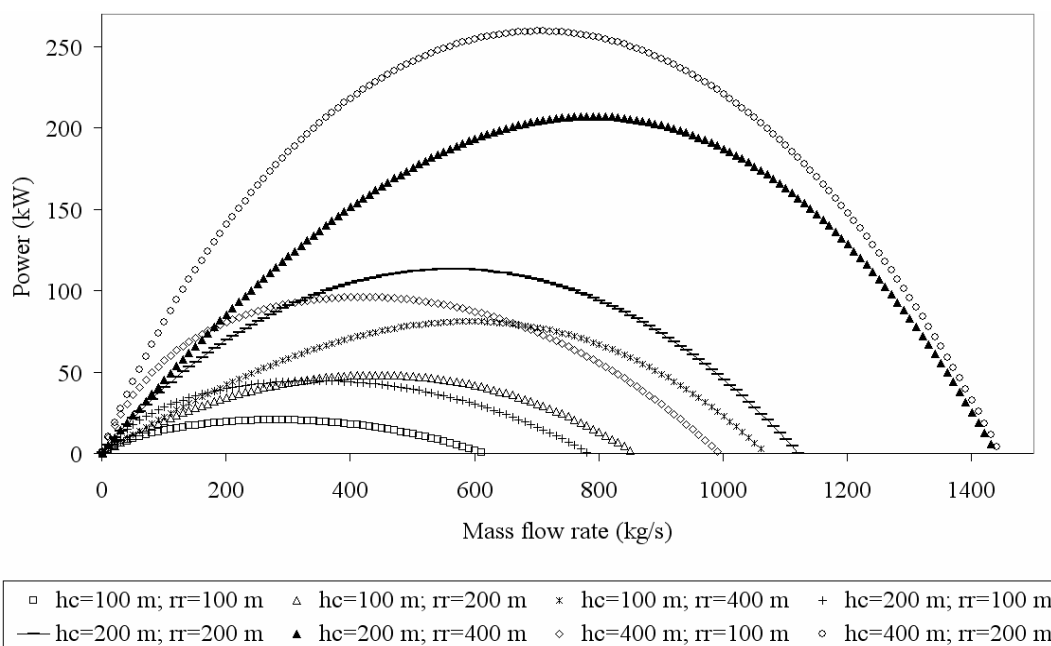


Figure 8.3 Influence of the mass flow rate on the power output for solar irradiation

$= 600 \text{ W/m}^2$. ($h_r = 2 \text{ m}$ and $r_c = 4 \text{ m}$ for all plants)

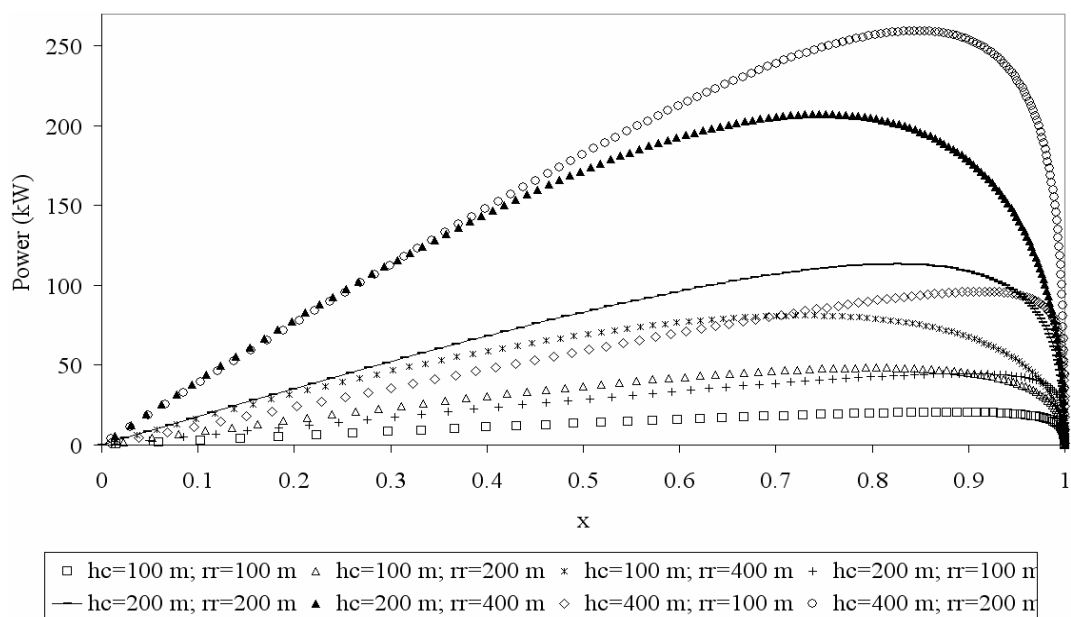


Figure 8.4 Influence of the pressure ratio [cf. Eq. (8.2)] on the power output for solar

irradiation = 600 W/m^2 . ($h_r = 2 \text{ m}$ and $r_c = 4 \text{ m}$ for all plants)

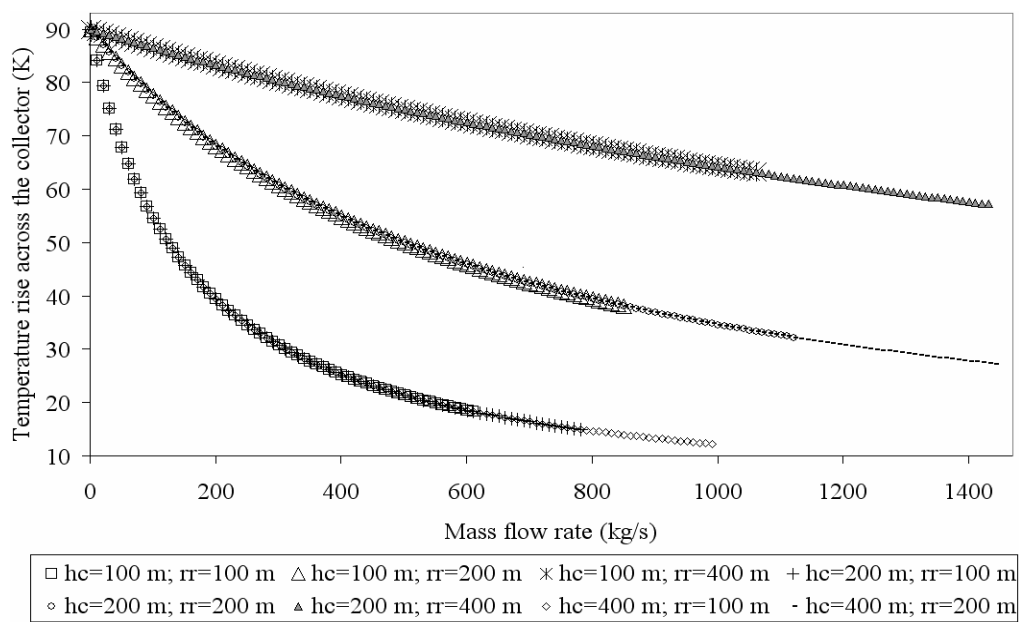


Figure 8.5 Influence of the mass flow rate on the collector temperature rise for solar

irradiation = 600 W/m^2 . ($h_r = 2 \text{ m}$ and $r_c = 4 \text{ m}$ for all plants)

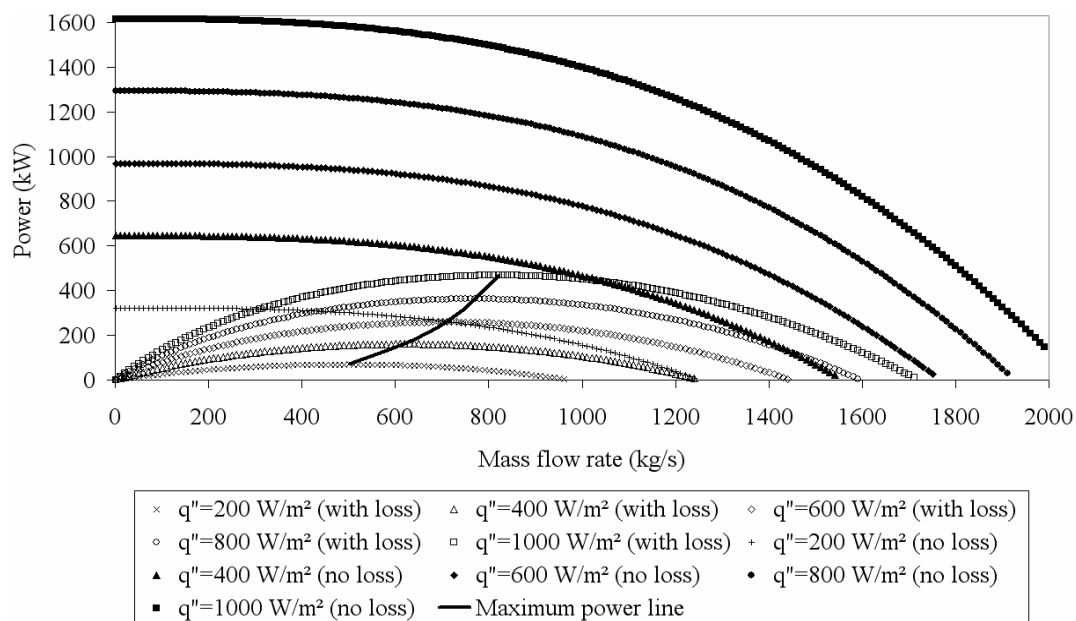


Figure 8.6 Influence of the mass flow rate on the power output along lines of constant solar irradiation. ($h_r = 2$ m, $r_r = 200$ m, $h_c = 400$ m and $r_c = 4$ m for all cases)

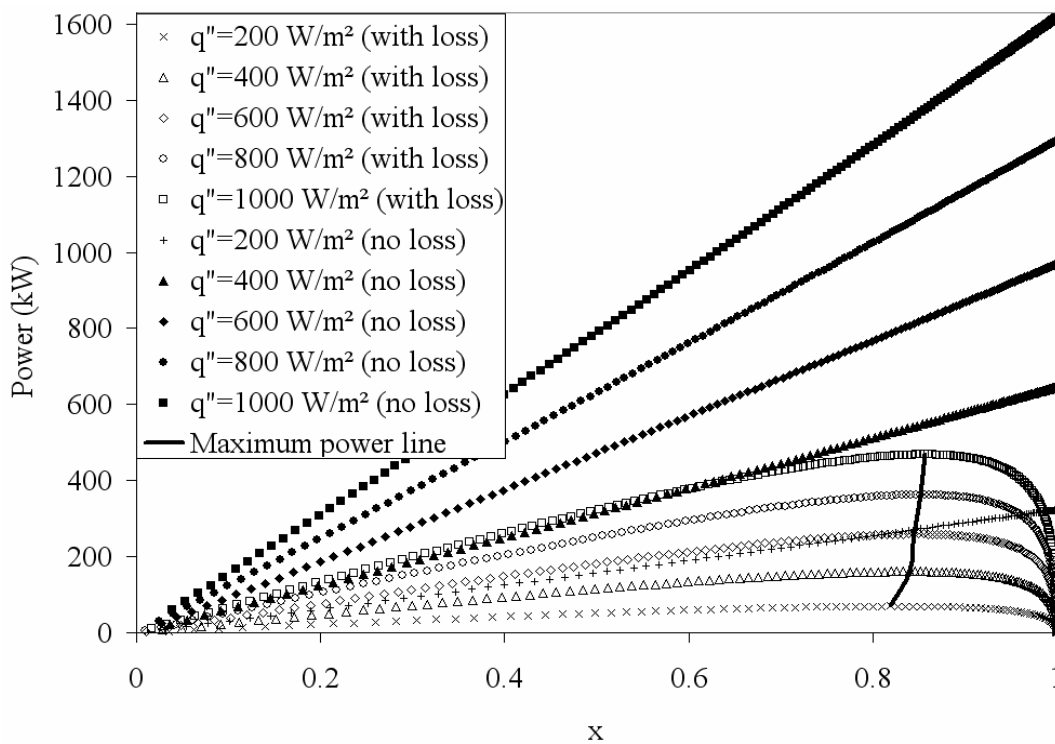


Figure 8.7 Influence of the pressure ratio on the power output along lines of constant solar irradiation. ($h_r = 2$ m, $r_r = 200$ m, $h_c = 400$ m and $r_c = 4$ m for all cases)

To investigate further the effect of plant size on the flow characteristics, Fig. 8.8 – 8.10 show the relationships between Δp_{13} , Δp_{23} , q'' and \dot{m} of different-size plants, including the favorable plant. It is clear that their relations depend on the plant sizes. Fig. 8.11 shows the collector efficiency that is defined as

$$\eta_{col} = \dot{m}c_p \Delta T_{12} / q'' A_r . \quad (8.26)$$

It is apparent that the collector efficiency is not a function of the solar heat gain. It depends on the plant size and there is no representative value. We observe that for all the collectors, the efficiency decreases with increasing the plant size. This can be explained by the fact that, when the plant size increases, the flow velocity increases and the time to extract the useful energy from the collector decreases.

Although the flow properties between plants are widely scattered as displayed in Fig. 8.8 – 8.11, it is important to notice from Fig. 8.12 that the values of $\frac{\Delta p_{13} A_c V_2}{q'' A_r g h_c \beta / c_p}$ are approximately equal to one for all plants. Koonsrisuk and Chitsomboon (2009) proposed that

$$\frac{\dot{m} V_2^2 / 2}{q'' A_r g h_c \beta / c_p} = 1 . \quad (8.27)$$

Assume that the whole pressure difference is used to accelerate the air and is thus converted completely into kinetic energy:

$$\Delta p_{13} A_c V_2 = \dot{m} V_2^2 / 2 . \quad (8.28)$$

Consequently,

$$\frac{\Delta p_{13} A_c V_2}{q'' A_r g h_c \beta / c_p} = 1, \quad (8.29)$$

confirmed by Fig. 8.12.

Figure 8.13 presents Δp_{loss} , which is the pressure difference between Δp_{13} and Δp_{23} . Surprisingly all data collapse into one single line and it is found that

$$\Delta p_{13} = 0.0002 \dot{m}^2 \quad (8.30)$$

regardless of the plant size or the solar heat flux. As a result, we can use Eqs. (8.29) and (30) together with the collector efficiency from Fig. 8.11 to approximate the turbine power of the plant of a specific size.

8.7 CONCLUSION

Theoretical simulations were conducted in order to evaluate the performance of the solar chimney power plant. The relationships between the x-factor and the mass flow rate, the temperature rise across the collector and the power output are presented. It was found that, for a system with constant pressure potential (available system pressure difference), the optimum ratio of the turbine pressure drop to the pressure potential is 2/3. For the system with the pressure potential not constant, it is clear that this optimum ratio is a function of the plant size and solar heat flux. This study may be helpful in preliminary plant design.

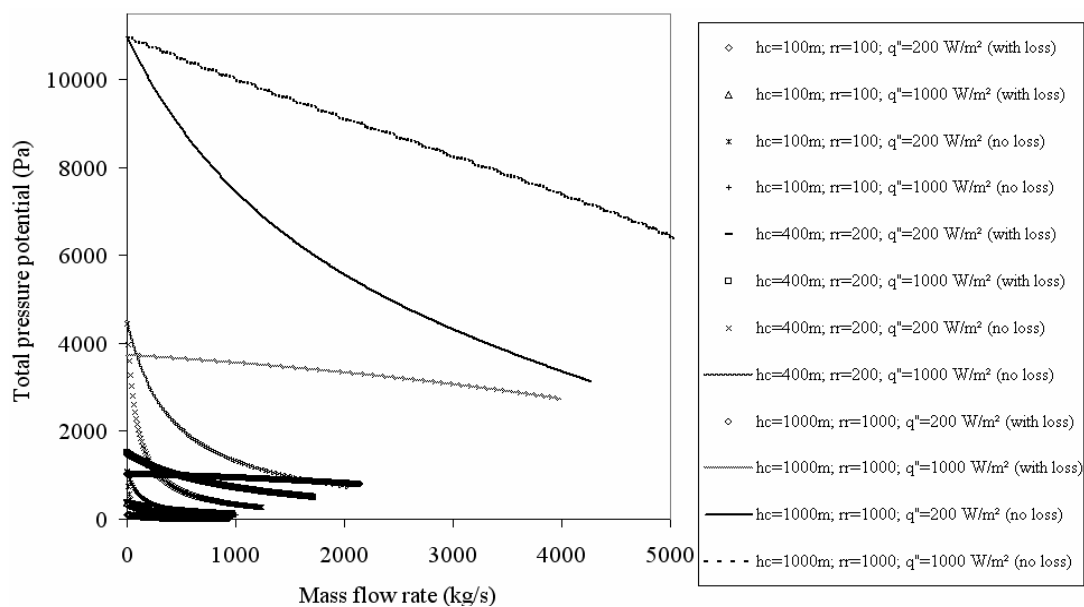


Figure 8.8 Influence of the mass flow rate on the total pressure potential along lines of constant solar irradiation. ($h_r = 2$ m and $r_c = 4$ m for all plants)

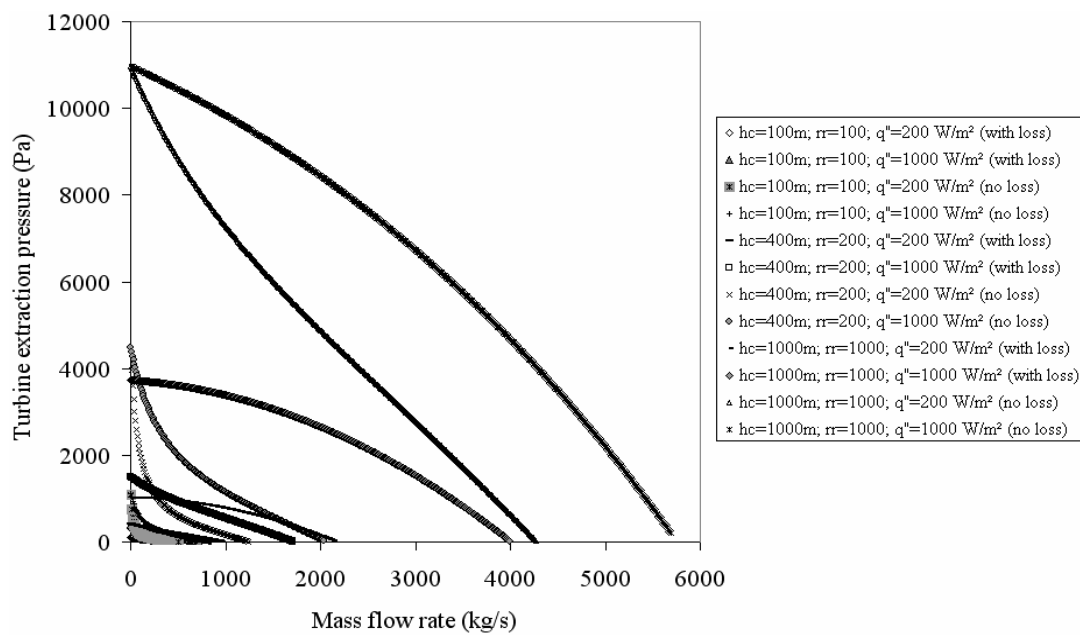


Figure 8.9 Influence of the mass flow rate on the turbine pressure drop along lines of constant solar irradiation. ($h_r = 2$ m and $r_c = 4$ m for all plants)

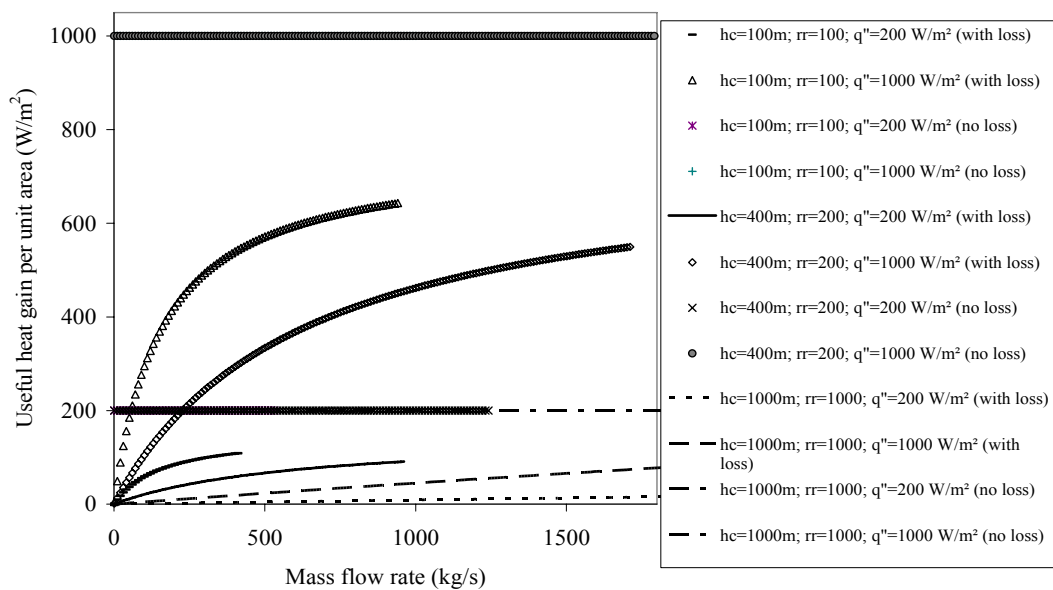


Figure 8.10 Influence of the mass flow rate on the useful heat gain extracted from the collector along lines of constant solar irradiation.

($h_r = 2$ m and $r_c = 4$ m for all plants)

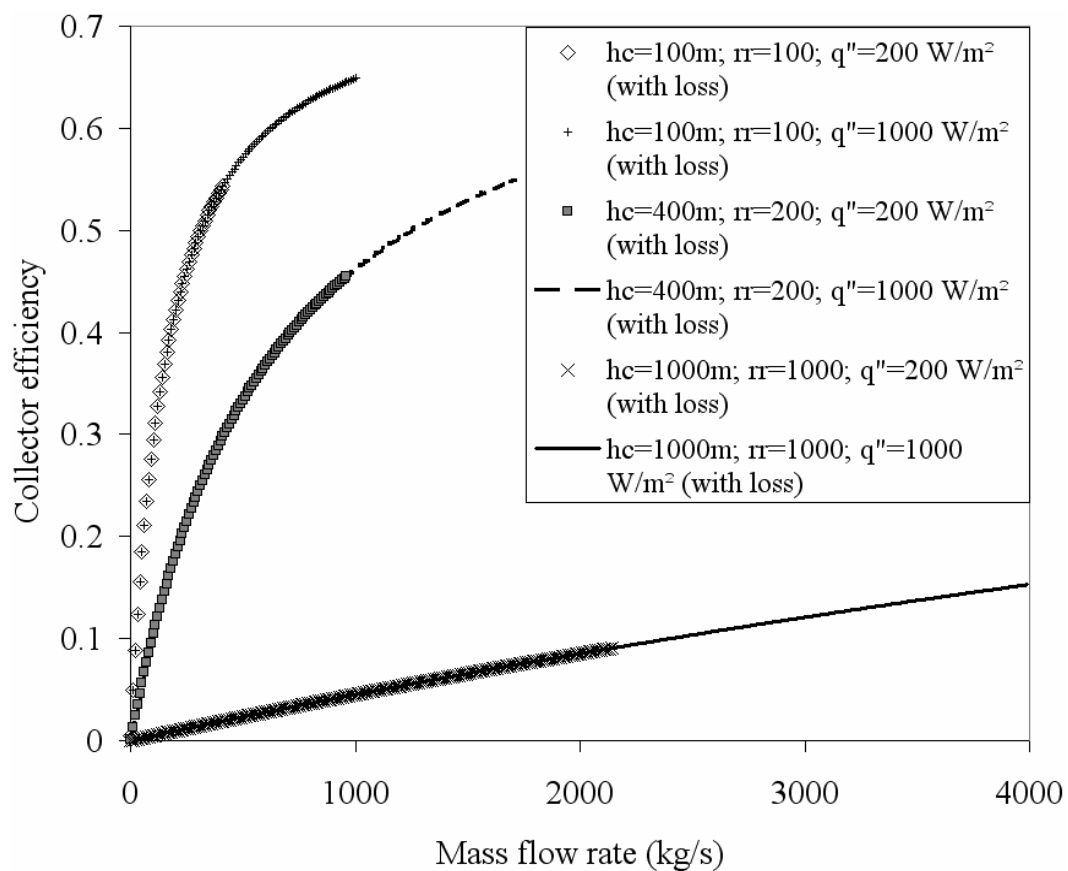


Figure 8.11 Influence of the mass flow rate on the collector efficiency [cf. Eq. (8.26)]

along lines of constant solar irradiation.

($h_r = 2\text{ m}$ and $r_c = 4\text{ m}$ for all plants)

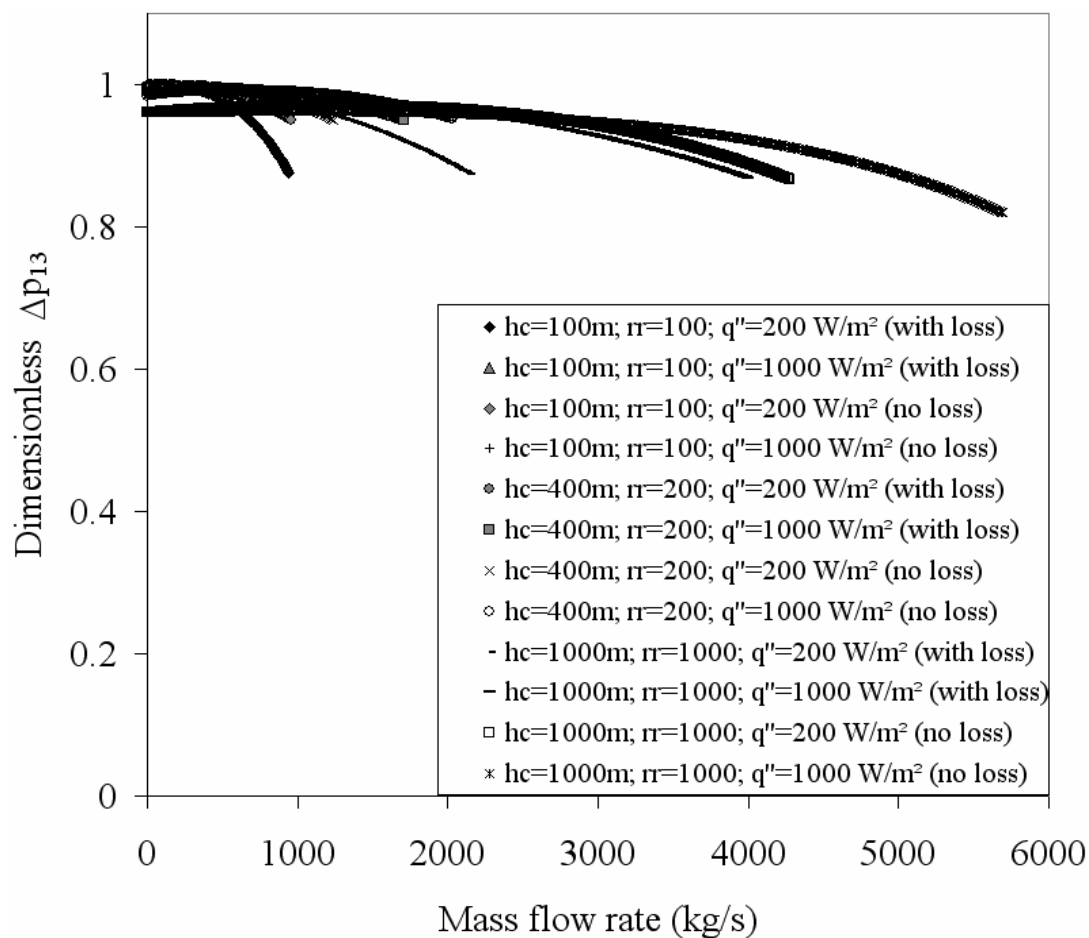


Figure 8.12 Influence of the mass flow rate on the dimensionless Δp_{13}

[cf. Eq. (8.29)] along lines of constant solar irradiation.

($h_r = 2 \text{ m}$ and $r_c = 4 \text{ m}$ for all plants)

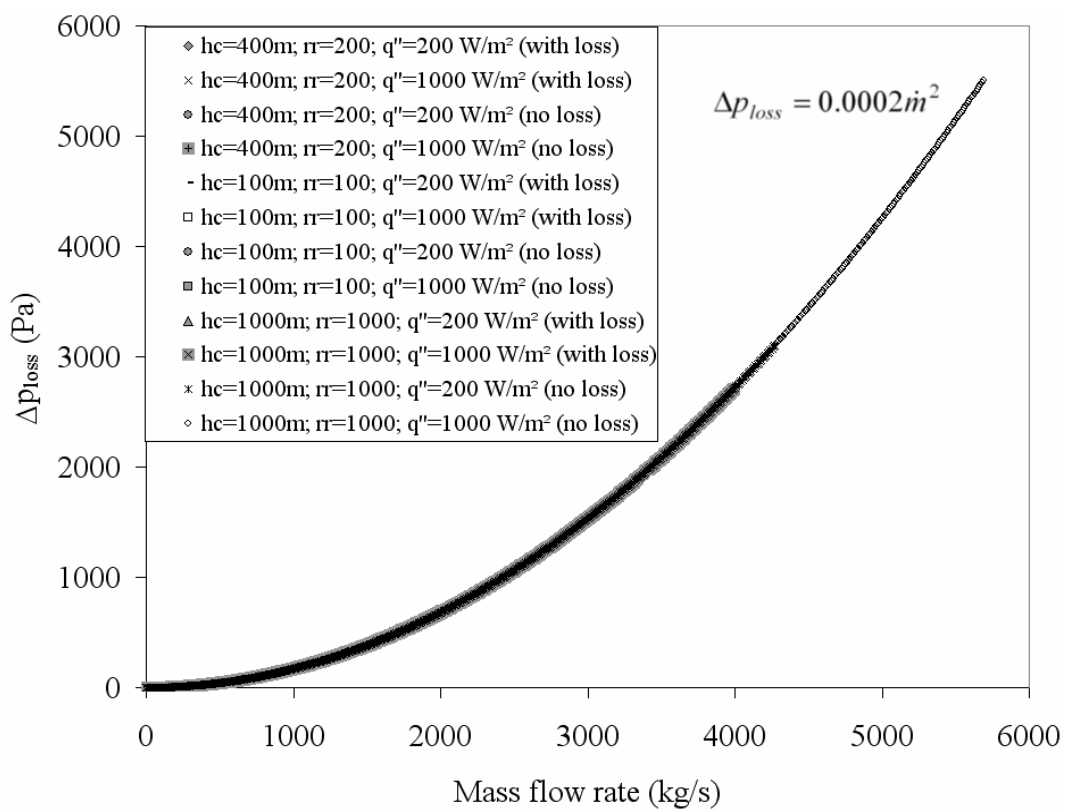


Figure 8.13 Influence of the mass flow rate on the plant total pressure loss along lines of constant solar irradiation. ($h_r = 2$ m and $r_c = 4$ m for all plants)

8.8 REFERENCES

- Bernardes, M. A., Dos, S., Voß, A., Weinrebe, G., 2003. Thermal and technical analyses of solar chimneys. **Solar Energy**, Vol. 75(6), pp. 511-524.
- Calvert, J. G. 1990. Glossary of atmospheric chemistry terms (Recommendations 1990). **Pure and applied chemistry**, Vol. 62(11), pp. 2167-2219.
- Chitsomboon, T. 2001. A validated analytical model for flow in solar chimney. **International Journal of Renewable Energy Engineering**, Vol. 3(2), pp. 339-346.
- Dai, Y. J., Huang, H. B., Wang, R. Z. 2003. Case study of solar chimney power plants in northwestern regions of China. **Renewable Energy**, Vol.28, pp. 1295-1304.
- Duffie, J., Beckman, W. A. 1991. **Solar Engineering of Thermal Processes**. 2nd ed. John Wiley & Sons, Inc., USA.
- Eggleston, D. M., Stoddard, F. S. 1987. **Wind Turbine Engineering Design**. Van Nostrand Reinhold Company, Inc., USA.
- Haaf, W., Friedrich, K., Mayr, G., Schlaich, J. 1983. Solar chimneys: part I: principle and construction of the pilot plant in Manzanares. **International Journal of Solar Energy**, Vol. 2, pp. 3-20.
- Haaf, W., 1984. Solar chimneys: part II: preliminary test results from the Manzanares plant. **International Journal of Solar Energy**, Vol. 2, pp. 141-161.
- Hedderwick, R. A., 2001. **Performance evaluation of a solar chimney power plant**. M.Sc. Eng.-thesis, University of Stellenbosch, Stellenbosch, South Africa.
- Koonsrisuk, A., Chitsomboon, T., 2009. A single dimensionless variable for solar tower plant modeling. **Solar Energy**. doi:10.1016/j.solener.2009.07.015.

- Lodhi, M. A. K. 1999. Application of helio-aero-gravity concept in producing energy and suppressing pollution. **Energy Conversion & Management**, Vol. 40, pp. 407-421.
- Mullett, L. B., 1987. The solar chimney - overall efficiency, design and performance. **Int. J. Ambient Energ.**, Vol. 8(1), pp. 35–40.
- Onyango, F. N., Ochieng, R. M., 2006. The potential of solar chimney for application in rural areas of developing countries. **Fuel**, Vol. 85, pp. 2561-2566.
- Pastohr, H., Kornadt, O., Gürlebeck, K. 2004. Numerical and analytical calculations of the temperature and flow field in the upwind power plant. **International Journal of Energy Research**, Vol. 28, pp. 495-510.
- Pasumarthi, N., Sherif, S.A. 1998. Experimental and theoretical performance of a demonstration solar chimney model – part I: mathematical model development. **International Journal of Energy Research**, Vol. 22, pp. 277-288.
- Provincial Electricity Authority of Thailand. 2007. **Annual report**. [On-line]. Available: <http://www.pea.co.th/annualreport/2007/PEA.swf>
- Schlaich, J. 1995. **The Solar Chimney**. Edition Axel Menges: Stuttgart, Germany.
- Schlaich, J., Bergemann, R., Schiel, W., Weinrebe, G. 2005. Design of commercial solar updraft tower systems utilization of solar induced convective flows for power generation. **Journal of Solar Energy Engineering**, Vol. 127, pp. 117–124.
- Von Backström, T. W., Gannon, A. J., 2000. The solar chimney air standard thermodynamic cycle. **SAIMEchE R&D Journal**, Vol. 16 (1), pp. 16–24.

- Weinrebe, G., Schiel, W., 2001. Up-draught solar tower and down-draught energy tower - a comparison. In: **Proceedings of the ISES Solar World Congress 2001**, Adelaide, Australia.
- Zhou, X., Yang, J., Xiao, B., Hou, G., 2007. Simulation of a pilot solar chimney thermal power generating equipment. **Renewable Energy**, Vol.32, pp. 1637-1644.

CHAPTER IX

EXPERIMENTAL PERFORMANCE OF A DEMONSTRATION SOLAR CHIMNEY MODEL

9.1 ABSTRACT

Four small-scale physical models of the solar chimney were constructed at Suranaree University of Technology, Nakhon Ratchasima Province, Thailand. The height of the roof inlet was adjustable in some plants, so that the ratio of flow areas between roof inlet and roof outlet could be varied. In addition, there were plants with constant-cross-sectional-area towers and a plant with a divergent tower. Also there was one plant with a novel roof shape designed by the researcher. To verify the reliability of the dimensionless variables predicted by previous studies, one plant, a half size of the others, was constructed. Through field measurements, results indicate that the flow power increases with the decrease in the ratio of flow areas between roof inlet and roof outlet. The divergent chimney also results in significant increase in flow power compared to that of the constant area chimney. It was observed that the system with the proposed novel roof shape provides approximately the same performance as the conventional shaped system, while the ratio of flow areas between roof inlet and roof outlet for the novel system could be practically reduced. Correspondingly the increase in performance to some specific value which is much lower than the typical system could be achieved. The experimental results are different from the predicted values, but show the same trends. This may be caused by the fluctuating solar heat

flux and the effect of the large chimney diameter when compared with the roof size. Moreover, the difference of dimensionless variables between the large and the small plant is noticeable, contrary to the theoretical and numerical predictions. Reasons could be the varying atmospheric conditions when the tests were run.

9.2 INTRODUCTION

A solar chimney is a combination of three established technologies, namely, the translucent circular roof (or solar collector), the chimney and the turbine. The chimney, a long tubular structure, is placed in the center of the roof, while the turbine is generally mounted at the chimney base. This unique combination accomplishes the task of converting solar energy into electrical energy. This solar-to-electric conversion involves two intermediate stages. In the first stage, conversion of solar energy into thermal energy is accomplished in the collector by means of the greenhouse effect. In the second stage, the chimney converts the generated thermal energy into kinetic and ultimately into electric energy by using a combination of a turbine and generator. Fig. 9.1 provides an overall view of a typical solar chimney system.

Previous theoretical and numerical research (Koonsrisuk and Chitsomboon, 2004; Koonsrisuk and Chitsomboon, 2006; Koonsrisuk and Chitsomboon, 2007; Koonsrisuk and Chitsomboon, 2009) led to the establishment of four small-scale experimental plants on a site at Suranaree University of Technology (Nakhon Ratchasima, Thailand). The experimental system was designed and constructed and was used to study the temperature and velocity profiles within the solar chimney. A numerical model for each plant was also developed and compared the simulated results with experimental observations.

9.3 THE PHYSICAL MODELS

Four physical models were built specifically for this study:

1. Experimental Set 1 has the roof with adjustable inlet height and constant-diameter chimney.
2. Experimental Set 2 has the roof with adjustable inlet height and divergent-top chimney.
3. Experimental Set 3 has the collector with a novel roof shape designed by the researcher and a constant-diameter chimney.
4. Experimental Set 4 is the half-size model of Experimental Set 1.

More details of the experimental sets are listed in Table 9.1.

9.4 EXPERIMENTAL METHODOLOGY

The characterization of airflow under the roof and inside the chimney involved the determination of meteorological and flow conditions. The thermal anemometer with separate velocity and temperature probe (Testo model 425) were used to measure ambient temperature, airflow temperatures and velocity. Incident solar radiation was measured with CM3 pyranometer of Kipp and Zonen B.V. Uncertainties of $\pm 5^{\circ}\text{C}$, ± 0.05 m/s and ± 25 W/m² were specified for the anemometer and pyranometer, respectively.

Table 9.2 shows the details of measuring locations along the collector and the chimney. The measurement at each location was made at different heights in the collector and different radii in the chimney as depicted in Fig. 9.7a and 9.7b, respectively. As a result, the variation of velocity and temperature over the cross-

section can be ignored, they being assumed to be constant and equal to the mean value (\bar{V} and \bar{T}), defined as

$$\bar{V} = \frac{\sum_{i=1}^n V_i A_i}{\sum_{i=1}^n A_i} \quad \text{and} \quad (9.1)$$

$$\bar{T} = \frac{\sum_{i=1}^n \rho A_i V_i T_i}{\sum_{i=1}^n \rho A_i \bar{V}} \quad (9.2)$$

respectively.

9.5 COMPUTATIONAL WORKS

The governing equations for mass, momentum, and energy for each plant are solved using the commercial CFD code (ANSYS, 2005). Experimental Sets 1, 2 and 4 are simplified to that of a horizontal disc above the ground with a vertical cylinder in the center of the disc as shown in Fig. 9.8a. The code is implemented in 3D through the axis-symmetry approximation. As illustrated in Fig. 9.8a, only a 5-degree pie-shape of the whole domain is modeled with the side faces treated as symmetric boundaries. In our previous work (Koonsrisuk and Chitsomboon, 2007), suitable grid and time step size were carefully chosen after performing grid and time step independence tests of the numerical results, thus those configurations are adopted in this work. The examples of grid-independence mesh system are presented in Fig. 9.8b-

d. Figure 9.9a displays the shape of Experimental Set 3. Again, to simulate the axis-symmetry condition, a 1/4 of the whole plant is modeled as depicted in Fig. 9.9b.

The boundary conditions used are shown in Fig. 9.10. At the center of the plant, axis-symmetric conditions were utilized. At the walls, free-slip and adiabatic boundary conditions were used. These conditions were applied at the roof, transition section, chimney wall and ground surface. The total pressure and temperature are prescribed at the roof inlet and the flow direction was set as normal to the roof perimeter. At the chimney top, the 'outlet' boundary condition with zero static gauge-pressure is imposed.

9.6 RESULTS AND DISCUSSION

Ten test cases as listed in Table 9.3 were set up and tested for their performance. It was found that experimental results obtained from each experimental set up varied little on different days. The experimental results presented were thus selected from an actual data set, not from an average of the days measured. The values from each experimental set are displayed in the form of two graphs: velocity versus flow path and temperature versus flow path. The flow path is the distance that the air current moves in the experimental set up, with zero value at the outer edge of the roof, and then assuming the value of the distance the air travels beneath the roof into the chimney. The final position of the distance displayed is at the chimney top. Each graph shows the actual measurement results at four points along the roof and two points along the chimney. The displayed numerical results are the average values across the flow area at the considered position.

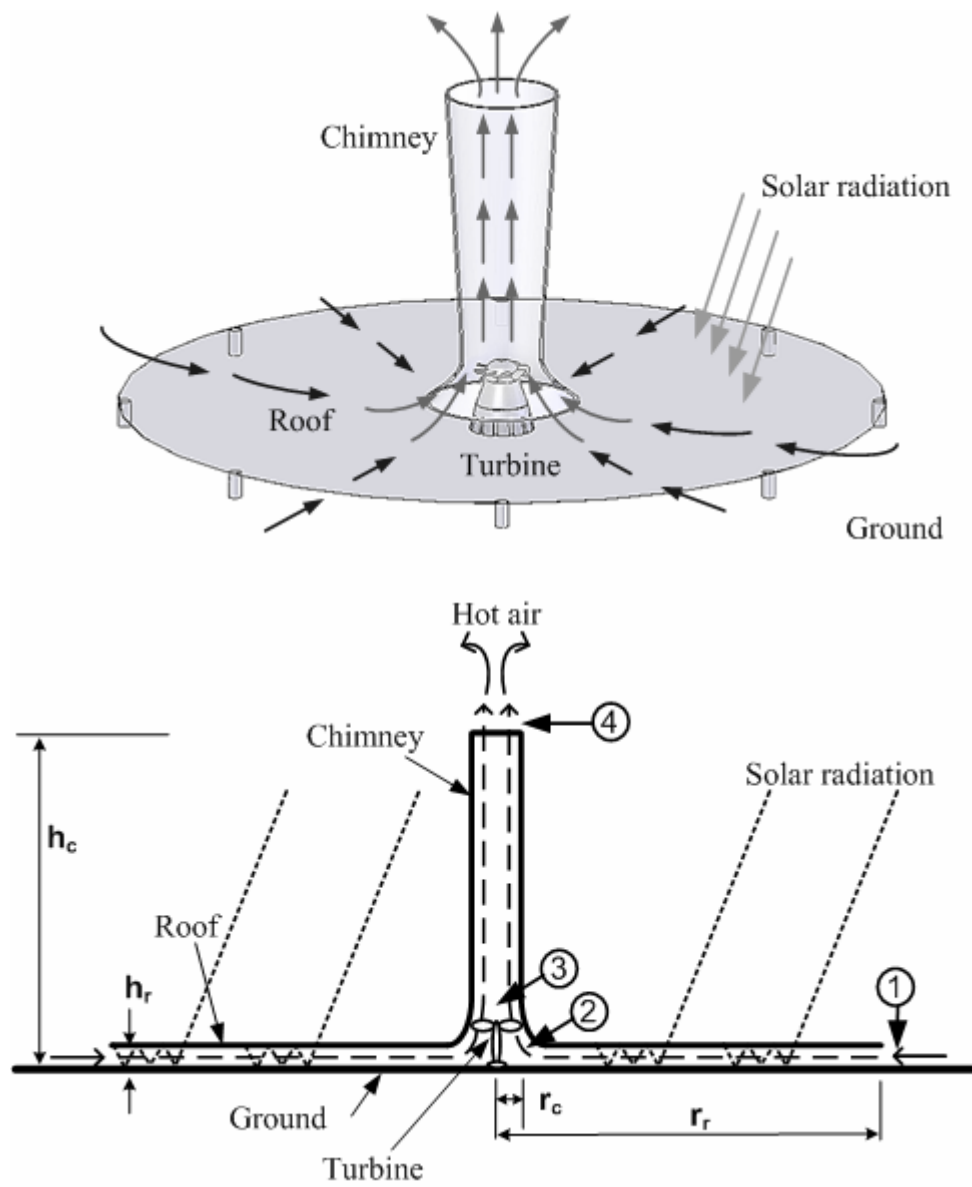
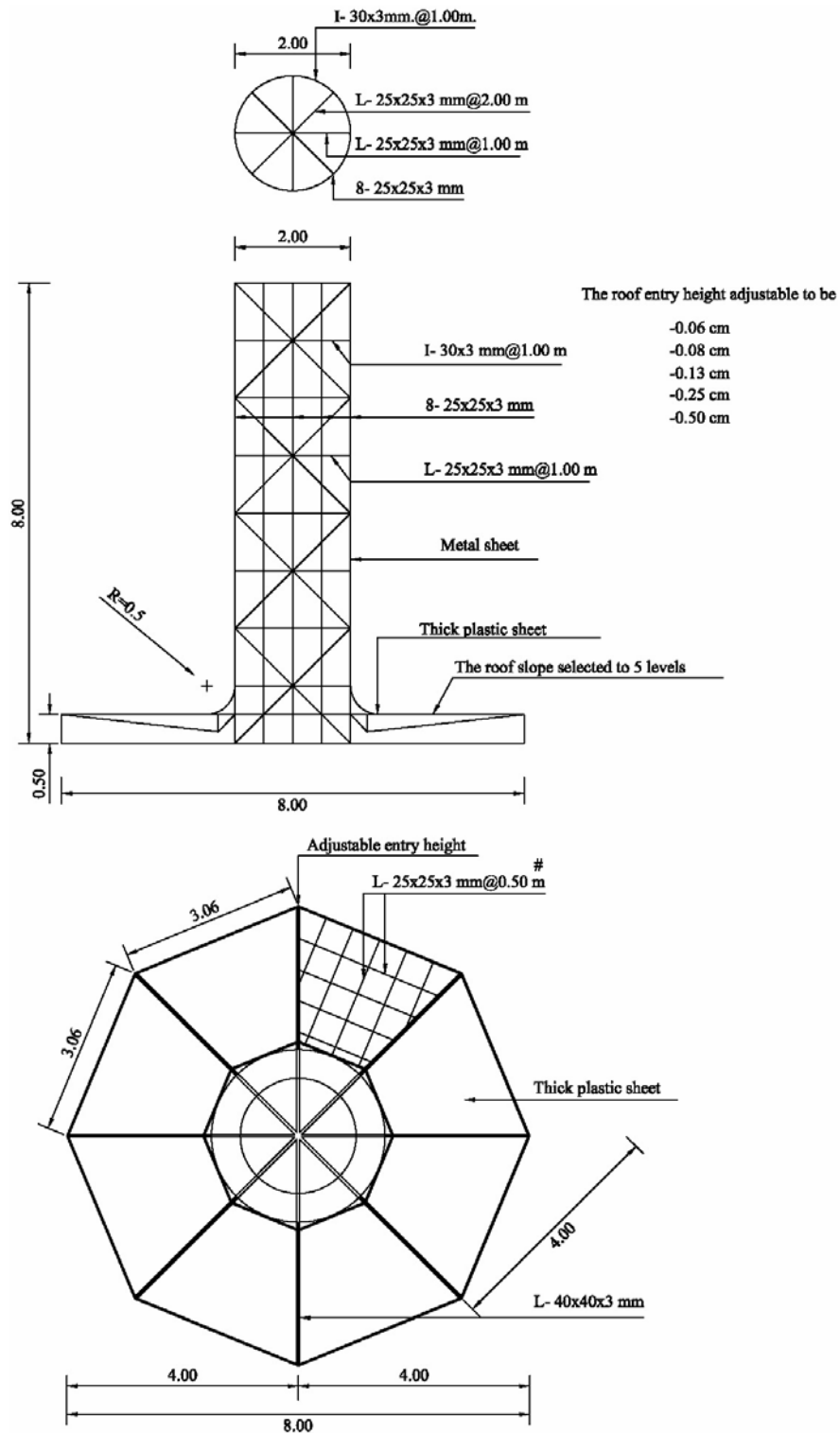


Figure 9.1 Schematic layout of solar chimney power plant.

Table 9.1 Specification of the Experimental Sets.

Model	Chimney height (m)	Roof description	Roof inlet height above the ground	Geometric sizes	Appearance	Note
1	8	Octagonal shape; fully opened at the edges.	selectable at 0.06, 0.08, 0.13, 0.25 and 0.5 m.	See Fig. 9.2a	See Fig. 9.2b	Reference plant; constant-diameter chimney
2	8	Octagonal shape; fully opened at the edges.	selectable at 0.06, 0.08, 0.13, 0.25 and 0.5 m.	See Fig. 9.3a	See Fig. 9.3b	The same size as model 1; divergent-top chimney
3	8	Squared shape; partially opened at the edges.	Fixed at 0.5 m.	See Fig. 9.4a	See Fig. 9.4b	The same roof area for solar collection as model 1; constant-diameter chimney
4	4	Octagonal shape; fully opened at the edges.	selectable at 0.04, 0.05, 0.07, 0.15 and 0.25 m.	See Fig. 9.5a	See Fig. 9.5b	Half size of model 1



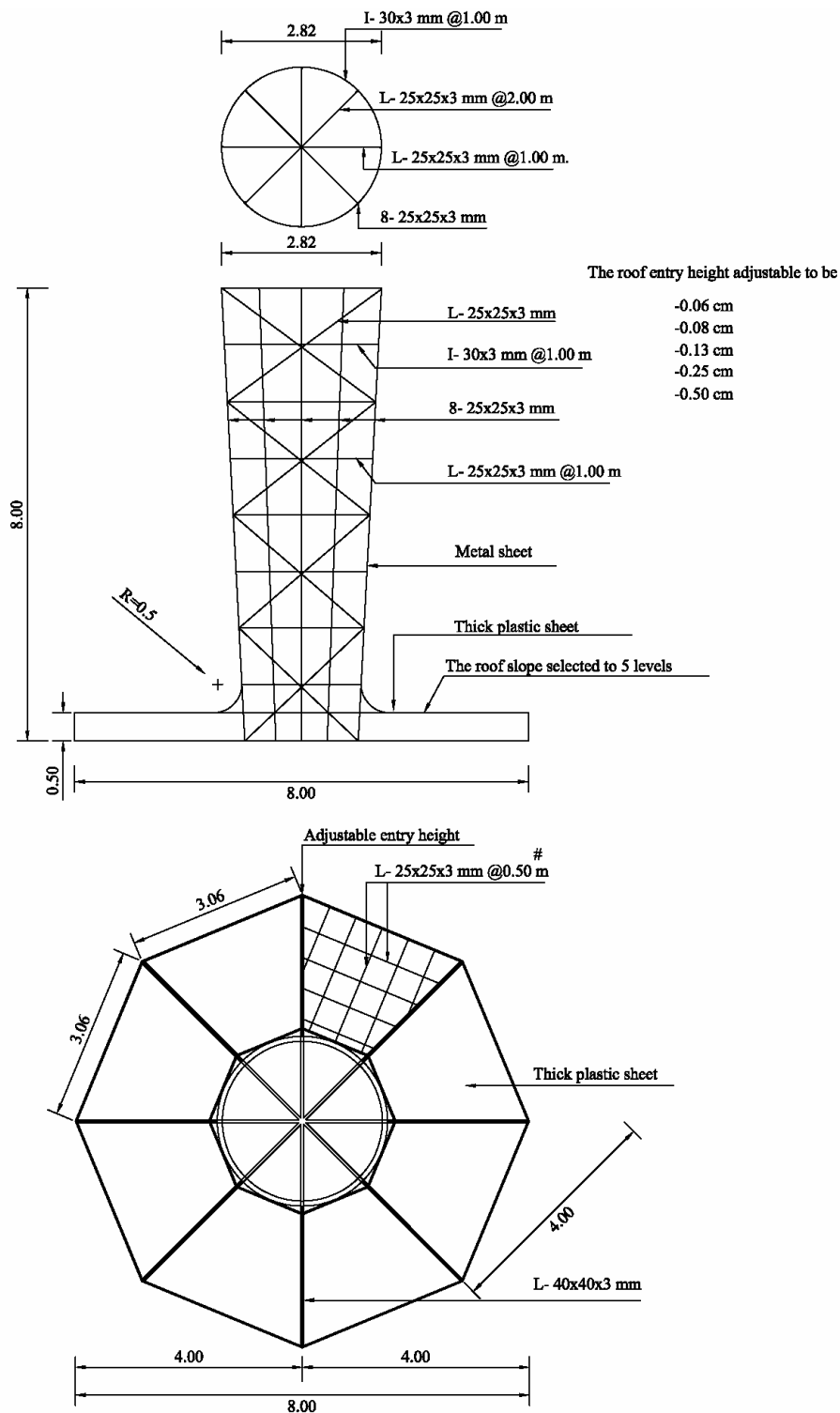
(a)

Figure 9.2 Layout of Experimental Set 1.



(b)

Figure 9.2 Layout of Experimental Set 1 (continued).



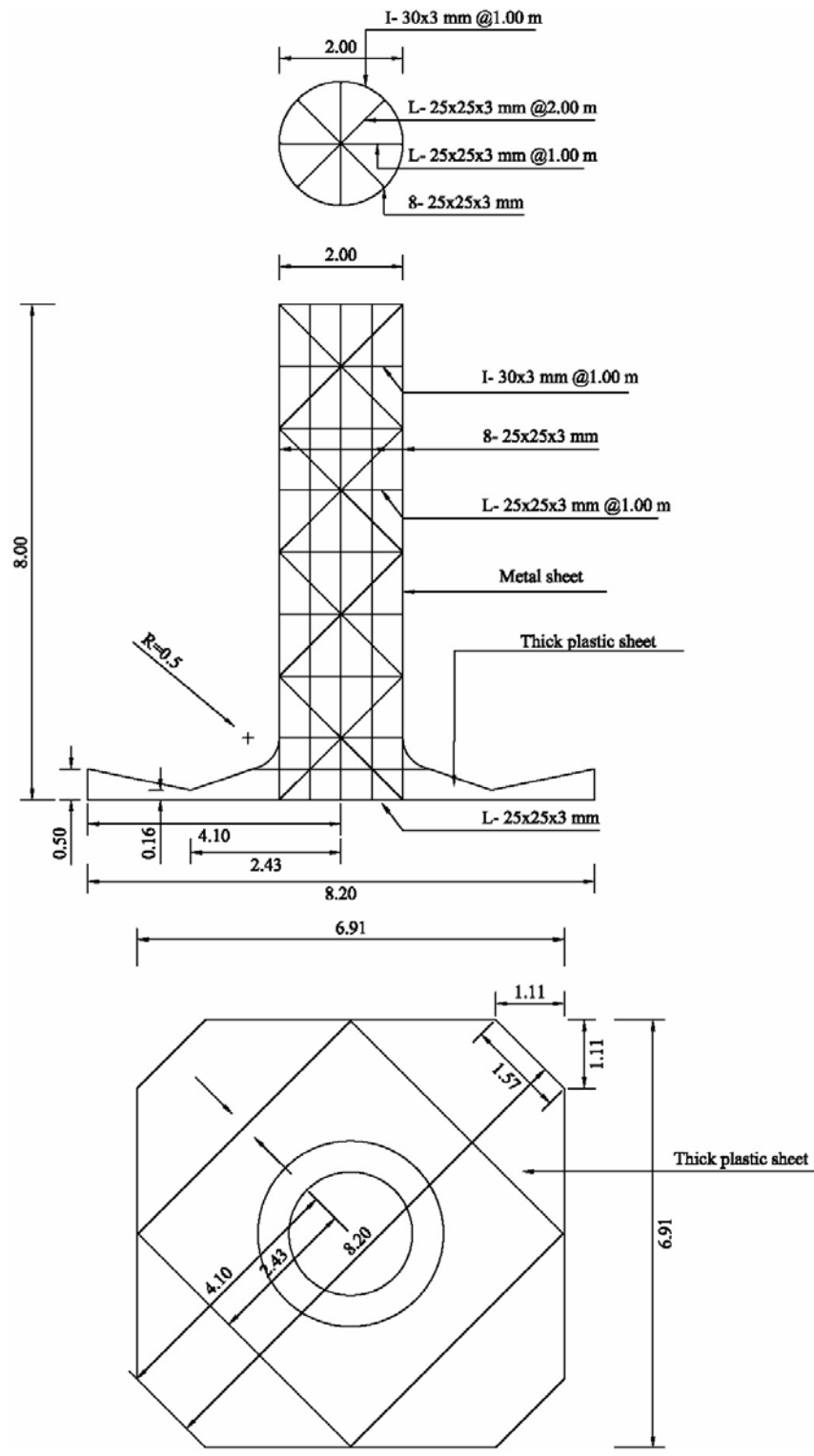
(a)

Figure 9.3 Layout of Experimental Set 2.



(b)

Figure 9.3 Layout of Experimental Set 2 (continued).



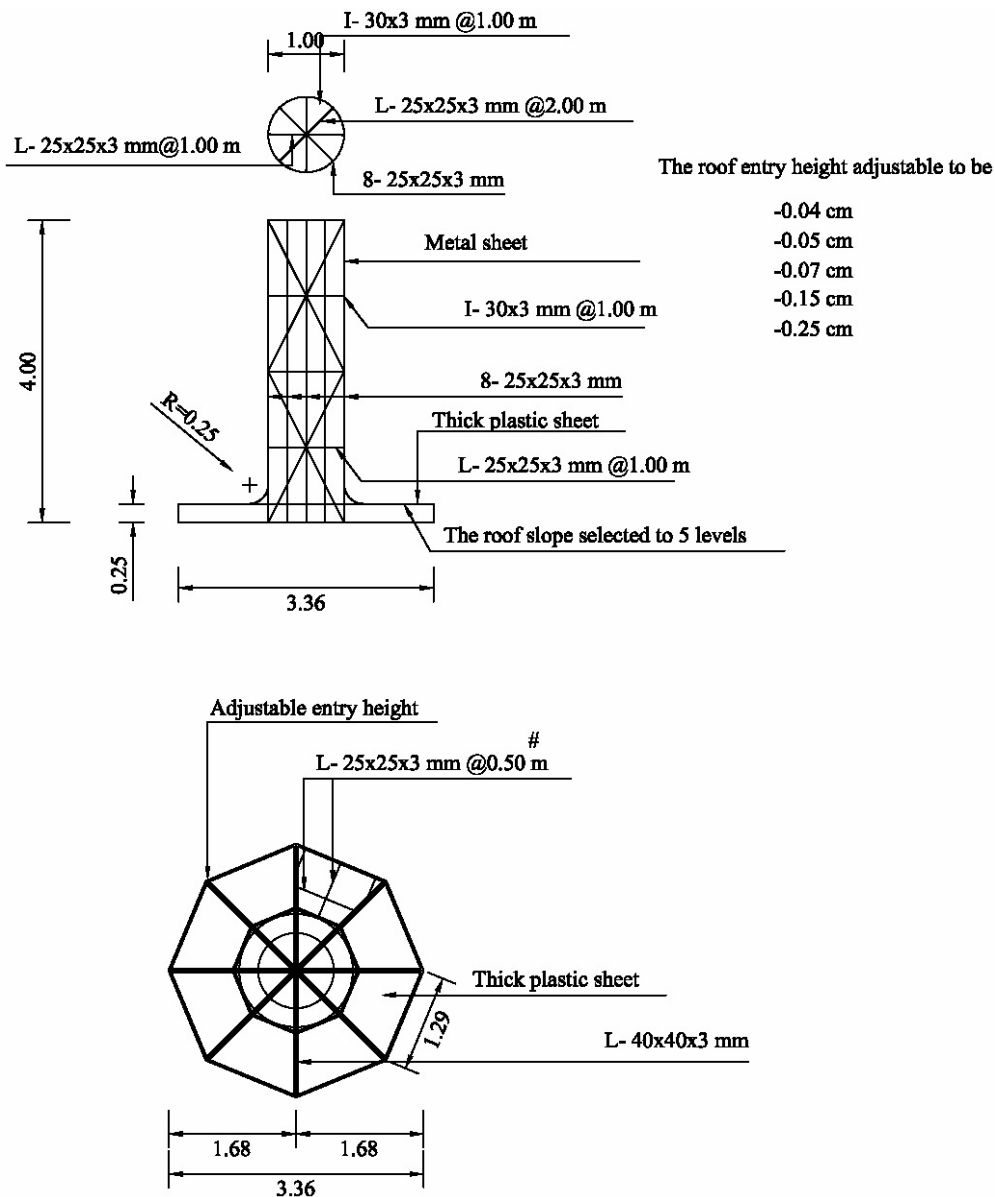
(a)

Figure 9.4 Layout of Experimental Set 3.



(b)

Figure 9.4 Layout of Experimental Set 3 (continued).



(a)

Figure 9.5 Layout of Experimental Set 4.

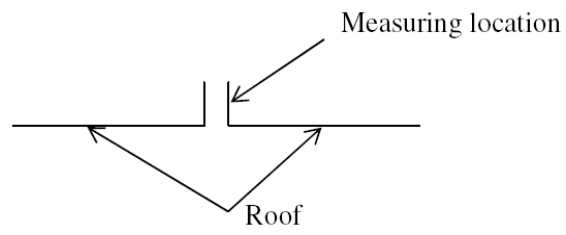


(b)

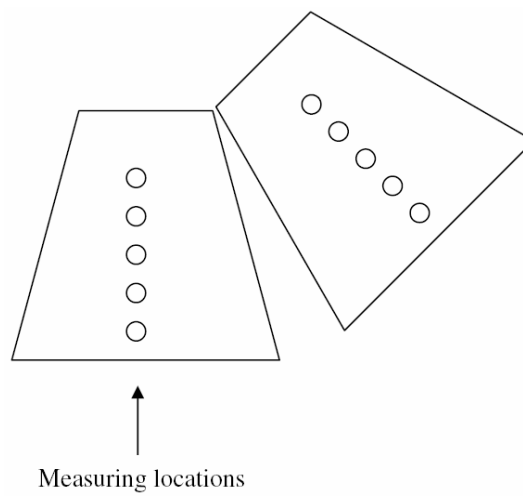
Figure 9.5 Layout of Experimental Set 4 (continued).

Table 9.2 Details of measuring locations.

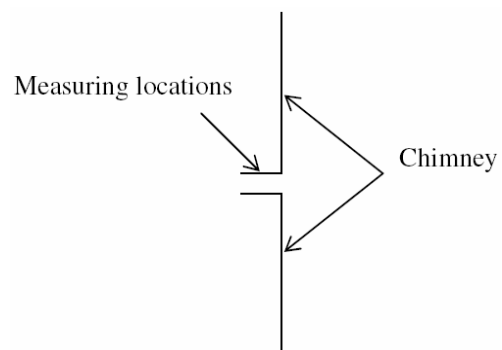
Model	Collector		Chimney		Note
	Number of measuring locations	Measuring positions measured from the roof perimeter	Number of measuring locations	Measuring positions measured above the ground	
1	4	At 0.1, 0.6, 1.1 and 1.6 m	2	At 1.5 and 2 m	See Fig. 9.6
2	4	At 0.1, 0.6, 1.1 and 1.6 m	2	At 1.5 and 2 m	
3	5	At 0.6, 1.1, 1.6, 2.1 and 2.5 m	2	At 1.5 and 2 m	
4	4	At 0.042, 0.252, 0.462 and 0.672 m	2	At 1.0 and 1.25 m	



(a)

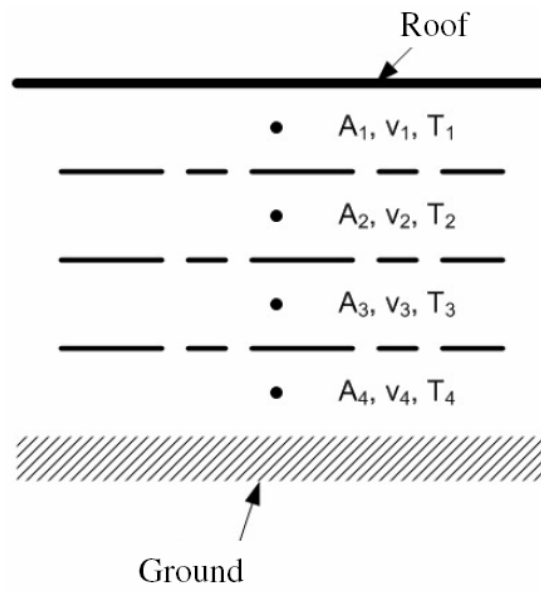


(b)

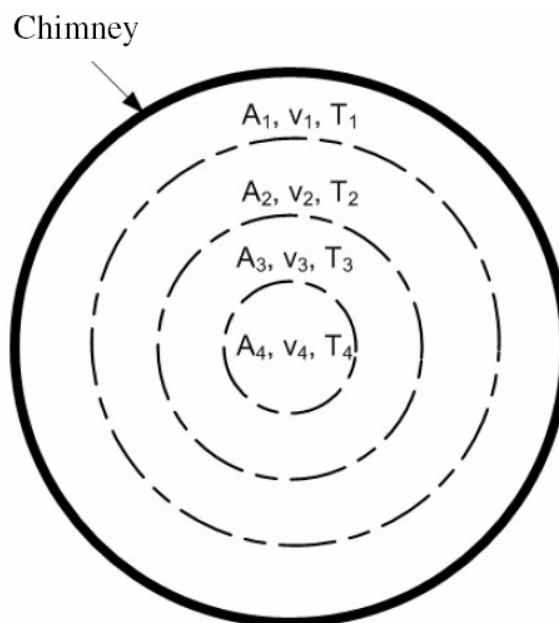


(c)

Figure 9.6 Layout of measuring locations.



(a)



(b)

Figure 9.7 Descriptions of flow parameters for the calculations of average properties.

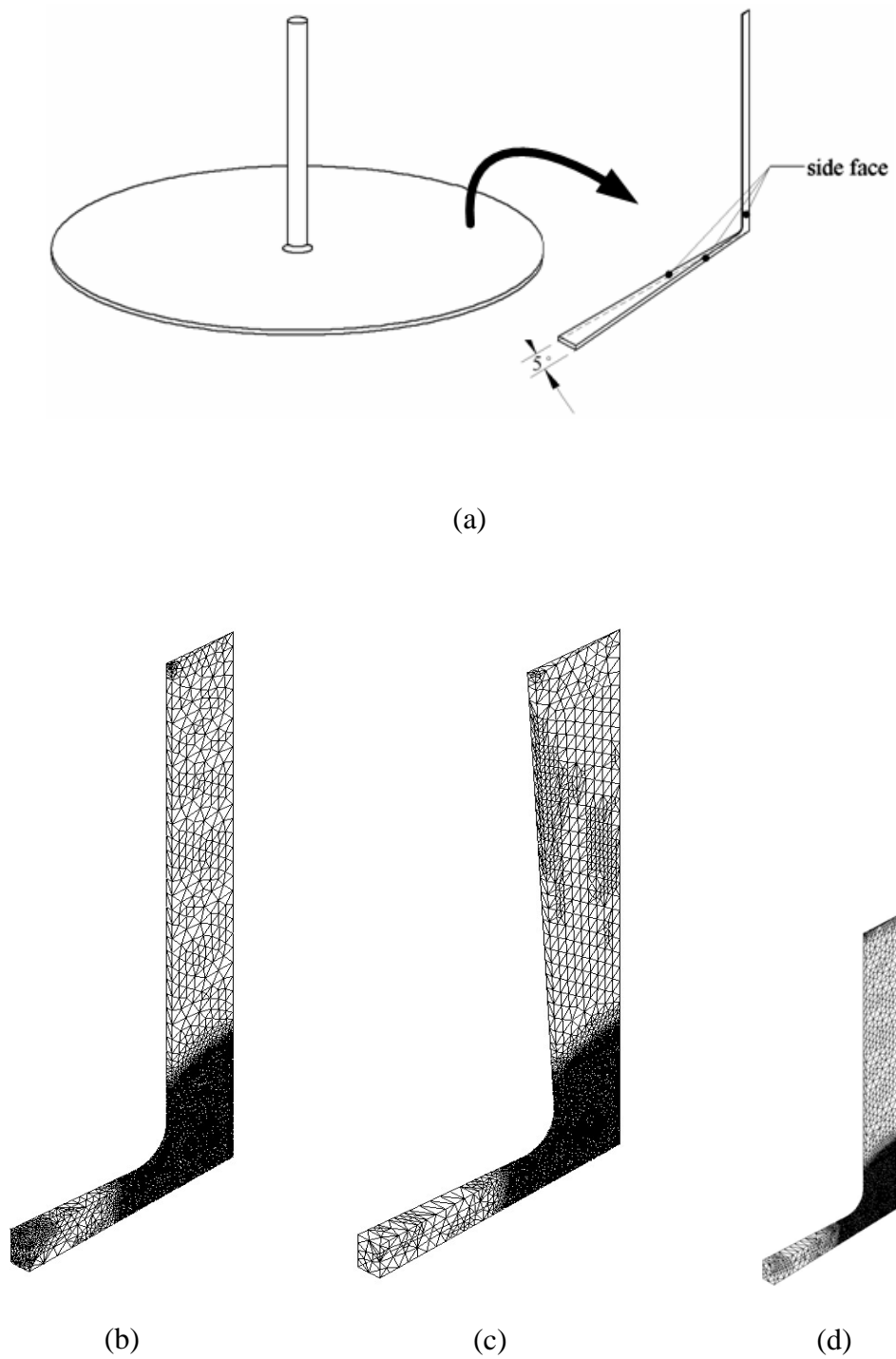
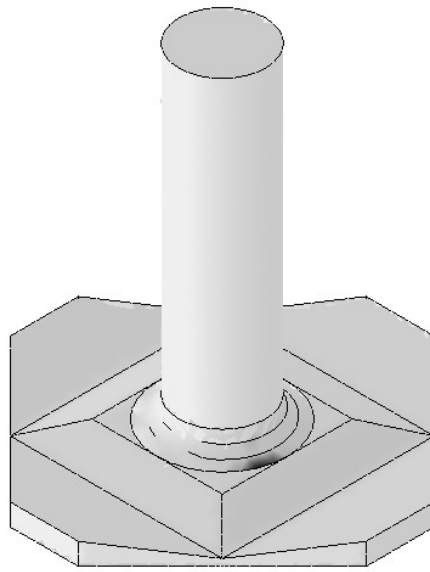
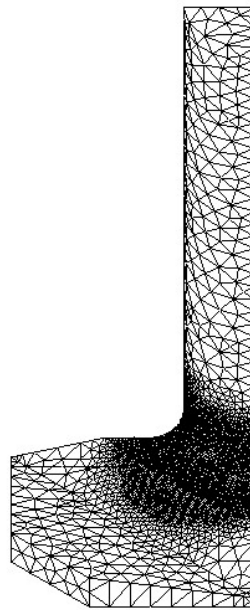


Figure 9.8 Computational domain of Experimental Sets 1, 2 and 4: (a) 5 degree axis-symmetric section; (b) computational grid of Experimental Set 1; (c) computational grid of Experimental Set 2; (d) computational grid of Experimental Set 4.



(a)



(b)

Figure 9.9 Computational domain of Experimental Set 3: (a) layout;

(b) computational grid.

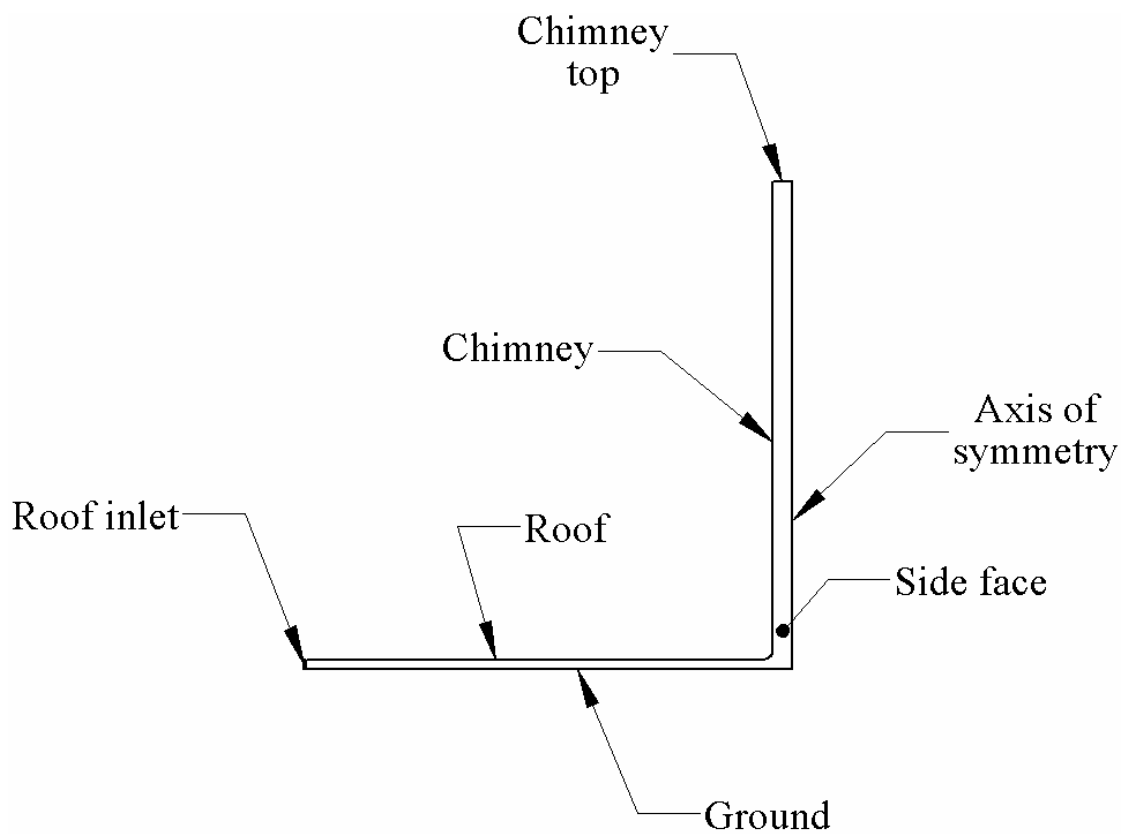


Figure 9.10 Boundary settings of computation domain.

The plots of the airflow temperatures and velocities of each case will present onward. The abscissas of all plots are the flow path, which is the streamwise location of the flow, equaling zero at inlet and ending at outlet (chimney top).

Case 1: Experimental Set 1 when the height of entry roof is 0.5 m.

As Experimental Set 1 has the constant-diameter chimney and the roof height setting allows the roof of Experimental Set 1 to have uniform height all over, the results of this experimental set thus serves as reference values for the other experimental sets. It is noted that AR_{12} for this set is approximately 4.0. The results of the experiments are shown in Fig. 9.11.

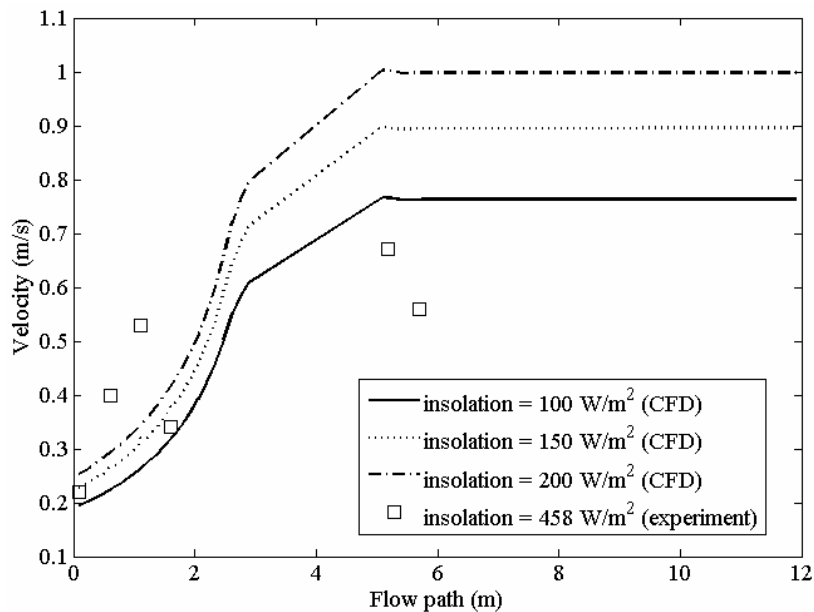
Numerical results indicate that velocity increases along flow path under the roof and remains constant in the chimney. It can be seen that the actual experimental values are very close and follow the numerical predictions. The temperature graph has the same characteristics.

However, it can be seen that the measured properties are very close to the values from numerical computations that correspond to lower sunlight intensities that actually measured. Some measured properties are different from those obtained from numerical computation when compared to values at other positions. For example, the measured results at the third position under the roof and both positions in the chimney are significantly different and can be explained as following:

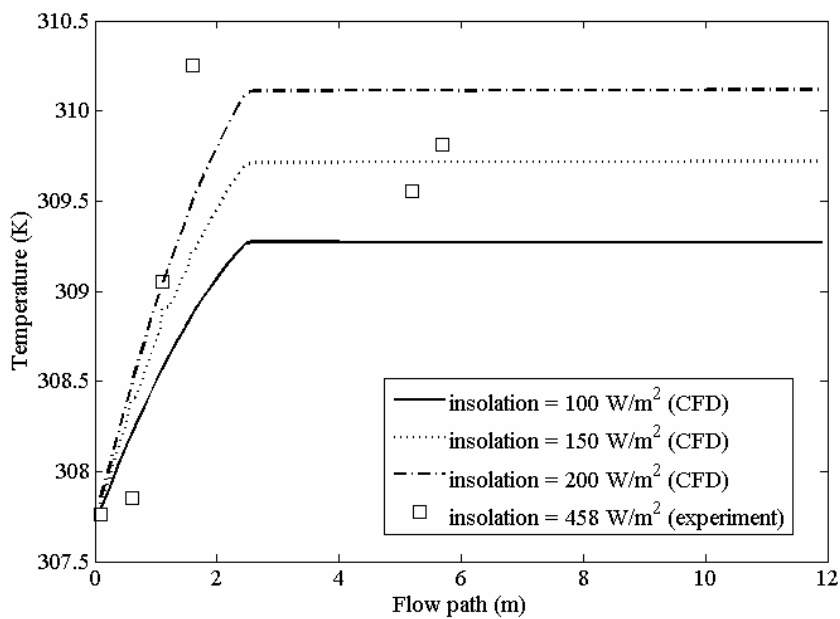
1. The numerical computation assumed that the sunlight, once entered, would not reflect. Along the flow line, it was assumed no heat loss from the walls. However in the actual experiment, some of the sunlight through the roof would be reflected. Some heat would be lost to the ground, as well as along the walls of the experimental

Table 9.3 Descriptions of the test cases.

Case	Model	Roof inlet	r_1 (m)	h_1 (m)	h_2 (m)	AR12	Chimney area	h_c (m)	r_2 (m)	r_3 (m)	AR43	Note
1	1	Fully opened	4	0.5	0.5	4	constant	8	1	1	1	A constant-height collector with a constant-area chimney (reference)
2	1	Fully opened	4	0.13	0.5	1.01	constant	8	1	1	1	Investigate the effect of AR12 = 1 on the system with a constant-area chimney
3	1	Fully opened	4	0.06	0.5	0.47	constant	8	1	1	1	Investigate the effect of AR12 = 0.5 on the system with a constant-area chimney
4	2	Fully opened	4	0.5	0.5	4	increasing with h_c	8	1	1.41	1.99	Investigate the effect of AR43 = 2 on the system with a constant-height collector
5	2	Fully opened	4	0.13	0.5	1.01	increasing with h_c	8	1	1.41	1.99	Investigate the effect of AR12 = 1 and AR43 = 2
6	2	Fully opened	4	0.06	0.5	0.47	increasing with h_c	8	1	1.41	1.99	Investigate the effect of AR12 = 0.5 and AR43 = 2
7	3	Partially opened	8.1	0.5	0.5	1	constant	8	1	1	1	Novel roof shape
8	4	Fully opened	1.68	0.25	0.25	3.36	constant	4	0.5	0.5	1	Inspect the dynamic similarity between cases 1 and 8
9	4	Fully opened	1.68	0.07	0.25	0.94	constant	4	0.5	0.5	1	Inspect the dynamic similarity between cases 2 and 9
10	4	Fully opened	1.68	0.04	0.25	0.54	constant	4	0.5	0.5	1	Inspect the dynamic similarity between cases 3 and 10



(a)



(b)

Figure 9.11 Airflow properties of experimental Case 1: (a) velocity distribution; (b) temperature distribution.

set. Thus the experimental values would correspond to numerical results assuming lower intensity of sunlight. In this case the values agreed most when sun heat flux of 200 W/m^2 was used.

2. The numerical computations did not take into account the wind outside the experimental set. The actual airflow speed inside the system was not too high compared to external wind speeds, even if the experiment had to wait for the wind outside to quiet and measurements were conducted numerous times to be averaged. However sometimes measurement in the presence of external wind speeds was unavoidable, such as after measurement of two positions, wind would occur. Waiting for the wind to subside to measure the third position may result in significant change of sunlight intensity due to clouds. These factors may have contributed to a deviation of experimental values from the numerical values expected.

3. Limitations of budget prohibited building an experimental set with a large roof compared to the diameter of the chimney. Actual construction found that the shadow of the chimney covered about an eighth of the roof as depicted in Fig. 9.12.

Numerical computation employed the presupposition that the air under the collector receives heat energy from the sun in a uniform manner, and that the pressure difference between the top of the chimney and the base of the chimney enables the air to flow from the outermost edge of the roof to the base of the chimney from all directions and subsequently rise past the top of the chimney. However in the experiment, since part of the roof did not receive sunlight along its radius, the direction of flow of some of the air current may have deviated from that dictated by hypotheses. This may be a cause that actual measurements in the chimney are different from the numerical values. Perhaps if there were more apertures for

measurement along the chimney circumference at each chimney height's measuring location to yield more measurements, the average value of such measurements may be more accurate.

Case 2: Experimental Set 1 when the height of entry roof is 0.13 m.

At such a roof height was found that AR_{12} has value of approximately 1.01. This case is a validation of previous theoretical work (Koonsrisuk and Chitsomboon, 2004), stating that if AR_{12} decreases, the potential of the system will increase. This potential is measured from the flow at the roof entry, $\frac{1}{2}\rho AV^3$, where ρ is air density, A is the flow cross sectional area and V is the flow velocity. Thus the increased potential of the Case 2 compared to Case 1 can be seen from the velocity at the roof entry point. If the velocity at the roof entry point increases from Case 1, it would imply that the system's potential has increased. Experimental results are displayed in Fig. 9.13a.

From numerical results, velocity at the roof entry point is high compared to the reference case (Experimental set 1 with 0.5 m height of the access roof). After that, the velocity decreases to a certain value and then increases until it remains constant in the chimney. The velocity decreasing and increasing in this manner is due to the change of the area under the roof: It is slightly larger than the chimney area at the roof entry point and then increases to a certain value and then decreases until it is the same as the size of the chimney entry point. Conservation of mass makes speed inversely proportional to flow cross sectional area. The cross sectional area varies in this manner because of construction. However the roof entry area being slightly larger than the chimney area is really due to the attempt to equalize the areas of the roof

entry and chimney inlet. However, due to the irrationality of 3.14159.... that is involved in the area of the circular chimney, and the roof entry is rectangular, it was not possible to exactly equalize the areas. The resulting design would have the roof entry point to be slightly larger in area than the chimney area, as seen from the fact that the speed at the roof entry point was slightly less than the speed in the chimney, agreeing with the predictions of the previous theoretical study.

The graph indicates that actual measured speeds tend to be close to numerical results, but less in value. This has been explained in Case 1. Computed and experimental temperatures have the same trend as Case 1 (Fig. 9.13b).

Case 3: Experimental Set 1 when the height of entry roof is 0.06 m.

When the access height is 0.06 meters, it was found that AR_{12} has value of 0.47. Case 3 is used to validate results following from Case 2, to see if AR_{12} is further decreased would result in further increase of potential. The results are displayed in the Fig. 9.14.

Numerical results indicate that the flow velocity in this Case 3 has a similar profile to Case 2, except that the velocity at the roof entrance is about twice as much of the speed in the chimney, a consequence of the design to have the roof entry area to be half of the cross sectional area of the chimney. Experimentally measured velocities tend to be as those predicted by numerical computation, but the velocity at the roof entry area is approximately equal to the speed in the chimney, probably due to the very low roof access point, with the position at the edge of the roof. The air flowing in may be turning from a higher position, while the equipment to measure speeds could only measure speeds in only one direction and thus could not measure rotating

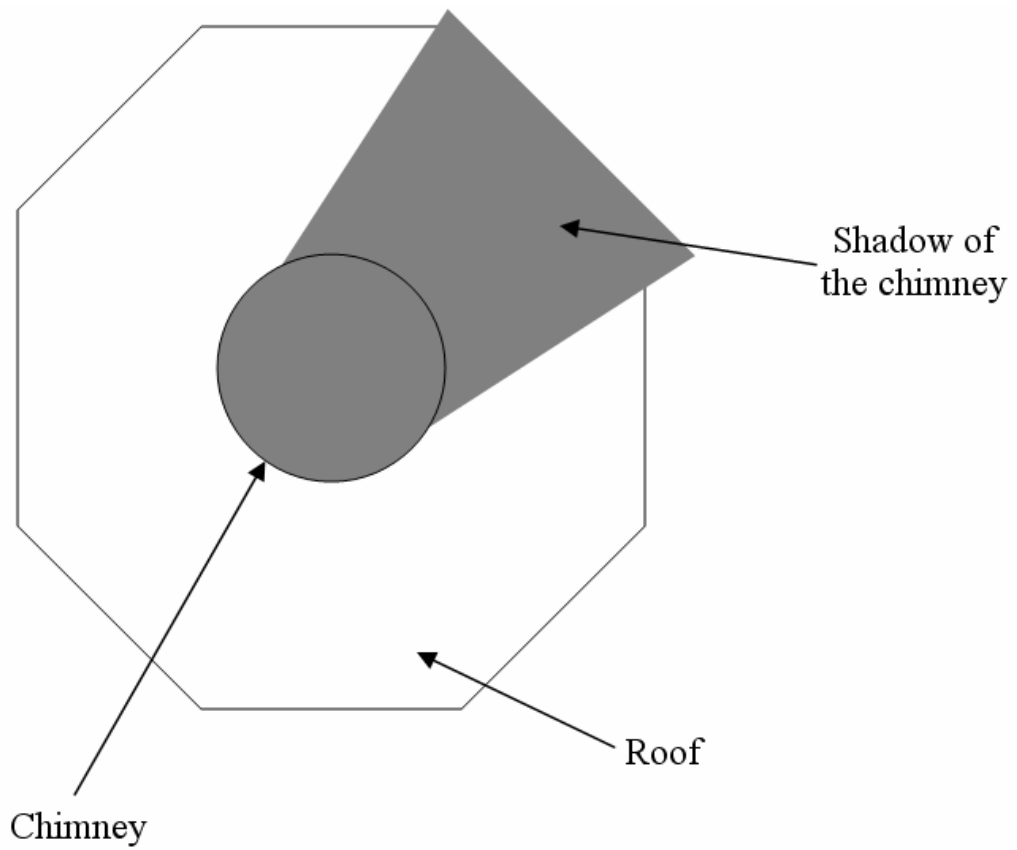
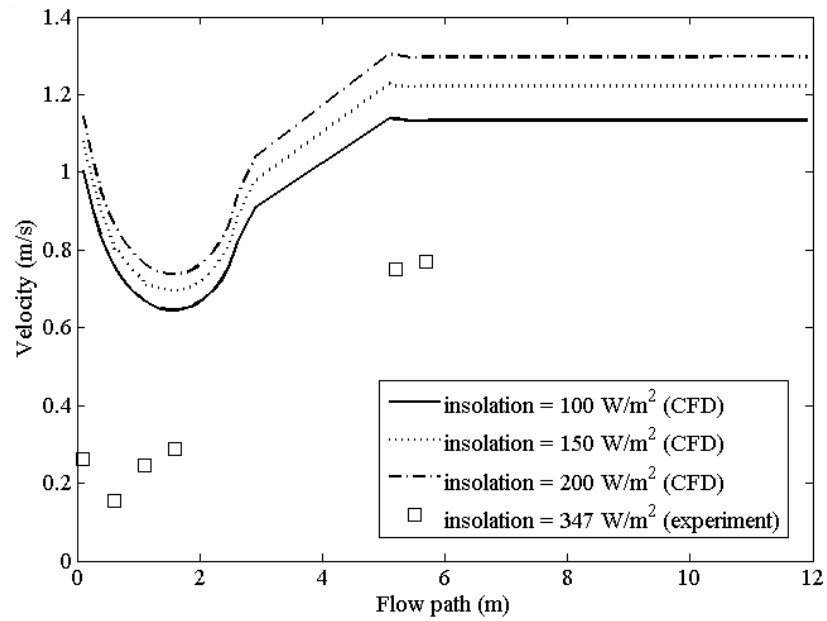
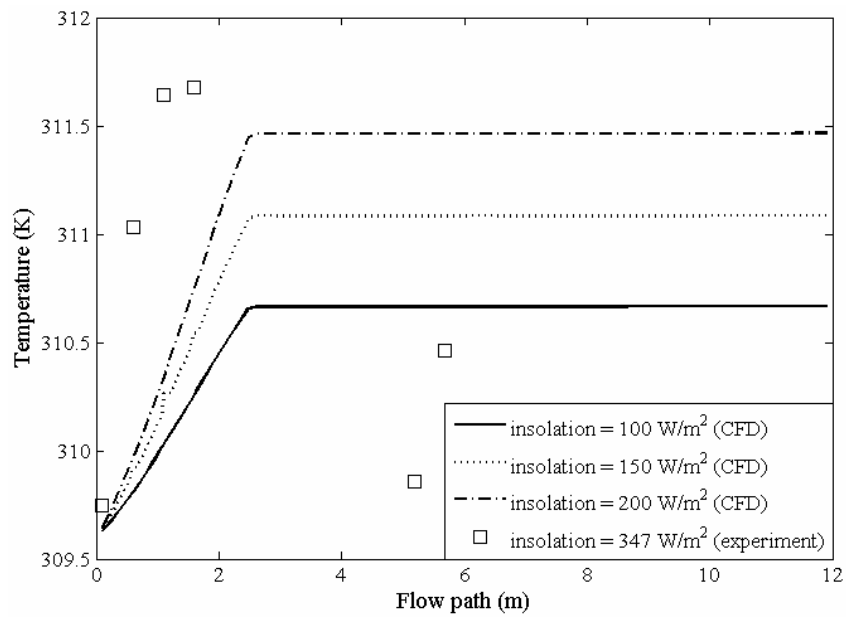


Figure 9.12 Illustration of the shadow of the chimney casting on the roof.



(a)



(b)

Figure 9.13 Airflow properties of experimental Case 2: (a) velocity distribution; (b) temperature distribution.

air speed correctly. Numerically predicted and experimental temperatures exhibit the same tendencies as in Case 1.

Case 4: Experimental Set 2 when the height of entry roof is 0.5 m.

As already stated in Case 1, the 0.5 meter height at access point is the height that allows the roof to be of uniform height all over. The second experiment set has the chimney diverging, with AR_{43} equal to 1.99. Case 4 is to observe results when the chimney diverges. Previous theoretical studies (Koonsrisuk and Chitsomboon, 2006) found the divergent chimney to have better potential than the straight chimney. This potential is measured from the flow power in the chimney, $\frac{1}{2}\rho AV^3$. Hence the increased potential in Case 4 compared to that of Case 1 can be seen from increased velocity in the chimney: if the velocity in the chimney increases, this means that the potential of the system has increased. Experimental results are displayed in Fig. 9.15.

Numerical results indicate an increase of air velocity at the flow path under the roof as in Case 1. Velocity at the base of the chimney in Case 4 is about 1.4 times of that of Case 1. The velocity then decreases until, at the chimney top, it is about the same as in Case 1. These profiles were as previous theoretical studies predicted.

The graph indicates that the measured velocities tend to be as the numerically computed velocities, but less in magnitude, a phenomenon already explained in Case 1. The numerically predicted and experimental temperatures have the same trends as in Case 1.

Case 5: Experimental Set 2 when the height of entry roof is 0.13 m.

This case is to test whether decreasing the ratio of areas of flow between roof inlet and roof outlet points as well as incorporating the divergent chimney would increase the potential of the system. Experimental results are displayed in Fig. 9.16.

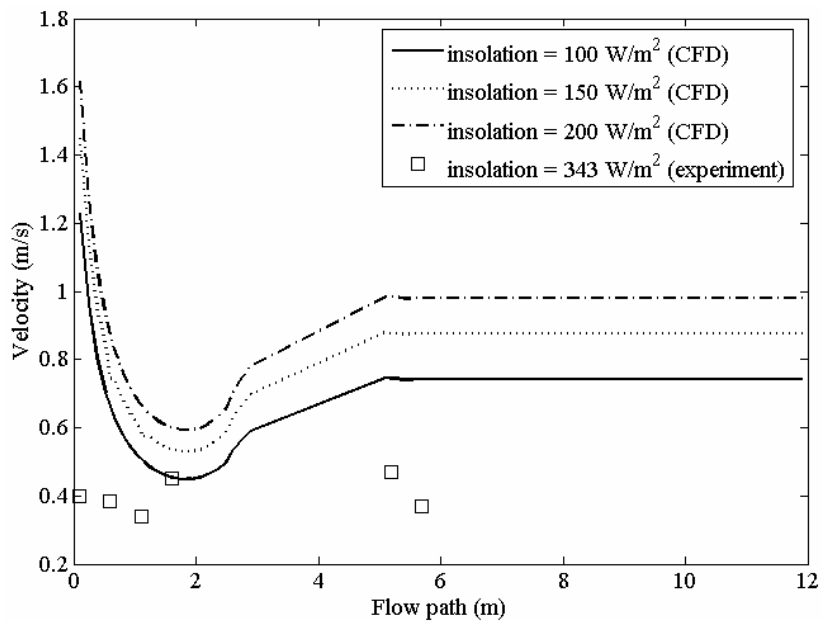
Numerical results indicate that the velocity graph is similar to joining the velocity under the roof of Case 2 with the velocity graph in the chimney in Case 4. It should be noted that the velocity at the roof entry point of Case 5 is slightly higher than that of Case 2, and that the speed in entry point of the chimney in Case 5 is slightly higher than that of Case 4 as well. This may be the result of slightly higher velocities in one part encouraging higher speeds in other parts. When the part under the roof drives the part in the chimney and the part in the chimney drives the part under the roof as well, the velocities become higher.

The graphs indicate that experimentally measured velocities have similar profiles to numerically predicted velocities, but are of less magnitude, a phenomenon explained in Case 1. Numerically predicted and experimentally measured temperatures exhibit the same tendencies as in Case 1.

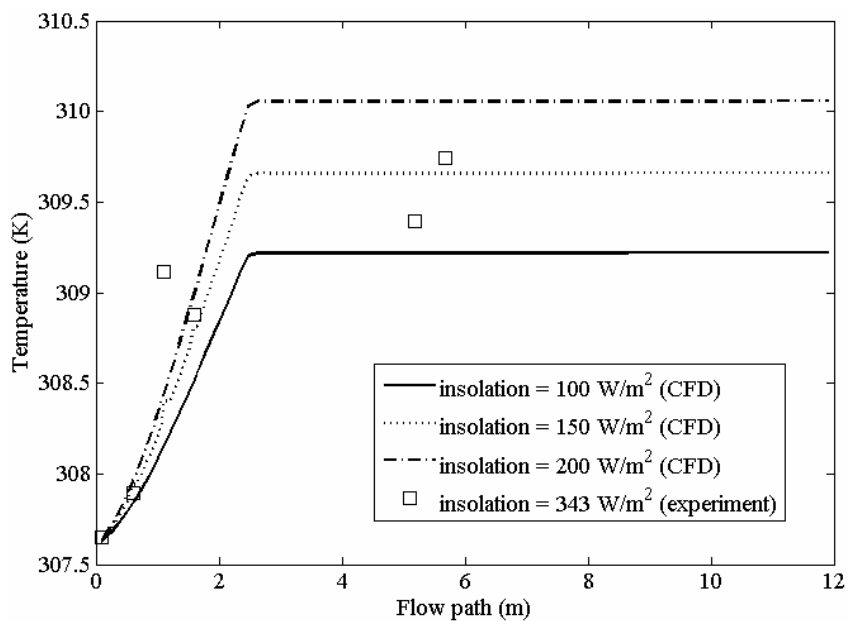
Case 6: Experimental Set 2 when the height of entry roof is 0.06 m.

Case 6 is used to follow up Case 5: if AR_{12} is further decreased, would the potential increase? The experimental results are displayed in the Fig. 9.17.

Numerical computations indicate that speeds in Case 6 are similar to that in Case 5: the speed graph is like joining the graph of the speed under the roof of Case 3 with the graph of the speed within the chimney of Case 4. The speed at the roof entry

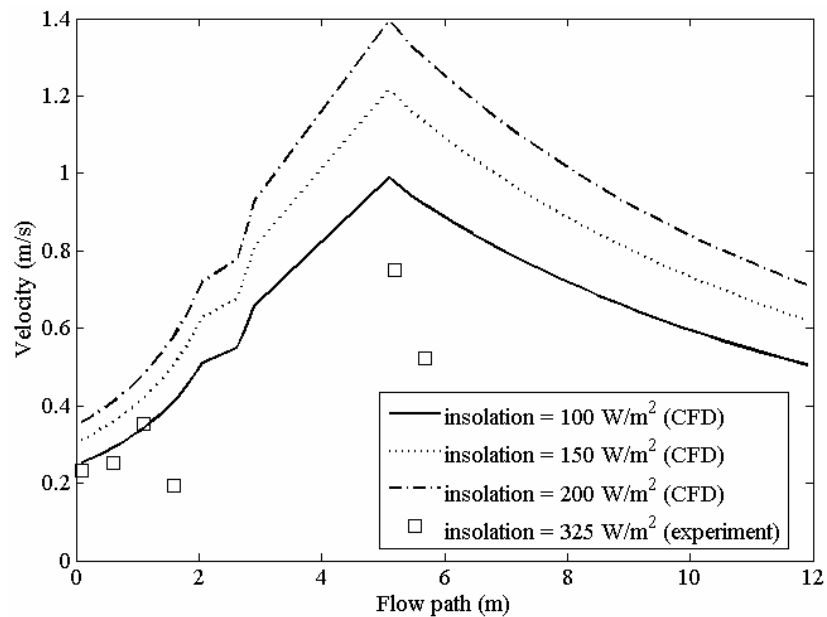


(a)

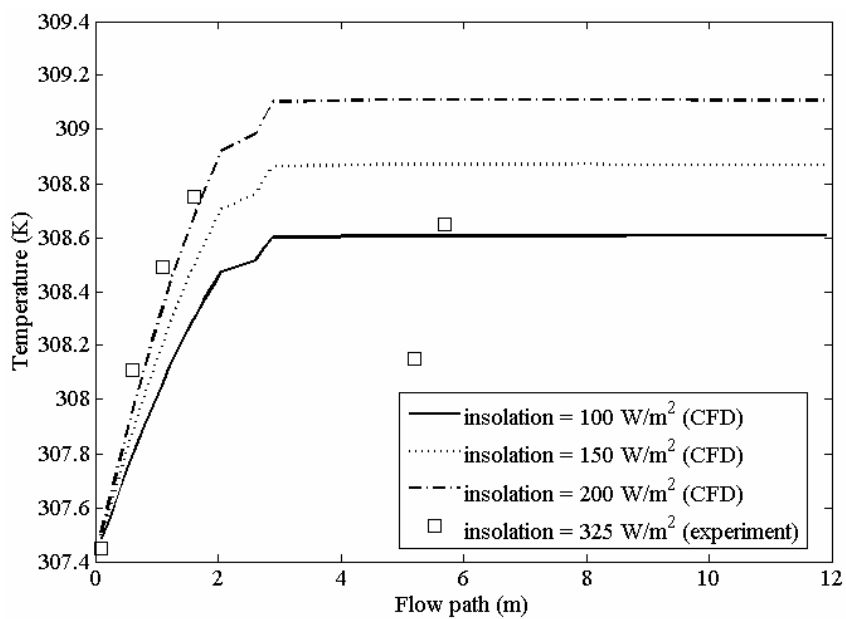


(b)

Figure 9.14 Airflow properties of experimental Case 3: (a) velocity distribution; (b) temperature distribution.

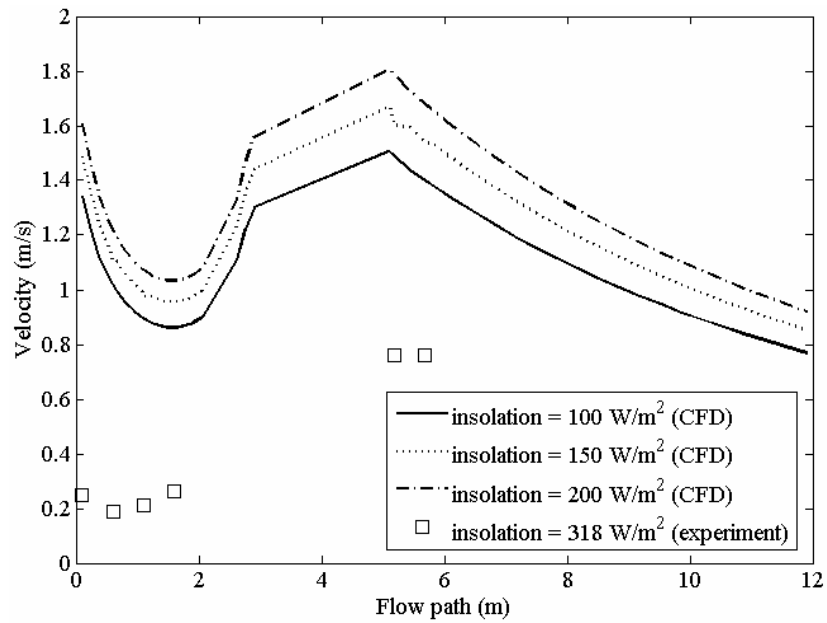


(a)

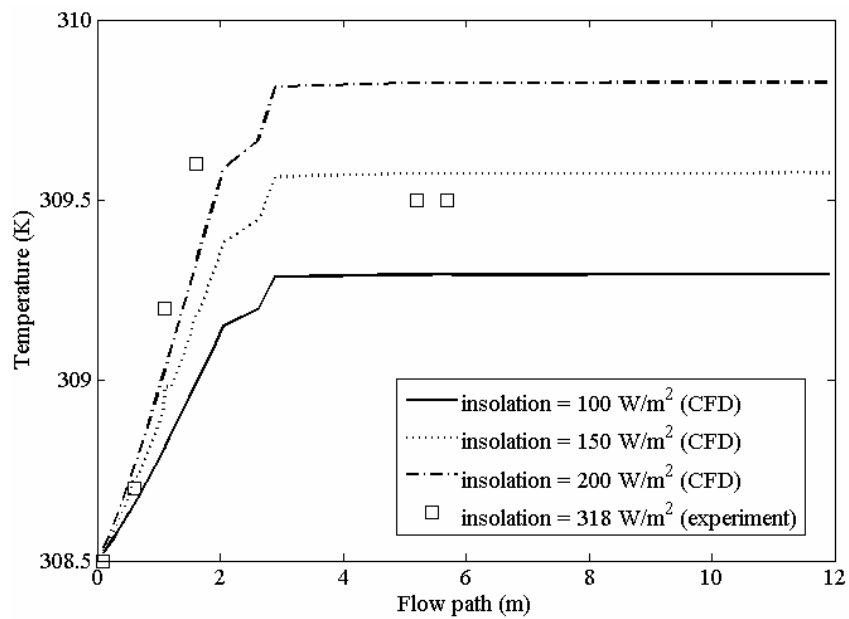


(b)

Figure 9.15 Airflow properties of experimental Case 4: (a) velocity distribution; (b) temperature distribution.

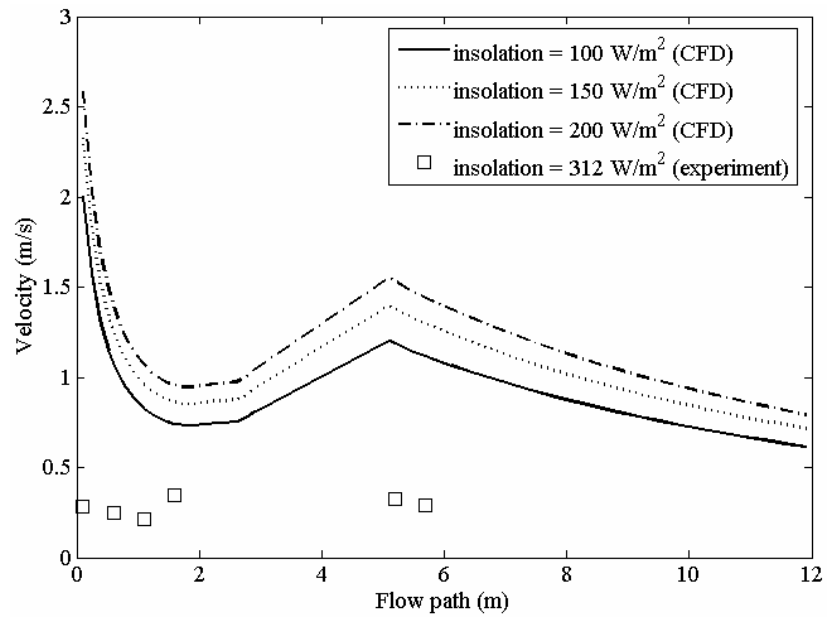


(a)

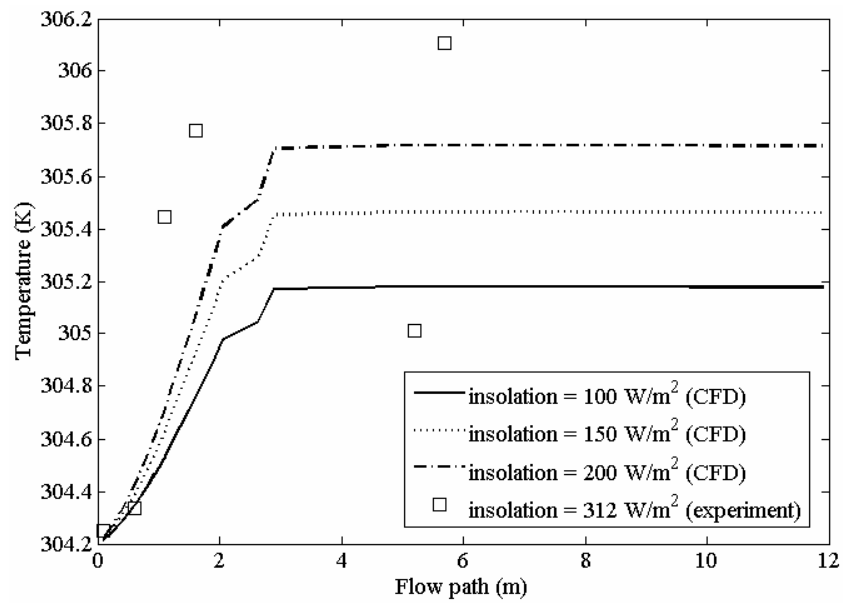


(b)

Figure 9.16 Airflow properties of experimental Case 5: (a) velocity distribution; (b) temperature distribution.



(a)



(b)

Figure 9.17 Airflow properties of experimental Case 6: (a) velocity distribution; (b) temperature distribution.

point of Case 6 is higher than that of Case 3, and the speed at the chimney access point in Case 6 is higher than that of Case 4, just as in Case 5, which may result from the mutual driving of speeds as explained in Case 5.

The graph indicates that actual measured velocities tend to be similar to those predicted by numerical computations, but lesser in magnitude. This phenomenon was explained in Case 1. The temperatures obtained from computation and experimental measurement exhibit the same trend as in Case 1.

Pairing Case 1 with Case 4, Case 2 with Case 5, and Case 3 with Case 6, it was found that the velocities at the roof entry points of each pair were very close: Pair 1 had a value of 0.2 m/s, Pair 2 had a value of 0.25 m/s, and Pair 3 had a value of about 0.3 – 0.4 m/s. Pair 1's value agreed very closely with numerical computations, while Pairs 2 and 3's values were lower than numerically computed values. Possible causes are:

1. Pair 1 consists of uniformly constant height of roof. The air flow under the roof should be parallel to the roof at all times. Thus the velocity measured under the roof would agree very closely with numerical predictions. Discrepancies at some points under the roof and in the chimney may have arisen from causes analyzed in No. 2 and 3 of Case 1.

2. Pairs 2 and 3 have smaller roof entry points and the roof makes an angle to the land, which may cause some parts of the air current to turn from outside and the direction of the air current from the roof's edge to the chimney is divergent according to the Law of Conservation of Mass. Since the speed measurement equipment for the experiment was effective in only one direction, and that direction was parallel to the

ground (as in Fig. 9.18), the measured velocity may have been less than the actual velocity.

As the measured velocity was less than the actual velocity, it is natural to ask if this measured velocity could be used for analysis. If we consider velocity to be a vector, which can be decomposed into three components perpendicular to each other, use of cylindrical coordinates requires us to have an axial direction along the chimney's axis; the second would be the radial direction of the chimney and the third would be the circumferential direction of the chimney. When considering the experimental flow conditions, it was found that the principle direction of flow under the roof was towards the chimney parallel to the ground, implying the negligibility of the circumferential component. The axial component's magnitude on the other hand would vary according to the degree of turning. However, the velocity in the chimney's axial direction would surely be less than the radial component, the principal direction. Thus it can be said that even though the measured velocity is less than the actual velocity, the trend of their magnitudes should correspond with actual conditions.

Cases 1–6's numerical results can be summarized as in Table 9.4. Table 9.4 indicates that decreasing AR_{12} increases wind energy potential. Increasing AR_{43} can increase wind energy potential as well. In the experimental set that decreased AR_{12} as well as increased AR_{43} , higher potential at the roof access point was obtained than just decreasing AR_{12} alone by an equal amount. Potential at the chimney base was also higher than the system that increased AR_{43} alone by an equal amount. However, even when decreasing AR_{12} helped increase potential, but continual decrease found that the height of the entry roof corresponding to the highest potential that could be

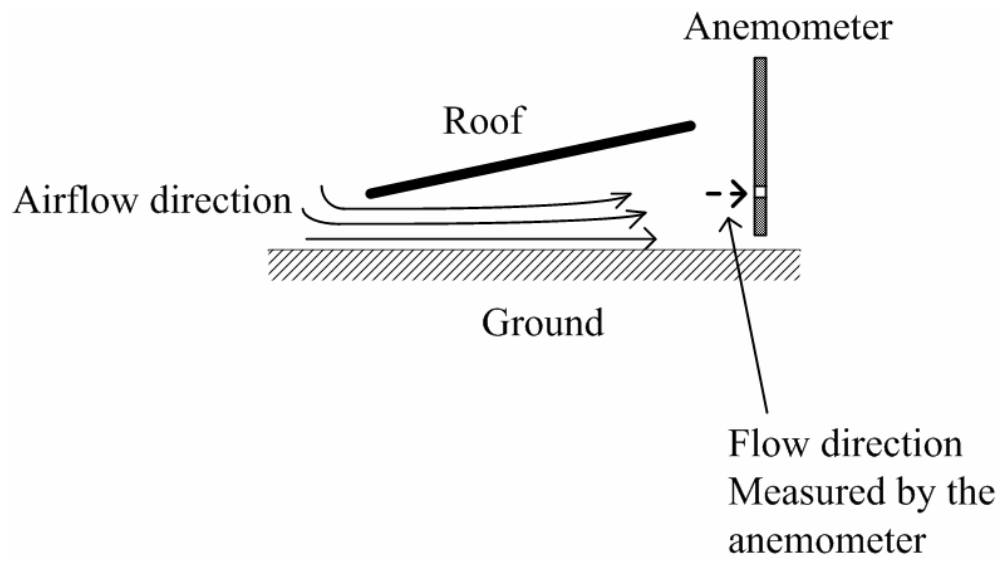


Figure 9.18 Illustration of the flow direction under the sloping roof.

Table 9.4 Power of the test cases scaled by the power of its reference case.

Case	Area ratio	Reference case	Area ratio of reference case	Power scaled by power of reference case						Position offers highest power
				At roof inlet			At chimney inlet			
				$q'' = 100$	$q'' = 150$	$q'' = 200$	$q'' = 100$	$q'' = 150$	$q'' = 200$	
2	AR12=1.01; AR43=1	1	AR12=4; AR43=1	26.54	22.48	20.38	2.21	1.86	1.69	in chimney
3	AR12=0.47; AR43=1	1	AR12=4; AR43=1	39.71	40.32	40.61	0.94	0.96	0.96	roof inlet
5	AR12=1.01; AR43=1.99	4	AR12=4; AR43=1.99	27.87	22.71	20.21	2.32	1.88	1.68	chimney base
6	AR12=0.47; AR43=1.99	4	AR12=4; AR43=1.99	62.07	55.64	52.30	1.47	1.32	1.24	roof inlet
4	AR12=4; AR43=1.99	1	AR12=4; AR43=1	1.70	1.88	1.98	1.66	1.83	1.93	chimney base
5	AR12=1.01; AR43=1.99	1	AR12=4; AR43=1	47.45	42.58	40.06	3.85	3.45	3.24	chimney base
6	AR12=0.47; AR43=1.99	1	AR12=4; AR43=1	105.70	104.33	103.64	2.45	2.41	2.39	roof inlet

obtained was too low to install turbines for production of electric energy at that point. It was thus proposed the roof as in Experimental Set 3, with partial apertures for air to enter the collector, and not opened all around as in the regular models. Even if AR_{12} were decreased, such apertures would be of sufficient size for turbine installation.

This case tests the possibility of changing the roof configuration from the standard model, the roof open all around, as used in Experiment Sets 1, 2 and 4, to be a partially accessible roof (details of apertures is depicted in Fig. 9.4). Cases 2 and 3 indicate that the smaller the roof access, the more the potential of the roof entry system. The limitation of this type of roof is that the smaller the entry points, the lower the entry roof, making actual construction and utilization very difficult. The roof of Experiment Set 3 controls the width and length of the apertures to be uniform, so that even if the accessibility sizes are decreased, the apertures are of sufficient size as to not be an obstacle to construction and actual use. Moreover, as the potential at

Case 7: Experiment set 3

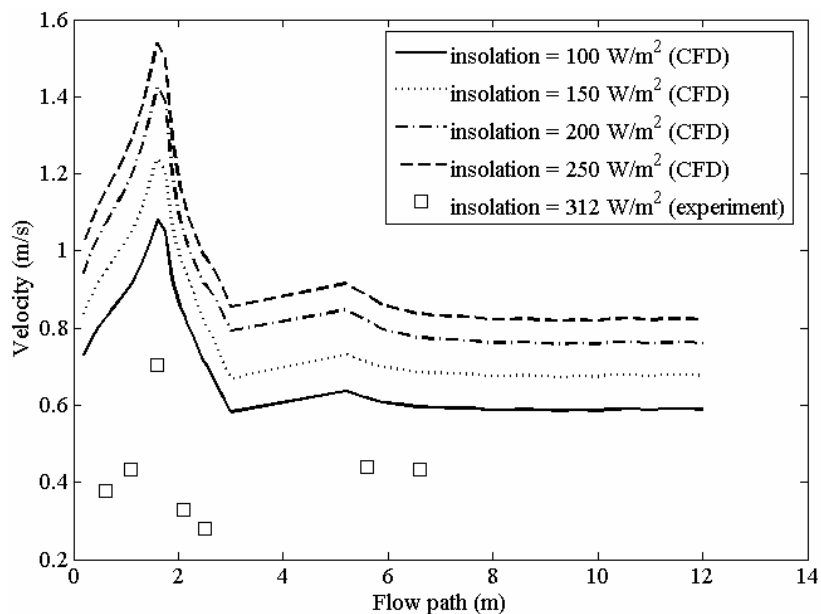
This case tests the possibility of changing the roof configuration from the standard model, the roof open all around, as used in Experiment Sets 1, 2 and 4, to be a partially accessible roof (details of apertures is depicted in Figure 4). Cases 2 and 3 indicate that the smaller the roof access, the more the potential of the roof entry system. The limitation of this type of roof is that the smaller the entry points, the lower the entry roof, making actual construction and utilization very difficult. The roof of Experiment Set 3 controls the width and length of the apertures to be uniform, so that even if the accessibility sizes are decreased, the apertures are of sufficient size as to not be an obstacle to construction and actual use. Moreover, as the potential at the roof entry points increases as the size of the apertures of the roof seem to be of

sufficient size, the idea arose to install the turbines at the apertures, which would be convenient to install and maintain, especially if this system is many hundred meters in size, the subject of future studies.

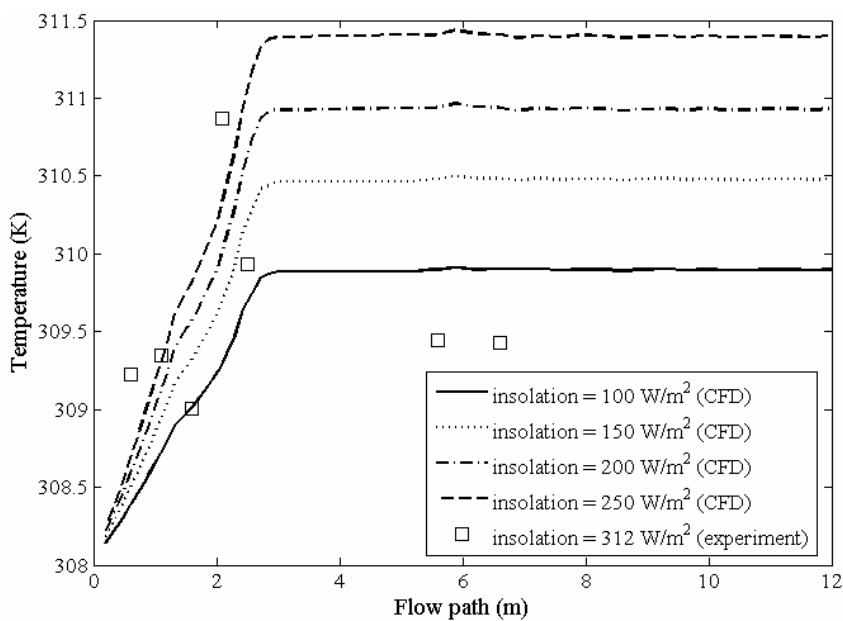
Design of Experiment Set 3 involved computation so that its sunlight receiving area would be near in size to that of Sets 1 and 2. (Note that the design, from an upper point of view, shows a different shape of the roof from Sets 1 and 2). It was determined that the total area of the apertures of Set 3 be close to the area of the cross section of the chimney (why the areas would not exactly match is in the discussion of Case 2): that is, the ratio of the area of the roof entry apertures to the area of the cross section of the chimney be approximately equal to 1. Theoretical studies indicate that the potential of this case at the roof access points and in the chimney would be close in size to that of Case 2. The experimental results are displayed in Fig. 9.19.

Numerical computations indicate that velocities at the roof entry points are very close to those of Case 2. After that, the velocities would increase to a certain value and then decrease to a constant value in the chimney. The velocity in the chimney is very close in value to that of Case 1, so that it can be said that theoretical predictions concerning potentials at the roof entry points and chimney entry points are quite accurate. However, it can be seen that the maximum velocity occurs at about half of the flow route in the chimney. The cause of such behavior should be the shape of the roof, readily explained as follows.

Fig. 9.20 displays a view of Experimental Set 3, viewed from above. The circle is the chimney and the octagon is the boundary of the roof, with four apertures as in the figure, and the remaining being closed walls. The cross sectional area of the roof



(a)



(b)

Figure 9.19 Airflow properties of experimental Case 7: (a) velocity distribution; (b) temperature distribution.

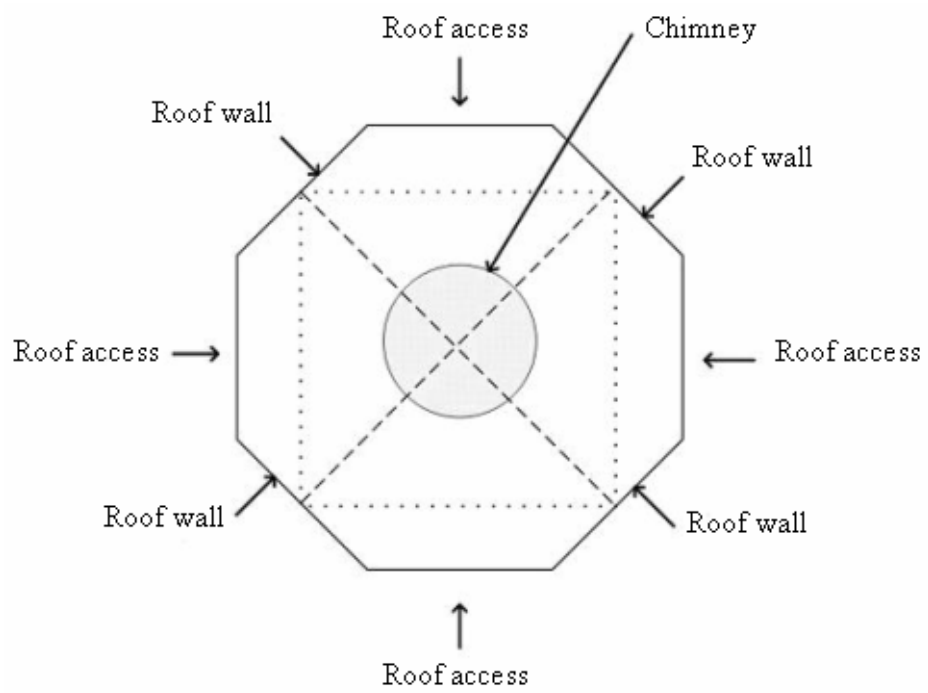
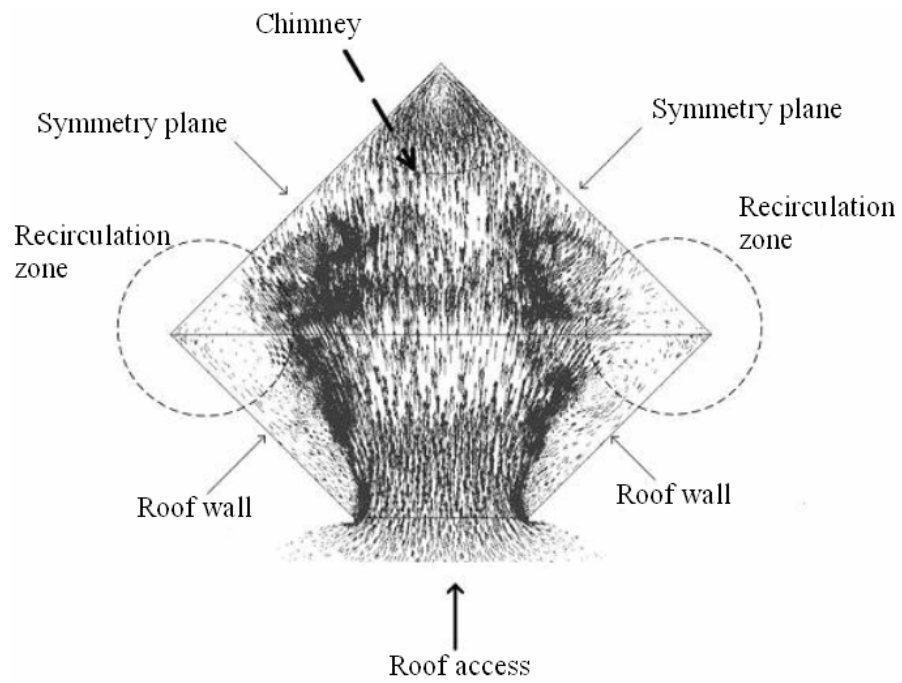


Figure 9.20 Illustration of the roof access system of Experiment Set 3.

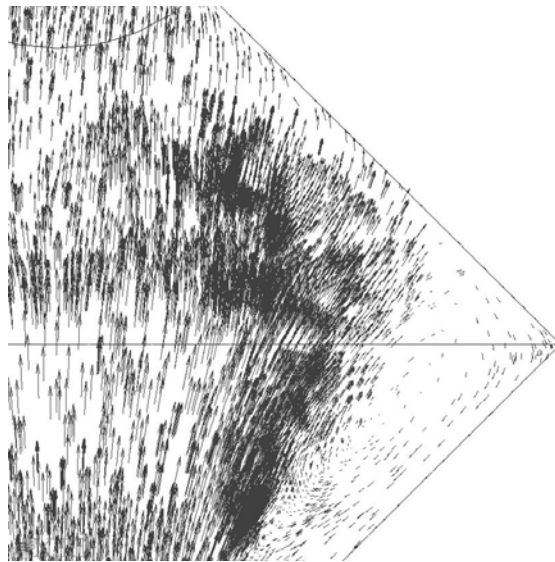
access apertures was designed to equal to the cross sectional area as showed by dotted lines, and the sum of the areas of the apertures of all four sides was designed to equal to the chimney cross sectional area. All this was to control the velocities that occurred. The broken diagonal lines indicate symmetry lines within the system, since numerical computations indicated that flow within Experimental Set 3, the air current divides into four parts via the four apertures of the roof according to the broken lines. The air currents then flow to combine in the chimney according to the Fig. 9.21a, which shows a part of the velocity vectors of flow under the roof. This part will join with other parts of the roof at the “symmetrical plane” in the picture. The other three parts have the same types of velocity vectors as in this figure. The figure shows that there is a turbulent area, indicated by broken line circles. Fig. 9.21b is a magnification of the recirculation zones.

Recirculation causes the flow cross sectional area to be less than it should be, so that velocities in this area are higher than the velocities at the roof entry points, even after designing them to have equal cross sectional areas. Thus improvement of shape is required for the position of highest velocity to be at the roof entry point or at the chimney entry point.

The graph indicates that actual measured speeds tend to be similar to those predicted by numerical computations, but lesser in magnitude. This phenomenon was explained in Case 1. The temperatures obtained from computation and experimental measurement exhibit the same trend as in Case 1.



(a)



(b)

Figure 9.21 (a) velocity vectors of flow under the roof of Experiment Set 3;

(b) magnification of the recirculation zone.

Case 8: Experimental Set 4 when the height of entry roof is 0.25 m.

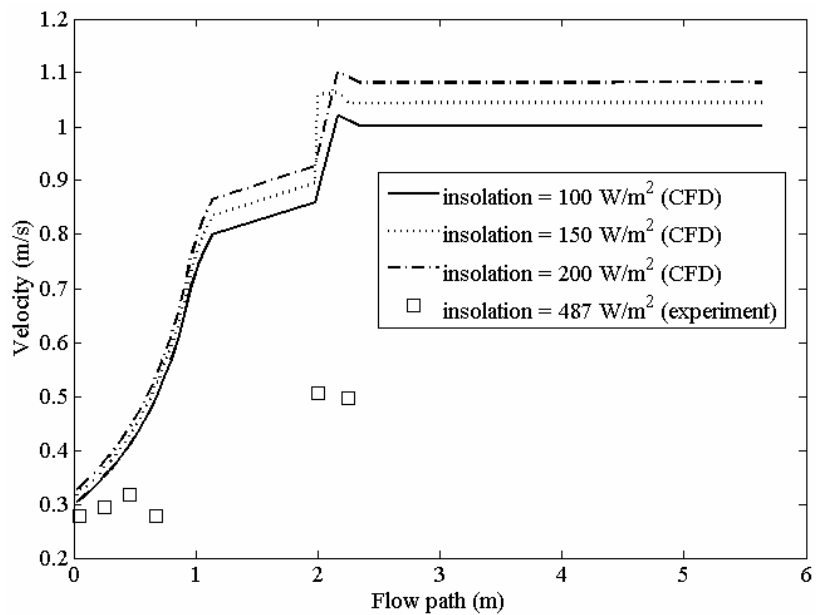
Experiment Set 4 was designed to test previous theoretical studies (Koonsrisuk and Chitsomboon, 2009) which predicted that two solar chimneys of different size under identical atmospheric conditions, receiving the same solar energy, may be constructed to achieve dynamic similarity through partial geometric similarity, under the following equations:

$$\frac{\frac{1}{2}\dot{m}V^2}{\rho h_c^{\frac{7}{2}}g^{\frac{3}{2}}} = f^n \left(\frac{q''A_r\beta}{\rho c_p h_c^{\frac{5}{2}}g^{\frac{1}{2}}} \right), \quad (9.3)$$

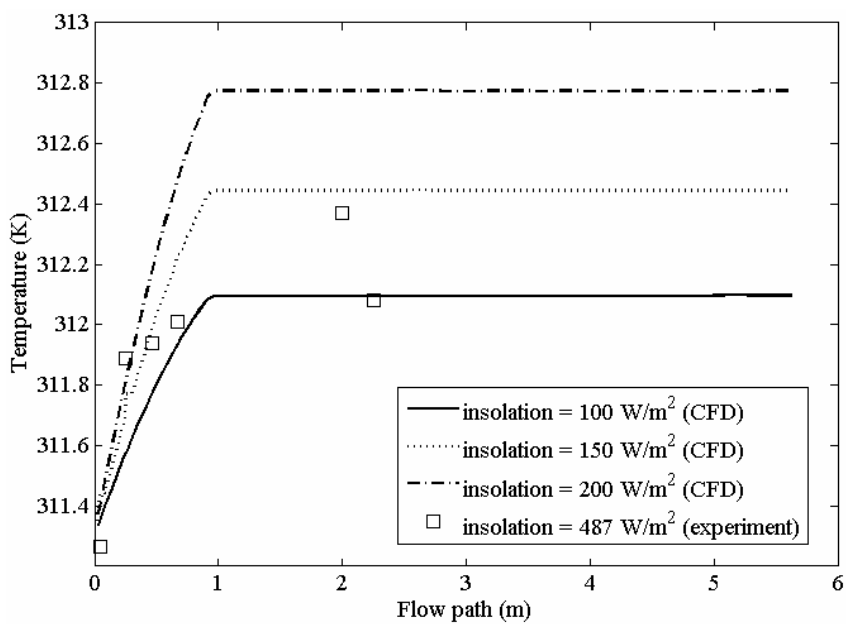
designating $\frac{1}{2}\dot{m}V^2 / \rho h_c^{7/2} g^{3/2}$ to be Π_1 and $q''A_r\beta / \rho c_p h_c^{5/2} g^{1/2}$ to be Π_2 .

The theory from the aforementioned work was used in designing Experiment Set 4: let every part be half the size of Experiment Set 1, except for the roof, which would be 0.42 of Experimental Set 1 (Koonsrisuk and Chitsomboon, 2009). If one performs Experiment Sets 1 and 4 under identical atmospheric conditions and solar heat fluxes, it would be found that Π_2 of both Experiment Sets were equal, and if both Experiment Sets achieve dynamic similarity, it would be found that Π_1 of both would be the same as well. Experimental results are as depicted in Fig. 9.22.

The graph indicates that actual measured velocities tend to be similar to those predicted by numerical computations, but lesser in magnitude. This phenomenon was explained in Case 1. The temperatures obtained from computation and experimental measurement exhibit the same trend as in Case 1.

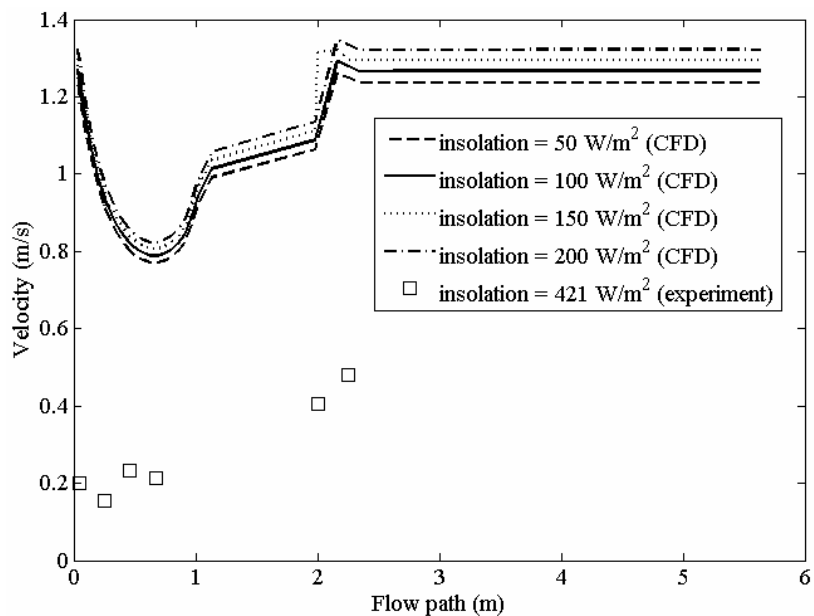


(a)

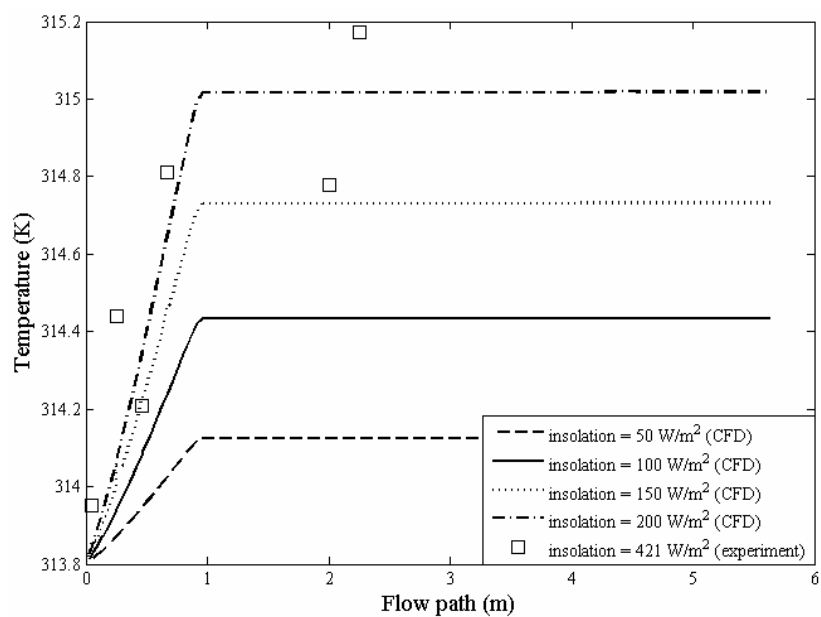


(b)

Figure 9.22 Airflow properties of experimental Case 8: (a) velocity distribution; (b) temperature distribution.

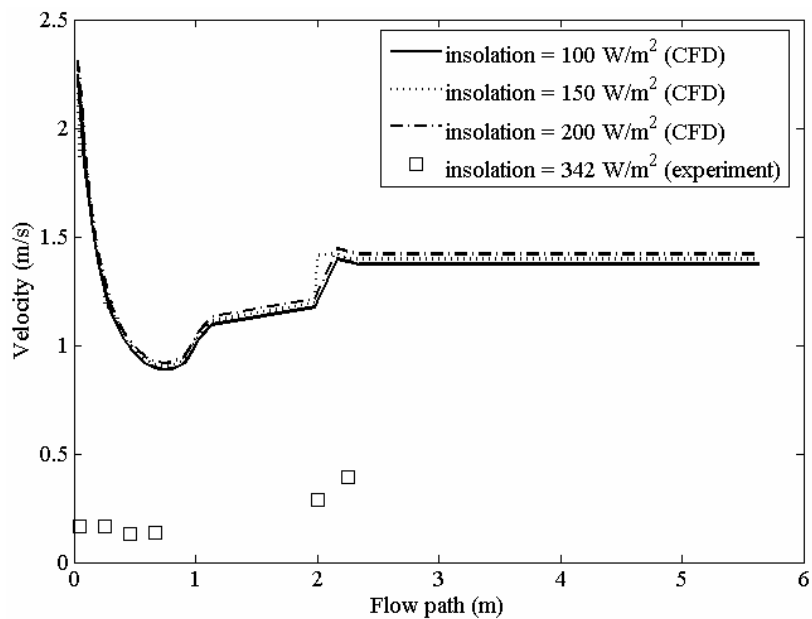


(a)

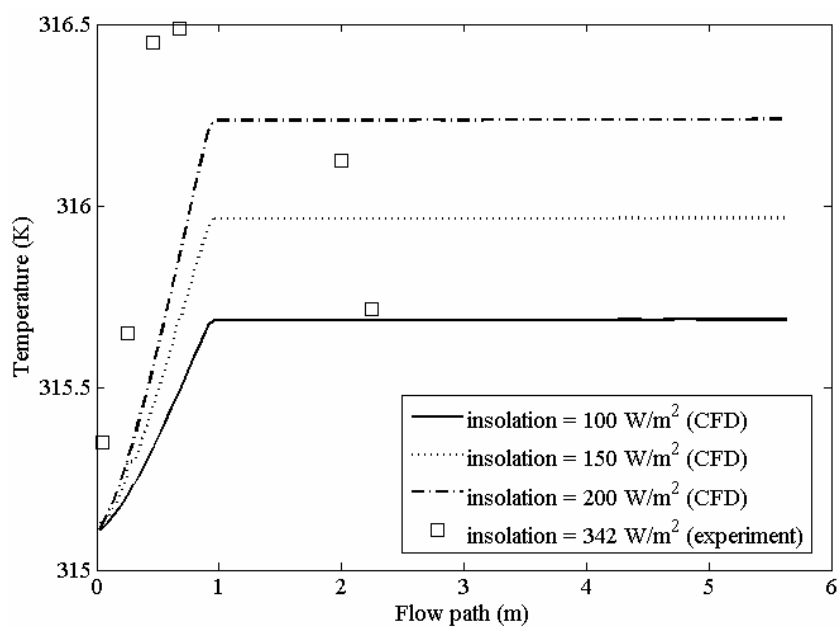


(b)

Figure 9.23 Airflow properties of experimental Case 9: (a) velocity distribution; (b) temperature distribution.



(a)



(b)

Figure 9.24 Airflow properties of experimental Case 10: (a) velocity distribution; (b) temperature distribution.

Table 9.5 Comparative data for dimensional analysis.

Pair	Case	Roof inlet temperature (K)	Solar heat flux (W/m²)	Π_2	Π_1
1	1	307.7	458	1.06E-05	1.06E-05
	8	311.3	487	9.82E-05	1.29E-05
2	2	309.6	347	8.06E-06	1.49E-05
	9	313.8	421	8.49E-05	6.59E-06
3	3	307.6	343	7.96E-06	3.67E-06
	10	315.1	342	6.89E-05	2.39E-06

Note: Entry point temperature points and solar heat fluxes are actual measurements, while the values of Π_1 and Π_2 are from calculation at Position 1 in the chimney.

Case 9: Experimental Set 4 when the height of entry roof was 0.07 m.

Case 9 can be used to check out the effect of AR_{12} , by comparing the results with Case 8 to see if the results are as in the comparison of Case 2 with Case 1. Thus Case 9 can be used to compare dynamic similarity with Case 2. Experimental results are displayed in Fig. 9.23.

The graph indicates that actual measured velocities tend to be similar to those predicted by numerical computations, but lesser in magnitude. This phenomenon was explained in Case 1. The temperatures obtained from computation and experimental measurement exhibit the same trend as in Case 1.

Case 10: Experiment Set 4 when the height of the entry roof is 0.04 meters.

Case 10 can be used to inspect the effect of AR_{12} , by comparing the results with Case 8 to see if the results are as in the comparison of Case 3 with Case 1. Thus Case 10 can be used to compare dynamic similarity with Case 2. Experimental results are displayed in Fig. 9.24.

The graph indicates that actual measured speeds tend to be similar to those predicted by numerical computations, but lesser in magnitude. This phenomenon was explained in Case 1. The temperatures obtained from computation and experimental measurement exhibit the same trend as in Case 1.

Entry point temperature values, average of solar heat fluxes, values of Π_1 and Π_2 , obtained from Cases 1, 2, 3, 8, 9 and 10 are displayed in Table 9.5. The table indicates that only the Π_1 in the first pair are close in value, and differ a little in the third pair. The Π_1 in the second pair however differ by 3 times, which should be consequence of different atmospheric conditions and sunlight intensities, indicated by

the differing Π_2 values of each pair. If numerical results are used by inputting actual atmospheric condition and solar heat flux values, the values of Π_1 and Π_2 of each pair would differ as well, but if the same values for atmospheric conditions and solar heat fluxes are used for each pair, it was found that the computed values of Π_1 and Π_2 of each pair are equal. The calculations were tested by experimenting at identical atmospheric conditions and solar heat fluxes, a very difficult feat, considering that two experimental sets had to be performed simultaneously. However there was only one set of measuring equipment and the time to collect data for a particular experimental set was required to be quite long, hence the inability to collect data from Set 1 and then Set 4 immediately after.

Experiment Set 4 yielded the profile of the velocity graph as discussed in the section following Case 6: the measured velocity were not too far away from the computed values of Case 8, which was the case of the roof parallel to the ground. With Cases 9 and 10, with the roof forming an oblique angle to the ground, the measured velocities tended to be similar to the computed velocities, but different in magnitude.

9.7 CONCLUSION

1. Decreasing of the AR_{12} yielded higher potential of wind energy at the entry point of the roof.
2. Increasing AR_{43} yielded higher potential of wind energy at the entry point to the chimney.

3. It was found that decreasing AR_{12} in conjunction with increasing AR_{43} allowed higher potential at the roof access point to be obtained rather than just individually decreasing AR_{12} or increasing AR_{43} by an equal amount.

4. The energy potential in the chimney of Experimental Set 3 was close to that of Cases 1 and 2, while its energy potential at the roof entrance was larger. This leads to the idea of installing the turbines at the apertures, which would be convenient to install and maintain.

5. The experimental results differ comparatively but have the same trends as to the predicted values. This may follow from the fluctuating solar heat flux and the effect of the large chimney diameter when compared with the roof size.

6. The difference of dimensionless variables between the large and the small plant is noticeable, contrary to the theoretical and numerical predictions. Reasons could be the varying atmospheric conditions when the tests were run.

9.8 PROBLEMS AND CHALLENGES IN THE RESEARCH

1. When studying the theory, it was found that there were a variety of directives in designs which needed to be tested experimentally, requiring an amendment to the budget request from the Thailand Research Fund (TRF). Once approved by the TRF, it was then the rainy season, causing further delays in the construction. Construction was completed at the end of the rainy season and beginning of winter, so the weather was unpredictable and rendered further obstacles in collecting data to compare to mathematical models. The mathematical models assumed constancy of the intensity of sunlight and no influence from outside wind currents, while the actual experimental atmospheric conditions varied with heavy

clouds leading to variable sunlight intensity and occasional winds in each day, rendering experimentation very difficult.

2. Due to the small size of the chimneys, in the design phase, it was found that the air flow velocity was larger than the actual atmospheric conditions. Actual experiments found that the flow velocity that occurred inside the chimney was just slightly higher than the external wind velocities, so that during experimentation, it was found that external winds had a noticeable effect on the wind currents inside the system. This problem persisted even in the summer, and would readily be rectifiable if a sufficiently large chimney could be built that would house internal air flow with many times the speed of that of the external winds.

9.9 REFERENCE

ANSYS, Inc. **ANSYS CFX**, Release 10.0: reference guide. ANSYS, 2005.

Koonsrisuk, A, Chitsomboon, T., 2004. The effect of roof height to the flow in solar chimney. In: **Proceedings of the RGJ-Ph.D. Congress V**. Chon Buri, Thailand.

Koonsrisuk, A., Chitsomboon, T., 2006. Effect of Tower Area Change on the Potential of Solar Tower. In: **Proceedings of the 2nd Joint International Conference on Sustainable Energy and Environment**, Bangkok, Thailand.

Koonsrisuk, A., Chitsomboon, T., 2007. Dynamic similarity in solar chimney modeling. **Solar Energy**, Vol. 81(12), pp. 1439-1446.

Koonsrisuk, A., Chitsomboon, T., 2009. Partial geometric similarity for solar chimney power plant modeling. **Solar Energy**, Vol. 83, pp. 1611-1618.

CHAPTER X

CONSTRUCTAL SOLAR CHIMNEY CONFIGURATION AND MULTI-SIZE DISTRIBUTION ON LAND

10.1 ABSTRACT

In this study the constructal-theory search for the geometry of a solar chimney is reported. The objective is to increase the power production over the area occupied by the plant. The optimal height/radius, maximum mass flow rate and maximum power under the constraints of a fixed area and volume are determined. The power generated per unit of land area is proportional to the length scale of the power plant. A more detailed mathematical model shows that the simple model proposed here may be useful in the initial estimation of plant performance. Pressure losses in terms of the dimensionless length scale of the system are illustrated graphically. Results indicate that the pressure drop at the collector inlet and at the transition section between the collector and chimney are negligible and the friction loss in the collector might be neglected when the svelteness [cf. Eq.10.39] is greater than 6.5. Because of the flow resistances associated with distributing the power over a territory, the size of the territory must be finite and optimally allocated to each power plant. Several patterns of the multi-scale plants on a square area are explored. The finding has strong intuitive appeal; the global performance of different patterns could be equated with lower compactness [cf. Eq. 10.56] for the design with larger plants, which are able to economize on extracting power from an available land area.

10.2 INTRODUCTION

The solar chimney is a power plant that uses (1) solar radiation to raise the temperature of the air, and (2) buoyancy to accelerate the air flowing through the system. The main features of the solar chimney are sketched in Fig. 10.1. Air is heated as a result of the greenhouse effect under a transparent roof (the collector). Because the roof is open around its periphery, the buoyancy of the fall air column draws a continuous flow from the roof perimeter into the chimney. A turbine is set in the path of the air current to convert the kinetic energy of the flowing air into electricity.

In 1981, a solar chimney prototype of 50 kW, with the chimney height and roof diameter nominally at 200 m, was built in Manzanares, Spain. The plant operated from 1982 to 1989, and was connected to the local power network between 1986 and 1989 (Schlaich, 1995). This project demonstrated the viability and reliability of the solar chimney concept. Since then, numerous investigations to predict the flow in solar chimneys have been conducted. Generally, it was found that the electricity yielded by a solar chimney is in proportion with the intensity of global solar radiation, collector area and chimney height. Based on a mathematical model, Schlaich (1995) reported that optimal dimensions for a solar chimney do not exist. However, if construction costs are taken into account, thermoeconomically optimal plant configurations may be established for individual sites. It was shown numerically in Pretorius and Kröger (2006) that plant power production is a function of the collector roof shape and inlet height. Maia *et al.* (2008) carried out a simulation study and found that the height and diameter of the chimney are the most important geometric dimensions for solar chimney design. Zhou *et al.* (2009) reported the maximum chimney height in order to

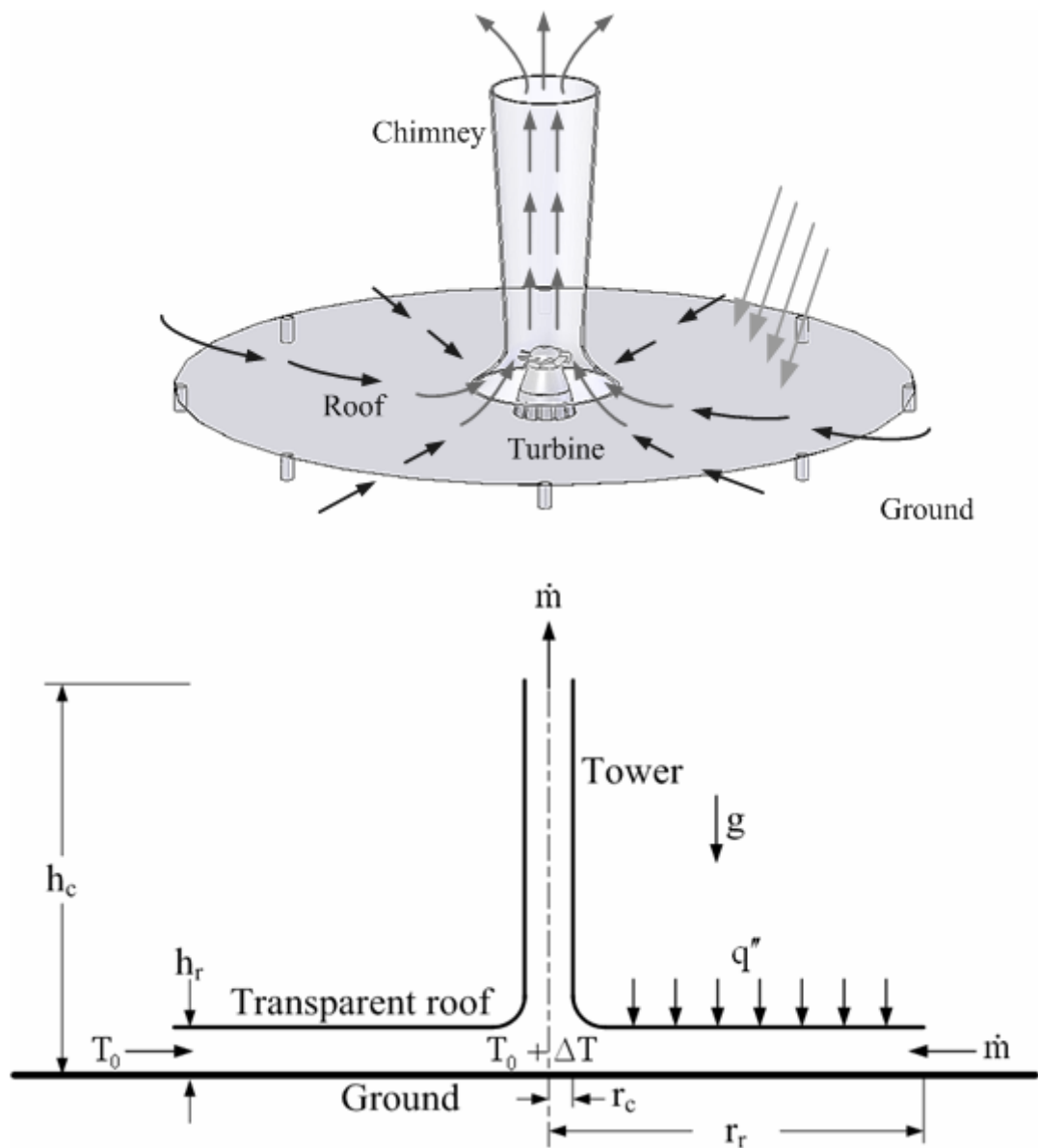


Figure 10.1 The main features of a solar chimney.

avoid negative buoyancy, and the optimal chimney height for maximum power output. They found that the maximum height and the optimal height increase with collector radius. A common feature in these findings is that the plant efficiency is very low, and that it increases with the plant size.

Consequently only large-scale plants, in which the chimney heights are 1,000 m or more, were proposed in the literature. In the 1990s, a project in which a solar chimney power plant with the capacity of 100 MW was proposed for construction in Rajasthan, India, and was about to be implemented. Its collector had a radius of 1,800 m and a chimney height and diameter of 950 m and 115 m, respectively (Rohmann, 2000). However, the project was cancelled owing to the potential danger of nuclear competition between India and Pakistan. The Australian government planned to build a 200 MW commercial plant with a chimney 1,000 m high. Recently, the plant was downsized to 50 MW and a 480 m-high chimney, in order to make it economically viable and eligible for government funding (EnviroMission, 2006). The construction and safety of a massive structure poses significant engineering challenges.

The work described in this paper is stimulated by the quest for better designs, and focuses on the generation of shape and structure by maximizing global performance of the flow system. It is based on the method of constructal design (Bejan and Lorente, 2008). This work shows that the configuration of the solar chimney can be determined, along with the scaling rules for being able to scale-up and scale-down the design.

10.3 GEOMETRY

The system geometry is simplified to that of a horizontal disc above the ground with a vertical cylinder in the center of the disc. The solar chimney configuration has the four dimensions shown in Fig. 10.1: r_c , h_c , r_r and h_r . We assume that the flow is fully developed and turbulent in all the flow passages, and that the friction factors in the vertical tube (f_y) and the horizontal channel (f_x) are approximately constant. The air flow rate (\dot{m}) enters at atmospheric temperature (T_0) and is heated with uniform heat flux (q'') as it flows to the base of the chimney, where its temperature reaches $T_0 + \Delta T$.

10.4 PUMPING EFFECT

The air stream is driven by the buoyancy effect due to the vertical column of hot air (height h_c , temperature $T_0 + \Delta T$), which communicates with the ambient air of the same height and lower temperature (T_0). The net pressure difference that drives the air stream in the tower is (Bejan, 2004)

$$\Delta p = \rho_{T_0} g h_c - \rho_{T_0 + \Delta T} g h_c = \rho \beta g h_c \Delta T \quad (10.1)$$

where ρ is the average air density, and β is the coefficient of volumetric thermal expansion.

The pumping effect Δp is opposed by friction forces in the vertical tube (Δp_y) and in the horizontal channel (Δp_x) and the acceleration due to flow area reduction (Δp_{acc}).

For the vertical tube, we write (Bejan, 1993)

$$\Delta p_y = f_y \frac{2h_c}{r_c} \frac{1}{2} \rho V_y^2 \quad (10.2)$$

where $V_y = \dot{m} / (\rho \pi r_c^2)$. The pressure loss along the horizontal channel is determined from a balance of flow resistance

$$A_{flow} \Delta p_x = \tau_w 2\pi r_r^2 \quad (10.3)$$

where $A_{flow} = 2\pi r_r h_r$, τ_w is the wall shear stress, and $2\pi r_r^2$ represents the roof and ground surface in the horizontal channel for shear stress computation. The wall shear stress in terms of friction factor is defined as (Bejan, 1993)

$$\tau_w = f_x \frac{1}{2} \rho V_x^2 \quad (10.4)$$

Consequently, the pressure loss in the horizontal passage is

$$\Delta p_x = f_x \frac{r_r}{h_r} \frac{1}{2} \rho V_x^2 \quad (10.5)$$

where V_x is the average air velocity at the entrance, $V_x = \dot{m} / (\rho 2\pi r_r h_r)$. The horizontal flow experiences acceleration and heating in a channel with variable cross-sectional area A_c (Chitsomboon, 2001)

$$dp = \frac{\rho V^2}{(1-M^2)} \left(\frac{dA_c}{A_c} - \frac{q'' dA_r}{\dot{m} c_p T} \right) \quad (10.6)$$

Next we assume that in the horizontal flow q'' , c_p , ρ and T are approximately constant. The Mach number, M , is negligible, and Eq. (10.6) reduces to

$$\Delta p_{acc} = \frac{\dot{m}^2}{2\rho_0} \left(\frac{1}{A_2^2} - \frac{1}{A_1^2} \right) - \frac{\dot{m}q''}{2\pi h_r^2 \rho_0 c_p T_0} \ln \frac{r_r}{r_c} \quad (10.7)$$

where 1 and 2 denote the channel entrance and channel exit, respectively. This equation shows that the pressure increases due to heat addition (the second term) while it decreases due to flow area reduction towards the roof center (the first term). An order of magnitude analysis reveals that the first term is much greater than the second term. In addition, because $A_1^2 \gg A_2^2$, Eq. (10.7) becomes

$$\Delta p_{acc} \cong \frac{\dot{m}^2}{2\rho_0 \pi^2 r_c^4} \quad (10.8)$$

The losses balance the driving pressure difference, $\Delta p = \Delta p_y + \Delta p_x + \Delta p_{acc}$, or

$$\rho \beta \Delta T g h_c = f_y \frac{h_c}{r_c} \rho \left(\frac{\dot{m}}{\rho \pi r_c^2} \right)^2 + f_x \frac{r_r}{2h_r} \rho \left(\frac{\dot{m}}{\rho 2\pi r_r h_r} \right)^2 + 2\rho \left(\frac{\dot{m}}{2\rho \pi r_c^2} \right)^2 \quad (10.9)$$

Equation (10.9) relates the flow rate (\dot{m}) to the excess temperature reached at the base of the cylinder (ΔT). The second equation needed for determining \dot{m} and ΔT is the first law of thermodynamics for the horizontal channel as a control volume:

$$q'' \pi r_c^2 = \dot{m} c_p \Delta T \quad (10.10)$$

We assumed that r_c is considerably smaller than r_r (cf. $A_1^2 \gg A_2^2$), so that the area serving as solar collector is roughly πr_r^2 , instead of $\pi(r_r^2 - r_c^2)$. By eliminating ΔT between Eqs. (10.9) and (10.10), we obtain

$$\dot{m}^3 = \frac{C_1 r_r^2 h_c}{\frac{C_2 h_c}{r_c^5} + \frac{C_3}{r_r h_r^3} + \frac{16}{r_c^4}} \quad (10.11)$$

where $C_{1,2,3}$ are three constants

$$C_1 = \frac{\rho^2 \beta g q'' \pi^3}{8 c_p} \quad (10.12)$$

$$C_2 = f_y / 8 \quad (10.13)$$

$$C_3 = f_x / 64 \quad (10.14)$$

The corresponding excess temperature at the base of the tower is

$$\Delta T = \frac{\pi q'' r_r^2}{\dot{m} c_p} \quad (10.15)$$

10.5 MORE AIR FLOW RATE

To see how the geometry influences the air mass flow rate, assume that the smaller dimensions (r_c, h_r) are fixed. In this case, \dot{m} increases monotonically with the tower height (h_c) when the roof radius (r_r) is fixed. On the other hand, if h_c is fixed, then \dot{m} increases monotonically with r_r . The large dimensions (h_c, r_r) cannot

increase independently because the global size of the installation is constrained. One global constraint is the weight of the whole plant, which is proportional to the surface area of the chimney and the roof,

$$A = 2\pi r_c h_c + \pi r_r^2 \quad (10.16)$$

To maximize the \dot{m} function (10.11) with respect to h_c and r_r , subject to constraint (10.16), is equivalent to seeking the extremum of the aggregate function formed by combining the right sides of Eqs. (10.11) and (10.16),

$$\Phi = \frac{C_1 r_r^2 h_c}{\frac{C_2 h_c}{r_c^5} + \frac{C_3}{r_r h_r^3} + \frac{16}{r_c^4}} + \lambda (2r_c h_c + r_r^2) \quad (10.17)$$

where λ is a Lagrange multiplier. Because h_c and r_r are of the same order, and both h_c and r_r are much greater than r_c and h_r , the terms $C_2 h_c / r_c^5$ and $1 / r_c^4$ dominate $C_3 / r_r h_r^3$ in the denominator of the first term on the right side of Eq. (10.17). Solving $\partial \Phi / \partial h_c = 0$ and $\partial \Phi / \partial r_r = 0$, and eliminating λ , we obtain

$$r_r = (C_2 h_c^2 + 2r_c h_c)^{1/2} \quad (10.18)$$

and the maximized air flow rate

$$\dot{m}_{\max} = \left(\frac{C_1 C_2 h_c^3 + C_1 2r_c h_c^2}{\frac{C_2 h_c}{r_c^5} + \frac{16}{r_c^4}} \right)^{1/3} \quad (10.19)$$

Note that h_r is neglected in Eq. (10.19) because of the order of magnitude reasoning. As a result, Eq. (10.19) shows only the effect of r_c , which until now was assumed fixed.

10.6 MORE POWER

The generation of power calls for a design that maximizes \dot{m} and Δp as a product, i.e. not \dot{m} alone. The thermodynamic ideal level of the power produced by a turbine inserted in a duct with the air stream \dot{m} driven by the pressure difference Δp is

$$\dot{W} \sim \dot{m}\Delta p/\rho \sim C_4 h_c r_r^2 \quad (10.20)$$

where

$$C_4 = \frac{\beta g q'' \pi}{c_p} \quad (10.21)$$

To determine the optimal h_c and r_r for which \dot{W} is maximized, we construct the linear combination of Eqs. (10.20) and (10.16),

$$\Psi = C_4 h_c r_r^2 + \lambda (2r_c h_c + r_r^2) \quad (10.22)$$

Again, after eliminating λ we obtain $h_c = r_r^2/(2r_c)$, or

$$\frac{h_c}{r_r} = \frac{(A/2\pi)^{1/2}}{2r_c} \quad (10.23)$$

The maximized power level that corresponds to the optimal configuration is

$$\dot{W}_{\max} = C_4 \frac{A^2}{8\pi^2 r_c} \quad (10.24)$$

This result shows that the power level increases rapidly as the available size increases. If $A^{1/2}$ represents the length scale of the entire flow system, then it is reasonable to anticipate that r_c will vary more or less in proportion with $A^{1/2}$. This leads to the conclusion that \dot{W}_{\max} scales with $A^{3/2}$.

In addition, because r_c^2 scales with A [cf. Eq. (10.16)], it follows that the maximum power generated per land area ($\dot{W}_{\max}/\pi r_c^2$) varies in proportion with the length scale of the installation, $A^{1/2}$. The important conclusion is that the maximum use of land surface requires the use of larger solar chimney power plants. The existence of “economies of scale” raises the question of how to extract most solar power from an available land area. We consider this fundamental question in Section 10.9.

10.7 VOLUME CONSTRAINT

An alternative to the wall area (or weight) constraint (10.16) is the total volume constraint,

$$Vol = \pi r_c^2 h_c + \pi r_r^2 h_r \quad (10.25)$$

The results of maximizing \dot{W} of Eq. (10.20) subject to the volume constraint are

$$\frac{h_c}{r_r^2} = \frac{h_r}{r_c^2} \quad (10.26)$$

$$r_r^2 = \frac{Vol}{2\pi h_r} \quad (10.27)$$

$$\dot{W}_{\max} = \frac{C_4 (Vol)^2}{4\pi^2 h_r r_c^2} \quad (10.28)$$

Once again, the power output increases with the total size squared. If h_r and r_c scale with the linear scale of the entire installation, $(Vol)^{1/3}$, then \dot{W}_{\max} scales with Vol , not $(Vol)^2$. In this case, the power produced per unit of land area $(\dot{W}_{\max}/\pi r_r^2)$ increases with $Vol/(Vol)^{2/3} = (Vol)^{1/3}$, which represents the length scale of the power plant. In conclusion, the economies-of-scale trend is the same as at the end of the preceding section.

10.8 MODEL VALIDATION

The work presented in Sections 10.5 and 10.6 was based on scale analysis. In order to validate its conclusions [Eqs. (10.24) and (10.28)], we also developed a detailed mathematical model for the flow in a solar chimney. The pressure change due to acceleration in the collector is computed using Eq. (10.7). The temperature is estimated from the energy equation across the roof portion

$$T_2 = T_1 + \frac{q'' A_r}{\dot{m} c_p} \quad (10.29)$$

The pressure changed along the chimney can be calculated from the momentum equation for flow through a constant area vertical tube,

$$p_3 = p_4 + \frac{1}{2}(\rho_3 + \rho_4)gh_c + \left(\frac{\dot{m}}{A_c}\right)^2 \left(\frac{1}{\rho_4} - \frac{1}{\rho_3}\right) \quad (10.30)$$

The hydrostatic equilibrium requires that

$$\frac{dp}{dz} = -\rho g \quad (10.31)$$

According to Calvert (1990), when the atmospheric air parcel is regarded as unsaturated medium and expands slowly to a lower atmospheric pressure without exchange of heat, the rate of temperature change with altitude is written as

$$T = T_1 - \frac{g}{c_p} z \quad (10.32)$$

Because air behaves as an ideal gas, Eqs. (10.31) and (10.32) yields

$$p_4 = p_1 \left(1 - \frac{g}{c_p T_1} h_c\right)^{c_p/R} \quad (10.33)$$

Consider that a dry adiabatic lapse rate can be applicable to the flow in a tower.

In accordance with Eq. (10.32),

$$T_4 = T_3 - \frac{g}{c_p} h_c \quad (10.34)$$

and

$$\rho_2 = \frac{p_2}{RT_2}, \rho_3 = \frac{p_3}{RT_3}, \rho_4 = \frac{p_4}{RT_4} \quad (10.35)$$

The turbine is not modeled in this analysis: the flow properties at point 2 are the same as those at point 3. The pressure potential is the available pressure difference between the tower base and the surroundings, therefore the available turbine power is

$$\dot{W} = \frac{\dot{m}}{\rho_2/2}(p_1 - p_2) \quad (10.36)$$

The application of the computational fluid dynamics code (ANSYS, 2005) has been carefully investigated and validated in Koonsrisuk and Chitsomboon (2007). Consequently, to verify the present model, we first compared its results with those of CFD simulations. Fig. 10.2 shows that the results of the model agree very well with those of CFD computations.

To validate Eqs. (10.24) and (10.28), we based the calculations on the Manzanares prototype. The collector had a diameter of 244 m and a height of 1.85 m, and it had a 194.6 m high chimney with a diameter of 10.16 m. Koonsrisuk and Chitsomboon (2009) tested several published mathematical models and found that changing h_r does not affect noticeably the power or efficiency of the system. Here we investigated two scenarios when h_c and r_r varied while r_c and h_r were kept constant and when h_c and r_c varied while r_r and h_r were kept constant. The constraints were fixed area or fixed volume.

Figure 10.3 shows that when we vary h_c and r_r the theoretical maximal power is in agreement with the prediction of Eqs. (10.24) and (10.28) for both cases of fixed surface and fixed volume. Because $h_c/r_r^2 = 1/(2h_r)$ when the surface is fixed [cf. Eq. (10.23)], and $h_c/r_r^2 = h_r/r_c^2$ when the volume is fixed [cf. Eq. (10.26)], we find that the optimal h_c of the fixed surface case is higher than the h_c for fixed volume (r_r, h_r and r_c are the same), resulting in more power when the surface is fixed.

Note from Fig. 10.3 that the case with fixed r_r and volume offers the highest maximal power. However, we cannot use Eq. (10.20) to determine the optimal chimney geometry (h_c and r_c relation). The highest maximal power occurs somewhere between the predictions made with Eqs. (10.24) and (10.28). In conclusion, we can use Eq. (10.24) to determine the optimal h_c/r_r^2 , and the optimal relation between h_c and r_c should be the subject of continuing research.

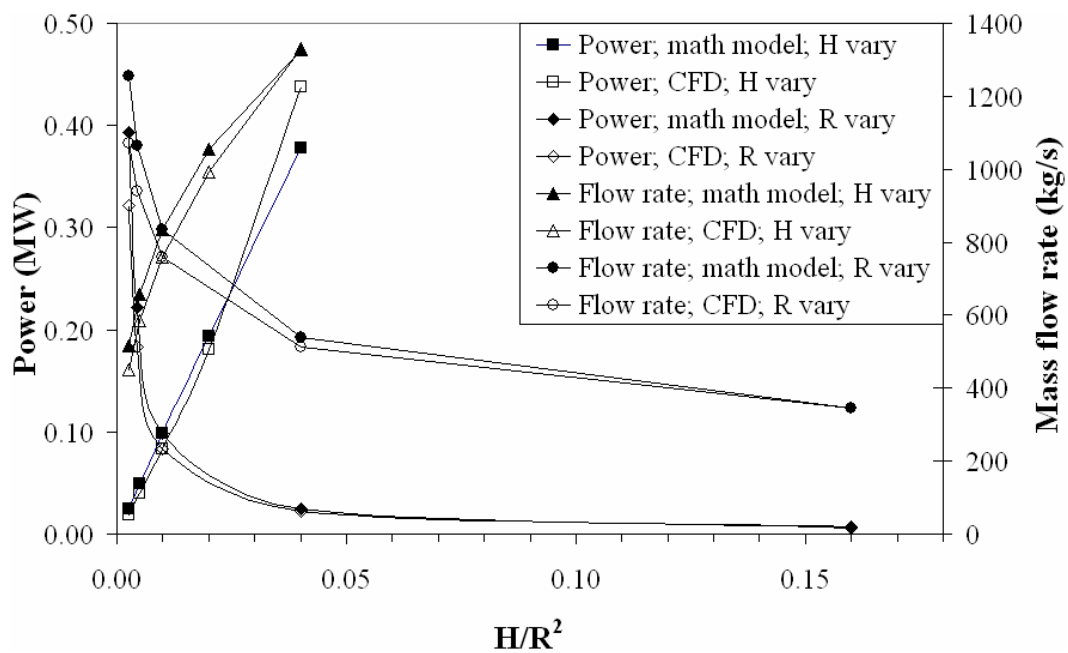


Figure 10.2 Comparison between theoretical model and numerical model

(In the figure H and R represent h_c and r_r , respectively).

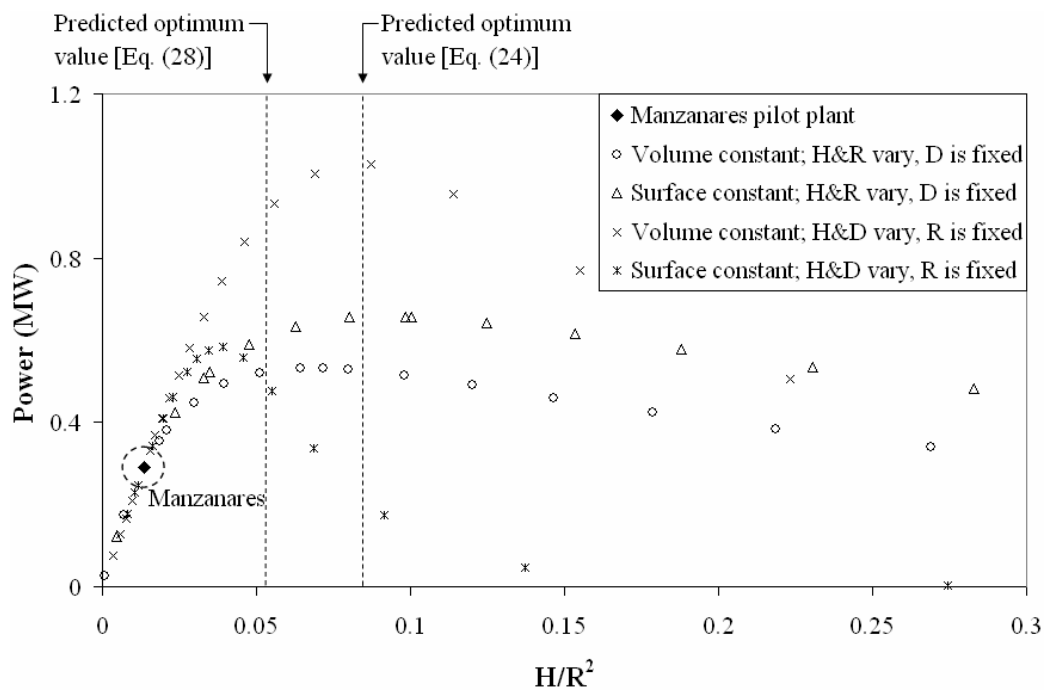


Figure 10.3 The power predictions from theoretical model (In the figure H , D and R represent h_c , $2r_c$ and r_r , respectively).

10.9 ADDITIONAL LOSSES

In the scale analysis of Section 3, only the pressure losses due to friction in the collector and chimney and due to acceleration in the collector were taken into consideration. In a real plant there are other losses, such as the collector inlet pressure drop (Δp_{inlet}), the local loss at the transition section between the collector outlet and the chimney inlet ($\Delta p_{junction}$) and the drag pressure drop due to obstructions such as supports or internal braces inside the collector and chimney. To justify the validity of the analysis of Section 3, we evaluated and compared the magnitude of these additional losses.

The effect of drag is not considered in the present study because we focus on the system with the simplest geometry first, i.e. collector and chimney without obstructions. Therefore we include Δp_{inlet} , Δp_{acc} [cf. Eq. (10.7)], Δp_x [cf. Eq. (10.5)], $\Delta p_{junction}$ and Δp_y [cf. Eq. (10.2)] into the model presented in Section 10.7. In Kröger and Buys (2001), the collector inlet pressure drop is defined as

$$\Delta p_{inlet} = K_{inlet} \rho_1 V_1^2 / 2 + \rho_1 V_1^2 / 2 \quad (10.37)$$

where K_{inlet} is the collector inlet loss coefficient and Hedderwick (2001) recommended $K_{inlet} = 1$. The pressure drop at the collector-to-chimney transition section is

$$\Delta p_{junction} = \varepsilon_{junction} \rho_2 V_2^2 / 2 \quad (10.38)$$

where $\varepsilon_{junction}$ is the loss coefficient at the junction. This coefficient depends on the inlet guide vane (IGV) stagger angle and the ratio of h_r/r_c . Kirstein and von Backström (2006) developed a semi-empirical formula to predict this coefficient. If the IGV stagger angle and h_r/r_c are 22.5° and 0.356, the loss coefficient is 0.056.

To evaluate the wall friction loss coefficient, we adopted from Von Backström *et al.* (2003) the chimney wall friction loss coefficient $f_y = 0.00846$. In addition, according to the numerical simulations the Reynolds number based on collector's diameter was of order 10^6 , therefore we use the relation $f_x = 0.046 \text{Re}^{-1/5}$ (Bejan, 1993) for collector wall friction.

To investigate the effect of power plant geometry on the significance of junction and other local losses, we used the concept of svelteness S_v , which is the global geometric property defined as (Lorente and Bejan, 2005)

$$S_v = \frac{r_r + h_c}{\left(\pi r_r^2 h_r + \pi r_c^2 h_c\right)^{1/3}} \quad (10.39)$$

The svelteness is the ratio between the external length scale and the internal length scale of the system. The external length scale is the distance from the roof entrance to the chimney top. The internal length scale is $\text{Vol}^{1/3}$, where Vol is the internal flow space of the entire system.

The numerical part of the analysis was conducted for the Manzanares plant with varying h_c and r_r . From the results plotted in Fig. 10.4 we see that Δp_{inlet} and $\Delta p_{junction}$ are negligible when compared with Δp_{acc} . This means that the neglect of local losses in Section 10.3 is justified.

Furthermore, Δp_x can be neglected when r_r is fixed and h_c is varied. On the other hand, when r_r is varied and h_c is fixed, $\Delta p_x/\Delta p_{acc}$ increases sharply when Sv approaches approximately 6. It is evident from Eq. (10.39) that Sv decreases as r_r increases. Therefore, when $Sv > 6.5$ the losses due to Δp_{inlet} , $\Delta p_{junction}$ and Δp_x can be neglected, and the analysis is much simpler. The threshold $Sv > 6.5$ is in good agreement with the $Sv > 10$ threshold derived in Ref. [1] for the design domain where local pressure losses are negligible.

10.10 FEW LARGE, OR MANY SMALL?

Larger power plants produce more power per unit of territory, and this can be exploited for benefit on a large fixed territory that is to be covered completely with power plants. To begin with, the power produced per unit area ($\dot{W}/\pi r_r^2$) is synonymous with the energy conversion efficiency of the power plant,

$$\eta = \frac{\dot{W}}{q'' \pi r_r^2} \quad (10.40)$$

because the solar heat input per unit area (q'') is a constant parameter of the region. The conclusion that η increases with the size of the installation (R , $A^{1/2}$, or $Vol^{1/3}$) agrees qualitatively with observations of scaling in power plants and refrigeration plants across the board (Kim *et al.*, 2009). The larger installations are more efficient.

This scaling has two important implications in energy design for global sustainability. The reason is that the surface on which power can be produced is fixed (S), because territory comes at a premium.

The first implication is that the drive toward more power pushes the design toward progressively larger sizes, ultimately toward one power plant assigned to an area of order S . Progress in this direction is not always possible. From the point of view of producing useful power per unit area, one counterproductive aspect of a larger area served by a single power plant is that the access of all the flows (in, out) that serve the power plant (and the inhabitants who depend on it) is impeded when the area increases. Every stream that flows has a flow rate that increases with S , and must overcome a resistance that increases with the distance that the stream travels, namely $S^{1/2}$.

For example, if the stream is the power generated by the solar plant, then the stream is proportional to ηS (or $S^{3/2}$), and the useful power destroyed in order to distribute the stream on S increases as $S^{3/2} \cdot S^{1/2} = S^2$. This means that the net power that reaches the population living on S has two components, one positive and the other negative

$$\dot{W}_{net} = aS^{3/2} - bS^2 \quad (10.41)$$

where (a, b) are two constants fixed by the technology of the time. When the two components are in balance, the net power is maximum. This happens when the surface allocated to the single (large) power plant has an optimal size,

$$S_0 \sim \left(\frac{a}{b}\right)^2 \quad (10.42)$$

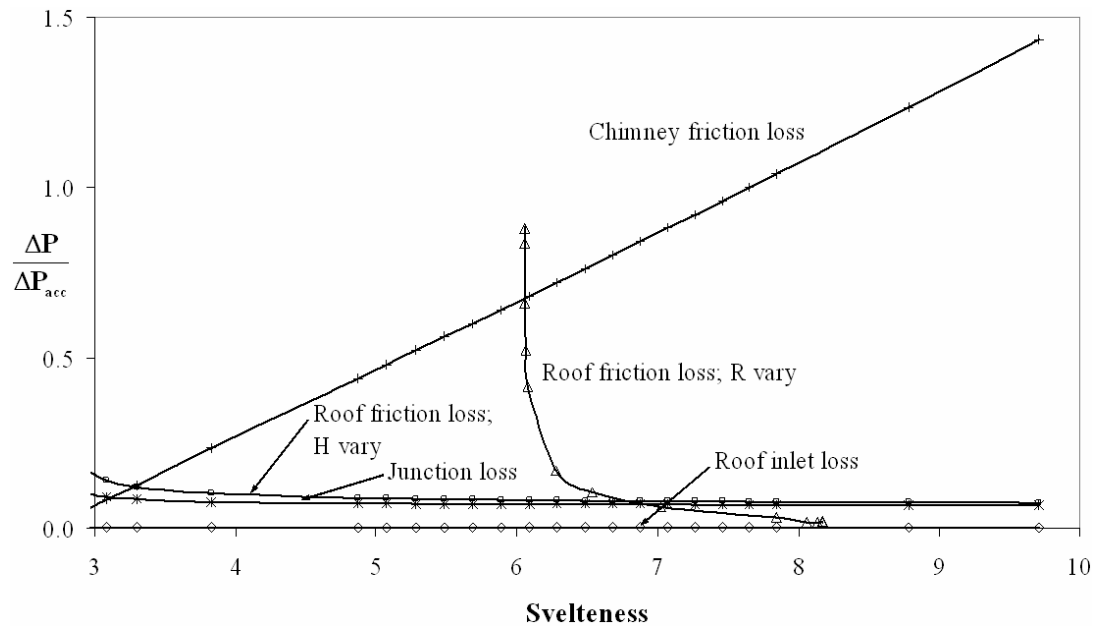


Figure 10.4 Pressure losses scaled by the pressure acceleration in a collector as a function of svelteness.

In this case $\dot{W}_{net,max}$ scales as a $S_0^{3/2}$, and the efficiency scales as $S_0^{1/2}$. One power plant on a larger surface would be more efficient and more productive, but it will be less efficient in its ability to distribute the power to its users on the area.

The second implication is this: because the largest size of a single power plant is fixed by the technology tradeoff shown in Eq. (10.41), how should a larger territory ($X^2 \gg S_0$) be covered with power plants of fixed size? Should X^2 be covered by a few large power plants, or by many small power plants? And, in what pattern, i.e. in what arrangement on the map?

To illustrate this second aspect of global design, consider the square territory designs shown in Fig. 10.5, where one disc area plays the role of S_0 in the preceding discussion. Each disc of diameter D_i is the land area allocated to the power plant of size πR_i^2 . The size D_i scales with R_i , and $D_i \gg R_i$. The power generated on the square territory by all the power plants is proportional to the sum:

$$\Sigma = n_0 D_0^3 + n_1 D_1^3 + n_2 D_2^3 + \dots \quad (10.43)$$

where n_0, n_1, n_2, \dots are the numbers of discs of sizes D_0, D_1, D_2, \dots that are inscribed in the area $X \times X$. The diameters D_i are cubed because of the earlier discussion, where the power generated by one plant increases as $S_0^{3/2}$, i.e. as the length scale cubed. Because the territory X^2 is fixed, we may use X as length scale to nondimensionalize all the D_i 's,

$$\tilde{D}_i = D_i / X \quad (10.44)$$

such that Eq. (10.43) becomes

$$\frac{\Sigma}{X^3} = n_0 \tilde{D}_0^3 + n_1 \tilde{D}_1^3 + n_2 \tilde{D}_2^3 + \dots \quad (10.45)$$

There is an infinite number of ways in which to fill the square with discs of many sizes, such that the largest has a diameter D_0 of order X [or of order $S_0^{1/2}$, cf. Eq. (10.42)]. In the design of Fig. 10.5a, the disc numbers and diameters are:

$$\begin{aligned} n_0 &= 1 & \tilde{D}_0 &= 1 \\ n_1 &= 1 & \tilde{D}_1 &= 2^{1/2} - 1 = 0.414 \\ n_2 &= 4 & \tilde{D}_2 &= (1.5 - 2^{1/2}) / (1.5 - 2^{-1/2}) = 0.108 \end{aligned} \quad (10.46)$$

The global performance of this design is

$$\frac{\Sigma_a}{X^3} = 1 \cdot (1)^3 + 1 \cdot (2^{1/2} - 1)^3 + 4 \cdot \left((1.5 - 2^{1/2}) / (1.5 - 2^{-1/2}) \right)^3 + \dots \cong 1.076 \quad (10.47)$$

Consider next a design where the largest power plants are more numerous, e.g. Fig. 10.5b. The downside of such a design is that when n_0 increases D_0 decreases.

The design of Fig. 10.5b has the following numbers and sizes of power discs:

$$\begin{aligned} n_0 &= 2 & \tilde{D}_0 &= 2^{-1/2} = 0.707 \\ n_1 &= 2 & \tilde{D}_1 &= 1 - 2^{-1/2} = 0.293 \\ n_2 &= 8 & \tilde{D}_2 &= \frac{3 - 2^{3/2}}{3 \cdot 2^{1/2} - 2} = 0.077 \end{aligned} \quad (10.48)$$

The global power generation rate in Fig. 10.5b is

$$\frac{\sum_b}{X^3} = 2 \cdot (2^{-1/2})^3 + 2 \cdot (1 - 2^{-1/2})^3 + 8 \cdot \left(\frac{3 - 2^{3/2}}{3 \cdot 2^{1/2} - 2} \right)^3 + \dots \cong 0.761 \quad (10.49)$$

The power decreases by 29 percent in going from design (a) to design (b).

Another possible design is shown in Fig. 10.5c, where the plant sizes, numbers and global performance are as follows:

$$\begin{aligned} n_0 &= 4 & \tilde{D}_0 &= 2^{-1} = 0.5 \\ n_1 &= 4 & \tilde{D}_1 &= 2^{-1/2} - 2^{-1} = 0.207 \\ n_2 &= 16 & \tilde{D}_2 &= \frac{3 - 2^{3/2}}{2(3 - 2^{1/2})} = 0.054 \end{aligned} \quad (10.50)$$

$$\frac{\sum_c}{X^3} = 4 \cdot (2^{-1})^3 + 4 \cdot (2^{-1/2} - 2^{-1})^3 + 16 \cdot \left(\frac{3 - 2^{3/2}}{6 - 2^{3/2}} \right)^3 + \dots \cong 0.538 \quad (10.51)$$

This power level is half of that of design (a). Note further that pattern (c) is the same as pattern (a), and that the length scale of the discs on (c) are half of the length scale on (a). In conclusion, if all the area elements shrink by a factor of 1/4 (because all the D_i 's are reduced by 1/2), then the aggregate power output of the $X \times X$ territory decreases by 1/2.

The patterns in Figs. 10.5a – c are diagonally symmetric. In order to increase the D_0 scale, the pattern must be asymmetric, as in Figs. 10.5d, e. For the design of Fig. 10.5d we obtain

$$\begin{aligned} n_0 &= 1/2 & \tilde{D}_0 &= 2^{1/2} = 1.414 \\ n_1 &= 2 & \tilde{D}_1 &= 2 + 2^{1/2} - 2 \cdot (1 + 2^{1/2})^{1/2} = 0.307 \\ n_2 &= 2 & \tilde{D}_2 &= 0.109 \end{aligned} \quad (10.52)$$

$$\frac{\sum_d}{X^3} \cong 1.475 \quad (10.53)$$

Here the power output is greater than in design (a). One reason is that the largest scale of design (d) (namely $D_{0,d}$) is 1.41 times larger than the D_0 scale in design (a). If we recalculate Eq. (10.53) by reducing all the D_i 's by the factor $(1.41)^{-1} = 0.71$ and adding more discs under an equivalence relation to cover the whole land area (as shown in Fig. 10.6d), the value of \sum_d/X^3 becomes approximately 1.049. This is comparable with the performance of design (a).

The corresponding geometry and performance of the design of Fig. 10.5e are

$$\begin{aligned} n_0 &= 1/4 & \tilde{D}_0 &= 2 \\ n_1 &= 1 & \tilde{D}_1 &= \frac{2^{3/2} - 2}{1 + 2^{1/2}} = 0.343 \\ n_2 &= 2 & \tilde{D}_2 &= \frac{(2 - \tilde{D}_1)^2}{8 \cdot (2^{1/2} + \tilde{D}_1^{1/2})} = 0.172 \\ n_3 &= 2 & \tilde{D}_3 &= \frac{2\tilde{D}_2}{2 + 2^{3/2} \cdot \tilde{D}_2^{1/2} + \tilde{D}_2} = 0.103 \end{aligned} \quad (10.54)$$

$$\frac{\sum_e}{X^3} \cong 2.061 \quad (10.55)$$

This large value is due to the fact that the largest element ($D_{0,e}$) is larger than in all the preceding designs. If $D_{0,e}$ is reduced to the size of $D_{0,a}$, as illustrated in Fig. 10.6e, then the value of \sum_e/X^3 drops from 2.06 to 1.03.

This calculation was performed for designs (b) and (c) as well, so that we may evaluate the five designs on the same basis: the same territory (X) and the same

largest element (D_0). The new version of these designs is shown in Fig. 10.6, where Fig. 10.6a is identical to Fig. 10.5a, and Figs. 10.6b - e derive from Figs. 10.5b - e, respectively. The comparison is presented in Table 10.1. The highest performance is offered by design (b), in which n_0 is the largest when compared with other designs.

In conclusion, the power generated depends primarily on the land area occupied by the largest plant. To investigate this effect more closely, we define the dimensionless measure

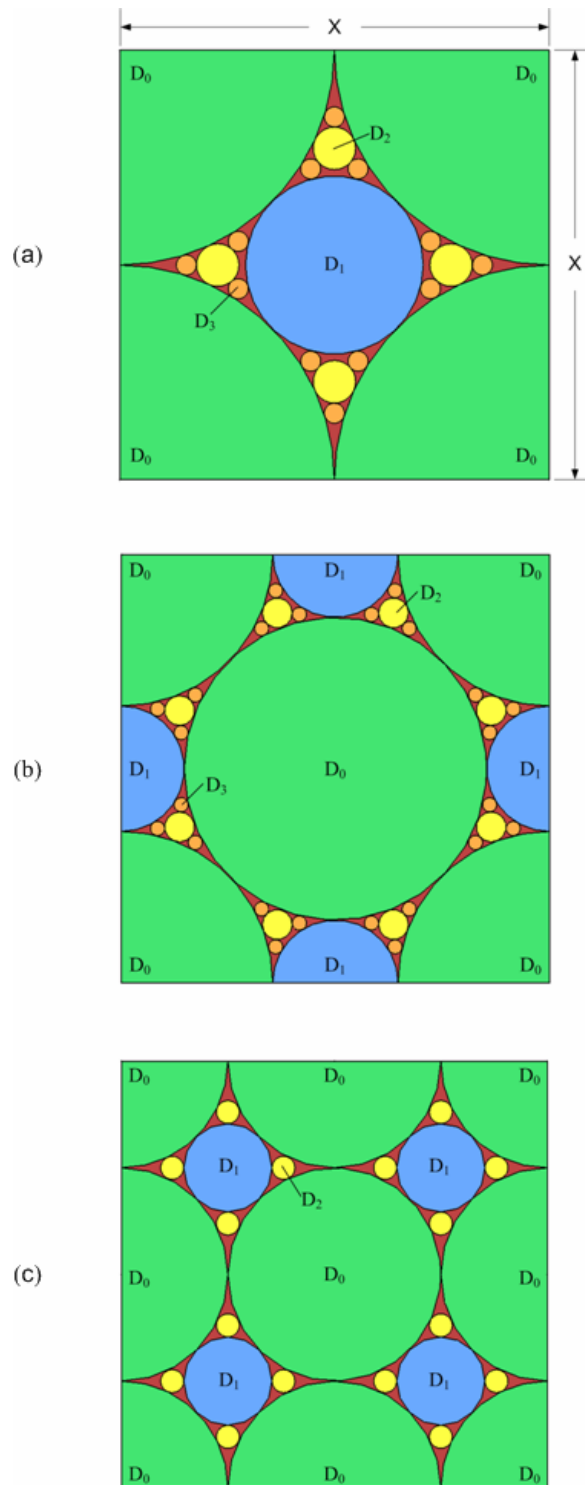


Figure 10.5 Designs of the projection pattern for multi-scale solar chimneys on the square land.

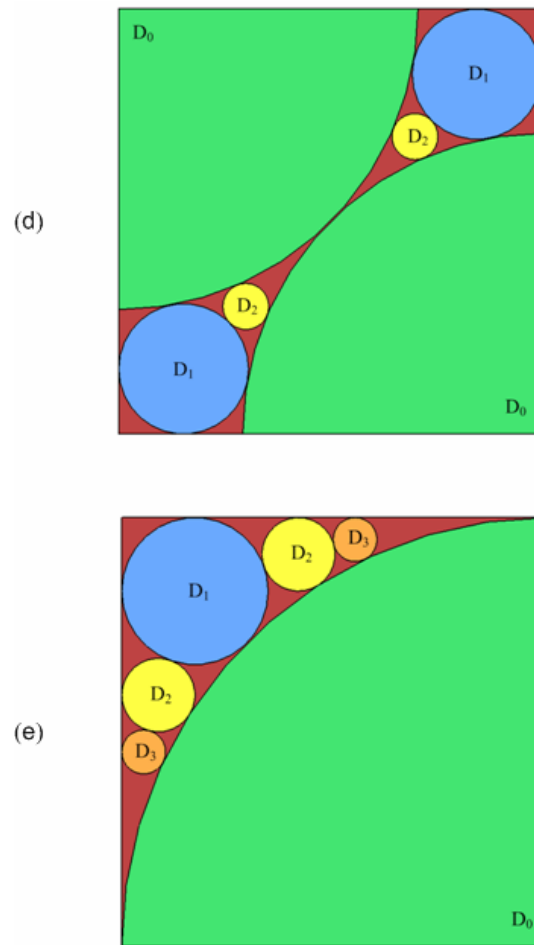


Figure 10.5 Designs of the projection pattern for multi-scale solar chimneys on the square land (Continued).

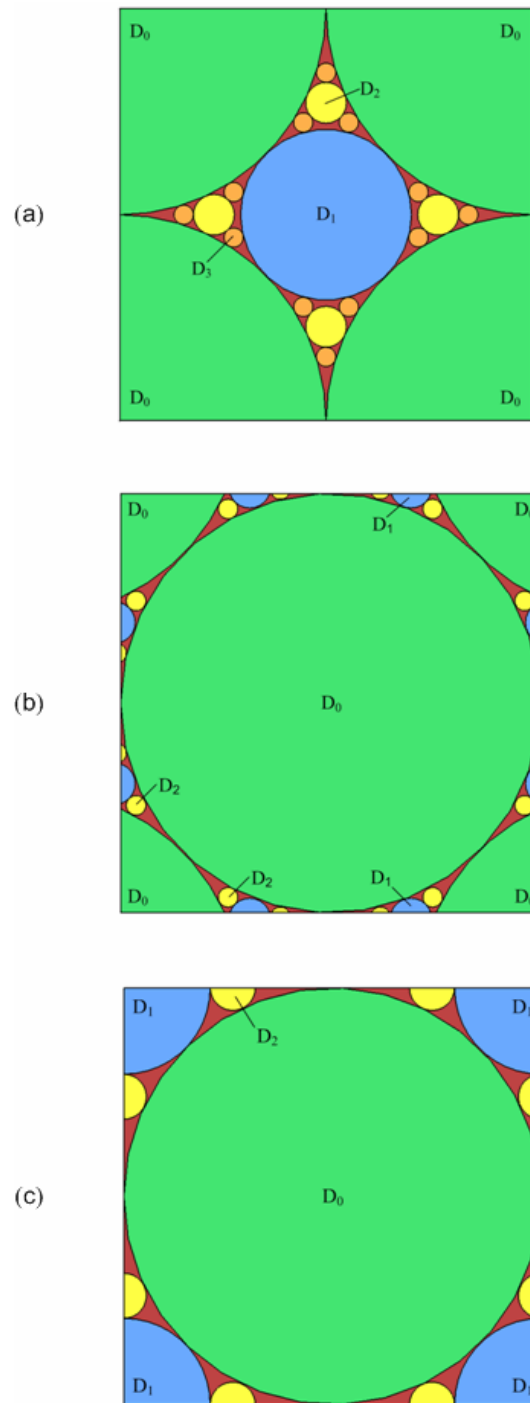


Figure 10.6 Redesign of the patterns in Fig. 10.5, in which all designs share the same territory (X) and the same largest element (D_0) (Fig. 10.6a is exactly the same as Fig. 10.5a).

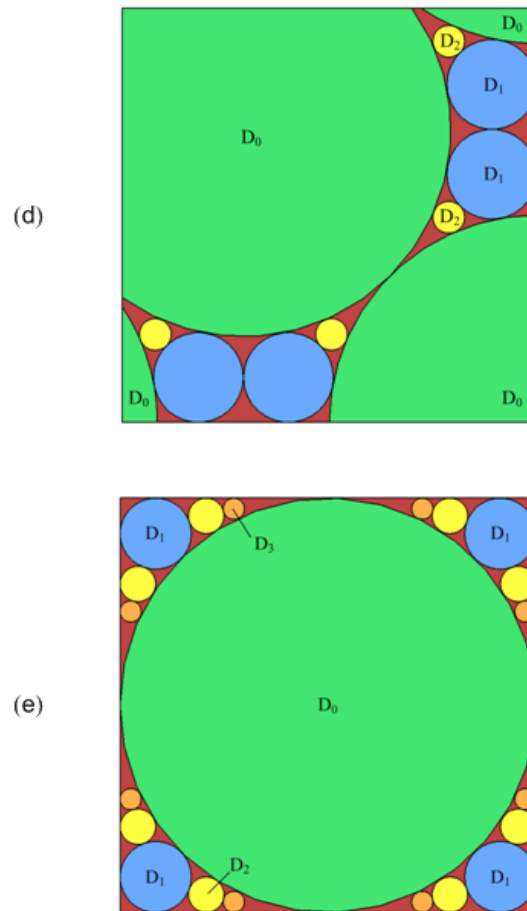


Figure 10.6 Redesign of the patterns in Fig. 10.5, in which all designs share the same territory (X) and the same largest element (D_0)

(Note: Fig. 10.6a is exactly the same as Fig. 10.5a) (Continued).

Table 10.1 The global power output of the multi-size arrangements (a) – (e) shown in Fig. 10.6 when the largest length scale (D_0) is the same in all the arrangements.

Design	Σ/X^3
a	1.076
b	1.199
c	1.076
d	1.049
e	1.025

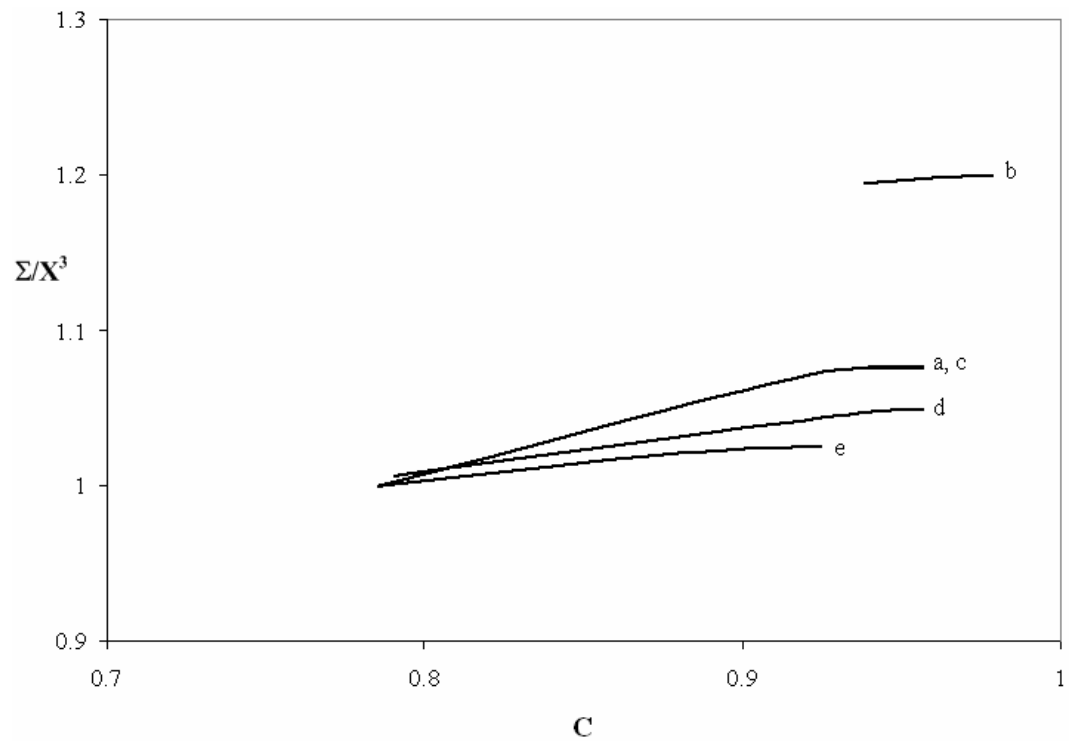


Figure 10.7 Compactness [cf. Eq. (10.56)] and dimensionless power [cf. Eq. (10.45)] of the power plants in Fig. 10.6.

$$\text{Compactness, } C = \frac{\text{area covered by power plants}}{\text{land area}} \quad (10.56)$$

More specifically,

$$C_0 = \frac{A_{D_0}}{X^2}, \quad C_{0,1} = \frac{A_{D_0} + A_{D_1}}{X^2}, \quad C_{0,1,2} = \frac{A_{D_0} + A_{D_1} + A_{D_2}}{X^2} \quad (10.57)$$

Figure 10.7 shows the comparison of the compactness between each pattern in Fig. 10.6 as a function of their corresponding dimensionless power output, Σ/X^3 . In this comparison the largest length scale of the pattern (D_0) is the same for all five patterns. Each curve in Fig. 10.7 is the result of curve-fitting three points that correspond to $C_0, C_{0,1}$ and $C_{0,1,2}$ of each design.

It is apparent from the results plotted in Fig. 10.7 that Σ/X^3 is a weak function of compactness. In other words, the global performance depends mainly on the land area used. Again, the Σ/X^3 value of design b is greater than those of other designs because it has the biggest n_0 . It should be noted that n_0 is the same in designs a, c, d and e, but the Σ/X^3 values of these designs are different. The trend now becomes a function of the D_1 value of each design. To conclude, the efficiency in power production of large plants is better than small plants, and an economy of scale emerges.

10.11 CONCLUSION

In this paper we presented the optimal solar chimney power plant configurations, based on the method of constructal design. The maximum mass flow rate and maximum flow power in terms of geometry are proposed. It was found that the maximum flow power is the function of plant length scale. Results indicate that the larger plants produce more power per unit of territory. Comparisons between the maximum power proposed and the prediction of the detailed mathematical model are also presented. The inclusion of pressure losses into the analysis indicated that the collector inlet pressure drop and the pressure drop over the junction between the collector and chimney are negligible. It was shown that when the svelteness [cf. Eq. (10.39)] is greater than 6.5 the friction loss in the collector can be neglected as well. Though one plant which occupies the whole area might generate the maximum power, but the study shows that it will be less efficient in power distribution. The proposed model demonstrates mathematically that the maximum power production can be obtained by allocating the optimal land area to the plant. This paper also presents some arrangement patterns for the multi-scale plants on the square area. It reveals that, to generate the electricity efficiently, the land area allocated for the largest plant is the most important factor. While the other plants, which are smaller than the largest plant, have only a small contributions to the whole power generated. Hence, there is economy, in the sense of efficiency for power production, to be gained on a larger scale.

10.12 REFERENCES

- ANSYS, Inc. **ANSYS CFX**, Release 10.0: reference guide. ANSYS, 2005.
- Bejan, A., 1993. **Heat Transfer**, Wiley, New York.
- Bejan, A., 2004. **Convection Heat Transfer**, 3rd ed., Wiley, Hoboken, NJ.
- Bejan, A., Lorente, S., 2008. **Design with Constructal Theory**, Wiley, Hoboken, NJ.
- Calvert, J. G., 1990. Glossary of atmospheric chemistry terms (Recommendations 1990). **Pure and applied chemistry**, Vol. 62(11), pp. 2167-2219.
- Chitsomboon, T., 2001. A validated analytical model for flow in solar chimney. **International Journal of Renewable Energy Engineering**, Vol. 3, pp. 339-346.
- EnviroMission's **Solar Tower Of Power**, 2006. [On-line]. Available: <http://seekingalpha.com/article/14935-enviromission-s-solar-tower-of-power>
- Hedderwick, R. A., 2001. **Performance evaluation of a solar chimney power plant**. M.Sc. Eng.-thesis, University of Stellenbosch, Stellenbosch, South Africa.
- Kim, Y. S., Lorente, S., Bejan, A., 2009. Distribution of size in steam turbine power plants, **International Journal of Energy Research**. doi:10.1002/er.1528
- Kirstein, C. F., Von Backström, T. W., 2006. Flow through a solar chimney power plant collector-to-chimney transition section, **ASME Journal of Solar Energy Engineering**, Vol. 128, pp.312–317.
- Koonsrisuk, A., Chitsomboon, T., 2007. Dynamic similarity in solar chimney modeling. **Solar Energy**, Vol. 81, pp.1439-1446.
- Koonsrisuk, A., Chitsomboon, T., 2009. Accuracy of theoretical models in the prediction of solar chimney power plant performance. **Solar Energy**. doi:10.1016/j.solener.2009.05.012.

- Kröger, D. G., Buys, J. D., 2001. Performance evaluation of a solar chimney power plant. **ISES 2001 Solar World Congress**, Adelaide, Australia.
- Lorente, S., Bejan, A., 2005. Svelteness, freedom to morph, and constructal multi-scale flow structures. **International Journal of Thermal Science**, Vol. 44, pp. 1123-1130.
- Maia, C. B., Ferreira, A. G., Valle, R. M., Cortez, M. F. B., 2008. Theoretical evaluation of the influence of geometric parameters and materials on the behavior of the airflow in a solar chimney. **Computers & Fluids**. doi: 10.1016/j.compfluid.2008.06.005
- Pretorius, J. P., Kröger, D. G., 2006. Solar chimney power plant performance. **Journal of Solar Energy Engineering**, Vol. 128, pp.302-311.
- Rohmann, M., 2000. **Solar Chimney Power Plant**. Bochum University of Applied Sciences.
- Schlaich, J., 1995. **The Solar Chimney**. Edition Axel Menges: Stuttgart, Germany.
- Von Backström, T. W., Bernhardt, A., Gannon, A. J., 2003. Pressure drop in solar power plant chimneys, **ASME Journal of Solar Energy Engineering**, Vol. 125 , pp.165–169.
- Zhou, X., Yang, J., Xiao, B., Hou, G., Xing, F., 2009. Analysis of chimney height for solar chimney power plant. **Applied Thermal Engineering**, Vol. 29, pp. 178-185.

CHAPTER XI

CONCLUSION AND RECOMMENDATION

This work investigates the behavior of the flow in solar chimney with the ultimate goal of a better design to obtain a higher efficiency. Dimensional analysis is applied to determine the dimensionless parameters that characterize the flow. CFD study in geometrically similar cases indicated that the proposed dimensionless variables are appropriate for obtaining similarity for flows in prototype and small-scale models of a solar chimney. The study shows that water is not suitable as a test working fluid because the solar heat absorption per unit volume required for similarity is too high. Using air for a small-scale model, though quite natural, requires lower insolation than that of the prototype for dynamic similarity; this requires roof material treatments such as tinting or using artificial insolation, which is difficult in practice.

Further study shows that a complete dynamic similarity for scaled models and a full scale solar chimney prototype, while maintaining the same insolation, is achievable if the model's roof radius is distorted from its fully similar configuration according to a prescribed rule that was proposed in the study. This 'partially similar' proposition is proved to be valid which is evident by the collapse of the scaled numerical results of the widely disparate test cases. The seemingly complicated similarity variables were interpreted simply as the characteristic output power (scaled kinetic energy) and the characteristic input power (scaled buoyant force).

A single dimensionless similarity variable for the solar chimney power plant is proposed and proved to be valid for both the fully similar case and the partially similar case. This should enable the experimental study of a solar chimney power plant to be simpler and more economical. This variable was interpreted as the total kinetic energy scaled by the buoyant energy of the rising hot air. The proposed variable was examined from various perspectives and was found to be related to the overall efficiency proposed by other researchers and also to the Richardson number. The equality of temperature rises across roof portions for the prototype and its fully and partially similar models was observed and explained in the context of similarity.

In addition, the influences of roof height, roof radius, tower height, tower radius, and insolation on solar chimney power plant performances have been studied by using five theoretical models from the literature and a carefully calibrated CFD procedure. Important observations are concluded. According to this study, the models of Schlaich *et al.* (2005) and Koonsrisuk and Chitsomboon (2009) are recommended because they compared more favorably with the CFD results than the other models for all the test cases that were investigated.

Furthermore, a solar chimney system with varying flow area is studied and its performance is evaluated. Theoretical analysis suggests that the solar chimney with sloping collector and divergent-top chimney would perform better than that of a conventional system. CFD calculations show that a divergent tower helps increase the static pressure, mass flow rate and power over that of the constant area tower. For the convergent tower, the power remains the same as the constant area case. The sloping collector helps increase the static pressure across the roof and the power at the roof

entrance. The system with the sloping collector and divergent-top chimney of tower area ratio of 16 can produce power as much as 400 times that of the reference case.

A detailed mathematical model of the solar chimney power plant is developed in order to evaluate the turbine work extraction. It appears that, for the system with a constant pressure potential (available system pressure difference), the optimum ratio of the turbine pressure drop to the pressure potential is $2/3$. For the system with the pressure potential is not constant, it is obvious that this optimum ratio is a function of the plant size and solar heat flux. This study may be helpful in the preliminary plant design.

Through field measurements on four small-scale models built at Suranaree University of Technology, results indicate that the flow power increases with the decrease in the ratio between roof inlet area and tower inlet area. The divergent chimney also results in significant increase in flow power compared to that of the constant area chimney. It was observed that the system with the proposed novel roof shape designed by the researcher provides approximately the same performance as the conventional shaped system, while the ratio of roof inlet area and tower inlet area for the proposed system could be practically reduced. Correspondingly the increase in performance, to some specific value which is much higher than the typical system could be achieved. The experimental results differ comparatively but have the same trends as to the predicted values. This may follow from the fluctuating solar heat flux and the effect of the large chimney diameter when compared with the roof size. Moreover, the difference of dimensionless variables between the large and the small plant is noticeable, contrary to the theoretical and numerical predictions. Reasons could be the varying atmospheric conditions when the tests were run.

The optimal solar chimney power plant configurations are based on the guiding of constructal design, the maximum mass flow rate and maximum flow power in terms of geometry are proposed. It was found that the maximum flow power is a function of plant length scale. Results indicate that the larger plants produce more power per unit of territory. Comparisons between the maximum power proposed and the prediction of the detailed mathematical model are also presented. The inclusion of pressure losses into the analysis indicated that the collector inlet pressure drop and the pressure drop over the junction between the collector and chimney are negligible. It was shown that when the svelteness is greater than 6.5, the friction loss in the collector can be neglected as well. Though one plant occupying the whole area might generate the maximum power, the study shows that it will be less efficient in power distribution. The proposed model demonstrates mathematically that the maximum power production can be obtained by allocating the optimal land area to the plant. This paper also presents some arrangement patterns for the multi-scale plants on the square area. It reveals that, to generate the electricity efficiently, the land area allocated for the largest plant is the most important factor. While the other plants, which are smaller than the largest plant, have only a small contributions to the whole power generated. Hence, there is economy, in the sense of efficiency for power production, to be gained on a larger scale.

APPENDIX A

A SET UP OF THE ANSYS-CFX 10.0 SOLVER

CFX Command Language for Run

LIBRARY:

MATERIAL: Air Ideal Gas

Material Description = Air Ideal Gas (constant Cp)

Material Group = Air Data, Calorically Perfect Ideal Gases

Option = Pure Substance

Thermodynamic State = Gas

PROPERTIES:

Option = General Material

ABSORPTION COEFFICIENT:

Absorption Coefficient = 0.01 [m⁻¹]

Option = Value

END

DYNAMIC VISCOSITY:

Dynamic Viscosity = 1.831E-05 [kg m⁻¹ s⁻¹]

Option = Value

END

EQUATION OF STATE:

Molar Mass = 28.96 [kg kmol⁻¹]

Option = Ideal Gas

END

REFRACTIVE INDEX:

Option = Value

Refractive Index = 1.0 [m m⁻¹]

END

SCATTERING COEFFICIENT:

Option = Value

Scattering Coefficient = 0.0 [m⁻¹]

END

SPECIFIC HEAT CAPACITY:

Option = Value

Reference Pressure = 1 [atm]

Reference Specific Enthalpy = 0. [J/kg]

Reference Specific Entropy = 0. [J/kg/K]

Reference Temperature = 25 [C]

Specific Heat Capacity = 1.0044E+03 [J kg⁻¹ K⁻¹]

Specific Heat Type = Constant Pressure

END

THERMAL CONDUCTIVITY:

Option = Value

Thermal Conductivity = 2.61E-2 [W m⁻¹ K⁻¹]

END

```
END
END
END
EXECUTION CONTROL:
PARALLEL HOST LIBRARY:
  HOST DEFINITION: cad201
    Remote Host Name = CAD2-01
    Host Architecture String = intel_p4.sse2_winnt5.1
    Installation Root = C:\Program Files\ANSYS Inc\CFX\CFX-%v
  END
END
PARTITIONER STEP CONTROL:
  Multidomain Option = Independent Partitioning
  Runtime Priority = Standard
MEMORY CONTROL:
  Memory Allocation Factor = 1.0
END
PARTITIONING TYPE:
  MeTiS Type = k-way
  Option = MeTiS
  Partition Size Rule = Automatic
END
END
RUN DEFINITION:
  Definition File = \
C:/CFX/work/freeWakeT/converdiver_2hr1_4rc4_MC5deg_0p55_0p0381_0p23_r10\
  _RefLo0c0c100_3adap2_inIN_1e7_outAverPs_TotalEnergy_q2p800.def
  Interpolate Initial Values = Off
  Run Mode = Full
END
SOLVER STEP CONTROL:
  Runtime Priority = Standard
EXECUTABLE SELECTION:
  Double Precision = On
END
MEMORY CONTROL:
  Memory Allocation Factor = 1.0
END
PARALLEL ENVIRONMENT:
  Number of Processes = 1
  Start Method = Serial
END
END
END
FLOW:
  DOMAIN: Domain 1
  Coord Frame = Coord 0
  Domain Type = Fluid
```

Fluids List = Air Ideal Gas
Location = B30,B37,B42
BOUNDARY: in
 Boundary Type = INLET
 Location = in
BOUNDARY CONDITIONS:
 FLOW DIRECTION:
 Option = Normal to Boundary Condition
 END
 FLOW REGIME:
 Option = Subsonic
 END
 HEAT TRANSFER:
 Option = Static Temperature
 Static Temperature = 308 [K]
 END
 MASS AND MOMENTUM:
 Option = Total Pressure
 Relative Pressure = 0 [Pa]
 END
END
END
BOUNDARY: out
 Boundary Type = OUTLET
 Location = out
BOUNDARY CONDITIONS:
 FLOW REGIME:
 Option = Subsonic
 END
 MASS AND MOMENTUM:
 Option = Average Static Pressure
 Relative Pressure = 0 [Pa]
 END
 PRESSURE AVERAGING:
 Option = Average Over Whole Outlet
 END
END
END
BOUNDARY: wall
 Boundary Type = WALL
 Location = wall
BOUNDARY CONDITIONS:
 HEAT TRANSFER:
 Option = Adiabatic
 END
 WALL INFLUENCE ON FLOW:
 Option = Free Slip
 END
END

```
END
END
BOUNDARY: ground
  Boundary Type = WALL
  Location = ground
BOUNDARY CONDITIONS:
  HEAT TRANSFER:
    Option = Adiabatic
  END
  WALL INFLUENCE ON FLOW:
    Option = Free Slip
  END
END
END
BOUNDARY: symXp
  Boundary Type = SYMMETRY
  Location = symXp
END
BOUNDARY: symXm
  Boundary Type = SYMMETRY
  Location = symXm
END
DOMAIN MODELS:
  BUOYANCY MODEL:
    Buoyancy Reference Density = 1.146 [kg m^-3]
    Gravity X Component = 0 [m s^-2]
    Gravity Y Component = -9.807 [m s^-2]
    Gravity Z Component = 0 [m s^-2]
    Option = Buoyant
  BUOYANCY REFERENCE LOCATION:
    Cartesian Coordinates = 0 [m], 0 [m], 100 [m]
    Option = Cartesian Coordinates
  END
END
DOMAIN MOTION:
  Option = Stationary
END
REFERENCE PRESSURE:
  Reference Pressure = 1 [atm]
END
END
FLUID MODELS:
  COMBUSTION MODEL:
    Option = None
  END
  HEAT TRANSFER MODEL:
    Option = Total Energy
  END
```

```
THERMAL RADIATION MODEL:
  Option = None
END
TURBULENCE MODEL:
  Option = Laminar
END
END
SUBDOMAIN: insolation
  Coord Frame = Coord 0
  Location = B42
SOURCES:
  EQUATION SOURCE: energy
  Option = Source
  Source = 400 [W m^-3]
  END
  END
  END
  END
INITIALISATION:
  Option = Automatic
INITIAL CONDITIONS:
  Velocity Type = Cartesian
  CARTESIAN VELOCITY COMPONENTS:
  Option = Automatic with Value
  U = 0 [m s^-1]
  V = 0 [m s^-1]
  W = 0 [m s^-1]
  END
  STATIC PRESSURE:
  Option = Automatic
  END
  TEMPERATURE:
  Option = Automatic with Value
  Temperature = 308 [K]
  END
  END
  END
OUTPUT CONTROL:
  RESULTS:
  File Compression Level = Default
  Option = Standard
  END
  END
SIMULATION TYPE:
  Option = Steady State
  END
SOLUTION UNITS:
  Angle Units = [rad]
```

Length Units = [m]
Mass Units = [kg]
Solid Angle Units = [sr]
Temperature Units = [K]
Time Units = [s]
END
SOLVER CONTROL:
ADVECTION SCHEME:
 Option = High Resolution
END
CONVERGENCE CONTROL:
 Length Scale Option = Conservative
 Maximum Number of Iterations = 80000
 Timescale Control = Auto Timescale
END
CONVERGENCE CRITERIA:
 Residual Target = 1.0e-07
 Residual Type = RMS
END
DYNAMIC MODEL CONTROL:
 Global Dynamic Model Control = On
END
PRESSURE LEVEL INFORMATION:
 Cartesian Coordinates = 0 [m], 0 [m], 100 [m]
 Option = Cartesian Coordinates
END
END
COMMAND FILE:
 Version = 10.0
 Results Version = 10.0
END

APPENDIX B

LIST OF PUBLICATIONS

Articles in Refereed Journals (5)

Koonsrisuk, A., Lorente, S. and Bejan, A. (2009). **Constructal solar chimney configuration.** *International Journal of Heat and Mass Transfer.* (accepted)

Koonsrisuk, A. and Chitsomboon, T. (2009). **A single dimensionless variable for solar chimney power plant modeling.** *Solar Energy.*
doi:10.1016/j.solener.2009.07.015.

Koonsrisuk, A. and Chitsomboon, T. (2009). **Accuracy of theoretical models in the prediction of solar chimney performance.** *Solar Energy.*
doi:10.1016/j.solener.2009.05.012.

Koonsrisuk, A. and Chitsomboon, T. (2009). **Partial geometric similarity for solar chimney power plant modeling.** *Solar Energy*, Volume 83, pp. 1611 - 1618.

Koonsrisuk, A. and Chitsomboon, T. (2007). **Dynamic similarity in solar chimney modeling.** *Solar Energy*, Volume 81, pp. 1439 - 1446.

Articles in Conference Proceedings (10)

Koonsrisuk, A. and Chitsomboon, T. (2007). **The Effect of Plant Geometry on the Potential of a Solar Tower,** In *Proceedings of the 11st Annual National Symposium on Computational Science and Engineering*, Phuket, Thailand.

Koonsrisuk, A. and Chitsomboon, T. (2006). **Effect of Tower Area Change on the Potential of Solar Tower.** In *Proceedings of the 2nd Joint International Conference on Sustainable Energy and Environment*, Bangkok, Thailand.

- Koonsrisuk, A. and Chitsomboon, T. (2006). **Partial Similarity in Solar Tower Modeling**. In *Proceedings of the 20th Conference on Mechanical Engineering Network of Thailand*, Nakhon Ratchasima, Thailand.
- Koonsrisuk, A. and Chitsomboon, T. (2005). **Actuator Disc Approximation for the Flow through Turbine in a Solar Tower**. In *Proceedings of the 1st Conference on Energy Network of Thailand*. Chon Buri, Thailand.
- Koonsrisuk, A. and Chitsomboon, T. (2004). **Similarity Analysis in Scale Modeling of a solar chimney**. In *Proceedings of the 18th National Mechanical Engineering Conference*. Khon Khaen, Thailand.
- Koonsrisuk, A. and Chitsomboon, T. (2004). **Frictional effect on the flow in a solar chimney**. In *Proceedings of the 4th National Symposium on Graduate Research*. Chiang Mai, Thailand.
- Koonsrisuk, A. and Chitsomboon, T. (2004). **The study of dynamic similarity in physical modeling of a solar chimney**. In *Proceedings of the RGJ Seminar Series 29: Engineering Applications*. Chiang Mai, Thailand.
- Koonsrisuk, A. and Chitsomboon, T. (2004). **Dynamic similarity in model testing of the flow in solar chimney**. In *Proceedings of the 15th International Symposium on Transport Phenomena*. Bangkok, Thailand.
- Koonsrisuk, A. and Chitsomboon, T. (2004). **The effect of roof height to the flow in solar chimney**. In *Proceedings of the RGJ-Ph.D. Congress V*. Chon Buri, Thailand.
- Koonsrisuk, A. and Chitsomboon, T. (2003). **Dimensional analysis for the flow through a solar chimney**. In *Proceedings of the 17th National Mechanical Engineering Conference*. Prachin Buri, Thailand, pp. EM56 - EM61.

BIOGRAPHY

Atit Koonsrisuk was born in Ubon Ratchathani Province on August 11, 1974, the son of Kaehua Saekoo and Neeracha Koonsrisuk. He attended high school at Sisaket Wittayalai in Sisaket Province and graduated in 1992. Atit received his Bachelor of Engineering degree in Mechanical Engineering from Suranaree University of Technology in 1997. In 1999, he enrolled in the Master's degree program in the School of Mechanical Engineering at Suranaree university of Technology. Later, he was awarded a scholarship for a Doctoral Degree, so he enrolled in the Ph.D. Program of the same School in 2002.

During his graduate work, Atit worked as a teaching assistant in the School of Mechanical Engineering. He was awarded a Royal Golden Jubilee (RGJ) Ph.D. Program Scholarship from the Thailand Research Fund (TRF) in 2002. He was also a recipient of the Basic Research Grant (BGJ) from the Thailand Research Fund (TRF) in 2004. In October 2008, he was a Visiting Scholar in the Constructal Design Group at Duke University, USA, with Prof. Adrian Bejan and Prof. Sylvie Lorente. His research focuses on optimizing the design of a solar chimney power plant.